

Chaos in the Buck Converter

by

Gerard Olivar

Grad. Mathematical Sciences

Universitat de Barcelona, 1987.

Submitted to the Department of
Applied Mathematics and Telematics
In Partial Fulfillment of the Requirements
for the Degree of

Doctor of Philosophy
in Mathematics

at the

Universitat Politècnica de Catalunya
April, 1997.

© Universitat Politècnica de Catalunya,
All Rights Reserved.

Submitted to_____

Department of Applied Mathematics and Telematics
April 30th, 1997.

Certified by_____

Enric Fossas
Associate Professor of Applied Mathematics
Thesis Supervisor

Accepted by_____

Department Committee on Graduate Students
Doctorate Programm of Applied Mathematics
May 14th, 1997

Chaos in the Buck Converter

by
Gerard Olivar

Submitted to the Department of Applied Mathematics and Telematics
on April 30, 1997 in partial fulfillment of the requirements for the Degree
of Doctor in Philosophy in Mathematics

Abstract

This thesis addresses the description of the bifurcational and chaotic behavior when the input voltage is varied in a model of a PWM controlled buck converter. It also deals with the stabilization of unstable periodic orbits which are embedded in the resulting chaotic attractor. Since the model is represented by a low dimensional system of differential equations which are piecewise-linear, analytical closed-form solutions are available. From the computational point of view, this means that the usual algorithms to compute trajectories, and consequently bifurcations and basins of attraction, can be considerably improved. Thus a thorough analysis can be made by means of numerical data, although some results can be analytically deduced.

Although the mathematics are quite simple, abundant results are obtained when dealing with non-smooth bifurcations. Non-smooth piecewise-linear systems have not been extensively studied in the literature, since the lack of smoothness does not allow the classical perturbation methods and series expansions.

Some questions are solved which are of interest to the practicing engineer. The bifurcation diagram is computed to show all the expected stationary behaviors. This includes several secondary evolutions which coexist with the main branch attractor yielding multistability. In this case, the basins of attraction are computed to predict the response of the system depending on the initial conditions. Furthermore, the boundary between desired operation and multiple pulsing is obtained in analytical closed-form, depending on the parameters of the circuit.

Although still in its infancy with respect to applications, the subject of control chaos is also studied in the buck converter. Several methods are proposed to stabilize unstable orbits which can improve the performance of the converter in terms of smaller output ripple and extension of the operational range. Some of these methods are checked against noise in the states or perturbations in the parameters. Numerical simulations indicate the feasibility of the design.

Thesis Supervisor: Enric Fossas, Associate Professor of Mathematical Sciences.

Dedication

This thesis is dedicated to my parents. They have been a constant source of love and support and the main guidance of my education.

Acknowledgements

This is the last page of the thesis, and from the very beginning I have found someone else to whom I must express my gratitude for his or her help at some stage of the work. First and foremost, I thank my advisor Professor Enric Fossas for years of patient guidance and for believing, one day some years ago, that I could start and finish a thesis. Besides sharing his technical expertise both as an undergraduate and as a postgraduate, I am indebted to him for introducing me to the switching piecewise-linear systems modelling power electronic dc-dc converters. His enthusiasm and energy devoted to the one thousand things he is able to do at the same time has been an example to follow.

I am very grateful to Professor Carles Batlle for his invaluable help at various points in this thesis. Being the wizard of (white) wizards in solving all the problems related to the computer equipment at our Department in Vilanova, he has brought from the net the important available software. He introduced me to L^AT_EX, then C, then MATHEMATICA, then MAPLE, and so on. Moreover, he is responsible for much of Chapter 6 of this thesis.

I am also very grateful to Mario di Bernardo at Bristol University. He made many valuable suggestions for Chapter 5. In particular, he introduced me to impact maps and grazing bifurcations, and his collaboration in Vilanova is very much appreciated.

I would like to thank Professors Amadeu Delshams, David Hamill, Hiroshi Kawakami, Paco Marquès, Luis Martínez, Rafael Ramírez, Giuseppe Rega and Toshimichi Saito for their guidance on particular points in this thesis. I also thank Professor Eusebius Doedel for his assistance in transporting and installing AUTO in our workstation. I am also grateful to Eliezer Toribio and his coworkers at the Laboratory for Applied Physics for building up experimental models of the buck converter. Also, many people at the Department of Electronics in Vilanova helped me to understand some concepts of power electronics. I would specially like to thank Domingo Biel, Spartacus Gomàriz, Francesc Guinjoan and Jesús Sánchez.

Chapter 7 was basically inspired in the work that some Final Project students made under my guidance; their work has been cited throughout the thesis. I am very grateful to all of them. I would also to thank Jeff Palmer for his patient revision and correction of the English manuscript.

I would like to thank all the members of the Department of Applied Mathematics and Telematics at Vilanova (and Toni Ras at Barcelona) for their comradery in terms of uncountable philosophical discussions while having breakfast

in the morning and on the long walk to the Aularium. Over the years, many individuals in this Department have influenced my life, specially Carles Batlle, Ester Simó and Marisa Zaragoza at the Zone-4 D-7 (*Jet Set*), which is the office we share at the EUPVG, plus Tomas Lázaro three doors away. He has occasionally been my local consultant on nonlinear systems (moreover, we have lost a lot of tennis games together).

An essential factor for the completion of this thesis has been financial support. This work has been supported mainly by the Department of Applied Mathematics and Telematics and by CICYT under Grant TAP94-0552-C03-02.

Finally, out of the University environment, I am grateful to many friends who have been a constant support while doing this thesis. I would like to thank specially Jordi Arnau, Leonor Buchmann, Enric Cabestany, José M. Crespo, Albert Dalmau, Ute Feldmann, Volksmann Fricks, Chus García, Ana Jardón, Jaume Martí, Neus Mas, Juan L. Miranda, Quico Prats, Yolanda Segarra, Fernando Tortella, Juan Tortella and Rosa Valcárcel who always were interested in the evolution of the work.

Everyone on the long list encouraged me to concentrate on the thesis throughout these years. Everyone but Carmen, who constantly tried to make me forget the work and enjoy the world outside with her. I owe much to her for the eventual completion of this thesis.

Contents

1	Introductory Chapter	1
1.1	Motivation	1
1.2	Introduction	4
1.3	Contents and Contributions	5
2	Background and Literature Review	7
2.1	Part One: DC-DC Switching Converters	7
2.1.1	State Space Models	9
2.1.2	Basic Converter Topologies	10
2.1.3	Pulsewidth Modulation	13
2.2	Part Two: Chaotic Behavior	15
2.2.1	A Word on History	16
2.2.2	Bifurcations, Transitions to Chaos and Crises	17
2.3	Part Three: Literature Review	19
2.3.1	Previous Work on Analyzing Chaos in Nonlinear Circuits	19
2.3.2	Previous Work on Chaotic Power Electronic Circuits	25
2.4	Part Four: Discussion	34
2.4.1	Modeling	34
2.4.2	Rigorous Mathematical Chaos	35
2.4.3	Preview of the Results in This Thesis	36
3	Basic Geometrical and Topological Features	39
3.1	General Considerations	39
3.2	DC-DC Buck Converter Controlled by PWM	43
3.3	Periodic Orbits	53
4	Study of the Stroboscopic Map	71
4.1	The Bifurcation Diagram for the Main Attractor	71
4.2	Existence of a Trapping Region	76
4.3	A First Numerical View of the Attractor	81
4.4	A Partition of the Phase Space	86
4.4.1	Existence of a $5T$ -Periodic Orbit	87
4.4.2	Mechanism for the Creation of the Regions	91
4.5	Images of the Regions by the Poincaré Map	101
4.5.1	Images of the Regions of Zero and One Crossing	101
4.5.2	A Horseshoe Mechanism	107

4.5.3	A Numerically Found Horseshoe	108
4.6	Summary	110
5	Secondary Bifurcations and Chaotic Attractors	115
5.1	Introduction	115
5.1.1	The Stroboscopic Map	118
5.1.2	The Impact Map	119
5.2	The Buck Converter Bifurcation Diagram	120
5.2.1	Analytically Computing the First Period-doubling	122
5.3	$P(\cdot, 3)$ Orbits and the Three-piece Chaotic Attractor	126
5.3.1	Two Branches of 3T-Periodic Orbits	126
5.3.2	The Invariant Manifolds and Basins of Attraction	134
5.4	Bifurcations of the $P(6, 6)$ and $P(12, 12)$ Orbits	140
5.4.1	$P(6, 6)$ Orbits	140
5.4.2	$P(12, 12)$ Orbits	145
5.5	$P(\cdot, 5)$ Orbits and the Jump to Larger Chaos	147
5.6	Tables of Local and Global Bifurcations	149
6	Control of Chaos in the Buck Converter	153
6.1	Introduction	153
6.2	Control of Chaos: The OGY Method	155
6.2.1	The Control Algorithm	155
6.2.2	Simulations	156
6.3	Time-delay Autosynchronization	157
6.3.1	ETDAS for Variable Structure Systems	159
6.3.2	Time-delayed Feedback for the Buck Converter	161
6.3.3	Numerical Analysis of $g(\mu^{-1})$	165
6.3.4	Stabilization of Higher Order Orbits	165
6.3.5	ETDAS Simulations	167
6.3.6	Another TDAS Scheme of Control	169
6.4	Stabilization by Control of the Switching Time	173
6.4.1	Two-topologies Systems	174
6.4.2	Simulations for the Buck Converter	177
7	Initial Explorations for Further Research	181
7.1	Introduction	181
7.2	Bidimensional Bifurcation Diagrams	184
7.3	A Smooth Version of the Buck Converter	185
7.3.1	An Autonomous System	187
7.3.2	A Smooth Version of the Ramp Voltage	187
7.3.3	A Smooth Version of the Switching Action	189
7.3.4	Choosing a Value for c	190
7.3.5	Simulations and Conclusions	190
7.4	Approximated Mappings for the Buck	195
7.4.1	A Second-order Approximation	195
7.4.2	A <i>Rotation Plus Translation</i> Mapping	196
7.5	Towards a General Classification	201

<i>CONTENTS</i>	xi
A Control of Switching Converters	207
B Basic Tools for Analyzing Chaos	215
C Bibliography	223

List of Figures

2.1	Scheme of a regulated line.	8
2.2	Scheme of a buck converter (in continuous-conduction mode). a) The switch is ON. b) The switch is OFF.	11
2.3	Scheme of a boost converter (in continuous-conduction mode). a) The switch is ON. b) The switch is OFF.	12
2.4	Scheme of a buck-boost converter (in continuous-conduction mode). a) The switch is ON. b) The switch is OFF.	13
2.5	Scheme of a Čuk converter (in continuous-conduction mode). a) The switch is OFF. b) The switch is ON.	14
2.6	Pulsewidth Modulation (PWM).	15
2.7	Chua's circuit.	22
2.8	Chua's oscillator.	23
2.9	v-i characteristic of Chua's diode.	24
2.10	Ripple-regulator circuit.	27
2.11	Switching regulator dc-dc converter with wideband feedback control.	28
2.12	Voltage-mode controlled Dc-dc buck converter.	29
2.13	Current-mode controlled Dc-dc buck converter.	30
2.14	R-L-Diode circuit.	31
2.15	Ferroresonant circuit incorporating saturating inductor.	31
2.16	Series-resonant converter employing slow rectifier diodes.	32
2.17	Current-mode controlled boost converter.	33
3.1	Two-topologies system of stable focus/saddle type.	41
3.2	Two-topologies sytem of stable focus/stable focus type, corresponding to the model of a buck converter.	41
3.3	Two-topologies system of stable node/stable node type, corresponding to the model of a buck converter.	42
3.4	Different relative positions for the equilibrium points and the switching curve.	42
3.5	Block diagram of the buck converter.	44
3.6	Orbit of the system 1 around its equilibrium point in the state space.	47
3.7	Orbit of the system 2 around its equilibrium point in the state space.	48

3.8	Orbit of systems 1 and 2 around its equilibrium point in the state space ($V_{in} = 20V$). The solid orbit corresponds to system 1 and the dashed one to system 2.	49
3.9	Typical trajectory of the control voltage.	50
3.10	Typical trajectory in the phase space.	50
3.11	Schematic representation of the global vector field of the system.	51
3.12	Sawtooth (or ramp) surface in the tridimensional space $(t, i, v_{co}) \in \mathbb{R}^3$	51
3.13	The space $\mathbb{R}^2 \times \mathbb{S}^1$ with the helicoidal surface determined by the ramp.	52
3.14	Cylindrical natural space $\mathbb{R}^2 \times \mathbb{S}^1$. Surface H represents the helicoidal sawtooth in this space. $H \cup \{t = 0, v_l < v < v_u\}$ is the boundary between the two topologies of the system.	53
3.15	The moving line is the boundary of the two linear topologies, which have X_1 and X_2 as equilibrium points when separated topologies are considered.	54
3.16	All the possible situations for m even or odd (exemplified by $m = 0$ and $m = 1$).	56
3.17	Scheme of the case $P(1, 1)$	57
3.18	Evolution of the duty cycle for the 1T-periodic orbits.	61
3.19	Schemes of the case \mathcal{B}	62
3.20	Evolution of the duty cycles for the 2T-periodic orbits.	65
3.21	2T-periodic orbit in the phase space (v, i) corresponding to $V_{in} = 25V$	66
3.22	$v_{co}(t)$ for the 2T-periodic orbit corresponding to $V_{in} = 25V$	67
3.23	In the picture at the top the evolution of the characteristic multipliers for the 1T-periodic orbits as a function of V_{in} is shown; at the bottom, the evolution of the characteristic multipliers for the 2T-periodic orbits is shown (the numbers are the values of V_{in}).	70
4.1	Bifurcation diagram of v_{co} taking V_{in} as a bifurcation parameter.	73
4.2	Bifurcation diagram of v_{co} taking V_{in} as a bifurcation parameter. First apparently chaotic zone. At a value near $V_{in} = 32.34V$, a sudden enlargement of the attractor occurs.	74
4.3	Strange attractor for $V_{in} = 35V$ (numerical simulation of 4000 iterations of the Poincaré map).	74
4.4	Joined phase-space corresponding to the two-topologies system.	77
4.5	Configuration of two orbits in the phase space.	77
4.6	A trapping region for one cycle of operation.	78
4.7	A trapping region for the system.	78
4.8	Projection of the three-dimensional trapping region in the phase-space.	79
4.9	Initial to final configurations for the two desired pieces of orbits.	80
4.10	Modified boundaries of the projection of the trapping region to obtain a strict one.	80
4.11	Scheme of the attractor for $V_{in} = 35V$	82

4.12	40 iterations of the Poincaré map ($V_{in} = 35V$).	82
4.13	The orbit in figure 4.12 in the phase plane (v, i)	83
4.14	The orbit in figure 4.12 in the temporal representation of the control voltage v_{co} and the ramp.	84
4.15	The 40 cycles of the orbit in figure 4.12 displayed in groups of 5.	85
4.16	Number of crossings in the ramp ($V_{in} = 35V$). Black stands for no crossings, gray for one crossing, light gray for two crossings and white for more than two crossings.	86
4.17	Number of crossings in the ramp. Detail of the central zone ($V_{in} = 35V$). Lighter gray corresponds to increasing number of crossings.	87
4.18	The control voltage when we take the central point $x_l = (v_l, i_l)$ as initial conditions, giving ∞ crossings in the ramp in the first cycle.	88
4.19	Images of the regions when the Poincaré map is applied to them ($V_{in} = 35V$). (a) Partial image of R_0 ; (b) Partial image of R_1 ; (c) $P(R_2)$; (d) $P(\cup_{n>2} R_n)$	89
4.20	Images of the regions R_4, R_5 and R_6 by the Poincaré map ($V_{in} = 35V$). (a) $P(R_4)$; (b) $P(R_5)$; (c) $P(R_6)$	89
4.21	Scheme of the possible routes for $V_{in} = 35V$. Dashed lines correspond to very improbable routes and heavy lines to most visited trajectories.	90
4.22	The two schemes for a 5T-periodic orbit close to that numerically observed in Fig. 4.15.	91
4.23	Crossing a <i>horizontal</i> boundary.	94
4.24	Crossing a <i>vertical</i> boundary.	94
4.25	Crossing a double boundary.	94
4.26	The phase space \mathbb{R}^2 is partitioned into infinitely many regions. The boundary of these regions is the union of two sets γ_1 and γ_2 . γ_1 is a vertical line and γ_2 is a piecewise smooth double spiral which focusses at x_l	95
4.27	Trajectory with initial condition at a point $x = (v_l, i_1)$ such that $P(x) = (v_u, i_2)$. Then x must belong to $\gamma_1 \cap \gamma_2$	95
4.28	Scheme for the boundary between the 0 and 1 zones.	96
4.29	Crossing the 0 and 1 zones. (a) $v < v_l$; (b) $v > v_l$	97
4.30	Crossing the 1 and 2 zones. (a) double boundary 0/1/2, $\alpha = 0$; (b) increasing the initial condition for the voltage; (c) maximum value for the initial condition for the voltage; (d) decreasing the initial condition for the voltage; (e) double boundary 1/2/3, $\alpha = \alpha_{max}$	99
4.31	Schemes for the 1/2 boundaries.	100
4.32	Initial condition for a) belongs to R_0^- , initial condition for b) belongs to R_0^+ and initial condition for c) belongs to R_1^+	102
4.33	Points labeled 1,2,3,4,5,6, α ,w in the phase space and images of the pieces of boundaries α -1 and 6-w.	104
4.34	Images of the points labeled 1,2,3,4,5,6, α ,w,X in the phase space.	104

4.35	Region R_0^- and its image by the Poincaré map. Dotted region: R_0^- ; region with lines: $P(R_0^-)$	105
4.36	Image of the region R_1^-	106
4.37	Qualitative picture of regions R_0^- , R_1^- , R_0^+ , R_1^+ , $P(R_0^-)$, $P(R_1^-)$, $P(R_0^+)$ and $P(R_1^+)$. The zones with lines correspond to $\bigcup_{i \geq 2} R_i$ and $P(\bigcup_{i \geq 2} R_i)$	107
4.38	(a) Scheme of the trajectories with initial conditions on r_u ; (b) A piece of $P(r_u)$	108
4.39	(a) Scheme of the rectangular region R with edges labeled 11-12-23-24; (b) $P(R)$. The dotted region is mapped to the dotted region, while the rectangular region is mapped to the spiraling region.	109
4.40	Some regions in the phase space and their respective images. The expanding-stretching in opposite directions and the folding mechanism is clearly seen. (a) Initial regions; (b) Respective images.	110
4.41	Image of a region in the phase space. (a) $R_k^- \cup R_{k+1}^-$; (b) $P(R_k^- \cup R_{k+1}^-)$. Heavy lines are mapped to heavy lines, and dashed lines to dashed lines.	111
4.42	Image by P^5 of a region in the phase space. Heavy lines are mapped to heavy lines, and dashed lines to dashed lines.	112
4.43	Points $(v_l, l_k), (v_l, l_k^*), (v_u, u_k)$ and (v_u, u_k^*)	113
4.44	$R_{13}^+ \cup R_{14}^+$ and $P(R_{13}^+ \cup R_{14}^+)$, showing an intersection which leads to an invariant set with horseshoe dynamics.	114
5.1	Possible behaviors: (a) multiple impacts and grazing, (b) P(2,2) orbit, (c) skipping phenomenon, (d) grazing and sliding.	117
5.2	The six different possibilities for the stroboscopic map, depending on the parity (n even or n odd) of the number of crossings in the ramp and the initial voltage ($v_0 < v_l$ or $v_0 > v_l$).	118
5.3	Different typical behaviors of the control voltage between two impacts: (a) OFF-OFF, (b) ON-OFF, (c) ON-ON.	120
5.4	Buck bifurcation diagram in the range (23,33)V. Several secondary bifurcations and attractors are outlined.	121
5.5	Non-standard bifurcation for $V_{in} = 11.752381V$	122
5.6	Successive enlargements of the main branch of the buck bifurcation diagram.	124
5.7	Three-piece chaotic attractor in the (v, i) phase space for $V_{in} = 24.160V$. v range is (11.41, 12.70) and i range is (0.42, 0.75).	127
5.8	Duty cycles $\alpha_1, \alpha_2, \alpha_3$ for the main (3,3) branch of (111) m type.	128
5.9	Scheme of the bifurcations of the types for the 3T-periodic unstable orbits. Dots stand for grazing bifurcations: the numbers are given accordingly to Fig.5.10. Every point in the branch stands for one of the three stroboscopic points of the orbit.	130
5.10	Patterns for the 3T-periodic unstable orbits. Dots stand for grazing points. Under each of the 36 patterns, the type of the orbit or the value of the input voltage is specified.	131

- 5.11 (a) Bifurcation of the 3T-attractor starting near $V_{in} = 13.376V$. After the non-smooth bifurcation creating the 3T-periodic orbit, a period-doubling bifurcation occurs. Next, instant chaos into a six-piece chaotic attractor is observed. An interior crisis of first kind producing merging bands turns the six-piece chaotic attractor into a three-piece chaotic attractor, and finally a boundary crisis destroys it. (b) Detail of the instant chaos bifurcation. . . 135
- 5.12 Evolution of the 3T-periodic orbit at $V_{in} = 13.376V$ in the phase-space (a) $V_{in} = 13.500V$ (6T-periodic attractor); (b) $V_{in} = 13.600V$ (six-piece chaotic attractor); (c) $V_{in} = 13.700V$ (six-piece chaotic attractor); (d) $V_{in} = 13.800V$ (three-piece chaotic attractor). 136
- 5.13 Invariant manifolds for the 3T-saddles in the 3T-branches. In the first 3T-branch, the interior part of the unstable manifold leads to the 1T-periodic attractor and the exterior part intersects the stable manifold; in the second 3T-branch, the interior and exterior parts of the unstable manifold intersect the stable manifold. (a) $V_{in} = 11.800V$, first 3T-branch; (b) $V_{in} = 11.800V$, second 3T-branch; (c) $V_{in} = 14.000V$, first 3T-branch; (d) $V_{in} = 14.000V$, second 3T-branch. 137
- 5.14 Invariant manifolds for the 3T-saddles of the 3T-branches and for the 2T-periodic inverse saddle created at the second period-doubling of the main branch attractor. (a) $V_{in} = 22.000V$, first 3T-branch; (b) $V_{in} = 22.000V$, second 3T-branch; (c) $V_{in} = 26.000V$, first 3T-branch; (d) $V_{in} = 32.200V$ 138
- 5.15 (a) Basins of attraction for $V_{in} = 13.800V$. Black corresponds to the 3T-attractor and white to the main 1T-attractor; (b) Basins of attraction for $V_{in} = 24.160V$. Black stands for the 1T-periodic basin, white for the three-piece chaotic attractor basin. 139
- 5.16 (a) Bifurcation diagram for the 6T attractor; (b) One of the 6 subbranches of the 6T attractor. 141
- 5.17 Six-piece chaotic attractor in the (v, i) phase space for $V_{in} = 30.170V$. v range is (11.95,12.17) and i range is (0.497,0.684). . . 141
- 5.18 (a) Basins of attraction for $V_{in} = 30.100V$. Black corresponds to the 6T basin, white to the 2T basin. v range is (11.74,12.28); i range is (0.40,0.80); (b) Invariant manifolds for the 6T-direct saddle. The stable manifold coincides with the basin boundary for the 2T-solution. $V_{in} = 30.000V$. v range is (11.69,12.57); i range is (0.39,0.71); (c) Invariant manifolds for the main inverse saddle just before the homoclinic tangency. $V_{in} = 29.000V$. v range is (11.70,13.13); i range is (0.38,0.70); (d) Invariant manifolds for the main inverse saddle just after the homoclinic tangency. Fractal boundary basins are expected. $V_{in} = 30.000V$. v range is (11.67,13.08); i range is (0.34,0.72). 143

5.19	(a) Basins of attraction for $V_{in} = 29.990V$. The 6T attractor lies inside the basin. Black corresponds to the 6T basin, white to the 2T basin. Part of the attractors are marked with rectangles. v range is (11.97,12.12); i range is (0.66,0.69); (b) Detail of the basins for $V_{in} = 29.990V$. v range is (11.95,11.99); i range is (0.65,0.68); (c) Basins of attraction for $V_{in} = 30.175V$, near the boundary crises. The 2T basin enters into the 6T basin. Black corresponds to the 6T basin, white to the 2T basin. v range is (11.9600,12.0600); i range is (0.6600,0.6795); (d) Basins of attraction for $V_{in} = 30.160V$, in the 6T-chaotic zone. The 6T basin shows some type of erosion. Black corresponds to the 6T basin, white to the 2T basin. v range is (11.74,12.28); i range is (0.40,0.80).	144
5.20	(a) Bifurcation diagram for the 12T; (b) Three subdomains of the 12T-attractor observing full chaos, crises and 3T windows in each of the three subbranches.	145
5.21	(a) Organization of the period-doubled 12T-periodic orbits. Crosses stand for the 12T, and circles for the coexisting 2T-stable periodic orbit; (b) Organization of the 12T-periodic orbits born at the saddle-node bifurcation. Crosses stand for the 12T, and circles for the coexisting 8T-stable periodic orbit.	146
5.22	Basins of attraction for $V_{in} = 32.150V$. White stands for the 8T-periodic basin, while black stands for the 12T basin.	146
5.23	(a) Phase plane portrait just after the enlargement has occurred. The small scale chaotic attractor can be still clearly observed; (b) Large scale five-zones chaotic attractor.	147
5.24	5T-periodic organising orbit.	148
5.25	(a) Average number of impacts per period as V_{in} is increased; (b) Total number of skippings over 2000 periods for different V_{in} values.	149
6.1	(a) Stabilized orbit for $V_{in} = 35V$. Initial conditions are taken at (0,0); no noise ($R = 0$) is added at the end of each cycle. (b) Stabilized orbit for $V_{in} = 35V$. Initial conditions are taken at the unstable 1T-periodic orbit. Random noise R of amplitude $\sigma = 10mV$ is added at every end of cycle, which is represented at the top of (b).	158
6.2	The two feedback schemes for time-delay autosynchronization of the buck converter.	162
6.3	Domains of control for the two feedback schemes and several values of r . Vertical axis: η from -10 to 10 . Horizontal axis: V_{in} from $20V$ to $35V$. Black = 0 (stable), Grey = 1 (unstable), White = 2 (unstable).	166

6.4	Domains of control for the first feedback scheme and 2T-periodic orbits and several values of r . Vertical axis: η from -10 to 10 . Horizontal axis: V_{in} from 25 V to 35 V. Black = 0 (stable), Dark gray = 1 (unstable), Light gray = 2 (unstable), White = 3 (unstable).	168
6.5	Load voltage chaotic waveform for $V_{in} = 35V$ (solid line) and time-delay feedback controlled orbit in the second scheme with $r = 0$ and $\eta = 4.0$ (dashed line). 50 cycles of the auxiliary ramp are shown.	169
6.6	ETDAS simulations for the buck converter.	170
6.7	Simulation checks of the analytically computed limits of the control domains.	171
6.8	Vertical axis: $M_1 \in (-1, 1)$ Horizontal axis: $M_2 \in (-10, 2)\Omega$. Black = 0 (stable), Grey = 1 (unstable), White = 2 (unstable).	173
6.9	Horizontal axis: $\eta \in (-1, 1)$ Vertical axis: V_{in} from $20V$ to $35V$. Black = 0 (stable), Grey = 1 (unstable), White = 2 (unstable).	173
6.10	Time-delay feedback simulations.	174
6.11	An unstable 3T-periodic orbit with 2+1+1 switching times for the buck converter. The periodic ramp is also plotted.	176
6.12	Ramp-controlled chaotic waveform for the buck converter ($V_{in} = 35V$). Voltage range is $0V$ to $20V$	178
6.13	Open loop controlled orbit for the buck converter ($V_{in} = 35V$). Voltage range is $0V$ to $20V$	179
6.14	Unstable 3T-periodic orbit with 2+1+1 switching times, in the state space. Voltage range is $11.6V$ to $12.5V$; current range is $0.4A$ to $0.7A$. Non-differentiable points correspond to the changes in the topology of the circuit.	180
6.15	Stable 5T-periodic orbit obtained when trying to stabilize an unstable 1T-periodic orbit of the original system for $V_{in} = 27V$; a sinusoidal perturbation of amplitude $1V$ and frequency $100w$ is continuously added to the input voltage.	180
7.1	Bidimensional bifurcation diagram for the buck converter. Vertical axe: parameter α ; Range: $(0, 80)$. Horizontal axe: parameter β ; Range: $(0, 100)$. Parameters k_1 and k_2 are fixed to 0.386847195 and 0.44 respectively. Colour codes: black, chaotic; dark grey, 1T-periodic; light gray, 2T-periodic; white, 4T-periodic. Some islands of periodicity are shown inside the chaotic region. Also, a zone of complicated behavior is distinguished, which is recomputed and shown in the next figure.	185

- 7.2 Bidimensional bifurcation diagram for the buck converter. Vertical axe: parameter α ; Range: (3,15). Horizontal axe: parameter β ; Range: (18,35). Parameters k_1 and k_2 are fixed to 0.386847195 and 0.44 respectively. Colour codes: black, chaotic and 3T-periodic; dark grey, 1T-periodic; light gray, 2T-periodic; white, 4T-periodic, 6T-periodic and 8T-periodic. Chaotic zones are found for low α to the right of the figure and also fractally intermingled in the 1T-periodic region. The rest of the black colour corresponds to 3T-periodic orbits, which are mixed with 6T-periodic behavior. 2T-periodic, 4T-periodic and 8T-periodic orbits are also found. Sudden changes probably occur because more than one attractor is present for the same bifurcation parameters. 186
- 7.3 Fourier series approximating the ramp voltage $Frac(t)$. (a) $n = 2$; (b) $n = 4$; (c) $n = 8$; (d) $n = 64$ 188
- 7.4 Attractors for different smoothing-constant c . (a) $c = 100$; (b) $c = 50$; (c) $c = 26$; (d) original system without smoothing. Notice in (a) and (b) the effect of smoothing, which produces a smoothed attractor. For $c = 26$, a different attractor is observed. 191
- 7.5 Bifurcation diagrams taking β as a bifurcation parameter. Different values for c are considered. (a) $c = 50$; (b) $c = 100$; (c) $c = 1000$; (b) $c = 500000$ 192
- 7.6 Branches of 1T-periodic and 2T-periodic orbits, computed with AUTO. Dashed trace corresponds to unstable orbits, continuous trace corresponds to stable orbits. Vertical axes correspond to the maximum value of the component in a cycle. (a) Branch of 1T-periodic orbits for $c = 50$. Some period-doubling bifurcations can be observed. (b) Detail of a period-doubling followed by a reverse period-doubling for $c = 50$. (c) A period-doubling bifurcation occurs at the point labeled 8. Then a new bifurcation in the 2T-periodic branch is found at the point labeled 15 ($c = 50$). (d) Some period-doubling bifurcations and possible folds in the 2T-periodic branch ($c = 100$). 193

7.7	(a), (b) and (c): 1T-periodic orbits for $c = 50$. (d), (e) and (f): comparison of the branches for different values of the smoothing parameter c . Notice in (e) a different vertical scale. (a) Solutions in the phase space. Label 12 corresponds to $\beta = 36.81$; label 15 corresponds to $\beta = 40.75$; label 19 corresponds to $\beta = 46.74$. (b) First-component waveforms of the periodic orbits that appear in (a); this component is related to the voltage in the original system. (c) Second-component waveforms of the periodic orbits that appear in (a); this component is related to the current in the original system. Peaks are associated to changes in the topology of the original system. (d) $c = 20$; (e) $c = 50$; (f) $c = 100$. Apart from the small 2T-branches, probably corresponding to the smoothing effect, a large 2T-branch is observed near $\beta = 43.5$; it could be related to the first period-doubling of the main attractor observed in the original system.	194
7.8	(a) and (b): Bifurcation diagrams for the second-order approximated map. (c) Bifurcation diagram for the original system. Notice that the range for the bifurcation parameter in (b) and (c) is (0,1000)V. While in the range (15,35)V the approximation is good (see (a)), in the range (35,1000)V, the approximation is bad. (d) Shape of the approximated attractor for $V_{in} = 35V$	197
7.9	Trajectory in the state space $x - y$ corresponding to $V_{in} = 35V$ in the original system. The trajectory is discontinuous in both components. The ramp voltage has been reduced to the point (0,0).	199
7.10	(a) Strange attractor for the approximated map of the buck converter. $\lambda = 0.85$, $R = 0.5$ and $\alpha = 3.0$. (b) Bifurcation diagram for $Re(z)$. $R = 0.5$ and $\alpha = 3$. (c) Bifurcation diagram for $Re(z)$. $R = 0.5$ and $\lambda = 0.85$. (d) Bifurcation diagram for $Re(z)$. $\lambda = 0.85$ and $\alpha = 3$	202
7.11	Scheme of the two-topologies system.	203
7.12	Experimental buck converter. (a) Measure instruments. (b) Buck prototype. (c) Experimental measures of the capacitor voltage and the inductor current. The input voltage corresponds to the periodicity range. (d) Experimental measure of the capacitor voltage. The input voltage corresponds to the chaotic range. (e) Experimental measures of the capacitor voltage and the inductor current in the phase space. The input voltage corresponds to the periodicity range.	205
B.1	Poincaré map $P : \Sigma^{\bar{\theta}_0} \rightarrow \Sigma^{\bar{\theta}_0}$	217

List of Tables

2.1	Mathematical models.	9
3.1	1T-Periodic orbits of P(1,1).	60
3.2	2T-Periodic orbits of P(2,1)	64
3.3	Characteristic Multipliers of the 1T-Periodic Orbits	69
3.4	Characteristic Multipliers of the 2T-Periodic Orbits	69
4.1	Values of the currents dividing the regions and their images. . .	111
5.1	Characteristic multipliers for the 6T-periodic orbits.	142
5.2	Bifurcations in the main attractor: ITB stands for instant torsion bifurcation, PD for period-doubling bifurcation, IC1 for interior crisis of first kind, IC2 for interior crisis of second kind, BC for boundary crisis, S^j for a j T-periodic sink, I^j for a j T-periodic inverse saddle and C^j for a j -piece chaotic attractor.	150
5.3	Bifurcations in the secondary 3T-branches: ITB stands for instant torsion bifurcation, SGR for stability change grazing bifurcation, PD for period-doubling bifurcation, ICB for instant chaos bifurcation, IC1 for interior crisis of first kind, BC for boundary crisis, GR for standard grazing bifurcation, SS for saddle-saddle grazing bifurcation, R- for a reverse bifurcation, CS for a chaotic saddle, GU^j for a grazing j T-periodic saddle, GS^j for a grazing j T-periodic sink, S^j for a j T-periodic sink, I^j for a j T-periodic inverse saddle and C^j for a j -piece chaotic attractor.	151
5.4	Bifurcations in the 6T-secondary attractor: SN stands for saddle-node bifurcation, PD for period-doubling bifurcation, IC1 for interior crisis of first kind, BC for boundary crisis, S^j for a j T-periodic sink, I^j for a j T-periodic inverse saddle, D^j for a j T-periodic direct saddle and C^j for a j -piece chaotic attractor. . . .	152
5.5	Bifurcations in the 12T-secondary attractor: SN stands for saddle-node bifurcation, PD for period-doubling bifurcation, IC1 for interior crisis of first kind, BC for boundary crisis, S^j for a j T-periodic sink, I^j for a j T-periodic inverse saddle, D^j for a j T-periodic direct saddle and C^j for a j -piece chaotic attractor. . . .	152

- 6.1 Mean number of cycles (M.N.C.) of stabilization and mean time (M.T.) of stabilization for different values of the input voltage. . 157
- 6.2 Mean percentage of the orbit under control (M.P.C.), depending on the noise amplitude σ . $V_{in} = 35V$. Initial conditions are taken in the unstable 1T-periodic orbit. 157

Chapter 1

Introductory Chapter

Abstract

This review part starts by setting out the aims and applications of power electronics for motivation. A very concise introduction to this field of research is outlined. In the last section, the structure of this thesis and a summary of the contents and contributions of this thesis is specified.

1.1 Motivation

Most branches of electronics are concerned with processing information or signals; in contrast power electronics deals with the processing of electrical energy. Power converters do not have an end of their own, but are always an intermediary between an energy producer and an energy consumer. Switching power converters are finding wide applications in the area of electrical energy conditioning, and are therefore of increasing importance: it is estimated that by 2000, over half the electrical energy generated will be processed by power electronics before its final consumption, a proportion that is likely to reach 90% during the next century [Hamill, 1995].

Power electronics is a *green* technology, with three main aims:

- To convert electrical energy from one form to another, facilitating its regulation and control.
- To achieve high conversion efficiency and therefore low waste heat.
- To minimise the mass of power converters and the equipment (such as motors) that they drive.

Intelligent use of power electronics will allow consumption of electricity to be reduced. Hence the rate of fossil fuel depletion may be slowed, and the associated problem of global warming eased. Minimisation of mass means a

reduction in the material and energy resources required for manufacture and use. Mass reduction is especially important for aerospace and vehicular applications, where it translates into lower fuel consumption.

Power electronics technology is increasingly to be found in the home and workplace [Bose, 1992; Tarter, 1993; Mohan, Undeland and Robbins, 1995]: familiar examples are the domestic light dimmer, and the switched mode power supplies of personal computers. Fields in which power electronics has been applied include:

- Heating and Lighting control
- Drives for industrial motion control
- Battery chargers
- Solid state relays and circuit breakers
- Fluorescent lamp ballasts
- Induction heating
- Traction applications such as locomotives
- Off-line dc power supplies
- Spacecraft power systems
- Switched mode audio amplifiers
- Electric power transmission
- Uninterruptible power supplies (UPS)
- Conditioning for alternative energy sources
- Automobile electronics and electric vehicles

There would seem to be two reasons for studying nonlinear dynamics in the context of power electronics:

- To understand better the nonlinear phenomena that occur in power converters, and thereby avoid undesirable effects.
- To allow converters to be engineered that deliberately make use of effects such as chaos.

Though the first objective has been achieved to some extent, there are as yet few practical power electronics applications in which subharmonics or chaos bring a distinct advantage. Nevertheless, with increasing awareness among power electronics practitioners of nonlinear dynamics, perhaps engineering uses will soon be found for nonlinear effects. It may be helpful to list the characteristics of chaos, and indicate some possible application areas.

Bounded erratic oscillation:

The apparently random but bounded character of chaos suggests that it might be used in place of a pseudo-random generator. A possible application is on-line parameter identification. For example, vector control of induction motors requires a knowledge of the rotor time constant, but this varies because the resistance of the copper rotor winding changes with temperature. Pseudo-random sequences have been applied to identify the time constant while the motor is running; perhaps chaos could be used instead.

Broadband spectrum:

Power converters produce interference concentrated at a harmonically related frequencies, and this may be undesirable. In drives that operate with switching frequencies in the audible range, acoustic noise may be produced and mechanical resonances excited. Pseudo-random generators have been employed to modulate the switching, spreading the acoustic energy over a wider spectrum and making it sound more acceptable (a hiss rather than a whine). Chaos may have a role to play here. Similarly, switching converters generate conducted and radiated electromagnetic interference at radio frequencies. Though matters can be improved with good design practice, filtering and shielding, it is difficult to meet international standards. Again, techniques such as pseudo-random sequences and frequency modulation have been applied to spread the interference spectrum, and chaos is another possible contender. Peaks might be reduced by 10-15dB, less expensively than by other methods.

Sensitivity to perturbations, and control:

The inherent sensitivity of chaotic systems to small perturbations may be exploited for synchronisation, targeting specific goals, and stabilising limit sets such as unstable equilibria or periodic orbits [Ott, Grebogi and Yorke, 1990]. However, applications in power electronics are less obvious, because it is already possible to force large changes in behaviour by means of the active switching devices. Recent work demonstrates that chaotic power converters may also be stabilised by appropriate feedback [Chakrabarty and Banerjee, 1995; Batlle, Fossas and Olivar, 1996b]. This begs the question: is there any point in making a power converter chaotic, in order to stabilise it? The answer is at present unknown, but such an approach may improve dynamic response. Fighter aircraft are designed to be open loop unstable but are then stabilised by feedback, making them more agile than conventional designs. Similarly, stabilised chaotic power converters may react more quickly, for instance in moving rapidly from one commanded output voltage to another. At present this suggestion is no more than speculation.

Validating nonlinear models:

It has been noted that the bifurcation sequence of a nonlinear system is peculiar to that system, whereas two quite dissimilar systems may display superficially similar attractors [Aguirre and Billings, 1994]. Thus it is a requirement that a model of a nonlinear system should display the same bifurcation pattern as the original system. Such "fingerprinting" could prove a very powerful method of validating models of power converters and other nonlinear systems. It is noteworthy that excellent bifurcation fingerprint agreement has been ob-

tained for the buck converter [Hamill, Deane and Jefferies, 1992], suggesting that the modelling approaches adopted have good validity over a wide domain.

1.2 Introduction

Since electrical power supplies can be either dc or ac, there are four basic types of power converter: ac-dc converters (rectifiers), dc-ac converters (inverters), dc-dc converters, and ac-ac converters.

A switching power converter is composed essentially of switches and energy storage elements, since it is designed to achieve high efficiency energy conversion. The nominal steady state operation of a dc-dc converter involves a cyclic operation of the switches to produce a commanded average output voltage or current from a specified dc input source. By modulating the nominal cyclic switching operation, dc-ac operation (inversion) can be obtained. In the case of an ac input source, ac-dc conversion (rectification) and ac-ac conversion (cycloconversion) can also be obtained by appropriately modulating the switching operation.

The control of switching power converters is an interesting and challenging research topic for many reasons. The control schemes investigated in the recent past were based on small signal models obtained by linearizing about a given steady state operating point or trajectory. Large signal transients such as those that occur at power-up or on overload recovery were handled in an ad hoc manner. Thus, the linearization step hides a phenomenon that may not be perceived in the converter but cannot be predicted by the model.

The state space averaging process has some evident flaws. First, all information about operation within a cycle is lost. Furthermore, the switching frequency f_s does not appear in the Continuous Conduction Mode (CCM) model, though it must certainly have some effect. A subtler point is that the duty factor d is purportedly a continuous-time variable; yet the duty factor is defined in terms of discrete time. Each switching cycle has an associated duty factor: it is meaningless to talk about changes in the duty factor within a cycle. If it is assumed that each of the phase variables are composed of a constant (dc) component and a small perturbation component, the paradox becomes important with fast perturbations; it can be shown that the averaging process is exact when the perturbation frequency is zero, but is further in error the higher the perturbation frequency. In fact the natural sampling PWM imposes a Nyquist limit of $f_s/2$, beyond which the model is meaningless. Another minor problem is that the true duty factor is constrained to $[0, 1]$, but the averaged variable d is not bounded (at least, not explicitly). In both the CCM example and the Discontinuous Conduction Mode (DCM) case studied by Tse, the conventional analysis using averaging is qualitatively wrong: it predicts stability for all input voltages, whereas in reality subharmonics and chaos are possible. Such a conclusion has worrying consequences where the reliability and safety of a system containing a buck converter is concerned. Considerable effort has been expended to validate and improve upon the basic averaging process [Sanders et al, 1991; Krein et al, 1990; Tymerski, 1991; Tymerski, 1994; Sira-Ramirez and Rios-Bolivar, 1994; Bass, Heck and Khan, 1994]. These investigations build on sound theoretical

bases, and usually discover state space averaging as the zero-order approximation, with higher terms giving more accurate results. Nonetheless, the simplistic averaging technique remains the most popular with practising power electronics engineers: it is easy to understand (if one does not probe too deeply), and straightforward to apply.

Modern control theory explores nonlinear design strategies. The possibly chaotic operation of power converters under various parameter assumptions and control designs has been receiving some attention but has not been fully investigated. The challenge here is, on the one hand to explore how chaos can be predicted and to avoid it through correct design or, on the other, to make the most of this situation and exploit it.

1.3 Contents and Contributions

This thesis studies the chaos phenomenon in the equations which model a buck converter with PWM control. From a mathematical point of view, it contributes to the study of piecewise-linear systems in a three-dimensional space, with emphasis on the geometrical point of view and on the numerical computing. Analytical expressions are available but, finally, one must resort to numerical methods to compute periodic orbits, bifurcations, invariant manifolds and basins of attraction. From an engineering point of view, this thesis both contributes to answering some questions about the behaviour observed in the experimental circuit, and to generating new questions to be answered by the engineering community. Among these, the experimental search for some secondary phenomena detected in the equations and the possibility of implementing some methods to control chaos in a experimental prototype.

Chapter 2 gives some background information on dc-dc switching converters, and on what type of behaviour can be expected in a nonlinear dynamical system. A discussion of the relevant literature on nonlinear circuits, specializing in chaotic power electronic circuits, is also given in this chapter, although the details are included throughout the thesis.

The piecewise-linear systems with two switching topologies are introduced in Chapter 3. Then, as a particular case, the equations for the buck converter with PWM control are given, and some basic properties of the solutions are stated. The basic technique to obtain periodic orbits is shown for 1T and 2T periodicity, and is also deduced for some special types of orbits in the general case of nT periodicity. A numerical scheme to find the stability is also given. An important part of this chapter and some sections of the next have already been published in the *IEEE Transactions on Circuits and Systems* [Fossas and Olivar, 1996].

An important approach to the analysis of the associated stroboscopic map is studied in Chapter 4. This chapter is geometrically oriented, although some computing is also needed to obtain the final results. The existence of a trapping region for the system is deduced, and horseshoe dynamics embedded in the stroboscopic map is found. The main tool in this chapter is the continuity of the map, which allows us to analytically deduce how different regions of the phase space are mapped. Analytical expressions for the boundary of 1T-operation

and nT -operation ($n > 1$) are computed. This is important since it enables the engineer to know when the phenomenon called *multiple pulsing* can occur. Basic description of this behaviour has been published in [Olivar and Fossas, 1996].

Chapter 5 is concerned with the secondary bifurcations which were found in addition to the main branch attractor. In this chapter, numerics are essential to compute bifurcation diagrams, invariant manifolds and basins of attraction. Much advantage is taken of the algorithms since the solutions are piecewise available in closed form, and only the switching time is approximated. Smooth and non-smooth bifurcations are found. An analytical expression for the characteristic multipliers can thus also be given; thus, computing bifurcations is straightforward. A large part of this chapter will be published in *The International Journal of Bifurcation and Chaos*.

Chapter 6 is somewhat removed from the general spirit of this thesis. Instead of the description of the observed dynamics, some methods to control chaos are suggested and simulations are produced to check the control action. Experimental realization is still to be done. Three known methods are proposed: first, the OGY method is specialized to the equations of the buck converter, giving good results when the level of noise is low. The main part of the chapter is concerned with time-delay feedback control. Three different schemes are tried with this method, leading to several domains of control in the parameter space. Finally, a third method based on open-loop control is given, and it is checked against some type of perturbations in the bifurcation parameter. Control of chaos in this system can be useful for reducing the chaotic output ripple and, thus, to extend the performance of the converter. A part of this chapter has already been published [Batlle, Fossas and Olivar, 1996c], and the time-delay feedback schemes will shortly be presented at international workshops and congresses.

Suggestions for future research are given in Chapter 7. Some simulations have been done with a smooth version of the equations and the package AUTO. Approximated mappings for the buck, including a second order approximation of the solutions and a qualitative approach by means of a *rotation plus translation* mapping are proposed. They permit faster simulations, but the approximation step must be deeply studied since some features of non-smooth systems are lost.

Chapter 2

Background and Literature Review

Abstract

This part starts by setting out a basis for chaotic behaviour in DC-DC switching converters. A very concise discussion of the development of nonlinear dynamics in electronic circuits and dc-dc power converters is stated in the literature review. Finally, a preview of the main results obtained in this thesis is outlined.

2.1 Part One: DC-DC Switching Converters

Dc-dc converters are widely used in regulated switch-mode dc power supplies and in dc-motor drive applications. The input to these converters is frequently an unregulated dc-voltage, which is obtained by rectifying the line voltage. Therefore it will fluctuate due to changes in the line-voltage magnitude. Switch-mode dc-to-dc converters are used to convert the unregulated dc input into a controlled dc-output at the desired level.

Since the object is to convert electrical energy at high efficiency, the ideal power converter would contain only lossless components. Two basic groups that can be approximated by real components are available:

Switching components, such as transistors and diodes. An ideal switch is either ON ($v = 0$) or OFF ($i = 0$), so its vi product is always zero and it never dissipates energy. Active switches such as transistors turn ON and OFF in response to an applied signal; passive switches (diodes) have a highly nonlinear $v - i$ characteristic.

Reactive (energy storing) components, such as inductors and capacitors. They are characterised by differential equations, $v = Ldi/dt$ for an inductor, $i = Cdv/dt$ for a capacitor. It can be shown that they absorb energy from a circuit, store it and return it.

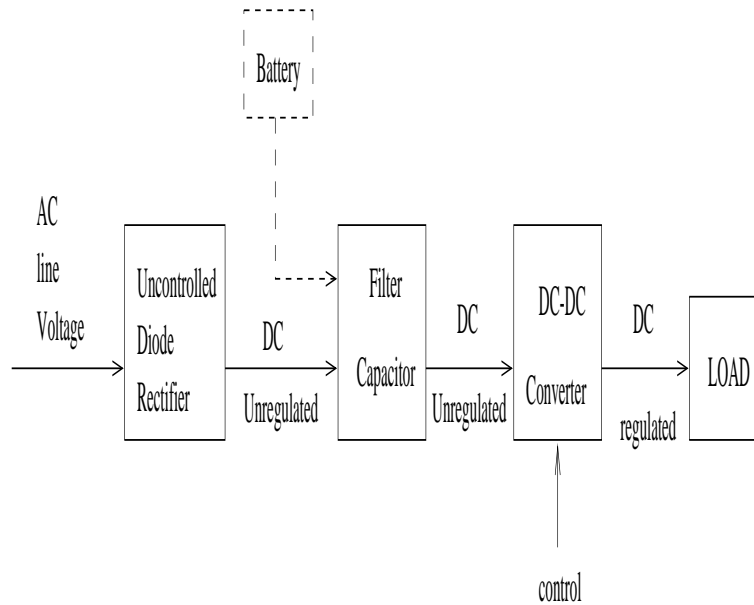


Figure 2.1: Scheme of a regulated line.

Power converters employ components from both groups. Energy is pumped around the circuit by the switching components, while the reactive components act as intermediate energy stores and input-output reservoirs. The presence of both types of components implies that the circuits are nonlinear, time-varying dynamical systems. Anyone familiar with nonlinear dynamics will appreciate that power converters are difficult to analyse, and are likely to show a wealth of curious behaviour. There are also several unavoidable sources of unwanted nonlinearity in practical power converters:

- The semiconductor switching devices have intrinsically nonlinear dc characteristics.
- They also have nonlinear capacitances, and most suffer from minority carrier charge storage.
- Nonlinear inductances abound: transformers, chokes, magnetic amplifiers, and saturable inductors used in snubbers.
- The control circuits usually involve nonlinear components: comparators, PWMs, multipliers, phase-locked loops, monostables and digital controllers.

The driven R-L-D circuit [Linsay, 1981] has a close relative in power converters: when a transformer feeds a rectifier diode, the leakage inductance resonates with the diode's nonlinear capacitance to give a chaotic transient when excited by the switches. A similar effect is ferroresonance: a tuned circuit involving a

saturating inductor [Chua, Hasler, Neirynck and Verburgh, 1982]. This, too, has practical relevance: it is exploited to regulate voltages, but unintended ferroresonance in power systems can cause excessive voltages and currents.

2.1.1 State Space Models

Roughly speaking, an state space modelling of a dynamical system, such as a converter, will be a system of ordinary differential equations describing the evolution over time of the state of a physical system. It must specify the functional dependence of the state variables on their initial values and system inputs.

Regarding their internal structure, the mathematical models can be discrete or continuous, time-varying or time-invariant, linear or non-linear. They may be summarized in Table 2.1

Table 2.1: Mathematical models.

MODEL	CONTINUOUS	DISCRETE
Time-varying		
Non-linear	$\dot{x}(t) = f(t, x(t), w(t))$	$x_{k+1} = \Phi(k, x_k, w_k)$
Linear	$\dot{x}(t) = F(t)x(t) + C(t)w(t)$	$x_{k+1} = \Phi(k)x_k + P(k)w_k$
Time-invariant		
Non-linear	$\dot{x}(t) = f(x(t), w(t))$	$x_{k+1} = \Phi(x_k, w_k)$
Linear	$\dot{x}(t) = F \cdot x(t) + C \cdot w(t)$	$x_{k+1} = \Phi \cdot x_k + P \cdot w_k$

where x is the vector of state variables and w is the vector of the inputs. With this classification, switched-mode converters can be thought as time-invariant or time-varying non-linear continuous systems. They are non-linear due to changes in the topology of the circuit due to the switching instants. In spite of this non-linearity, they are linear between two consecutive switching times. For example, suppose that a converter can switch between two linear topologies depending on turning a transistor (ON: $u = 1$; OFF: $u = 0$). Under $u = 1$, suppose that the model is given by $\dot{X} = A_1X + B_1w$, and, under $u = 0$, the model is given by $\dot{X} = A_0X + B_0w$, where X is the state vector of the capacitors voltages and inductors currents, and w is the vector of voltages and current sources values. An ensemble non-linear model can then be obtained thus

$$\dot{X} = [A_0 + u(A_1 - A_0)]X + [B_0 + u(B_1 - B_0)]w.$$

This is termed a bilinear state-space model because the control u enters multiplicatively with the state, as well as linearly. In the more general case, where nonlinear circuit elements are present in a switching converter, the ensemble model would take the more general form

$$\dot{x} = f_0(x) + u(f_1(x) - f_0(x))$$

When the switched-circuit admits a finite number of distinct configurations, say $m + 1$, the state-space model takes the form

$$\dot{x} = (1 - u_1 - u_2 - \cdots - u_m)f_0(x) + u_1f_1(x) + u_2f_2(x) + \cdots + u_mf_m(x)$$

Each of the inputs u_k can take only the discrete values 0 and 1, with at most one input equals to 1 at a given time instant. So, the correspondence to the $m + 1$ switch configurations to the inputs u_k are in the following way:

$$f_0(x) \leftrightarrow u_1 = \cdots = u_m = 0, \quad f_1(x) \leftrightarrow u_1 = 1, \dots, f_m(x) \leftrightarrow u_m = 1$$

2.1.2 Basic Converter Topologies

In this chapter, the following dc-dc converters are introduced:

- Step-down (buck) converter
- Step-up (boost) converter
- Step-down/up (buck-boost) converter
- Ćuk converter

Only the step-down and the step-up are the basic converter topologies. Both the buck-boost and the Ćuk converters are combinations of the two basic topologies. Resonant converters are introduced later as a way to avoid some of the disadvantages of pulse-width modulation when it is applied as a control method.

The buck converter

Figure 2.2 shows the step-down dc-dc converter. During the interval when the switch is ON, the diode becomes reverse biased and the input provides energy to the load as well as to the inductor. During the interval when the switch is OFF, the inductor current flows through the diode, transferring some of its stored energy to the load.

During standard operation, the switch S opens and closes periodically at the switching frequency f_s , with a duty factor d . The cut-off frequency of the LC filter is much lower than f_s , removing most of the switching ripple and delivering a relative smooth output voltage v to the load resistance R . The output can be varied by changing the duty factor d , i.e. by pulsewidth modulation (PWM). The operation described is known as continuous conduction mode (CCM), since the inductor passes current without a break. However, if the output is only lightly loaded, the inductor current can become zero for part of the cycle as the diode comes out of conduction: this is known as discontinuous conduction mode (DCM). In practice, it is necessary to regulate v against changes in the input voltage and the load current, by adding a feedback control loop. If a simple proportional controller is chosen, a constant reference voltage V_{ref} is subtracted from the output voltage and the error v_e , is amplified with gain A

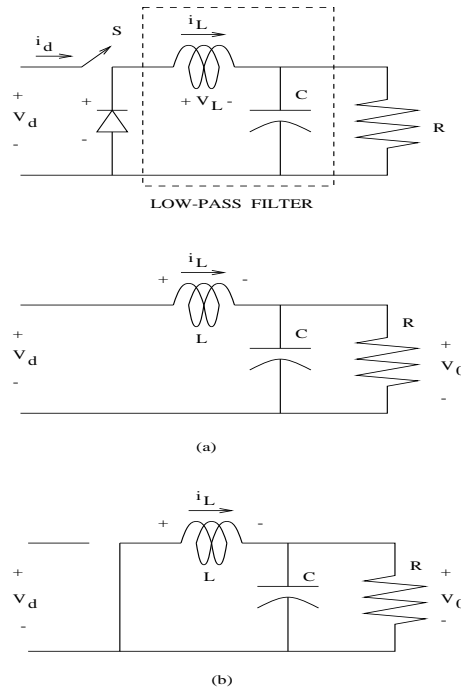


Figure 2.2: Scheme of a buck converter (in continuous-conduction mode). a) The switch is ON. b) The switch is OFF.

to form a control signal. The intended mode of operation is a steady state in which the output voltage stays close to V_{ref} .

The boost converter

In the boost converter, when the switch is ON, the diode is reverse biased, thus isolating the output stage. The input supplies energy to the inductor. When the switch is OFF, the output stage receives energy from the inductor as well as from the input.

The buck-boost converter

A buck-boost converter can be obtained by the cascade connection of the two basic converters: the step-down converter and the step-up converter. This cascade connection can be combined into a single buck-boost converter shown in figure 2.4. When the switch is closed, the input provides energy to the inductor and the diode is reverse biased. When the switch is open, the energy stored in

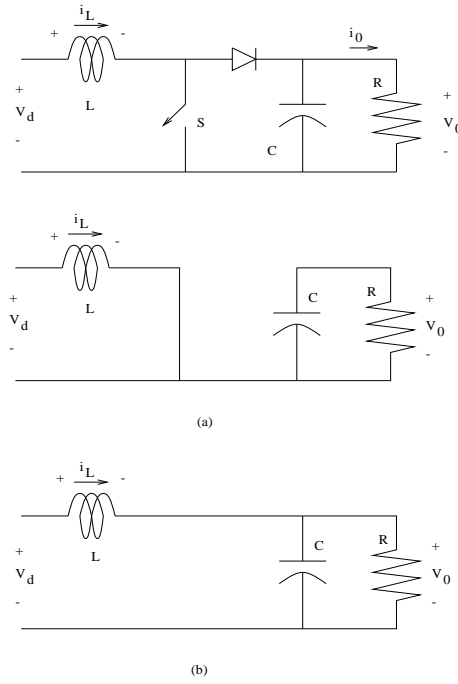


Figure 2.3: Scheme of a boost converter (in continuous-conduction mode). a) The switch is ON. b) The switch is OFF.

the inductor is transferred to the output. No energy is supplied by the input during this interval.

The Čuk converter

Similar to the buck-boost converter, the Čuk converter provides a negative polarity regulated output voltage with respect to the common terminal of the input voltage. Here, the capacitor C_1 acts as the primary means of storing and transferring energy from the input to the output.

When the switch is OFF, the inductor currents flow through the diode. C_1 is charged through the diode by energy from both the input and L_1 ; i_{L_1} decreases, because V_{C_1} is larger than V_d . Energy stored in L_2 feeds the output. Therefore, i_{L_2} also decreases. When the switch is ON, V_{C_1} reverse biases the diode. The inductor currents i_{L_1} and i_{L_2} flow through the switch. C_1 discharges through the switch, transferring energy to the output and L_2 . Therefore, i_{L_2} increases. The input feeds energy to L_1 causing i_{L_1} to increase.

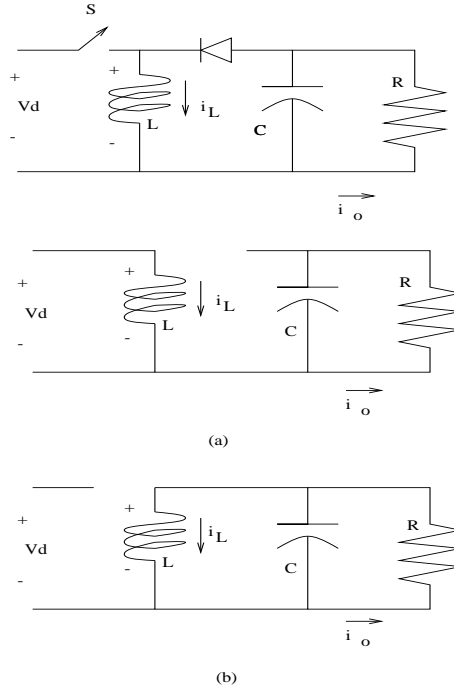


Figure 2.4: Scheme of a buck-boost converter (in continuous-conduction mode). a) The switch is ON. b) The switch is OFF.

2.1.3 Pulsewidth Modulation

One of the methods for controlling the output voltage employs switching at a constant frequency (hence, a constant switching time period $T = t_{on} + t_{off}$), and adjusting the ON-duration of the switch to control the average output voltage. In this method, called pulsewidth modulation (PWM) switching, the switch duty ratio D , which is defined as the ratio of the ON-duration to the switching time period, is varied.

In the PWM switching at a constant switching frequency, the switch control signal, which controls the state (ON or OFF) of the switch, is generated by comparing a signal level control voltage $V_{control}$ with a periodic waveform. The control voltage signal generally is obtained by amplifying the error, or the difference between the actual output voltage and its desired value. When the amplified error signal is greater than the repetitive waveform, the switch control signal becomes high, causing the switch to turn ON. Otherwise, the switch is OFF.

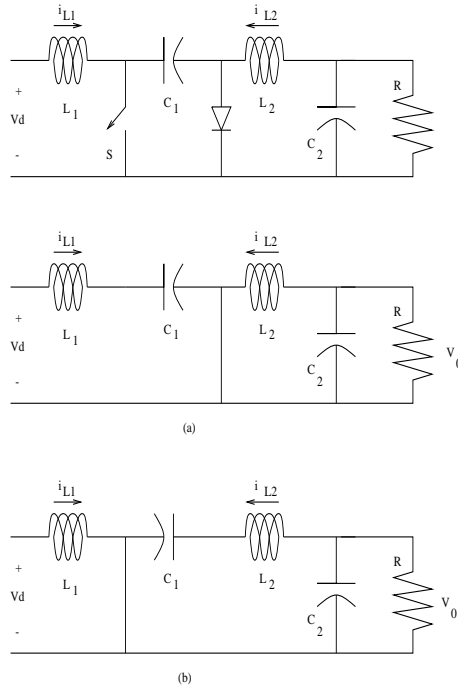


Figure 2.5: Scheme of a Čuk converter (in continuous-conduction mode). a) The switch is OFF. b) The switch is ON.

Resonant converters

In all pulsewidth modulated converter topologies, the controllable switches are operated in a switch mode where they are required to turn ON and turn OFF the entire load current during each switching. So the switches are subjected to high switching stress and high switching power loss that increases linearly with the switching frequency of the pulsewidth modulation. Another significant drawback of the switch-mode operation is the electromagnetic interference (EMI) produced due to large di/dt and dv/dt caused by a switch-mode operation. These shortcomings of switch-mode converters are exacerbated if the switching frequency is increased in order to reduce the converter size and weight, and hence to increase the power density. Therefore, to realize high switching frequencies in converters, the aforementioned shortcomings are minimized if each switching in a converter changes its status when the voltage across it and/or the current through it is zero at the switching instant. These topologies, which result in zero-voltage and/or zero-current switchings, are broadly classified as resonant converters since most of them require some form of LC resonance.

The switch stresses can be reduced by connecting simple dissipative snubber circuits in series and parallel with the switches. However, these dissipative

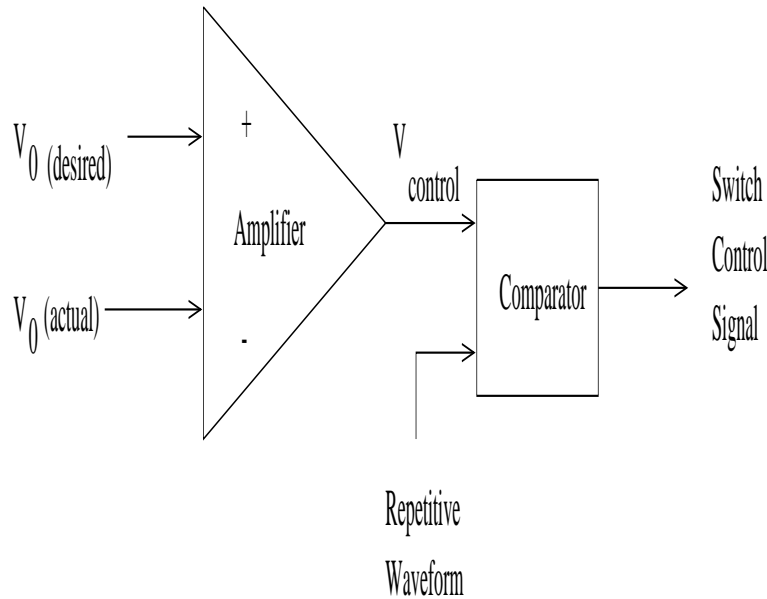


Figure 2.6: Pulsewidth Modulation (PWM).

snubbers shift the switching power loss from the switch to the snubber circuit, and therefore do not provide a reduction in the overall switching power loss.

In contrast to dissipative snubbers in switch-mode converters, the combination of proper converter topologies and switching strategies can overcome the problems of switching stresses, switching power losses and the EMI by turning ON and turning OFF each of the converter switches when either the switch voltage or the switch current is zero.

2.2 Part Two: Chaotic Behavior

One of the basic tenets of science is that deterministic systems are completely predictable; given the initial conditions and the equations describing a system, the behaviour of the system can be predicted for all time. The discovery of chaotic systems has eliminated this viewpoint. Simply put, a chaotic system is a deterministic system that exhibits random behaviour.

Though identified as a robust phenomenon only twenty years ago, chaos has almost certainly been encountered by scientists and engineering many times during the last century, only to be dismissed as physical noise. Chaos is such a wide-spread phenomenon that it has now been reported in virtually every scientific discipline: astronomy, biology, biophysics, chemistry, engineering, geology, mathematics, medicine, meteorology, plasmas, physics and even the social sciences.

It is no coincidence that during the same two decades, during which chaos

has grown into an independent field of research, computers have permeated society. It is, in fact, the wide availability of inexpensive computing power that has spanned much of the research in chaotic dynamics. The reason is simple: the computer can calculate a solution of a nonlinear system.

This is no small feat. Unlike linear systems, where closed-form solutions can be written in terms of the system's eigenvalues and eigenvectors, few nonlinear systems and virtually no chaotic systems possesses closed-form solutions.

The computer allows nonlinear systems to be studied in a way that was undreamt by the pioneers of nonlinear dynamics. One can perform numerical experiments quickly and easily. Parameters can be changed, system equations modified, and solutions displayed, all at a touch of a key. Before the advent of low-cost computing, the ability to perform such simulations was restricted to researchers with access to a large computing facility. Today, anyone with a personal computer can simulate a nonlinear system.

Simulations are a powerful tool for gaining intuition about nonlinear systems and for exploring the exciting terrain of chaotic dynamics, but they do have their limitations. Computers have finite precision and inevitably generate errors when evaluating floating-point expressions. Furthermore, computers are discrete-time in nature and there are unavoidable errors when they are used to simulate continuous-time systems. Finally, a simulation is of little or no help in providing theoretical results; even if the result of a simulation were completely accurate, it is just one solution of one system from one initial condition using one set of parameter values.

The moral is that even though simulations are a useful tool, simulation data must be interpreted carefully, checked against intuition and theory, and used only for purposes for which it is suited [Parker and Chua, 1989].

2.2.1 A Word on History

Modern dynamical systems theory has a relatively short history. Analysis remained the favoured tool for the study of dynamical problems until Poincaré's work in the late nineteenth century showed that perturbation methods might not yield correct results in all cases, because the series used in such calculations diverged. Poincaré (1880, 1890, 1899) then went on to do extensive analysis and geometry in his development of a qualitative approach to the study of differential equations. To Poincaré, a global understanding of the gross behaviour of all solutions of the systems was more important than the local behaviour of particular, analytically-precise solutions.

Poincaré's point of view was enthusiastically adopted and furthered by Birkhoff (1927) in the first part of the twentieth century. Birkhoff realized the importance of the study of mappings and emphasized discrete dynamics as a means of understanding the more difficult dynamics arising from differential equations.

The infusion of geometric and topological techniques during this period gradually led mathematicians away from the study of the dynamical systems themselves to the study of the underlying geometric structures. Manifolds, the natural state-spaces of dynamical systems, became objects of study in their own right. Fields such as differential topology and algebraic topology were born and

eventually flourished. Rapid advances in these fields gave mathematicians new and varied techniques for attacking geometric problems. Meanwhile, the study of the dynamical systems themselves languished in relative disfavor, except in the Soviet Union, where mathematicians such as Lyapounov (1949), Pontryagin, Andronov and others (1937, 1966, 1971, 1973), continued to study dynamics from various points of view.

All this changed around 1960, due mainly to the influence of Moser and Smale (1967) in the United States, Peixoto in Brazil, and Kolmogorov, Arnold and Sinai in the Soviet Union (1973, 1978, 1982). Differential topology techniques enabled Smale, Peixoto and their followers to understand the chaotic behaviour of a large class of dynamical systems known as hyperbolic or Axiom A systems. Geometry combined with hard analysis allowed Kolmogorov, Arnold and Moser to push through their celebrated KAM theory. Smooth ergodic theory, topological dynamics, Hamiltonian mechanics, and the qualitative theory of ordinary differential equations all developed as disciplines in their own right.

However, until the mid-1970's the new tools were largely in the hand of pure mathematicians, although a number of potential applications had been sketched, notably by Ruelle and Takens (1971), who suggested the importance of strange attractors in the study of turbulence.

More recently, dynamical systems have benefited from an infusion of interest and techniques from a variety of fields. Physicists such as Feigenbaum have rekindled interest in low dimensional discrete dynamical systems. Break-throughs in mathematical biology and economics have attracted a diverse group of scientists to the field. The discovery of stable chaotic systems such as the Lorenz system from meteorology have convinced scientists that there are many more stable types of dynamical behaviour than just stable equilibrium points and limit cycles. Last, but by no means least, computer graphics has shown that the dynamics of simple systems can be at once beautiful and complex.

Over the past few years, applications in solid and structural mechanics, as well as fluid mechanics, have appeared. There is now widespread interest in the engineering and applied science communities in strange attractors, chaos and dynamical systems theory.

2.2.2 Bifurcations, Transitions to Chaos and Crises

Bifurcations

Systems of physical interest typically have parameters which appear in the defining systems of equations. As these parameters are varied, changes may occur in the qualitative structure of the solution for certain parameter values. These changes are called bifurcations and the parameter values are called bifurcation values. There are evident limitations as to how far one can proceed with a systematic bifurcation theory. In parameter regions consisting of structurally unstable systems, such as those encountered in the Lorenz system, the detailed changes in the topological equivalence class of a flow can be exceedingly compli-

cated. Many important aspects of this situation are poorly understood and lack the satisfying completeness of the structural stability theory for second-order systems [Wiggins, 1990].

Global bifurcations will be defined as bifurcations which are not local, i.e., a qualitative change in the orbit structure of an extended region of phase space. Typical examples are homoclinic and heteroclinic bifurcations. In both of these examples the complete story is far from known, mainly because techniques for the global analysis of the orbit structure of dynamical systems are just now beginning to be developed [Wiggins, 1988].

Routes to chaos

There are three most important routes or transitions to chaos, in which nonlinear systems can become chaotic if an external control parameter is varied. Interestingly enough, all these routes can be realized experimentally, and they show a fascinating universal behaviour which is reminiscent of the universality found in second-order equilibrium phase transitions. In this context, universality means that there are basic properties of the system (such as critical exponents near the transition to chaos) that depend only on some global features of the system.

The most recent route to chaos has been found by Grossmann and Thomase (1977), Feigenbaum (1978) and Coullet and Tresser (1978). They considered a simple difference equation which, for example, has been used to describe the time dependence of populations in biology, and found that the population oscillated in time between stable values (fixed points) whose number doubles at distinct values of an external parameter. This continues until the number of fixed points becomes infinite at a finite parameter value, where the variation in time of the population becomes irregular.

Feigenbaum has shown, and this was a major achievement, that these results are not restricted to this special model but are in fact universal and hold for a large variety of physical, chemical and biological systems. This discovery has triggered an explosion of theoretical and experimental activity in this field.

A second approach to chaos, the so-called intermittency route, has been discovered by Manneville and Pomeau (1979). Intermittency means that a signal which becomes regularly (or laminarly) in time becomes interrupted by statistically distributed periods of irregular motion (intermittent bursts). The average number of these bursts increases with the variation of an external control parameter until the motion becomes completely chaotic. This route also has universal features and provides a universal mechanism for $1/f$ noise in nonlinear systems.

Yet a third possibility was found by Ruelle and Takens (1971) and Newhouse (1978). In the seventies, they suggested a transition to turbulent motion which was different from that proposed much earlier by Landau (1944),(1959). Landau considered turbulence in time as the limit of an infinite sequence of instabilities (Hopf bifurcations), each of which creates a new basic frequency. However, Ruelle, Takens and Newhouse showed that after only two instabilities, in the third step, the trajectory becomes attracted to a bounded region of the phase

space in which initially close trajectories separate exponentially, such that the motion becomes chaotic. These particular regions of phase space are called strange attractors.

Crises

Crises are collisions between a chaotic attractor and a coexisting unstable fixed point or periodic orbit. Grebogi, Ott and Yorke (1983) were the first to observe that such collisions lead to sudden changes in the chaotic attractor. A simple example occurs in the period-three window of the logistic map, where three stable and three unstable fixed points are generated by tangent bifurcations. The unstable fixed points, having entered the chaotic regions, immediately repel the trajectory out of the sub-band in such a way that the regions between the bands are also filled chaotically. Similar crises also occur in two and three-dimensional maps and in three-dimensional flows.

As the discontinuity is approached, one often finds transient chaos, i.e. seemingly chaotic orbits which decay exponentially towards periodic orbits with a decay rate that follows a power law of the distance (in parameter space) from the discontinuity. It has been conjectured by Grebogi, Ott and Yorke that almost all sudden changes in chaotic attractors are due to crises [Schuster, 1988].

2.3 Part Three: Literature Review

The literature on analyzing chaos in electronics is extensive. In the following, a very concise summary is given for certain topics developed in the last two decades.

2.3.1 Previous Work on Analyzing Chaos in Nonlinear Circuits

The most complete results on chaos have been obtained in nonlinear circuits, because the experimental conditions can be more precisely controlled and the circuits can be well represented by ordinary differential equations or maps with only a few variables [Carroll and Pecora, 1995].

Most of the multiple experimental systems capable of displaying chaotic behaviour are nonlinear circuits. They have taken advantage of the progress made by physicists in nonlinear science, mainly in an effort to explain turbulence in hydrodynamics. The work of Takens, Eckmann and Ruelle deals in this line. [Eckmann, 1981] describes the three well known routes to chaos (or scenarios): the Ruelle-Takens-Newhouse (or quasiperiodic), The Feigenbaum (or period-doubling) and the Pomeau-Manneville (or intermittent) routes to chaos. The influence of noise is also studied in this paper. Later, [Eckmann and Ruelle, 1985] present the theory of chaos and strange attractors from an ergodic point of view, which contains a remarkable part of measure theory and dimensions.

Bibliography on chaotic circuits has rapidly grown since 1980, and any attempt to summarize it completely is a difficult task. Although the papers on chaotic circuits are scattered among many different journals which have been briefly reviewed, as indicated in the references, most of the following has been taken from the publications of the IEEE - mainly in the TRANSACTIONS ON CIRCUITS AND SYSTEMS, the TRANSACTIONS ON POWER ELECTRONICS, and the international symposiums of their respective organizations. In addition, books on this subject and monographs of concrete topics have been written since the eighties. The former contain basic ideas of bifurcations, the latter include more precise and quantitative results. To name but a few, the books [Guckenheimer and Holmes, 1983; Schuster, 1988; Devaney, 1989; Arrowsmith and Place, 1990; Drazin, 1992; Ott, 1993; Hoppenstadt, 1993] and the basic but modern book [Strogatz, 1994] (the last two books contain some ideas on controlling chaos) are examples of excellent written results on basic topics; a good text for applied numerical bifurcations is that of [Seydel, 1994]; most of the interesting references to the researcher in bifurcations and chaos can be found in the more theoretical and detailed books of Wiggins [Wiggins, 1988; Wiggins, 1990] and [Kuznetsov, 1995]: Finally, there should be mention of the Kapitaniak and Wojewoda monograph on nonchaotic strange attractors [Kapitaniak and Wojewoda, 1993], and the compilation of very interesting articles on chaos [Bai-Lin, 1984; Bai-Lin, 1990].

The earlier work

Chaotic effects in electronic circuits were first noted by Van der Pol in 1927 [Van der Pol and Van der Mark, 1927; Kennedy and Chua, 1986]. A relaxation oscillator comprising a battery, a neon bulb, a capacitor and a resistor, was driven by a 1 kHz sinusoidal signal and tuned to obtain subharmonics, but *an irregular noise* was often heard. There was little interest in explaining such spurious oscillations for about 50 years.

Earlier work on nonlinear circuits was carried out on systems of many coupled nonlinear oscillators in 1977 and 1978 [Rössler, 1977; Gollub, Brunner and Danly, 1978]. Complicated combinations of periods and chaos were indeed observed, but could not be fitted into simple systematics as has now been done. Rössler, in one of his papers, studies a hysteresis oscillator whose motion takes place in a two-dimensional manifold. He also studies the associated Poincaré map in a similar way to Lorenz in 1963. The perfect delay convention that Rössler assumes in his paper is later reviewed and brought up to date [Diener, 1981] and a thorough study of constrained equations can be found later, for example in the paper [Veitch, 1993].

Most of the subsequent experiments dealt with a single nonlinear oscillator driven by a periodic signal ([Linsay, 1981; Buskirk and Jeffries, 1985]). In 1981, Linsay published the first modern experimental report of electronic chaos [Linsay, 1981]: a driven resonant circuit, employing a varactor diode as a nonlinear capacitor. Chaos in nonlinear feedback systems is firstly studied in [Baillieul, Brockett and Washburn, 1980] from simulation work on a PWM control scheme

used in connection with a dc-to-dc voltage converter, making the first step towards research into chaos in power electronics, where some criteria for chaos is stated. The relation of chaos with a lack of synchronization is studied by [Tang, Mees and Chua, 1983] in an astable multivibrator. This original paper was reviewed recently in 1993 by Sharkovsky and Chua, and led to the introduction of a certain type of one-dimensional discontinuous maps, piecewise monotonic and locally expansive whose most interesting feature is the analytically proven existence of an invariant measure, absolutely continuous with respect to the Lebesgue measure and with nonzero topological entropy [Sharkovsky and Chua, 1993].

The work [Freire, Franquelo and Aracil, 1984] on chaos in electronic circuits was one of the first that dealt with unforced circuits. The system considered is autonomous and three dimensional, and thus belongs to the simplest type of dynamical systems in which chaotic motions may occur. It consists of a resonant circuit and two nonlinear conductances, one negative and the other positive. Their current-voltage characteristics are approximated by cubic equations, which allow a more analytical study of the stability and bifurcations. The circuit shows a great variety of dynamical behaviours (equilibrium points, periodic oscillations, chaotic motions, ...) and the analysis proceeds to catalog them all through a bifurcation study (pitchfork, Hopf and flip bifurcations). The paper includes theoretical study, numerical simulations and circuit experimentation. Spectral analysis and Poincaré maps, guided by the bifurcation analysis, allows the classification of the regions of different qualitative behaviour. Many results come from direct experimentation with the circuit or from the numerical simulation using the state equations.

Kennedy and Chua, in 1986, study a driven relaxation oscillator circuit, first presented by Van der Pol, which gives an experimental confirmation of the period-adding route to chaos that was introduced by Feigenbaum in 1975 [Kennedy and Chua, 1986].

The work on Chua's circuit

Many of the phenomena expected when chaos is present have been visualized in Chua's circuit (1984). The roads to chaos that were pointed out in physical papers [Eckmann, 1981; Kadanoff, 1983] have been obtained experimentally in Chua's circuit.

This simple autonomous circuit with a piecewise-linear resistor (Chua's diode) develops a Shilnikov-type chaotic attractor (the double scroll). This model has been studied in great detail since then, both experimentally and theoretically. Matsumoto, Chua and Komuro, in 1985, give a complete analysis of the geometric structure [Matsumoto, Chua and Komuro, 1985], calculating also the dimensions and the Lyapunov exponents; the result is an excellent agreement between experiments and simulations. The double scroll is also obtained when the operational amplifiers used in the original paper are replaced by two transistors [Matsumoto, Chua and Tokumasu, 1986]. A geometric structure analysis along the same line was also given in [Tokunaga, Komuro, Matsumoto and Chua,

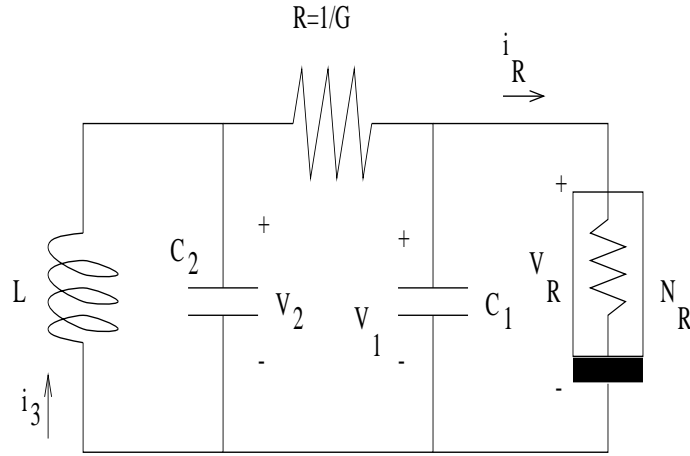


Figure 2.7: Chua's circuit.

1989] with reference to the Lorenz attractor, simulated via an electrical circuit with uncoupled continuous piecewise-linear resistors.

Chua's circuit family was also reported by Wu in a special issue on chaotic systems by the IEEE in 1987, responding to the exponential growth of attention given to chaos in the engineering community. This issue gave a theoretic overview on this subject (Parker, Chua, Mees, Sparrow and Holmes), and some important examples, including neon bulbs and the R-L-Diode circuit, were given by Hasler. Discrete maps associated with switched capacitor circuits and their practical realization were developed by Rodríguez and coworkers, and Matsumoto clearly stated how chaos in electronic circuits should be studied, giving the first word of caution on proving chaos. Matsumoto's strategy to prove chaos in a given circuit deals with the following: First, from an experimental point of view; then, numerically simulating the differential equations or discrete maps that describe the evolution of the circuit and, finally, rigorously (i.e. mathematically) proving that chaos is present, carefully assuring that the hypothesis of the mathematical theorems invoked are satisfied. Chua's circuit is, in fact, one of the few physical systems for which the presence of chaos (in the sense that the motion on the double scroll is technically equivalent to the full Bernoulli shift on two symbols) has been proven mathematically.

More recently, by adding a linear resistor in series with the inductor, Chua's circuit has been generalized to the canonical Chua's oscillator. This circuit is canonical in the sense that it contains every continuous three-dimensional odd-symmetric three-region piecewise-linear vector field. With the appropriate choice of the parameters, this circuit can be made to follow the classic period-doubling, intermittency, and torus-breakdown routes to chaos. The equations

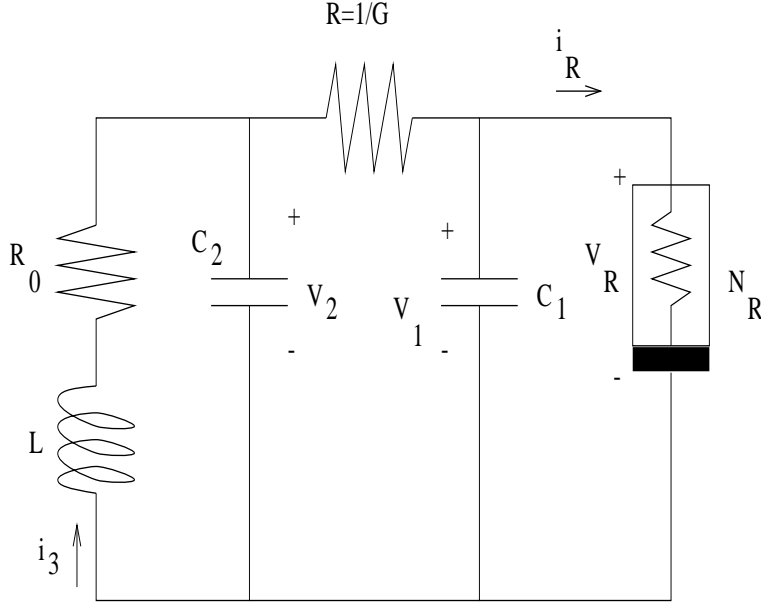


Figure 2.8: Chua's oscillator.

of Chua's oscillator are

$$\begin{aligned}\frac{dv_1}{dt} &= \frac{1}{C_1}[G(v_2 - v_1) - f(v_1)] \\ \frac{dv_2}{dt} &= \frac{1}{C_2}[G(v_1 - v_2) + i_3] \\ \frac{di_3}{dt} &= -\frac{1}{L}(v_2 + R_0 i_3)\end{aligned}$$

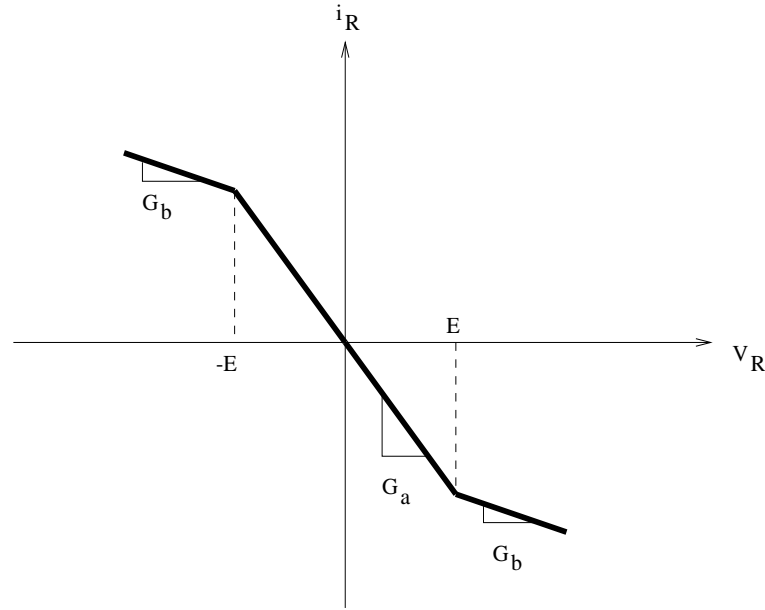
where $G = \frac{1}{R}$ and $f(v_1) = G_b v_1 + \frac{1}{2}(G_a - G_b)\{|v_1 + E| - |v_1 - E|\}$, which, by a change of variables, can be transformed into dimensionless form:

$$\begin{aligned}\frac{dx}{d\tau} &= k\alpha(y - x - f(x)) \\ \frac{dy}{d\tau} &= k(x - y + z) \\ \frac{dz}{d\tau} &= k(-\beta y - \gamma z)\end{aligned}$$

where $f(x) = bx + \frac{1}{2}(a - b)\{|x + 1| - |x - 1|\}$, and $k = \frac{RC_2}{|RC_2|}$.

Because of the generality of these equations, other chaotic systems can be modeled using Chua's oscillator. Examples include some of the systems studied by Sparrow (1981), Brockett (1982), Ogorzalek (1989) and Nishio (1990).

A sequence of visual snapshots showing the detailed dynamical evolution that leads to the birth of distinct strange attractors corresponding to several studied routes to chaos has been provided by [Kevorkian, 1993]. Among others,

Figure 2.9: v - i characteristic of Chua's diode.

- time evolution of the double scroll Chua's attractor,
- period-doubling route to chaos,
- intermittency route to chaos,
- torus-breakdown route to chaos,
- homoclinic orbit,
- heteroclinic orbit, and
- collision between two spiral Chua's attractors

are precisely represented in this paper, which belongs to the 1993 special issues of October and November of the *TRANSACTIONS ON CIRCUITS AND SYSTEMS*. In these issues, [Anischenko, Safonova and Chua, 1993] show that all three scenarios of transition to chaos due to torus breakdown

- 1) period-doubling bifurcation of the phase-locked limit cycles,
- 2) saddle-node bifurcation in presence of a homoclinic structure, and
- 3) soft transition due to the loss of torus smoothness

take place in Chua's circuit, in complete agreement with the Afraimovich-Shilnikov theorem.

A feedback control chaos approach was recently proposed by Chen and Dong, and also by Ogorzalek in 1993, where a chaotic trajectory can be guided towards one of the various unstable limit cycles of the dynamic system.

The last word on Chua's circuit seems far from being said. Shilnikov, in 1993, establishes in his paper [Shilnikov, 1993] that some of the attractors that occur in Chua's circuit are new and essentially more complicated objects than they seemed before. This conclusion is based on subtle results of systems with homoclinic tangencies and homoclinic loops of a saddle focus. Thus, such an attractor differs essentially from the hyperbolic and the Lorenz attractors. Shilnikov states that a complete description of the dynamics and bifurcations in Chua's equations is impossible, as it is for many other models. This result has to be interpreted as an important second advisory caution note when analyzing possible chaotic systems.

Other recent works

More recently, research into bifurcations and chaos by physicists in other subjects, such as lasers and thermal instabilities, has its counterpart in the research into chaotic circuits. Among others, symbolic dynamics of piecewise linear maps have been reported [Wu and Chua, 1994]. The persistence of saddle-node bifurcations in circuits and power systems when slow and fast variables are distinguished has also been presented recently [Chiang and Fekih-Ahmed, 1993]. Bifurcations and routes to chaos in resonant circuits and dc-motors have recently been examined.

Most of the state-of-the-art on nonlinear and chaotic circuits was reported in the cited IEEE special issues ending 1993, and a second general tutorial of theoretic material on this subject was given by Kennedy and Hasler in the international symposium ISCAS'94. At this congress, an important and recent overview on control chaos was reported by Ogorzalek, giving some of the fundamental ideas that have appeared regarding this topic research in this decade.

Synchronization of chaotic circuits has been pioneered in the articles of Pecora and Carroll [Pecora and Carroll, 1990; Carroll and Pecora, 1991; Pecora and Carroll, 1991a; Pecora and Carroll, 1991b], receiving nowadays much of the recent investigation in chaotic circuits. Apart from the work of Ott, Grebogi and York, yielding the OGY-control method, multiple papers have been elaborated giving applications mainly to secure communications [Cuomo, Oppenheim and Strogatz, 1993; Abarbanel and Linsay, 1993]. In [Saito and Mitsubori, 1994] control of piecewise-linear chaos is studied, and in [Dedieu and Ogorzalek, 1994] robust methods for controlling Chua's circuit are given. A long list of references has recently been compiled by [Chen, 1994].

2.3.2 Previous Work on Chaotic Power Electronic Circuits

In this work, research into chaotic power electronic circuits is reported, giving some of the ideas that were advanced in the eighties and which have been

considerably extended in the present decade.

One of the first studies on chaotic behaviour regarding power electronic circuits can be found in the [Baillieul, Brockett and Washburn, 1980]. Difference equations modeling power converters,

$$x_{k+1} = f(x_k), \quad (2.1)$$

where

$$f(x) = \begin{cases} m_1x + b_1, & x \leq \delta \\ m_2x + b_2, & x > \delta \end{cases} \quad (2.2)$$

are studied. The vector difference equation

$$x_{k+1} = A \cdot x_k + b \cdot f(c \cdot x_k) \quad (2.3)$$

is also analyzed, where f is a piecewise-linear function satisfying some Lipschitz-like condition. Some criteria for chaotic operation is given. This paper was reviewed later in detail by Veitch in 1992, with important observations about the sense in which the term chaos was defined in [Baillieul, Brockett and Washburn, 1980], using some important features of bimodal maps.

Later, chaos in power electronics has been studied almost at the same time by Wood (1989) on the one hand, and basically by Hamill and Deane (1988) on the other. In his paper [Wood, 1989], deals with a particular form of buck regulator circuit without PWM drive, and without inductor-current sensing, i.e. a form of ripple regulator, in an experimental and simulated manner. Wood shows a transition via period doubling from periodic to chaotic operation. A PWM buck regulator with a method of current limiting is also studied in this paper. In an overcurrent condition, this circuit behaves chaotically; so this is an example of a very practical circuit which operates quite satisfactorily in chaotic mode. A buck regulator which employs direct state-feedback with a digital delay to limit switching frequency is also analyzed in this reference. It is concluded that stabilization of the limit cycle of the ripple regulator is inherently difficult since it has a natural capacity for displaying chaotic behaviour. Phase-plane trajectories are drawn in the simulations that show chaotic behaviour and limit cycles for certain values of the parameters. In this paper, distinction is made among laboratory chaos, numerical simulation chaos and strictly mathematical chaos. Only the latter is not discussed with examples.

In the paper [Krein and Bass, 1990], chaos and instabilities in simple power circuits are also studied. For discussion, a power converter is assumed to correspond to the differential equation

$$\dot{x} = F(x, t, h)$$

where the switching function $h = h(x, t)$ and F are discontinuous in either time or the states. The dc-dc boost converter under current-mode control is simulated and experimented. Bifurcation diagrams are shown with simulated data and are also visualized in the oscilloscope. Unbounded trajectories, chattering behaviour and chaotic waveforms are introduced as three different types of instability in a power converter. Also, the problem of multistability is introduced (perhaps for the first time) in power converters.

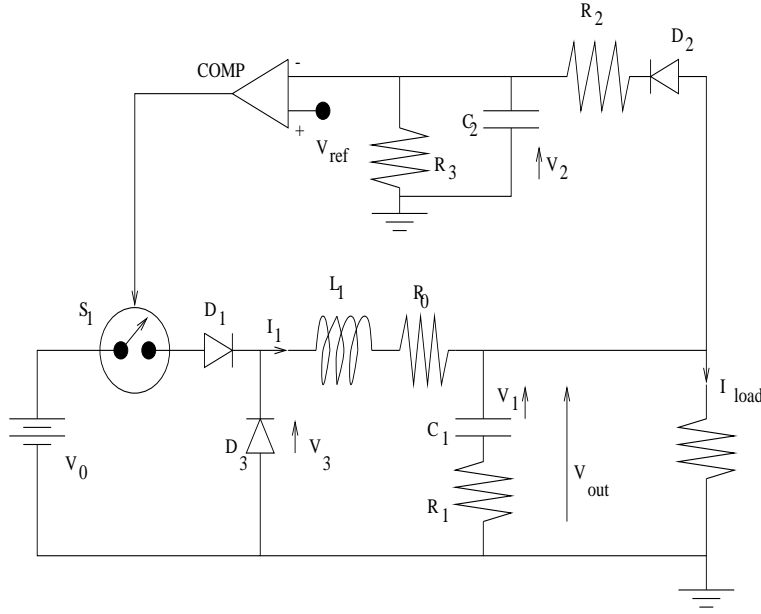


Figure 2.10: Ripple-regulator circuit.

The work of Hamill and coworkers

A buck converter is also studied in [Hamill and Jeffries, 1988], and [Jefferies, Deane and Johnstone, 1989], where chaos in electronic circuits as the R-L-Diode is reviewed and the chaotic buck converter is introduced. A difference equation is derived for the closed-loop case including a saturation function

$$x_{n+1} = x_n + b \cdot \text{sat}(a \cdot (1 - x_n)) - c \quad (2.4)$$

where

$$\text{sat}(e_n) = \begin{cases} 0, & e_n \leq 0 \\ e_n, & 0 < e_n < 1 \\ 1, & e_n \geq 1 \end{cases} \quad (2.5)$$

This difference equation may be represented graphically by a one-dimensional piecewise-linear folded return map. Numerical iteration was performed with a variety of parameter values, resulting in a bifurcation diagram and obtaining a classical Feigenbaum route to chaos, followed by the period-adding phenomenon. Stable and unstable regions are expressed in terms of the parameters, and the *sat* function is replaced by a cubic spline, comparing the results from the smooth and non-smooth case.

In 1990, at the PESC'90 Conference, a seminal paper [Deane and Hamill, 1990a] which seems to be the first detailed study of the chaotic operation of the buck converter controlled by PWM in continuous conduction mode, is discussed by Deane and Hamill.

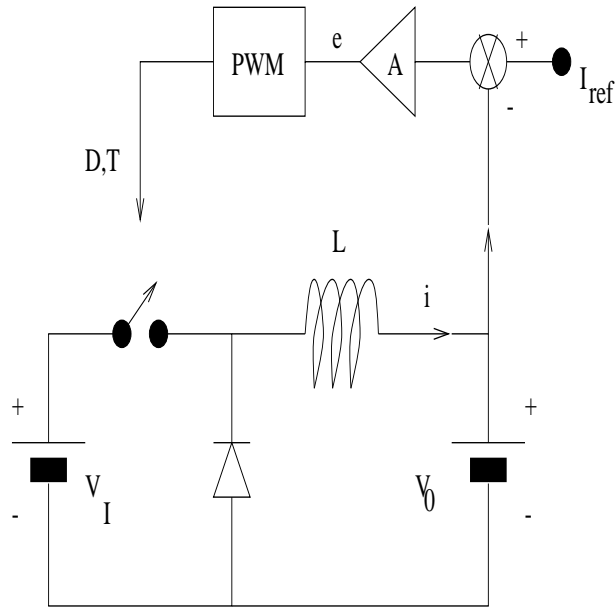


Figure 2.11: Switching regulator dc-dc converter with wideband feedback control.

Two versions are treated, a first order and a second order circuit. Their behaviour is modeled analytically, numerically and also experimentally. The first order circuit admits an entirely analytical treatment, and so, conditions are given that lead to multiple pulsing, although chaotic behaviour is disregarded. The second order circuit is close to that of many real buck converters. Although it cannot be analytically investigated because a transcendental equation is involved, subtle and careful numerical integration of the trajectories allows one to obtain striking agreement between simulations and experimental behaviour (although parasitic effects are not taken into account). The method for computing trajectories will then be followed by other researchers. Every cycle of the ramp is divided in N intervals (with N between 100 and 1000) of the same length and a check is carried out at every point to see if the trajectory crosses the ramp voltage. Once a crossing is detected in the interior of an interval, the Newton-Raphson method is applied to find with high precision the crossing value. Then, the topology is changed at this point until another change of topology is detected. This is called by the authors *exact numerical analysis*, meaning that no additional approximations are made, other than the inevitable (though small) errors entailed in solving numerically the transcendental equation. Periodic state trajectories of periods $2^i, i = 0, \dots, 3$ and chaotic waveforms are also obtained.

Keeping all the parameters constant but changing the input dc-dc voltage from 15 to 40 volts, a bifurcation diagram is plotted, clearly showing a period-doubling route to chaos. The ratio of the differences between the values of

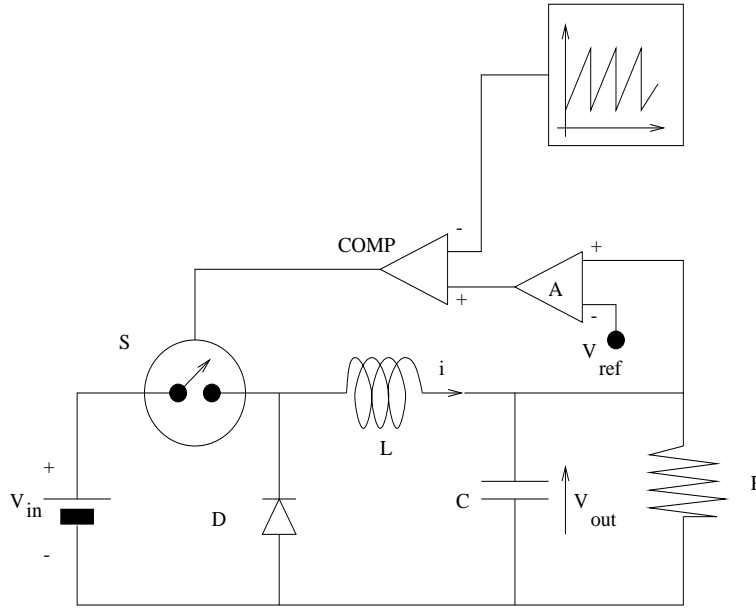


Figure 2.12: Voltage-mode controlled Dc-dc buck converter.

the dc-dc input parameter required to obtain successive period-doublings is found to be around 6.5, compared to the asymptotic value of around 4.7 to be expected for universal chaotic behaviour. This remains an open question about the circuit. A strange attractor is also obtained both in the oscilloscope and in a numerically computed plot.

An approximate one-dimensional closed-form mapping is also derived by the authors in [Deane and Hamill, 1991] for a current-mode controlled buck converter in continuous conduction mode, leading to a stability criterion. The mapping is of the form

$$i_{n+1} = 1 - [\beta + \alpha(i_n)] \mod 1$$

which has been rigorously proved to produce a chaotic sequence if the function α is non-negative and Lipschitz, with Lipschitz constant strictly greater than the unity.

In a later article [Deane and Hamill, 1990b], the difficulties in the averaging and small signal model are set out. When the state-space averaging technique is applied to the analysis of a switched-mode converter, the resulting nonlinear equations are usually linearized to obtain a small signal model. While such an approach is often useful in determining the stability of a switched-mode converter, it does not predict the possibility of subharmonic oscillation, which is an eventually nonlinear phenomenon and may occur in practice. Moreover, if large-signal effects are to be taken into account, analytical difficulties like those stated before usually force one to resort to numerical simulation. In this

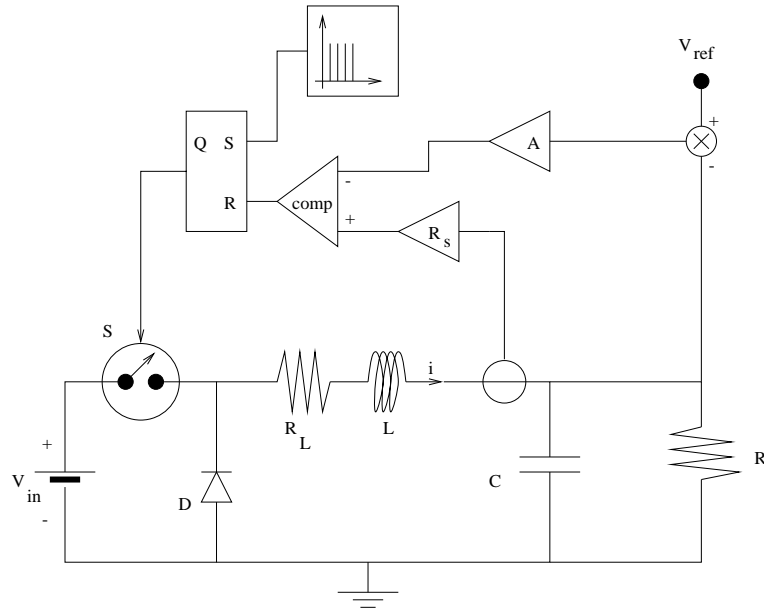


Figure 2.13: Current-mode controlled Dc-dc buck converter.

paper, a very interesting review of nonlinearity in power electronics is exposed, including BJT's, MOSFET's, IGBT's, SIT's, thyristors and diodes.

The R-L-Diode circuit was analyzed by Deane and Hamill, since it is representative of a number of situations found in practical converters, as, for instance, in a series-resonant converter. This simple R-L-D circuit is an example of a situation common in power electronics (a diode associated with inductance and resistance). If the diode has substantial charge storage, instability is likely to occur even though no active components are involved. Charge storage is not important below 100 KHz, but above 1 MHz, diode recovery times become significant. With converter frequencies being pushed even higher, diode-induced instabilities will arise. In this paper, chaotic ferroresonant circuits and thyristor rectifier circuits are also described, observing chaotic waveforms and strange attractors. Finally, a buck converter is also investigated. An experimental bifurcation diagram shows chaotic bands interspread with periodic cycles. The period adding route in the R-L-Diode circuit, which is a common scheme in power electronics, is experimentally simulated, and also numerically simulated with SPICE.

The SPICE codes for these simulations and the convenient comments are put all together in a later article by Hamill in 1993, where chaos in simple passive and active circuits, and also in power conversion circuits, is studied by means of SPICE simulations, including waveforms, state-space trajectories, spectrum and bifurcation diagrams [Hamill, 1993]

The paper [Hamill, Deane and Jefferies, 1992], also signals the difficulties

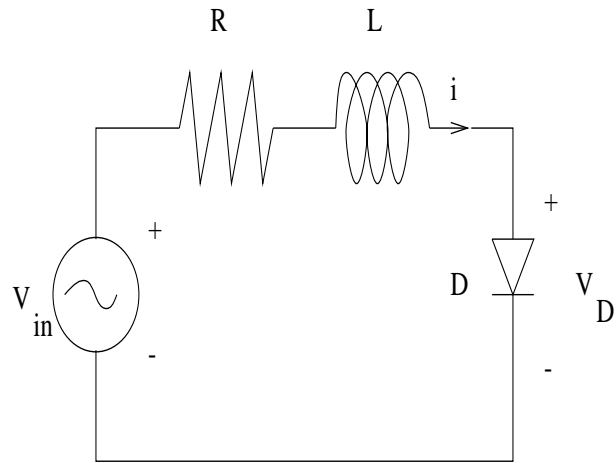


Figure 2.14: R-L-Diode circuit.

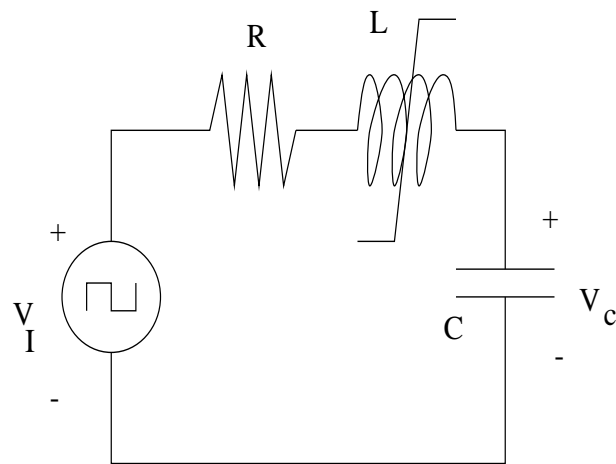


Figure 2.15: Ferroresonant circuit incorporating saturating inductor.

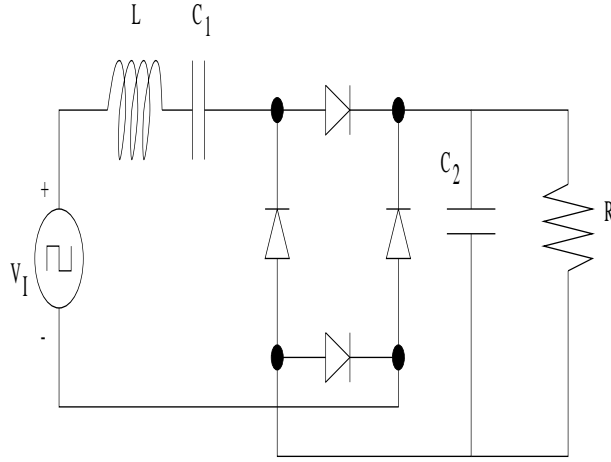


Figure 2.16: Series-resonant converter employing slow rectifier diodes.

in averaged models to predict subharmonic instability. As was discussed at the PESC in 1990, from a basic theoretic study, a combined experimental-SPICE-numerical method is employed, giving a very good degree of resemblance with the laboratory experiments in the range of parameters utilized.

In 1992, in a IEE Colloquium on Static Power Conversion [Hamill, 1992], in London, Hamill stated that the feedback switching frequency ripple interferes with the intended PWM operation, producing chaos. When feedback is applied to a dc-dc converter with switching frequency f_s , the practical gain-bandwidth product is conventionally restricted to about $f_s/4$, to allow modelling techniques such as state-space averaging to be employed. The approximation becomes worse if the signal frequency approaches $f_s/2$ owing to the inherent sampling properties of PWM. If the feedback loop has significant gain at $f_s/2$ and above, the converter becomes unstable. In this conference the current-mode controlled buck converter and boost converter are analysed, and some possible benefits of chaotic operation, mainly, high sensitivity and bounded oscillation are discussed.

More recently, another mapping was derived in closed form for an idealized current-mode controlled boost converter operating in continuous conduction mode by [Deane, 1992]. This map is two-dimensional and describes exactly the motion in the discrete state-space. In dimensionless variables, this two-dimensional mapping is described by

$$\begin{aligned}
 x_{n+1} &= \alpha - e^{-kt'_n} \{ (\alpha kT + 1 - y_n e^{-2kTx_n}) \frac{\sin(\omega t'_n)}{\omega T} + \alpha \cos(\omega t'_n) \} \\
 y_{n+1} &= 1 - e^{kt'_n} \{ \left(\frac{k}{\omega} (y_n e^{-2kTx_n} - 1) - \frac{\alpha T}{\omega LC} \sin(\omega t'_n) - \right. \\
 &\quad \left. - (y_n e^{-2kTx_n} - 1) \cos(\omega t'_n) \right) \}
 \end{aligned}$$

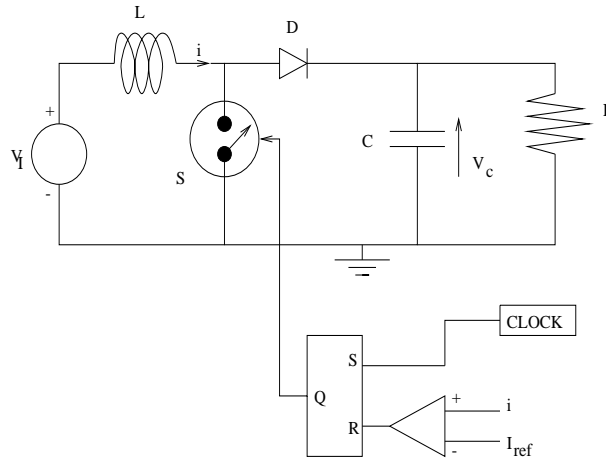


Figure 2.17: Current-mode controlled boost converter.

where

$$t'_n = T(1 - x_n \bmod 1)$$

A current bifurcation is plotted by numerical simulation of the mapping. The presence of bifurcations, subharmonics and chaotic behaviour is in a standard period-doubling route to chaos. The fact that the map is available in closed form makes numerical calculation of the Lyapunov exponents straightforward. The possible presence of a strange attractor is yet to be investigated. Non-smooth bifurcations are outlined, which could not be detected with standard smooth bifurcations packages like AUTO.

Other recent works

From the very important seminal work of Hamill, Deane and Jefferies, other researchers have dealt with nonlinear dynamics regarding the basic converter cells. Some of these works belong to Tse [Tse, 1994a; Tse, 1994b; Tse and Chan 1994]. In [Tse, 1994a], a boost operating in discontinuous conduction mode is analyzed quite analytically by means of truncating the series of the exponential matrix involved in the solutions. Thus, an approximate one-dimensional Poincaré map can be derived and analytically investigated. This truncation includes some differences between the analytical considerations and the numerical simulations which are performed with the non-truncated (numerical) exponential. Characteristic multipliers, subharmonics, flip bifurcations and a period-doubling route to chaos are obtained in the simulations. The same techniques are applied in [Tse, 1994b] for a buck converter acting in discontinuous conduction mode. Also, by means of the truncated series, a Poincaré approximated map is derived, yielding characteristic multipliers, flip bifurcations and subhar-

monics. Finally, in [Tse and Chan, 1994], a fourth order Čuk converter under current control is studied by means of the same techniques.

In the paper [Zafrany and Ben-Yaakov, 1995], a deeper study of the current mode boost converter which was initially studied by Deane is derived, with a variety of different models which include a slope compensation. Also in 1995, in a communication [Toribio and Toribio, 1995], some software for simulating the buck converter operating in continuous conduction mode is exposed, and a state densities approach to analyzing chaos in a boost converter [Font, Rodríguez-Manero and Verghese, 1995] is presented.

Chakrabarty, Banerjee and coworkers have also written some papers regarding the chaotic behaviour of the buck converter. Concretely, in [Chakrabarty and Banerjee, 1995] and [Poddar, Chakrabarty and Banerjee, 1995], a control scheme is derived to stabilize some unstable orbits for a buck converter. This appears to be the first paper which deals with control chaos in power converters. In this scheme, benefit is derived from the linear character in each of the topologies.

In their more recent paper [Chakrabarty, Poddar and Banerjee, 1996], the bifurcation behaviour is studied with detail in a version of a buck converter which is slightly different from the one studied by Hamill. Concretely, one-dimensional bifurcation diagrams are drawn for L as the bifurcation parameter and also for T and C . In all the cases, a period-doubling route to chaos is found. Two-dimensional bifurcation diagrams are also plotted taking V_{in} as a first parameter and R, L, T as second parameter. This work is largely numerical and describes the bifurcation diagrams for engineering use.

Not only the period-doubling route to chaos has been reported regarding converters. Recently, in a communication, quasi-periodic behaviour has been stated regarding the boost converter, in open-loop and closed-loop when it is disturbed with a sinusoidal function in the forcing term [di Bernardo, Garofalo, Glielmo and Vasca, 1996]. A Neimark-Sacker bifurcation and torus breakdown are also reported.

More recent research in this field includes submitted papers such as [di Bernardo, Garofalo, Glielmo and Vasca, 1997], which includes an analytical treatment for the flip bifurcation in the buck converter reported [Deane and Hamill, 1990; Fossas and Olivar, 1996], via an impact map inspired in impact oscillators appearing in mechanics. Also, a local infinity stretching condition equivalent to that in [Fossas and Olivar, 1996] is given.

Also, in two recent submitted papers [Banerjee, 1997] and [di Bernardo, Fossas, Olivar and Vasca, 1997], secondary bifurcations, fractal basin boundaries and crises are discussed.

2.4 Part Four: Discussion

2.4.1 Modeling

High efficiency solid state power conversion has become possible through the continuing development of high power semiconductor devices. The operation of these devices as switches, which is necessary for high efficiency, means that power

electronic circuits are essentially nonlinear, time-varying dynamical systems. Though this makes them difficult to study, the effort is well worthwhile because they have many practical applications and are becoming increasingly important in the delivery and utilisation of electrical energy. The conventional modelling approach effectively ignores nonlinear phenomena, and can sometimes mislead the designer into thinking a circuit will perform acceptably when in practice it will not. Thus the traditional approach does not always produce reliable models.

Electrical and electronic circuits can be modeled in continuous time form by a system of possible non-autonomous ordinary differential equations, or in discrete time form by a generally nonlinear mapping. The latter version is usually preferred in some specific situations; for instance, when the system is driven by a T -periodically action, the T -time map being the most preferable choice. This is specially satisfactory in power electronic circuits. In this case, a nonlinear mapping can be derived from its intracycle operation of the circuit. The long term, cycle-to-cycle behaviour is determined by iterating the map. In many cases of practical interest, the map is too complicated to be expressed analytically and calls for numerical computation.

Another important question in favour of the discrete time approach is the type of vector field that appears in power converters when they are modeled by differential equations. Owing to the switching function that is inherent to power converters, the vector field can be discontinuous, usually being piecewise continuous and piecewise linear. Thus, lack of smoothness implies that almost none of the known mathematical theorems can be directly applied, and that different results from the continuous case can also be expected. In spite of this, the case of discontinuous piecewise linear vector fields allows some easy analytical treatment inside the regions of linearity, and thus some results can be stated.

Discrete nonlinear modelling offers another way of looking at the circuits, one that is more accurate and able to reproduce nonlinear effects such as sub-harmonics and chaos. Unfortunately, it demands a mental shift on the part of power electronics engineers, away from linear systems thinking and towards the unfamiliar realm of nonlinear dynamics [Lonngren, 1991; Hamill, 1993; Lobry and Trecat, 1995]. These techniques have not yet been widely adopted by power electronics practitioners, and there is much work still to be done.

2.4.2 Rigorous Mathematical Chaos

Almost all chaotic and bifurcation phenomena have been experimentally and numerically simulated in electronic circuits. Piecewise linear maps, quadratic maps including bifurcations, universality, Lyapunov exponents and period doubling route to chaos have been experienced from the discrete time approach. In addition, local bifurcations confirming the theory concerning normal forms and center manifolds, and maps on the circle, have been computed numerically. Experimentally, the oscilloscope allows visualizing fractal attractors and bifurcation diagrams. From the continuous time approach, all three routes to chaos have been experimentally obtained in some circuits; Chua's oscillator is the main one that has been studied in detail. Moreover, crises and local and

global bifurcations have also been visualized and numerically computed.

Strange attractors in dissipative systems, fractal basin boundaries, invariant manifolds, bifurcation diagrams and dimension computing have also been performed in continuous-time systems that describe nonlinear electronic circuits. As in almost all applied science, mutual benefit has been accomplished between theoretical and applied subjects, though in this case, engineering is indebted to physics and mathematics. Practical control chaos has prompted some mathematical research, but this is an exception. Usually, mathematics have provided the basis of simulations and experimental chaos. In spite of this, very few circuits have been rigorously proven to be chaotic. Although practical evidence is strong, and analytical theorems can be stated, for example some special criteria for chaos (hyperbolic and non-hyperbolic case leading to invariant sets, and Shilnikov-like homoclinic and heteroclinic motions) [Wiggins, 1988; Wiggins 1990], analytical methodology concluding chaos is difficult to apply in a concrete nonlinear circuit. Some exceptions are invariant sets and homoclinic orbits in Chua's circuit, Melnikov's method applied recently to conclude transverse homoclinic orbits in a phase-locked loop demodulator, and some criteria to distinguish between strange nonchaotic attractors and strange nonchaotic transients. Power converters are no exception to this rule. Rigorous mathematical justification of chaos in power dc-to-dc converters remains to be given.

As pointed out in a recent paper by Shilnikov, some caution has to be exercised when chaotic behaviour is simulated. Some nonlinear circuits displaying bifurcations and strange attractors may be more complicated than expected. In this sense, rigorously-proven mathematical results are very revealing when explaining observed chaotic phenomena [Shilnikov, 1993].

2.4.3 Preview of the Results in This Thesis

The work of Hamill and Deane in the buck converter, controlled by a PWM scheme, describes an experimental and numerical point of view of the system. This is one of the most practical schemes that can be encountered in applications. The work is certainly complete in the first order circuit, but some phenomena remain to be explained and clarified in the second order circuit. In particular, a deeper study should include the details in the transition to chaotic behaviour and in the possible strange attractor that was found. Thus, work in this type of buck converter has been studied along the following lines:

- i) Analytical results concerning the existence of periodic orbits and its stability (preparatory work must be done in computing the periodic orbits and its characteristic multipliers) have been given.
- ii) A careful study of the discrete nonlinear Poincaré map (or T -time map) associated with the system has been carried out, to conclude results on the phenomenon of multiple pulsing that has been treated analytically in the first order system by Deane and Hamill.
- iii) Numerical evidence of the different possible routes to chaos in the circuit, as some control parameters are varied (for example, the dc-input voltage and the dc-reference voltage), has been obtained.

- iv) Secondary bifurcations, basins of attraction metamorphosis and crises have been described with detail, including certain non-smooth bifurcations of new type.
- v) Some methods for controlling chaos have been deduced and applied to this system and related ones, taking advantage of the linear topologies.

The main objective of this work is to give an exhaustive explanation of the phenomena observed experimentally in some dc-to-dc controlled converters, giving detailed results concerning the chaotic behaviour and control of chaos of these systems.

Chapter 3

Basic Geometrical and Topological Features

Abstract

In this chapter, basic geometrical and topological aspects are first exposed for the class of systems to be studied. Then, a DC-DC buck converter controlled by a PWM in continuous conduction mode, which is the main object under study in this thesis, is introduced. This converter gives rise to a great variety of behaviours depending on the values of the parameters of the circuit. We show different graphical representations for the solutions of the system of differential equations. The Poincaré map that is considered naturally arises from the sampling process in the oscillatory forced system. The 1T-periodic and 2T-periodic orbits which cross the voltage ramp once per cycle are analysed, and their stability is studied numerically computing the characteristic multipliers associated with each one.

3.1 General Considerations

Consider dynamical systems of the following type:

$$\dot{X}(t) = f(X, t) \equiv \begin{cases} A_1 X + b_1 & \text{if } u = 0 \\ A_2 X + b_2 & \text{if } u = 1 \end{cases} \quad (3.1)$$

where $A_i \in \mathcal{M}(2 \times 2, \mathbb{R})$, $b_i \in \mathcal{M}(2 \times 1, \mathbb{R})$, $X = (x_1, x_2)^t \in \mathbb{R}^2$ and u is a two-valued function.

These types of systems are called switching systems or variable structure systems, due to the function u , which changes the topology depending on $u = 0$ and $u = 1$. Of course, this can be generalized to n topologies but, in the following, only two topologies will be considered. It is worth noting that in each topology the system is linear, so analytical solutions can easily be computed.

Then, solutions for system (3.1) can be obtained by joining the solutions computed for both topologies. As it will be apparent, the complexity and possible chaotic behavior strongly depend on the considered function u . One of the choices for u is taking

$$u = \begin{cases} 0 & \text{if } mX < a \\ 1 & \text{if } mX > a \end{cases} \quad (3.2)$$

where $m = (m_1, m_2) \in \mathbb{R}^2$ and $a \in \mathbb{R}$.

In this case, there exists a curve of discontinuity in the phase space which is given by the equation

$$mX = a \quad (3.3)$$

called the switching equation.

Then, this system is two-dimensional and chaos can be discarded, although interesting dynamics can be obtained. Let us look more closely at each system. Supposing that A_1 and A_2 both have full rank, we can obtain two equilibrium points for the systems. Namely,

$$X_1 = -A_1^{-1}b_1$$

in the first topology, and

$$X_2 = -A_2^{-1}b_2$$

in the second one. Let us also assume that these points do not belong to the switching curve. Depending on the matrices A_1, A_2 , different types of dynamics can be obtained. For example, X_1 can be a stable focus and X_2 a saddle, as in Fig. 3.1. So, for different choices of the matrices A_1, A_2 , the different modelling equations for the basic cells of dc-dc converters are obtained. Equation (3.1) is the general form for a dc-dc converter, while if the particular case of $A_1 = A_2$ and $b_1 = 0$ is chosen, then, the cell of a buck converter is obtained. We will choose this particular cell for further study; more precisely, the stable focus version, which is represented in Fig. 3.2.

Note also that, as $A_1 = A_2$, the two equilibrium points are of the same type, including the same eigenvalues and eigenvectors. Other configurations have been considered in the literature for the buck converter. While Fig. 3.2 corresponds to the one chosen by Hamill and coworkers [Deane and Hamill, 1990], a stable node version was chosen for study by Chakrabarty and coworkers [Chakrabarty, Poddar and Banerjee, 1996].

Some of the multiple schemes are easy to analyze. For example, if in the node version (see Fig. 3.3), we choose the control function u to be defined as in (3.4), then, depending on the initial condition X_0 , the asymptotic behavior is obvious. But, if u is defined such that

$$u = \begin{cases} 0 & \text{if } mX > a \\ 1 & \text{if } mX < a \end{cases} \quad (3.4)$$

the behavior is not so obvious because the system does not have X_1 and X_2 as equilibrium points. In this case, if there exists an equilibrium point, it must be located in the switching curve, and the existence of periodic orbits cannot be

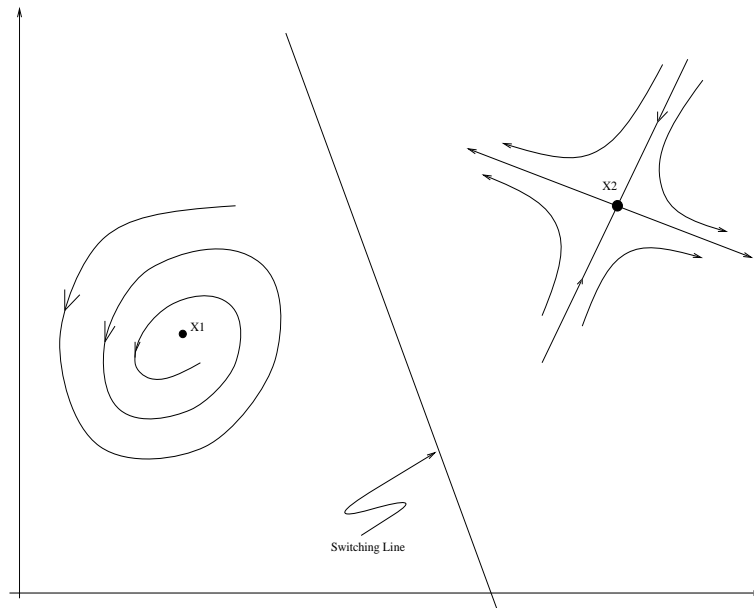


Figure 3.1: Two-topologies system of stable focus/saddle type.

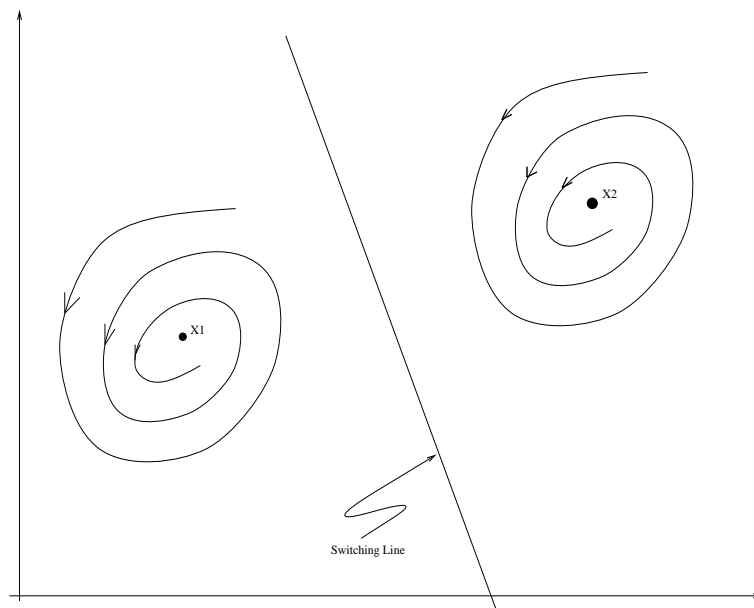


Figure 3.2: Two-topologies system of stable focus/stable focus type, corresponding to the model of a buck converter.

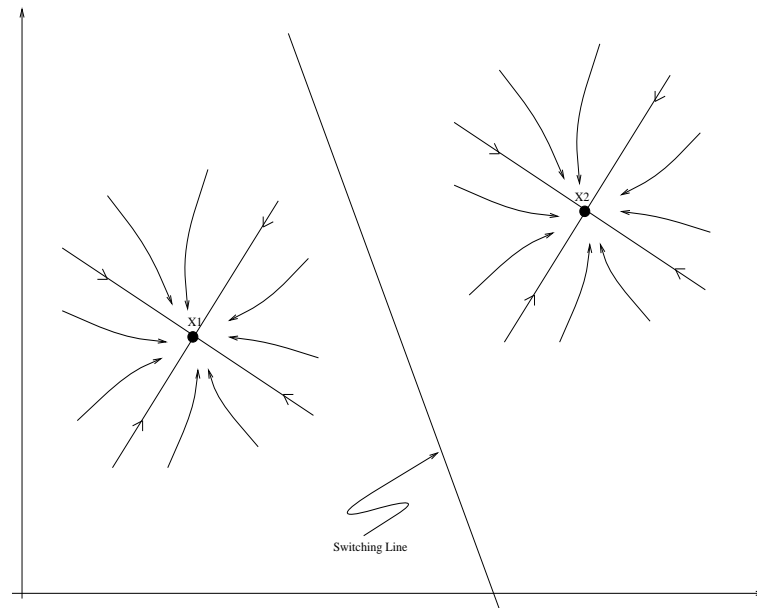


Figure 3.3: Two-topologies system of stable node/stable node type, corresponding to the model of a buck converter.

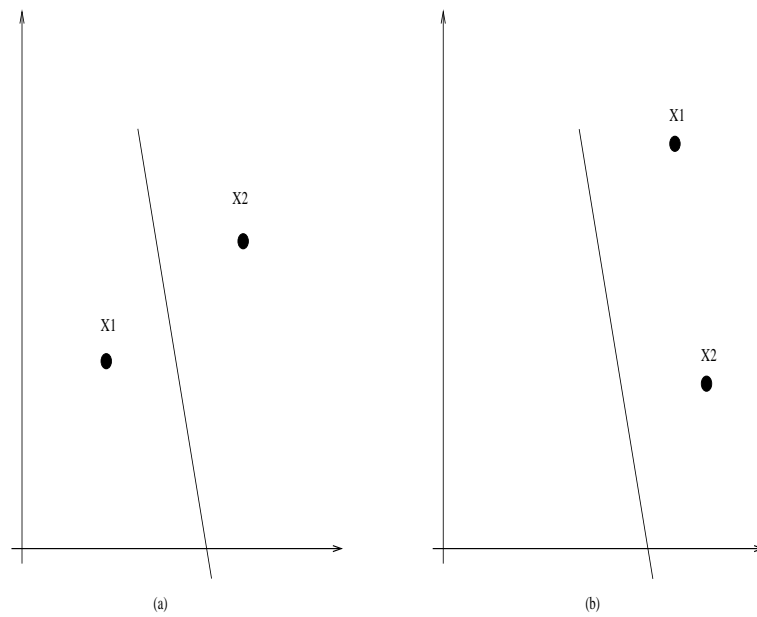


Figure 3.4: Different relative positions for the equilibrium points and the switching curve.

discarded. Note also that the relative position of the switching curve can be decisive (see Fig. 3.4).

Although these systems can display intricate behavior, they cannot display chaos due to the fact that they are two-dimensional flows. Instead, if the function u is allowed to depend on t , this can lead to chaotic behaviour. For the usual scheme which models many commercial converters, the function u is of the following type:

$$u = \begin{cases} 0 & \text{if } mX > \gamma(t) \\ 1 & \text{if } mX < \gamma(t) \end{cases} \quad (3.5)$$

being $\gamma(t)$ a T -periodic function.

3.2 DC-DC Buck Converter Controlled by PWM

The experimental basis of the present study is a DC-DC buck converter whose output voltage is controlled by a PWM with natural sampling and constant frequency, working in continuous conduction mode. The circuit we study is of second order and its block diagram is shown in Fig. 3.5. A detailed description of this converter can be found in [Deane and Hamill, 1990; Hamill, Deane and Jefferies, 1992] which are the main references for our work. This circuit is one of the simplest but most useful power converters, a chopper circuit that converts a dc input to a dc output at a lower voltage (many switched mode power supplies employ circuits closely related to it). An application of current importance is conversion of the standard 5V dc supply used in computers to the 3.3V needed by a Pentium CPU chip. A buck converter for this purpose can achieve a practical efficiency of 92%, whereas a linear regulator would be only 66% efficient, producing six times as much waste heat. Although this example is at a low power level, buck converters are also used at several kilowatts.

Next we review the notation and main concepts in [Hamill, Deane and Jefferies, 1992].

A dynamical system may be described by a system of differential equations

$$\frac{dx}{dt} = f(x, t)$$

where $f(x, t)$ is a n -dimensional vector field and $x = x(t)$ represents the state of the system. We have $x = (v, i)$, where v is the voltage through the capacitor and i is the intensity of the current at the inductor. In our case the function f is a discontinuous one, for the circuit has a switch commuting between two topologies, depending on the state x of the system.

Keeping the notation of [Deane and Hamill, 1990; Hamill, Deane and Jefferies, 1992], the parameters of the circuit are: R , C , and L , the resistance, the capacitance and the inductance of the circuit; V_L and V_U , the lower and upper voltages of the ramp and T , its period; a , the gain of the amplifier; V_{ref} , the reference voltage, and V_{in} , the input voltage (see Fig. 3.5). It is assumed to have ideal switches. The converter we are going to study works as follows: the voltage v of the capacitor is applied to the positive pole of the amplifier with

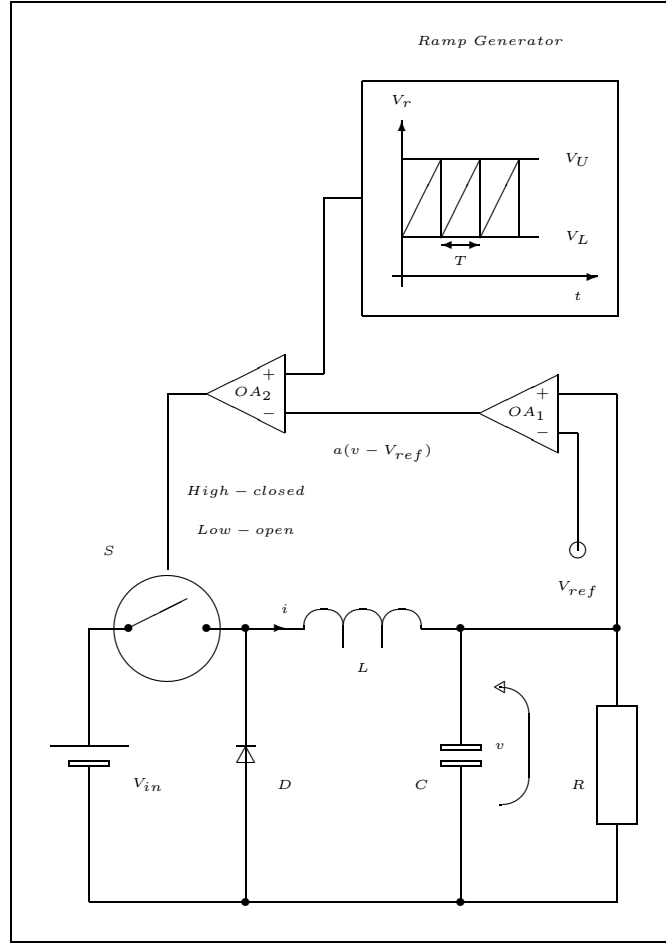


Figure 3.5: Block diagram of the buck converter.

gain a , and the reference voltage V_{ref} , to the negative pole. The output voltage, which we will call the control voltage $v_{co}(t)$, is thus

$$v_{co}(t) = a(v(t) - V_{ref})$$

Then, both v_{co} and V_r , the voltage of the ramp, are applied to the comparator, and every time the output difference changes its sign, the position of the switch S is commuted in such a way that it is open when the control voltage exceeds the ramp voltage and it is closed otherwise. Thus the circuit shows two topologies which simulate the effect of the diode. The operation described is known as continuous conduction mode (CCM), since the inductor passes current without a break. However, if the output is only lightly loaded, the inductor current can become zero for part of the cycle as the diode comes out of conduction: this is discontinuous conduction mode (DCM). (The terms *continuous*

and *discontinuous* are used in a non-mathematical sense here.)

When $v_{co}(t) < V_r(t)$, the voltage at the diode, v_d , is the input voltage V_{in} , and when $v_{co}(t) > V_r(t)$, then $v_d = 0$. These two topologies are described by two systems of differential equations:

System 1: $v_{co}(t) > V_r(t)$

$$\frac{d}{dt} \begin{pmatrix} v(t) \\ i(t) \end{pmatrix} = \begin{pmatrix} -1/(RC) & 1/C \\ -1/L & 0 \end{pmatrix} \begin{pmatrix} v(t) \\ i(t) \end{pmatrix} \quad (3.6)$$

System 2: $v_{co}(t) < V_r(t)$

$$\frac{d}{dt} \begin{pmatrix} v(t) \\ i(t) \end{pmatrix} = \begin{pmatrix} -1/(RC) & 1/C \\ -1/L & 0 \end{pmatrix} \begin{pmatrix} v(t) \\ i(t) \end{pmatrix} + \begin{pmatrix} 0 \\ V_{in}/L \end{pmatrix}$$

For any $\mathcal{S} \subseteq \mathbb{R}$ we introduce the characteristic function

$$u(t) = \begin{cases} 0 & \text{if } t \notin \mathcal{S} \\ 1 & \text{if } t \in \mathcal{S} \end{cases}$$

Using the notation $x = (v(t), i(t))^t$, (we denote y^t the transpose of y), both systems can be written in the same form

$$\frac{dx}{dt} = f(x, t)$$

where

$$f(x, t) = \begin{pmatrix} -1/(RC) & 1/C \\ -1/L & 0 \end{pmatrix} x(t) + \begin{pmatrix} 0 \\ V_{in}/L \end{pmatrix} u(t)$$

with

$$\mathcal{S} = \{t \geq 0 : v_{co} < V_r(t)\} \quad (3.7)$$

The voltage of the ramp is given by

$$V_r(t) = V_L + (V_U - V_L)t/T$$

periodically extended with period T . This can also be written as

$$V_r(t) = V_L + (V_U - V_L)Frac(t/T)$$

denoting by $Frac(y)$ the fractionary part of y . Observe that the time, t , explicitly appears in the expression of f , concretely in the term $u(t)$, that somehow represents the control ramp. Due to the explicit appearance of t , the system is non-autonomous.

If we fix a set of initial conditions $v_0 = v(t_0)$ and $i_0 = i(t_0)$, as the systems of differential equations are linear, we will be able to compute exactly the solution of each one.

Let us write

$$k = \frac{1}{2RC} \quad w = +\sqrt{\frac{1}{LC} - k^2}, \quad (3.8)$$

and supposing that

$$\frac{1}{LC} - k^2 > 0 \quad (3.9)$$

we can define the real matrix

$$A = \begin{pmatrix} -k/w & 1/(Cw) \\ -1/(Lw) & k/w \end{pmatrix}$$

and we have the following solutions for the systems:

System 1: $v_{co}(t) > V_r(t)$

$$\begin{pmatrix} v(t) \\ i(t) \end{pmatrix} = e^{-k(t-t_0)} [I \cos w(t-t_0) + A \sin w(t-t_0)] \begin{pmatrix} v_0 \\ i_0 \end{pmatrix}$$

System 2: $v_{co}(t) < V_r(t)$

$$\begin{pmatrix} v(t) \\ i(t) \end{pmatrix} = \begin{pmatrix} V_{in} \\ V_{in}/R \end{pmatrix} + e^{-k(t-t_0)} [I \cos w(t-t_0) + A \sin w(t-t_0)] \begin{pmatrix} v_0 - V_{in} \\ i_0 - V_{in}/R \end{pmatrix}$$

where I is the identity matrix. These expressions of the solutions are equivalent to those obtained in [Deane and Hamill, 1990] and [Hamill, Deane and Jefferies, 1992]. It follows that, between two commutation consecutive times, we know exactly the state variables of the system. Essentially, they are a combination of exponential and sinusoidal functions.

For the system 1 ($v_{co}(t) > V_r(t)$), we have as equilibrium point $\bar{x} = (\bar{v}, \bar{i})$, verifying

$$\begin{pmatrix} -1/(RC) & 1/C \\ -1/L & 0 \end{pmatrix} \begin{pmatrix} \bar{v} \\ \bar{i} \end{pmatrix} = \begin{pmatrix} 0 \\ 0 \end{pmatrix} \Leftrightarrow \bar{v} = \bar{i} = 0 \Leftrightarrow \bar{x} = 0$$

Then,

$$Df(\bar{x}) = \begin{pmatrix} -1/(RC) & 1/C \\ -1/L & 0 \end{pmatrix}$$

and the eigenvalues are obtained as the roots of the characteristic polynomial

$$\begin{vmatrix} -1/(RC) - x & 1/C \\ -1/L & -x \end{vmatrix}$$

which are

$$\lambda_1 = -k + iw \quad \lambda_2 = -k - iw$$

Being $-k < 0$, we obtain that \bar{x} is an asymptotically stable equilibrium point and the orbits around it will be as in Fig. 3.6.

If we make similar computations for system 2, the equilibrium point we have now is $(V_{in}, V_{in}/R)$, with the same eigenvalues. So, the phase diagram around it will be very similar to the one computed for system 1, as is shown in Fig. 3.7.

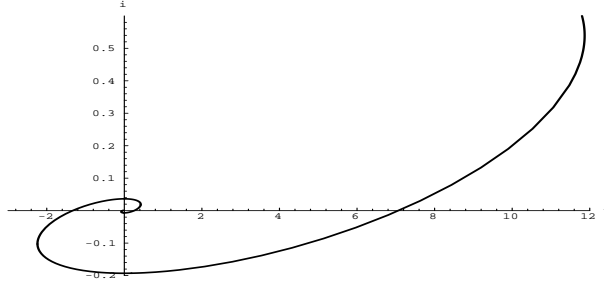


Figure 3.6: Orbit of the system 1 around its equilibrium point in the state space.

Thus, the evolution of each system, considered separately, is trivial, and corresponds to damped oscillations around the equilibrium point. But when the systems are taken together as a global system, as in the buck converter, the behaviour is radically different. When a trajectory is near the equilibrium point of system 1, one has $v_{co} < V_r$, the circuit switches its topology and the orbit is attracted to the equilibrium point of system 2, because this is the system that is working. When the trajectory, attracted to the equilibrium point of system 2, moves near it, system 1 begins to work, attracting the trajectory to the equilibrium point of system 1 (see Fig. 3.8). This wandering between the two equilibrium points of the separate systems produces a highly non-trivial evolution, without any equilibrium point in the global system. In the range of values of the parameters suggested in [Deane and Hamill, 1990] and [Hamill, Deane and Jefferies, 1992], a typical trajectory of the control voltage is shown in Fig. 3.9. In the phase space (v, i) , the same trajectory is drawn in Fig. 3.10.

We will now try to show a schematic representation of the global vector field of the system. Let us write

$$v_l = V_{ref} + \frac{V_L}{a} \quad v_u = V_{ref} + \frac{V_U}{a} \quad v_r(t) = v_l + \frac{v_u - v_l}{T} \text{Frac}(t/T)$$

and assume

$$V_{in} > v_u > v_l > 0 \quad (3.10)$$

as in [Deane and Hamill, 1990; Hamill, Deane and Jefferies, 1992] (this is the

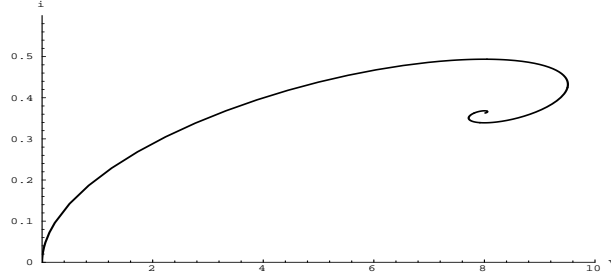


Figure 3.7: Orbit of the system 2 around its equilibrium point in the state space.

case that gives rise to non-trivial behaviours in the system). We may divide the state space into three regions:

- i) region 1: $S_1 = \{(v, i) : v < v_l\}$ (half-plane)
- ii) region 2: $S_2 = \{(v, i) : v_l < v < v_u\}$ (strip)
- iii) region 3: $S_3 = \{(v, i) : v > v_u\}$ (half-plane)

In all the points of S_1 , due to the fact that $v < v_l$, we have

$$v_{co} = a(v - V_{ref}) < a(v_l - V_{ref}) = V_L$$

and the phase diagram corresponding to this region is that of Fig. 3.7, because the dynamics is given by system 2.

On the points of S_3 , as $v > v_u$, we have

$$v_{co} = a(v - V_{ref}) > a(v_u - V_{ref}) = V_U$$

and the corresponding phase diagram is shown in Fig. 3.6, because it is system 1 that is now working.

For the points in the strip S_2 the behaviour is not so clear because, depending on the state of the global system when the ramp is crossed, it is system 1 or system 2 that is in command (see Fig. 3.11). Notice that, as shown in Fig. 3.9, multiple pulsing can occur, where the switches change the topology of the circuit

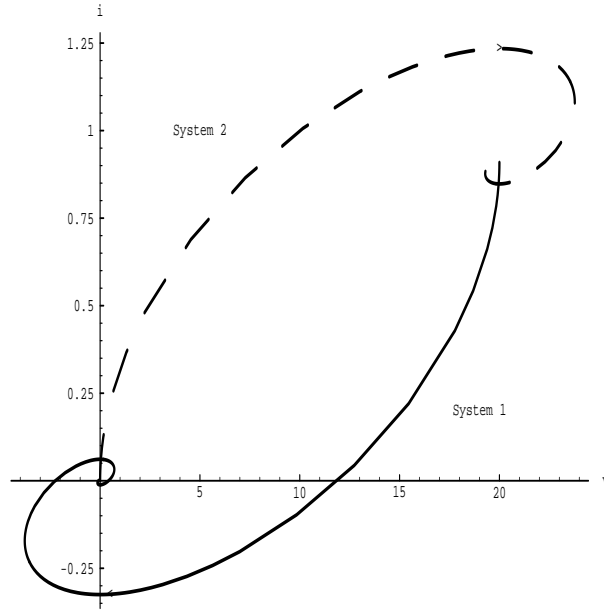


Figure 3.8: Orbit of systems 1 and 2 around its equilibrium point in the state space ($V_{in} = 20V$). The solid orbit corresponds to system 1 and the dashed one to system 2.

many times per ramp cycle. This is very undesirable in practice as it greatly increases the switching losses. One way to avoid it is to use a latch. With a latched PWM, multiple pulsing is eliminated but subharmonics and chaos is still possible [Deane and Hamill, 1991].

We have represented the solutions of the global system both in the phase plane (v, i) (see Fig. 3.10), and in the control plane $(t, v_{co}(t))$ together with the ramp (see Fig. 3.9). If we wish to see how the voltage and current are changing with time, we need a tridimensional representation $(t, v(t), i(t))$. When increasing $t \geq 0$, the curve described in the space gives the solution of the system starting at $v_0 = v(0)$ and $i_0 = i(0)$ as initial conditions. More visual information is obtained if we choose the control voltage v_{co} instead of v (remember the affine relation between v_{co} and v , $v_{co} = a(v - V_{ref})$), and we plot the ramp as well. In the tridimensional case, the ramp is represented by the planes (see Fig. 3.12)

$$ramp = \{(t, i, V_r(t)) : t \geq 0\}$$

As already mentioned, the system of differential equations we are studying is non-autonomous due to the presence of $u(t)$ in the expression of $f(x, t)$. The function u introduces T -periodicity in the dynamical system, plus the correspondent additional variable. This new dynamical system then enlarges its dimension by one and so chaotic behavior cannot now be discarded. As the system is now periodic, it is more convenient to consider it in the cylindrical space

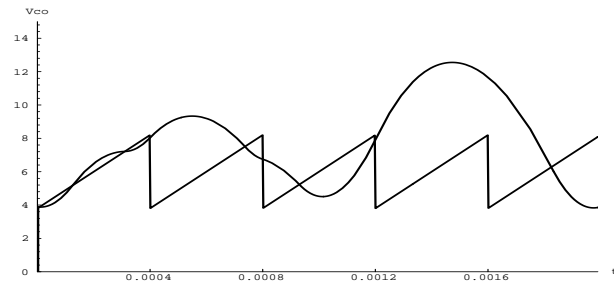


Figure 3.9: Typical trajectory of the control voltage.

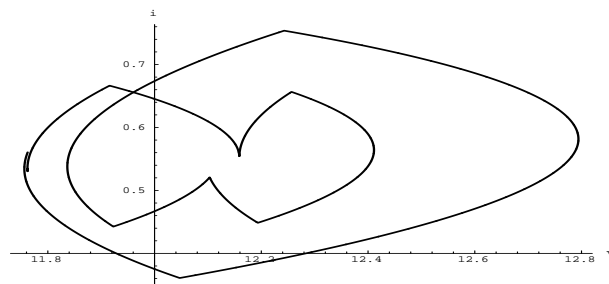


Figure 3.10: Typical trajectory in the phase space.

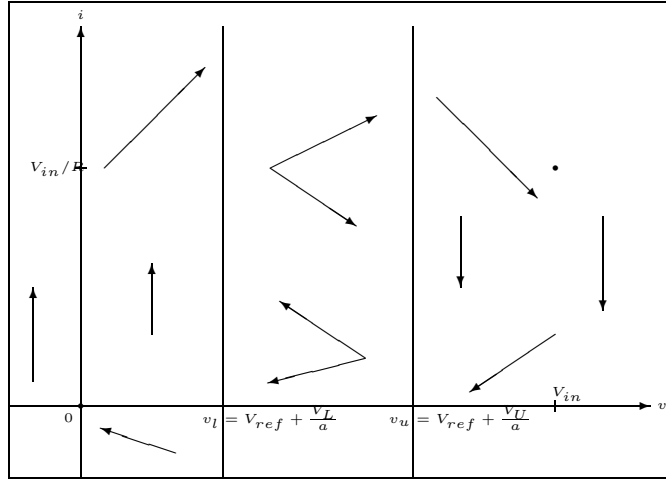


Figure 3.11: Schematic representation of the global vector field of the system.

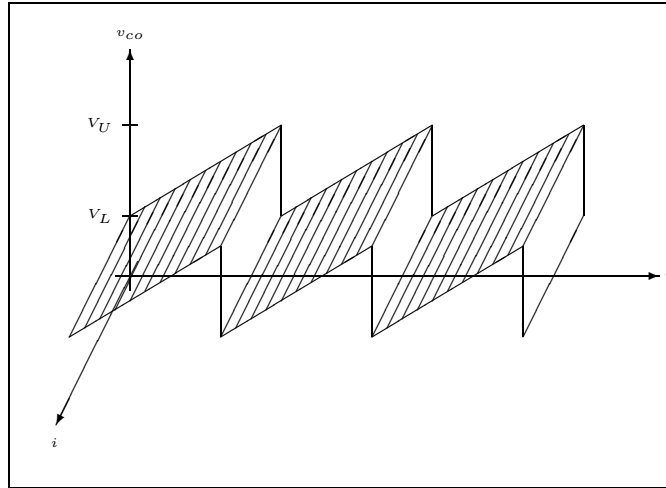


Figure 3.12: Sawtooth (or ramp) surface in the tridimensional space $(t, i, v_{co}) \in \mathbb{R}^3$.

$\mathbb{R}^2 \times \mathbb{S}^1$, identifying the points $(t = 0, v, i)$ and $(t = T, v, i)$, $\forall (v, i) \in \mathbb{R} \times \mathbb{R}$. This new space can be represented geometrically by a cylinder, as shown in Fig. 3.14. In this space, a trajectory of the circuit is a curve in the cylinder and the ramp surface is transformed in a helicoidal surface around the axis of the infinite cylinder due to the identification of $t = 0$ and $t = T$. There, the surface H together with the piece of *vertical* plane $\{t = 0, v_l < v < v_u\}$ is the boundary for the two connected regions which display the two different topologies. In

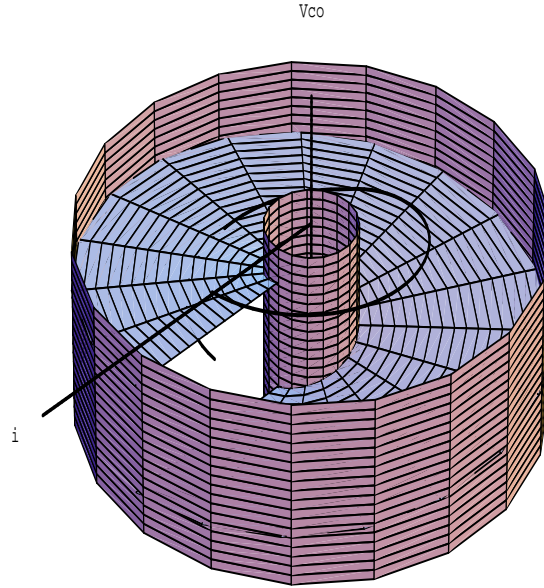


Figure 3.13: The space $\mathbb{R}^2 \times \mathbb{S}^1$ with the helicoidal surface determined by the ramp.

Fig. 3.13, a trajectory in this cylindrical space has been simulated (notice that the angular coordinate around the axe of the cylinders always increases). It is also worth noting the effect that the T -periodicity of the function u introduces in the phase space of the variables (v, i) . Now, instead of a curve separating the two topologies, there is a moving (t -dependent) curve which moves between $v = v_l$ and $v = v_u$ monotonically in each cycle of the ramp (see Fig. 3.15). This moving line is responsible for the observed chaotic behavior in this dynamical system.

The advantage of using this cylindrical space to represent the solutions of the system is that we can observe the evolution of the state of the system, $x(t)$, as a function of time $t \in [0, T]$, and easily visualize the possible periodic orbits. With this representation, periodic orbits are indeed closed curves while with the euclidian tridimensional representation, we also observe the temporal dependence of the state variables (v, i) , but periodic orbits are no longer closed. Finally, the phase space representation shows periodic orbits as closed curves, but the temporal dependence cannot be distinguished.

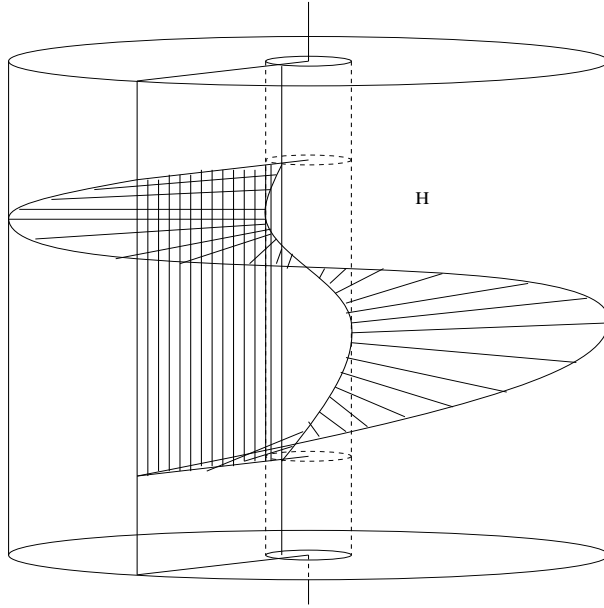


Figure 3.14: Cylindrical natural space $\mathbb{R}^2 \times \mathbb{S}^1$. Surface H represents the helicoidal sawtooth in this space. $H \cup \{t = 0, v_l < v < v_u\}$ is the boundary between the two topologies of the system.

3.3 Periodic Orbits

In the last section, some basic algebra showed that the equilibrium points X_1 and X_2 for each of the linear systems are stable focus if separated topologies are considered. When the two topologies are considered together, the equilibrium points disappear, and the trajectories evolve very near the band $[v_l, v_u] \times \mathbb{R}$, despite the far X_1 and X_2 .

In this section, we will look for periodic orbits of our global system. Having fixed the parameters, $L = 20mH$, $C = 47\mu F$, $R = 22\Omega$, $a = 8.4$, $V_{ref} = 11.3V$, $V_L = 3.8V$, $V_U = 8.2V$ and $T = 400\mu s$, as in [Deane and Hamill, 1990; Hamill, Deane and Jefferies, 1992], we will study for which values of the input voltage V_{in} we may have periodic orbits, and whether they are stable or not.

Definition:

For $n \geq 1$, we will say that \mathcal{O} is a nT -periodic orbit iff n is the smallest positive integer for which

$$\begin{cases} v(nT) &= v(0) \\ i(nT) &= i(0) \end{cases}$$

that is, an orbit of the phase space (v, i) which closes itself after n cycles of the

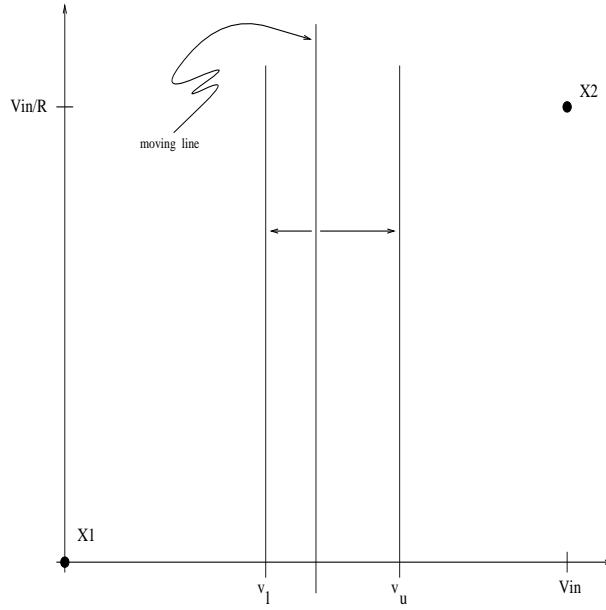


Figure 3.15: The moving line is the boundary of the two linear topologies, which have X_1 and X_2 as equilibrium points when separated topologies are considered.

ramp. Because of $v_{co} = a(v - V_{ref})$, the above conditions are equivalent to

$$\begin{cases} v_{co}(nT) &= v_{co}(0) \\ i(nT) &= i(0) \end{cases}$$

Observation:

In fact, the description (3.6,3.7) of the dynamical system is not complete, due to the fact that trajectories cross the ramp surface. At one of these switching instants t_s , we have

$$v(t_s) = v_r(t_s) \quad (3.11)$$

and consequently the vector field is not defined at this point. To overcome this difficulty, and to be consequent with the analysis of Hamill and the physical device modelling, we must add the following conditions:

Assume that $v(t_s) = v_r(t_s)$ and $t_s \neq mT$, $m \in \mathbb{Z}$, and $h > 0$ exists such that for all $t \in (t_s - h, t_s)$, it is satisfied that $v(t) < v_r(t)$. Then, we define $u(t_s, v(t_s)) = 1$. However, if $v(t) > v_r(t)$ is satisfied, then $u(t_s, v(t_s)) = 0$.

Assume now that $v(mT) = v_r(mT)$ for any $m \in \mathbb{Z}$. If

$$\lim_{t \rightarrow mT^-} v'(t) < \frac{v_u - v_l}{T} (= \lim_{t \rightarrow mT^+} v_r'(t))$$

then we define $u(mT, v(mT)) = 1$. On the other hand, if

$$\lim_{t \rightarrow mT^-} v'(t) > \frac{v_u - v_l}{T} (= \lim_{t \rightarrow mT^+} v_r'(t))$$

then $u(mT, v(mT)) = 0$.

For other cases with tangencies within the cycle of the ramp ($v(t_s) = v_r(t_s)$ with $v'(t_s) = v_r'(t_s)$), which can occur for $V_{in} < v_u + \frac{L}{RT} \frac{V_U - V_L}{a} \approx 13.467V$, it is considered that the signal $v(t)$ does not cross the ramp and thus $u(t_s^+) = u(t_s^-)$. Finally, for a tangency at the beginning of a cycle $t = mT$, the function $u(mT, v(mT))$ will be defined later in order to obtain continuity in the associated Poincaré map. These additional conditions stated above were not specified in the papers by Hamill and coworkers, but they were implicitly applied when computing numerical solutions for the system.

The fidelity of these equations to the experimental model was shown in [Deane and Hamill, 1990]. In their paper, experimental data at the oscilloscope was shown to agree exceptionally well with the computer simulated data from the equations. So, at least in the range of parameter values considered, the physical device is modelled quite well by the equations.

Since the trajectories may cross the ramp several times in a cycle, we may define different problems for periodic orbits. Thus, if $m \geq 0$ and $n \geq 0$, we define

$$P(m, n) = \{nT\text{-periodic orbits switching exactly } m \text{ times per } nT\text{-period}\}. \quad (3.12)$$

It can be proved that, in the range of values of the parameters of [Deane and Hamill, 1990] and [Hamill, Deane and Jefferies, 1992], (essentially (3.10)), the problem of computing $P(0, n)$ is trivial:

$$P(0, n) = \emptyset \quad \forall n \geq 1$$

Indeed, if $v(nT) = v(0)$, $i(nT) = i(0)$, and the ramp cannot be crossed, one of the following alternatives must be true:

- i) $v(0) = v(nT) < v_l$
- ii) $v(0) = v(nT) > v_u$

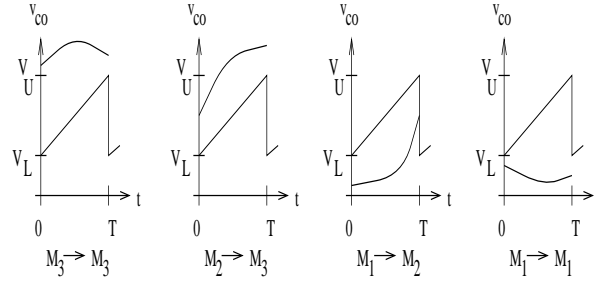
for if $v(0) \in [v_l, v_u]$, the ramp would necessarily be crossed.

In case *i*), system 2 gives the dynamics all the time, which have no periodic orbits other than its equilibrium point $(V_{in}, V_{in}/R)$ (see Fig. 3.7). But, as we are supposing (3.10), this equilibrium point cannot be considered in case *i*). Along the same lines, one can prove that in case *ii*), when the dynamics is given all the time by the system 1, that we also arrive at a contradiction with $v(0) = v(nT)$, $i(0) = i(nT)$, and so the statement is proved. Naturally, the more interesting cases $m \geq 1$ are more difficult to study. Let us consider the following partition of the range of the values of v_{co} :

$$M_1 = (-\infty, V_L) \quad M_2 = [V_L, V_U] \quad M_3 = (V_U, +\infty)$$

Once the values of the parameters are fixed, we observe that if we are looking for an orbit in $P(m, 1)$ verifying $v_{co}(0) \in M_2$, then m must be odd, while if

m even:



m odd:

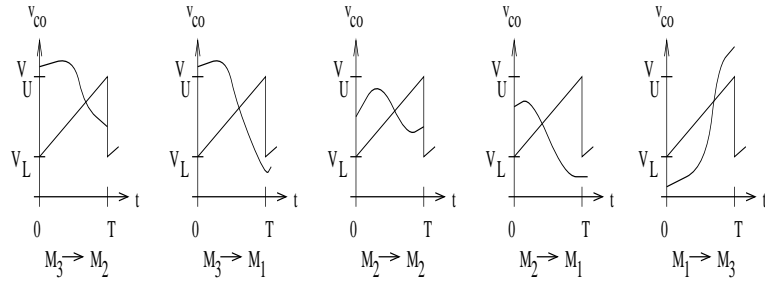


Figure 3.16: All the possible situations for m even or odd (exemplified by $m = 0$ and $m = 1$).

$v_{co}(0) \in M_2^c$, then m must be even. Fig. 3.16 shows all the possibilities, and justifies the above statement, which in a more compact form reads as follows

Proposition:

Let \mathcal{O} be a $1T$ -periodic orbit. Then

$$\exists m \geq 1 \quad \mathcal{O} \in P(2m, 1) \Leftrightarrow v_{co}(0) \in M_2^c$$

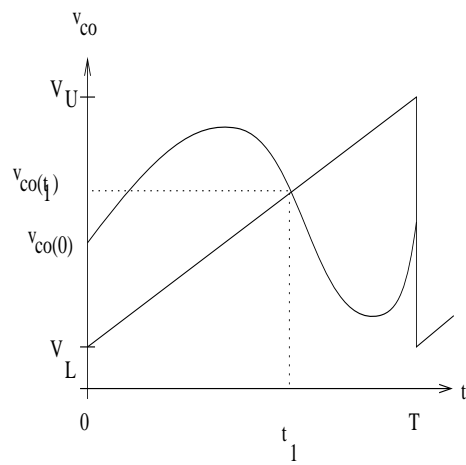
We will study $P(1, 1)$ in more detail. According to the previous note, an orbit \mathcal{O} in $P(1, 1)$ must start with $v_{co}(0) \in M_2$. Thus, it is system 1 that initially draws the orbit; at some time $t_1 < T$, v_{co} crosses the ramp and system 2 enters into action till $t = T$, when one must have

$$\begin{cases} v_{co}(T) &= v_{co}(0) \\ i(T) &= i(0) \end{cases}$$

This is graphically represented in Fig. 3.17.

In terms of $v(0)$, we have

$$v_{co}(0) \in [V_L, V_U] \Leftrightarrow v(0) \in [v_l, v_u]$$

Figure 3.17: Scheme of the case $P(1, 1)$.

The time $t_1 \in [0, T]$ must verify

$$\begin{pmatrix} v(t_1) \\ i(t_1) \end{pmatrix} = e^{-kt_1} [I \cos wt_1 + A \sin wt_1] \begin{pmatrix} v(0) \\ i(0) \end{pmatrix} \quad (3.13)$$

and

$$a(v(t_1) - V_{ref}) = V_L + \frac{V_U - V_L}{T} t_1$$

From t_1 to T , system 2 gives the dynamics and so we must have

$$\begin{aligned} \begin{pmatrix} v(0) \\ i(0) \end{pmatrix} &= \begin{pmatrix} v(T) \\ i(T) \end{pmatrix} = \begin{pmatrix} V_{in} \\ V_{in}/R \end{pmatrix} + \\ &+ e^{-k(T-t_1)} [I \cos w(T-t_1) + A \sin w(T-t_1)] \begin{pmatrix} v(t_1) - V_{in} \\ i(t_1) - V_{in}/R \end{pmatrix} \end{aligned}$$

Lemma:

The map

$$N : \mathbb{R} \rightarrow \mathcal{M}_{2 \times 2}(\mathbb{R})$$

defined by

$$N(\alpha) = e^{-kT\alpha} [I \cos wT\alpha + A \sin wT\alpha]$$

has the following properties:

- a) $N(0) = I$
- b) $N(\alpha + \beta) = N(\alpha)N(\beta)$
- c) $\det(N(\alpha)) = e^{-2kT\alpha}$

Proof:

a) is trivial;

b) With the help of trigonometric identities,

$$\begin{aligned} N(\alpha + \beta) &= e^{-kT(\alpha+\beta)} [I \cos wT(\alpha + \beta) + A \sin wT(\alpha + \beta)] = \\ &= e^{-kT\alpha} e^{-kT\beta} [I(\cos wT\alpha \cos wT\beta - \sin wT\alpha \sin wT\beta) + \\ &\quad + A(\cos wT\alpha \sin wT\beta + \sin wT\alpha \cos wT\beta)] \end{aligned}$$

On the other hand,

$$N(\alpha)N(\beta) = e^{-kT\alpha} [I \cos wT\alpha + A \sin wT\alpha] e^{-kT\beta} [I \cos wT\beta + A \sin wT\beta].$$

Multiplying these matrices, and using $A^2 = -I$, b) is proved.

c) Only $\det(I \cos wT\alpha + A \sin wT\alpha) = 1$ has to be proved. This is true since

$$I \cos wT\alpha + A \sin wT\alpha = \begin{pmatrix} \cos wT\alpha - \frac{k}{w} \sin wT\alpha & \frac{1}{Cw} \sin wT\alpha \\ -\frac{1}{Lw} \sin wT\alpha & \cos wT\alpha + \frac{k}{w} \sin wT\alpha \end{pmatrix}$$

and thus, the determinant is

$$\begin{aligned}
 (\cos wT\alpha - \frac{k}{w} \sin wT\alpha)(\cos wT\alpha + \frac{k}{w} \sin wT\alpha) + (\frac{1}{Cw} \sin wT\alpha)(\frac{1}{Lw} \sin wT\alpha) = \\
 = \cos^2 wT\alpha - (\frac{k}{w})^2 \sin^2 wT\alpha + \frac{1}{LCw^2} \sin^2 wT\alpha = \\
 = \cos^2 wT\alpha + (\frac{1}{LCw^2} - (\frac{k}{w})^2) \sin^2 wT\alpha
 \end{aligned}$$

Now, since

$$w^2 = \frac{1}{LC} - k^2,$$

the lemma is proven.

In terms of N , if we write $t_1 = \alpha_1 T$, $\alpha_1 \in (0, 1)$, (so α_1 is the duty cycle), the condition (3.13) we have imposed is equivalent to

$$f_1(V_{in}, \alpha_1) = 0$$

where

$$f_1(V_{in}, \alpha_1) \equiv V_{ref} + \frac{V_L}{a} + \frac{V_U - V_L}{a} \alpha_1 - (1, 0) \cdot N(\alpha_1) \begin{pmatrix} v_0(V_{in}, \alpha_1) \\ i_0(V_{in}, \alpha_1) \end{pmatrix}$$

with

$$\begin{pmatrix} v_0(V_{in}, \alpha_1) \\ i_0(V_{in}, \alpha_1) \end{pmatrix} = V_{in} [N(0) - N(1)]^{-1} [N(0) - N(1 - \alpha_1)] \begin{pmatrix} 1 \\ 1/R \end{pmatrix}$$

Let us observe first that $N(0) - N(1)$ has an inverse, for

$$N(0) - N(1) = I - e^{-kT} [I \cos wT + A \sin wT]$$

and,

$$\det(I - e^{-kT} [I \cos wT + A \sin wT]) = (e^{-kT} - e^{iwT})(e^{-kT} - e^{-iwT}) \neq 0$$

After substitution of $v_0(V_{in}, \alpha_1)$ and $i_0(V_{in}, \alpha_1)$ in $f_1(V_{in}, \alpha_1)$, we have to solve

$$f_1(V_{in}, \alpha_1) = 0$$

numerically for V_{in} and α_1 . Table 3.1 and Fig. 3.18 show the numerical values obtained for α_1 (duty cycle) and the initial conditions v_0, i_0 , when V_{in} varies in the range studied in [Deane and Hamill, 1990; Hamill, Deane and Jefferies, 1992].

Notice that the conditions we imposed to obtain periodic orbits are necessary, but they are not sufficient, for t_1 may not be the first time the control voltage crosses the ramp. Or if it is the first, it may not be the last. Thus, after computing numerically the values of v_0, i_0 , we must check that the obtained trajectory is really of the desired kind. The condition $v_0 \in [v_l, v_u]$ is guaranteed by a previous note.

Table 3.1: 1T-Periodic orbits of P(1,1).

V_{in}	α_1 (duty cycle)	v_0	i_0
12	0.0200	11.7628990	0.5368860
13	0.0932	11.8016963	0.5468476
14	0.1560	11.8354047	0.5555837
15	0.2104	11.8649043	0.5633096
16	0.2582	11.8908888	0.5701924
17	0.3005	11.9139243	0.5763639
18	0.3381	11.9344727	0.5819300
19	0.3719	11.9528954	0.5869757
20	0.4023	11.9695182	0.5915722
21	0.4250	11.9845501	0.5957756
22	0.4551	11.9982391	0.5996361
23	0.4781	12.0107287	0.6031931
24	0.4993	12.0221661	0.6064811
25	0.5187	12.0326767	0.6095296
26	0.5367	12.0423969	0.6123654
27	0.5534	12.0513809	0.6150086
28	0.5690	12.0597006	0.6174780
29	0.5835	12.0674514	0.6197913
30	0.5970	12.0746723	0.6219622
31	0.6097	12.0814180	0.6240036
32	0.6216	12.0877326	0.6259268
33	0.6328	12.0936731	0.6277426
34	0.6434	12.0992565	0.6294590
35	0.6533	12.1044963	0.6310831
36	0.6627	12.1094372	0.6326229
37	0.6717	12.1141164	0.6340855
38	0.6801	12.1185505	0.6354764
39	0.6881	12.1227560	0.6368005
40	0.6958	12.1268896	0.6380695
41	0.7031	12.1305014	0.6392647
42	0.7100	12.1340774	0.6404133
43	0.7166	12.1375290	0.6415138
44	0.7230	12.1407958	0.6425658
45	0.7290	12.1439058	0.6435733
46	0.7347	12.1468568	0.6445382
47	0.7403	12.1497160	0.6454661
48	0.7456	12.1524421	0.6463568
49	0.7507	12.1550773	0.6472141
50	0.7556	12.1575615	0.6480367

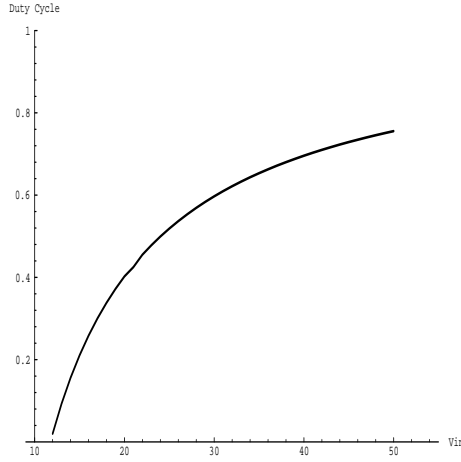


Figure 3.18: Evolution of the duty cycle for the 1T-periodic orbits.

As will be seen later, the $P(1, 1)$ periodic orbits which were obtained before bifurcate into 2T-periodic orbits with one switch in each of the two cycles. Therefore, it would be interesting to find these 2T-periodic orbits and related ones. So now a study is made for the 2T-periodic orbits that cross the ramp at most once per cycle, which is a subset \mathcal{B} of $P(2, 2)$. We have seven different situations, which are represented in Fig. 3.19.

However, we observe that, given an orbit $\mathcal{O} \in \mathcal{B}$, if we interchange the two cycles that form \mathcal{O} , we get another orbit $\mathcal{O}' \in \mathcal{B}$. Hence, if we interchange the two cycles of an orbit of type (3), (6) or (7), we get an orbit of type (1), (4) or (2) respectively. We may say that there exists a duality between the types (1) and (3), (2) and (7), and (4) and (6), while (5) is selfdual. We will restrict ourselves to the study of types (1), (2), (4) and (5), which have in common the fact that $v_{co}(0) \in M_1 \cup M_2$ and that the first time the orbits cross the ramp they do so during the first cycle.

We will study first the type (5) which, in a sense, is the most general. If we denote by $t_1 = \alpha_1 T$ the first time the control voltage crosses the ramp, we will have, with the notation previously introduced

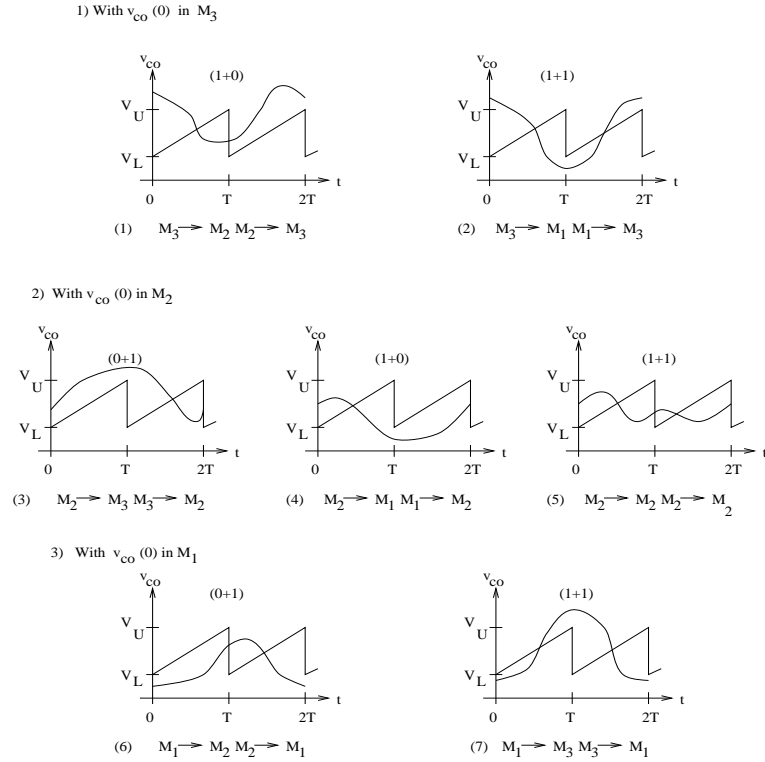
$$\begin{pmatrix} v(t_1) \\ i(t_1) \end{pmatrix} = N(\alpha_1) \begin{pmatrix} v_0 \\ i_0 \end{pmatrix}$$

and

$$a(v(t_1) - V_{ref}) = V_L + \frac{V_U - V_L}{T} t_1$$

After t_1 , system 2 acts until the end of the cycle and we will have

$$\begin{pmatrix} v(T) \\ i(T) \end{pmatrix} = N(1 - \alpha_1) \begin{pmatrix} v(t_1) - V_{in} \\ i(t_1) - V_{in}/R \end{pmatrix} + \begin{pmatrix} V_{in} \\ V_{in}/R \end{pmatrix}$$

Figure 3.19: Schemes of the case \mathcal{B} .

During the second cycle, the ramp is crossed at $t = t_2 = \alpha_2 T$, and we will have

$$\begin{pmatrix} v(t_2) \\ i(t_2) \end{pmatrix} = N(\alpha_2) \begin{pmatrix} v(T) \\ i(T) \end{pmatrix}$$

and

$$a(v(t_2) - V_{ref}) = V_L + \frac{V_U - V_L}{T} t_2$$

During the second part of the second cycle the dynamics is given again by system 2 and

$$\begin{pmatrix} v(2T) \\ i(2T) \end{pmatrix} = N(1 - \alpha_2) \begin{pmatrix} v(t_2) - V_{in} \\ i(t_2) - V_{in}/R \end{pmatrix} + \begin{pmatrix} V_{in} \\ V_{in}/R \end{pmatrix}$$

Finally, to get a $2T$ -periodic orbit, we must impose

$$\begin{pmatrix} v(2T) \\ i(2T) \end{pmatrix} = \begin{pmatrix} v_0 \\ i_0 \end{pmatrix}$$

In a similar way as in the case of $P(1, 1)$, we obtain

$$\begin{pmatrix} v_0 \\ i_0 \end{pmatrix} = V_{in} [N(0) - N(2)]^{-1} [N(0) - N(1 - \alpha_2) + N(1) - N(2 - \alpha_1)] \begin{pmatrix} 1 \\ 1/R \end{pmatrix}$$

with the additional conditions

$$\begin{cases} a(v(t_1) - V_{ref}) = V_L + \frac{V_U - V_L}{T} t_1 \\ a(v(t_2) - V_{ref}) = V_L + \frac{V_U - V_L}{T} t_2 \end{cases}$$

If we substitute the values of $v(t_1)$ and $v(t_2)$ in terms of v_0 and i_0 , the previous conditions are equivalent to

$$\begin{cases} f_1(V_{in}, \alpha_1, \alpha_2) = 0 \\ f_2(V_{in}, \alpha_1, \alpha_2) = 0 \end{cases}$$

where

$$f_1(V_{in}, \alpha_1, \alpha_2) = V_{ref} + \frac{V_L}{a} + \frac{V_U - V_L}{a} \alpha_1 - (1, 0) \cdot N(\alpha_1) \begin{pmatrix} v_0(V_{in}, \alpha_1, \alpha_2) \\ i_0(V_{in}, \alpha_1, \alpha_2) \end{pmatrix}$$

and

$$f_2(V_{in}, \alpha_1, \alpha_2) = V_{ref} + \frac{V_L}{a} + \frac{V_U - V_L}{a} \alpha_2 - (1, 0) \cdot [N(1 + \alpha_2) \begin{pmatrix} v_0(V_{in}, \alpha_1, \alpha_2) \\ i_0(V_{in}, \alpha_1, \alpha_2) \end{pmatrix} + V_{in}(N(\alpha_2) - N(1 - \alpha_1 + \alpha_2)) \begin{pmatrix} 1 \\ 1/R \end{pmatrix}]$$

Before going on, let us notice that in cases (1), (2) and (4) we obtain similar expressions. For instance, in case (1), the expression for (v_0, i_0) is the same as in case (5) with $\alpha_2 = 1$ (see Fig. 3.19). Now, the condition $f_2(V_{in}, \alpha_1, \alpha_2) = 0$ must not be imposed and we obtain

$$\begin{pmatrix} v_0 \\ i_0 \end{pmatrix} = V_{in}[N(0) - N(2)]^{-1}[N(1) - N(2 - \alpha_1)] \begin{pmatrix} 1 \\ 1/R \end{pmatrix}$$

with

$$f_1(V_{in}, \alpha_1) = 0$$

Case (4) can also be studied in a similar way, but from Fig. 3.19 we see that it is the same as case (5) with $\alpha_2 = 0$. Since there is no second crossing with the ramp we do not have to impose $f_2(V_{in}, \alpha_1, \alpha_2) = 0$, and we obtain

$$\begin{pmatrix} v_0 \\ i_0 \end{pmatrix} = V_{in}[N(0) - N(2)]^{-1}[N(0) - N(2 - \alpha_1)] \begin{pmatrix} 1 \\ 1/R \end{pmatrix}$$

with

$$f_1(V_{in}, \alpha_1) = 0$$

Case (2) is different from the previous ones because the second cycle starts with system 2 and ends with system 1. Similarly to what we did in case (5), we get

$$\begin{pmatrix} v_0 \\ i_0 \end{pmatrix} = V_{in}[N(0) - N(2)]^{-1}[N(1 - \alpha_2) - N(2 - \alpha_1)] \begin{pmatrix} 1 \\ 1/R \end{pmatrix}$$

with the additional conditions

$$\begin{cases} a(v(t_1) - V_{ref}) = V_L + \frac{V_U - V_L}{T} t_1 \\ a(v(t_2) - V_{ref}) = V_L + \frac{V_U - V_L}{T} t_2 \end{cases}$$

Table 3.2: 2T-Periodic orbits of P(2,1)

V_{in}	α_1	α_2	v_0	i_0
24.516	0.5100	0.5091	12.02770291	0.608082543
25	0.4454	0.5920	12.02908570	0.589501296
26	0.4089	0.6644	12.04264887	0.574309887
27	0.3891	0.7175	12.05963717	0.562583104
28	0.3757	0.7620	12.07860282	0.551941125
29	0.3658	0.8009	12.09901661	0.541756863
30	0.3582	0.8357	12.12059136	0.531772010
31	0.3521	0.8674	12.14314265	0.521859291
32	0.3471	0.8963	12.16653982	0.511949901
33	0.3430	0.9231	12.19068428	0.502004804
34	0.3395	0.9479	12.21549835	0.492001437
35	0.3366	0.9710	12.24091859	0.481926928
36	0.3340	0.9927	12.26689209	0.471774304

and $v_{co}(0) \in M_3$. In all the cases, three comments should be made before starting the numerical computations. First, when computing the duty cycles for a given value V_{in} , if a pair (α_1, α_2) is obtained, then (α_2, α_1) must also be a solution (interchanging the two cycles of the orbit), provided that (v_0, i_0) and $(v(T), i(T))$ are also interchanged. Second, solutions of the form $\alpha_1 = \alpha_2$ must exist which correspond to orbits $\mathcal{O} \in P(1, 1)$. Third, we recall that the conditions imposed are necessary and not sufficient, for the same reason as in case $P(1, 1)$. So, once (v_0, i_0) have been obtained, we must draw the full orbit over the two cycles to see that the number of crossings in the ramp is correct. Numerical computations in case (5) are shown in Table 3.2 and Fig. 3.20.

From V_{in} near 24.516V onwards we start getting duty cycles $(\alpha_1, \alpha_2) \in [0, 1] \times [0, 1]$, till we arrive near to $V_{in} = 36V$, when $\alpha_2 = 1$ and $\alpha_1 = 0.3340$. The initial conditions (v_0, i_0) are also tabulated. Fig. 3.21 shows the 2T-periodic orbit corresponding to $V_{in} = 25V$ in the phase space (v, i) and Fig. 3.22 shows the same orbit in time, with the control voltage $v_{co}(t)$ and the ramp.

Numerical computations are not as easy as in the case of $P(1, 1)$.

For fixed V_{in} , we should find $(\alpha_1, \alpha_2) \in [0, 1] \times [0, 1]$ such that

$$\begin{cases} f_1(V_{in}, \alpha_1, \alpha_2) = 0 \\ f_2(V_{in}, \alpha_1, \alpha_2) = 0 \end{cases}$$

Graphically, one can represent the surfaces (with V_{in} fixed)

$$\begin{aligned} z &= f_1(V_{in}, \alpha_1, \alpha_2) \\ z &= f_2(V_{in}, \alpha_1, \alpha_2) \end{aligned}$$

together with the plane $z = 0$ for $(\alpha_1, \alpha_2) \in [0, 1] \times [0, 1]$. It turns out that f_1 and f_2 are too close to see how many times they intersect. It is better to

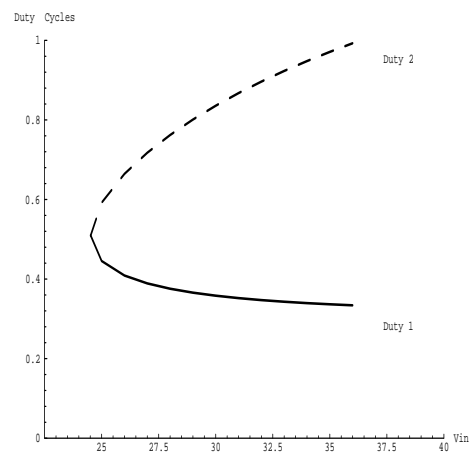


Figure 3.20: Evolution of the duty cycles for the 2T-periodic orbits.

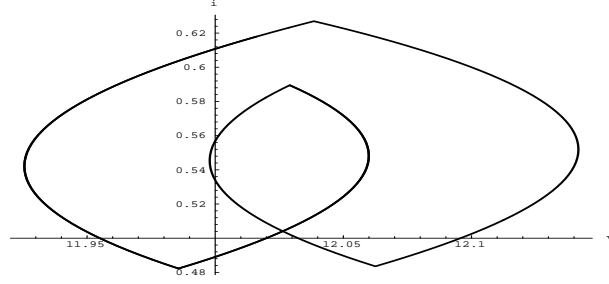


Figure 3.21: 2T-periodic orbit in the phase space (v, i) corresponding to $V_{in} = 25V$.

represent instead

$$\begin{aligned} z &= f_1(V_{in}, \alpha_1, \alpha_2) - f_2(V_{in}, \alpha_1, \alpha_2) \\ z &= f_1(V_{in}, \alpha_1, \alpha_2) \end{aligned}$$

and $z = 0$, which have the same intersection set as the previous equations. For values above $V_{in} = 24.516V$ one observes three points of intersection. One of them is of the form (α, α) , corresponding to an orbit of $P(1, 1)$ and the other two are of the form (α_1, α_2) and (α_2, α_1) , as we anticipated.

In the general case of nT -periodic orbits, a general expression can be deduced when exactly one crossing per cycle occurs and $v_{co}(0) \in M_2$. In this case we get

$$\begin{pmatrix} v_0(V_{in}, \alpha_1, \dots, \alpha_n) \\ i_0(V_{in}, \alpha_1, \dots, \alpha_n) \end{pmatrix} = V_{in}[N(0) - N(n)]^{-1} \left[\sum_{j=0}^{n-1} (N(j) - N(j+1 - \alpha_{n-j})) \right] \begin{pmatrix} 1 \\ 1/R \end{pmatrix}$$

with the additional conditions

$$\begin{cases} f_1(V_{in}, \alpha_1, \dots, \alpha_n) &= 0 \\ \vdots \\ f_n(V_{in}, \alpha_1, \dots, \alpha_n) &= 0 \end{cases}$$

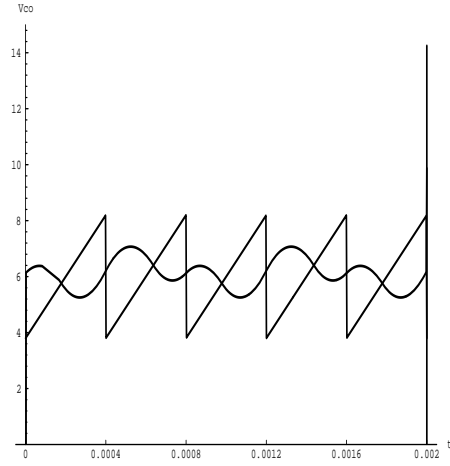


Figure 3.22: $v_{co}(t)$ for the 2T-periodic orbit corresponding to $V_{in} = 25V$.

where

$$f_j(V_{in}, \alpha_1, \dots, \alpha_n) = V_{ref} + \frac{V_L}{a} + \frac{V_U - V_L}{a} \alpha_j - (1, 0) \cdot N(\alpha_j) \begin{pmatrix} v_{j-1} \\ i_{j-1} \end{pmatrix}$$

with

$$\begin{pmatrix} v_j \\ i_j \end{pmatrix} = N(1) \begin{pmatrix} v_{j-1} \\ i_{j-1} \end{pmatrix} + V_{in}[N(0) - N(1 - \alpha_j)] \begin{pmatrix} 1 \\ 1/R \end{pmatrix}$$

Thus, the problem of finding the periodic orbits, in this case, is reduced to numerically solving the equations

$$\begin{cases} f_1(V_{in}, \alpha_1, \dots, \alpha_n) = 0 \\ \vdots \\ f_n(V_{in}, \alpha_1, \dots, \alpha_n) = 0 \end{cases}$$

in the region $(\alpha_1, \dots, \alpha_n) \in [0, 1]^n$ and then check that $v_{co}(0) \in M_2$.

To conclude this section we propose to study the stability of previously computed 1T-periodic and 2T-periodic orbits.

Given a periodic orbit, we will say that it is asymptotically stable if, given initial conditions (v_0, i_0) sufficiently close to the periodic orbit, then the trajectory in the phase space from (v_0, i_0) asymptotically approaches that of the periodic orbit. The test to decide whether a periodic orbit is stable or not is that of the characteristic multipliers. It is known [Parker and Chua, 1989; Chua, 1987] that if the norms of all the characteristic multipliers of a periodic orbit are less than 1, then the orbit is stable, while if one characteristic multiplier with norm greater than 1 suffices to render the periodic orbit unstable.

The characteristic multipliers are computed as follows: we construct the Poincaré maps, which are given by

$$\begin{aligned} P^1 : \mathbb{R}^2 &\longrightarrow \mathbb{R}^2 \\ (v_0, i_0) &\longrightarrow P^1(v_0, i_0) = (P_1^1(v_0, i_0), P_2^1(v_0, i_0)) = (v(T), i(T)) \end{aligned}$$

for a 1T-periodic orbit and

$$\begin{aligned} P^2 : \mathbb{R}^2 &\longrightarrow \mathbb{R}^2 \\ (v_0, i_0) &\longrightarrow P^2(v_0, i_0) = (P_1^2(v_0, i_0), P_2^2(v_0, i_0)) = (v(2T), i(2T)) \end{aligned}$$

for a 2T-periodic orbit.

These maps give us the state of the system after 1 or 2 cycles respectively, starting from the initial conditions (v_0, i_0) . The characteristic multipliers are then the eigenvalues of $DP^k(\bar{v}_0, \bar{i}_0)$, $k = 1, 2$, where (\bar{v}_0, \bar{i}_0) are the initial conditions corresponding to a given periodic orbit ([Parker and Chua, 1989; Chua, 1987]). We have computed numerically $DP^k(v_0, i_0)$ using an approximation with central differences and Richardson extrapolation [Dahlquist and Björck, 1974] and the results are shown in Tables 3.3 and 3.4 and Fig. 3.23.

Namely, to find the eigenvalues of $DP^k(\bar{v}_0, \bar{i}_0)$, $k = 1, 2$, we first compute approximations for $\frac{\partial P_i^k(\bar{v}_0, \bar{i}_0)}{\partial v}$ and $\frac{\partial P_i^k(\bar{v}_0, \bar{i}_0)}{\partial i}$ for $i = 1, 2$. These approximations are central differences

$$\begin{aligned} \frac{\partial P_i^k(\bar{v}_0, \bar{i}_0)}{\partial v} &\approx \frac{P_i^k(v_0 + h, i_0) - P_i^k(v_0 - h, i_0)}{2h} \\ \frac{\partial P_i^k(\bar{v}_0, \bar{i}_0)}{\partial i} &\approx \frac{P_i^k(v_0, i_0 + h) - P_i^k(v_0, i_0 - h)}{2h} \end{aligned}$$

with order h^2 . Once these approximations are computed for h , $h/2$, $h/4$ and $h/8$, a Richardson extrapolation numerical scheme is applied to obtain an approximation of order h^8 . In practice, h was taken to be 0.01, yielding quite good approximations for all the partial derivatives. With the derivatives, $DP^k(\bar{v}_0, \bar{i}_0)$ is obtained, and the computations for the multipliers are straightforward.

In Fig. 3.23(a) we draw in the complex plane the evolution of the characteristic multipliers of the 1T-periodic orbits when V_{in} sweeps the range from 12V to 25V. We observe first that the characteristic multipliers are complex conjugates that move on a circle of radius $r \approx 0.82$, and so the orbit is asymptotically stable. Near $V_{in} = 24V$, both characteristic multipliers become real, and when V_{in} reaches a certain value between $V_{in} = 24V$ and $V_{in} = 25V$ one of the characteristic multipliers has norm greater than 1, and so the periodic orbit becomes unstable. After $V_{in} = 25V$, it remains unstable.

Fig. 3.23(b) shows the same kind of diagram in the case of 2T-periodic orbits. Near $V_{in} = 25V$ both multipliers enter the circle of radius $r = 1$, yielding stable orbits. Next, they move on the circle of radius $r = 0.679$ till $V_{in} = 31V$ is reached. After $V_{in} = 31V$, one of the multipliers goes out of the unit circle and the stability is lost and not recovered.

Table 3.3: Characteristic Multipliers of the 1T-Periodic Orbits

V_{in}	α (duty cycle)	v_0	i_0	m_i (multipliers)	$\max m_i $
12	0.0200	11.7628990	0.5368860	-0.7401±0.3625 i	0.824
13	0.0932	11.8016963	0.5468476	-0.6633±0.4891 i	0.824
14	0.1560	11.8354047	0.5555837	-0.6278±0.5341 i	0.824
15	0.2104	11.8649043	0.5633096	-0.6134±0.5504 i	0.824
16	0.2582	11.8908888	0.5701924	-0.6145±0.5489 i	0.824
17	0.3005	11.9139243	0.5763639	-0.6239±0.5377 i	0.824
18	0.3381	11.9344727	0.5819300	-0.6422±0.5162 i	0.824
19	0.3719	11.9528954	0.5869757	-0.6651±0.4861 i	0.824
20	0.4023	11.9695182	0.5915722	-0.6915±0.4480 i	0.824
21	0.4250	11.9845501	0.5957756	-0.7218±0.3984 i	0.824
22	0.4551	11.9982391	0.5996361	-0.7533±0.3343 i	0.824
23	0.4781	12.0107287	0.6031931	-0.7860±0.2472 i	0.824
24	0.4993	12.0221661	0.6064811	-0.8205±0.0703 i	0.824
25	0.5187	12.0326767	0.6095296	-0.6201,-1.0931	1.093
30	0.5970	12.0746723	0.6219622	-0.4002,-1.7014	1.701
35	0.6533	12.1044963	0.6310831	-0.3090,-2.2035	2.203
40	0.6958	12.1268896	0.6380695	-0.2532,-2.6804	2.680
45	0.7290	12.1439058	0.6435733	-0.2144,-3.1513	3.151
50	0.7556	12.1575615	0.6480367	-0.1874,-3.6153	3.615

Table 3.4: Characteristic Multipliers of the 2T-Periodic Orbits

V_{in}	α_1	α_2	v_0	i_0	m_i (multipliers)	$\max m_i $
24.516	0.5100	0.5091	12.02770291	0.6080825432	0.4613,1.0002	1.0002
25	0.4454	0.5920	12.02908570	0.5895012958	0.6139±0.2906 i	0.6792
26	0.4089	0.6644	12.04264887	0.5743098865	0.3766±0.5652 i	0.6792
27	0.3891	0.7175	12.05963717	0.5625831038	0.1460±0.6632 i	0.6792
28	0.3757	0.7620	12.07860282	0.5519411251	-0.0780±0.6747 i	0.6792
29	0.3658	0.8009	12.09901661	0.5417568634	-0.2945±0.6120 i	0.6792
30	0.3582	0.8357	12.12059136	0.5317720101	-0.5041±0.4552 i	0.6792
31	0.3521	0.8674	12.14314265	0.5218592911	-0.5104,-0.9039	0.9039
32	0.3471	0.8963	12.16653982	0.5119499008	-0.3073,-1.5010	1.5010
33	0.3430	0.9231	12.19068428	0.5020048037	-0.2359,-1.9557	1.9557
34	0.3395	0.9479	12.21549835	0.4920014373	-0.1946,-2.3705	2.3705
35	0.3366	0.9710	12.24091859	0.4819269277	-0.1669,-2.7633	2.7633
36	0.3340	0.9927	12.26689209	0.4717743041	-0.1521,-3.0337	3.0337

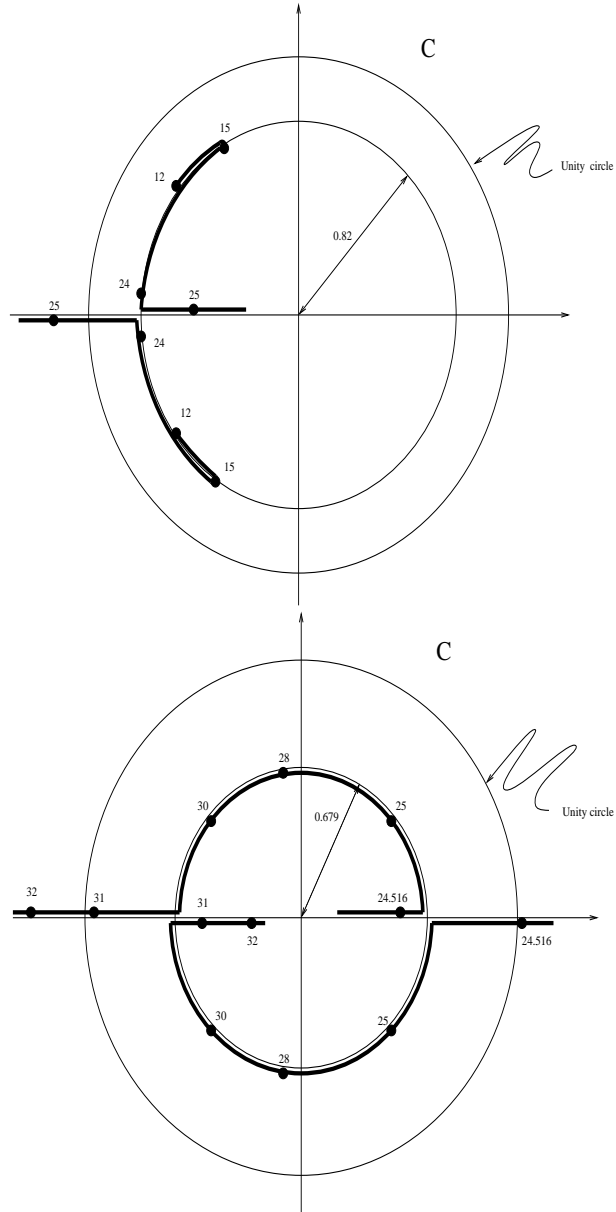


Figure 3.23: In the picture at the top the evolution of the characteristic multipliers for the 1T-periodic orbits as a function of V_{in} is shown; at the bottom, the evolution of the characteristic multipliers for the 2T-periodic orbits is shown (the numbers are the values of V_{in}).

Chapter 4

Study of the Stroboscopic Map

Abstract

This chapter is mainly geometric-oriented. Subharmonics, bifurcations, and the presence of a strange attractor are first observed with numerical simulations. A plot of the number of crossings in the ramp is drawn. This becomes a helpful tool to investigate the evolution of the trajectories when they are close to the attractor. Then the existence of the attractor is analytically justified by means of the special properties of the Poincaré map. In addition, the existence of a horseshoe mechanism embedded in the Poincaré map is analyzed. When analytic computations are not possible, numerical algorithms are used to simulate the orbits.

4.1 The Bifurcation Diagram for the Main Attractor

From the equations (3.6), it can be observed that the vector field of the system being studied belongs to the class of discontinuous and piecewise linear vector fields. Then we wish to deduce which class the associated stroboscopic map belongs to. In accordance, we define globally, a Poincaré map (a stroboscopic map), sampling the flow at $t = T$. Namely, we consider

$$\begin{aligned} P : \mathbb{R}^2 &\longmapsto \mathbb{R}^2 \\ X_0 &\longmapsto P(X_0) = \phi_T(X_0) \end{aligned} \tag{4.1}$$

where ϕ_t is the flow generated by the solutions of the system.

To deduce some of the properties of P , it is interesting to look at the solutions which in this case are available in a piecewise expression. As has been mentioned,

in each of the two topologies the system of differential equations is linear and thus can be solved analytically. With the notation introduced in the previous chapter, the solutions can be written in compact form as

$$X(\alpha) = V_{in}[I - N(\alpha - \alpha_0)]bu + N(\alpha - \alpha_0)X(\alpha_0) \quad (4.2)$$

As the vector field is piecewise linear, the solutions of the system, which are obtained by joining pieces of solutions in each topology, are continuous but only piecewise differentiable, being non-smooth (i.e. non-differentiable) at the switching instants. This means that the flow $\phi_t(x)$ is continuous but only piecewise smooth. This property is then inherited by the Poincaré map P . Thus, P belongs to the class of continuous but only piecewise smooth maps. In fact, P was defined everywhere except at $x_l = (v_l, i_l)$, the point in the phase space such that the trajectory $\phi(t) = (v(t), i(t))$ with initial conditions at x_l satisfies

$$v(0) = v_r(0) \quad \text{and} \quad v'(0) = v'_r(0)$$

At this point, the vector field itself was not defined. Since P is a homeomorphism which maps the punctured space $\mathbb{R}^2 - \{x_l\}$ to $\mathbb{R}^2 - \{x_u\}$, to get continuity of P over all \mathbb{R}^2 , it must be defined as

$$P(x_l) = x_u \quad (4.3)$$

with $x_u = (v_u, i_u)$, the point in the phase space such that the trajectory $\phi(t) = (v(t), i(t))$ with initial conditions at x_u satisfies

$$v(0) = v_r(T) \quad \text{and} \quad v'(0) = v'_r(T).$$

Taking this definition for P is equivalent to imposing the condition that the trajectory starting at x_l must verify

$$(v(t), v'(t)) = (v_r(t), v'_r(t)) \quad \text{for all } t \in [0, T] \quad (4.4)$$

and so it sticks to the ramp for one cycle (in this case, the trajectory is also contained in the surface H defined in Chapter 3).

One of the fundamental means by which a dynamical system can be studied is the bifurcation diagram. With this aim, taking V_{in} as the bifurcation parameter [Deane and Hamill, 1990a; Hamill, Deane and Jefferies, 1992] a bifurcation diagram for P is plotted in the region of interest. Having fixed an initial condition (v_0, i_0) , successive 5000 iterates of P are taken, and to avoid the transient dynamics only the last 100 first components of P (the voltages) are plotted. This process is repeated for every discrete value of the bifurcation parameter in the interval $[12, 40]V$. As was computed in the last chapter, a stable 1T-periodic orbit is initially found and continued until some value near 24.5V. Then, a first period-doubling bifurcation occurs, and the stability of the 1T-periodic orbit is lost in favour of the 2T-periodic orbit which appears at this value. This 2T-periodic orbit also loses stability in a period-doubling bifurcation near 31.5V. The unstable orbits cannot appear in a bifurcation diagram, and this is why those computed in the previous chapter cannot be seen

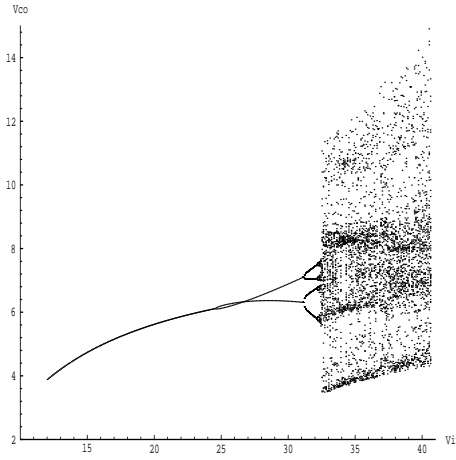


Figure 4.1: Bifurcation diagram of v_{co} taking V_{in} as a bifurcation parameter.

in the diagram. Near the last period-doubling bifurcation, suddenly and at approximately $32.5V$, there is a large chaotic behaviour, as can be seen in Fig. 4.1.

When the interval $[32.0, 32.5]V$ is enlarged, further period-doubling bifurcations are observed which accumulate near $32.3V$, where a four-piece chaotic behaviour is observed. At $32.34V$, the sudden expansion is localized, and is caused by a crisis, as it will be shown later.

Then, for higher values of V_{in} it follows a cascade of period-doublings, till an apparently chaotic zone is reached. This zone is shown in detail in Fig. 4.2.

Let us consider the Poincaré map (4.1) for one cycle again, and iterate P 4000 times from an initial condition (v_0, i_0) .

When after a cascade of period-doublings one reaches the chaotic zone, for instance $V_{in} = 35V$, we obtain a picture like that in Fig. 4.3.

Both in [Deane and Hamill, 1990a; Hamill, Deane and Jefferies, 1992] this possibly strange attractor was experimentally obtained, and in [Hamill, Deane and Jefferies, 1992] it was also numerically computed, obtaining only part of the experimental simulation. This was due to the experimental process, in which the signal was sampled two times per cycle, at the middle and at the end.

Dimension measures have been computed to obtain more knowledge of the structure of this attractor. Concretely, for $V_{in} = 35V$, Lyapounov, capacity, information and correlation dimensions are computed by following the definitions almost directly. Computing with the direct definitions is quite efficient in this case because the map is only two-dimensional.

Definitions:

Let A be a set in \mathbb{R}^n , covered by $N(\epsilon)$ elemental volumes of diameter ϵ . Let P_i

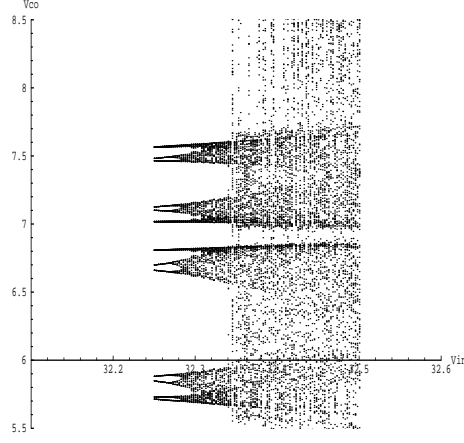


Figure 4.2: Bifurcation diagram of v_{co} taking V_{in} as a bifurcation parameter. First apparently chaotic zone. At a value near $V_{in} = 32.34V$, a sudden enlargement of the attractor occurs.

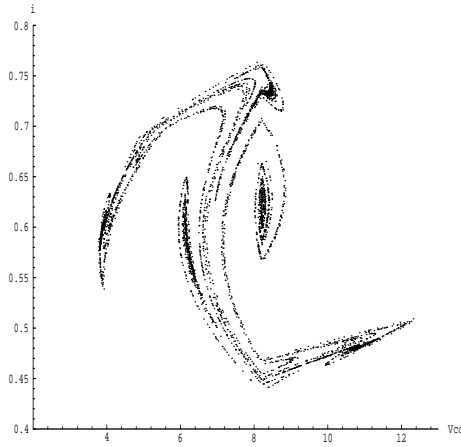


Figure 4.3: Strange attractor for $V_{in} = 35V$ (numerical simulation of 4000 iterations of the Poincaré map).

be the frequency at which the trajectory visits the i th elemental volum. Define

$$H(\epsilon) = - \sum_{i=1}^{N(\epsilon)} P_i \log(P_i)$$

Then, the capacity dimension D_{cap} , the information dimension D_I and the correlation dimension D_c of A are defined as

$$D_{cap} = \lim_{\epsilon \rightarrow 0} \frac{\log(N(\epsilon))}{\log(1/\epsilon)} \quad D_I = \lim_{\epsilon \rightarrow 0} \frac{H(\epsilon)}{\log(1/\epsilon)} \quad D_c = \lim_{\epsilon \rightarrow 0} \frac{1}{\log(\epsilon)} \log \sum_{i=1}^{N(\epsilon)} P_i^2$$

Definition:

Let $\lambda_1 \geq \dots \geq \lambda_n$ be the Lyapounov exponents of an attractor of a map, and let j be the largest index such that $\lambda_1 + \dots + \lambda_j \geq 0$. Then the Lyapounov dimension is defined as

$$D_L = j + \frac{\lambda_1 + \dots + \lambda_j}{|\lambda_{j+1}|}$$

To find D_{cap} the points $(\log(N(\epsilon)), \log(1/\epsilon))$ are plotted in a bivariant diagram for different values of ϵ . These points are then adjusted by a minimum squares procedure to a straight line, and the slope of this line is taken as an approximate value for the dimension. For the information dimension a similar method is employed, with the plot of $H(\epsilon)$ against $\log(1/\epsilon)$, and in the case of D_c , the axes are $\log \sum_{i=1}^{N(\epsilon)} P_i^2$ and $\log(\epsilon)$.

It is worth noting that the values for ϵ can only be taken in a reasonable range due to the limitations in the machine precision and in the number of points which can be processed, i.e., the minimum ϵ that can be taken is bounded by ϵ_0 . To make the computations efficient, the points in the attractor are rounded and mapped to the square $[0, 2^{16}) \times [0, 2^{16})$, and they are then put into binary form. With this method, the maximum ϵ_{max} that can be taken is $\epsilon_{max} = 2^{16}\epsilon_0$. This scheme for computing the dimensions is efficient in lower dimensions and does not require a special amount of memory in the machine [Carbonell and Olivar, 1994].

Taking into account that for very small and very large ϵ , the results can be distorted, they are rejected when adjusting to a line. The computed dimensions for the attractor when $V_{in} = 35V$ are

$$D_{cap} = 1.519860 \quad D_I = 1.479653 \quad D_c = 1.473991 \quad D_L = 1.449$$

This confirms that a certain fine structure is present in the attractor. Furthermore, due to the fact that the value of the dimension is quite far from 1, the reduction of the map to a one-dimensional approximated map, as in the case of the Lorenz system, is not possible. Thus, the dynamics must be studied in the two-dimensional phase space, and the simplification of the one-dimensional dynamics cannot be carried over.

Once it is found numerically that a chaotic strange attractor can be present in this system, and in order to prove mathematically that it is a strange attractor, the first step is to show the existence of a trapping region [Wiggins, 1990].

4.2 Existence of a Trapping Region

In the three-dimensional cylindrical space which was introduced in Chapter 3 we will find U such that

$$\phi(t, U) \subseteq U \quad \forall t \in U$$

Then, for the two-dimensional phase space, the projection of U will be a trapping region for P . Figure 4.4 shows the joined phase space corresponding to the two topologies of the system. The precise point of switching is not plotted in this picture, but it is known to occur somewhere between the two lines $\{(v, i) : v = v_l\}$ and $\{(v, i) : v = v_u\}$.

Let us assume that $V_{in} > v_u$ and $\varphi_1(t)$ and $\varphi_2(t)$ are two pieces of orbits in the phase space with the configuration in Fig. 4.5; that is, there exist times t_1, t_2, t_3, t_4 with $t_1 < t_2$ and $t_3 < t_4$ such that $\pi_1(\varphi_k(t_j)) = h$ for $k = 1, 2$, $j = 1, 2, 3, 4$ and some $h \in (v_l, v_u)$ and $\pi_2(\varphi_2(t_1)) < \pi_2(\varphi_1(t_4)) < \frac{v_l}{R} < \frac{v_u}{R} < \pi_2(\varphi_2(t_2)) < \pi_2(\varphi_1(t_3))$, (with π_1 and π_2 the projection maps of the first and second coordinates respectively), φ_1 being a piece of orbit of the first linear topology (the one which has $(0, 0)$ as fixed point), and φ_2 a piece of orbit of the second linear topology (the one which has $(V_{in}, V_{in}/R)$ as fixed point). With this situation, Fig. 4.6 shows a trapping region for one cycle of operation. However, obtain a trapping region for one cycle is not required. Instead, a trapping region for all time must be found. As the three-dimensional space is cylindrical, this can easily be accomplished by making a slight modification of the trapping region in Fig. 4.6. Figure 4.7 shows this desired trapping region and Fig. 4.8 shows its projection in the phase space.

So in order to state the existence of this trapping region, such pieces of trajectories φ_1, φ_2 must be found.

Note:

Every solution of one of the systems can be obtained as a translation of a solution of the other system by a translation vector $(V_{in}, V_{in}/R)$.

Finally, Fig. 4.9 shows how the configuration of the scheme presented in Fig. 4.5 can be obtained. Fix h between v_l and v_u , and consider the only two lines which are orthogonal to the family of spiral solutions of the first linear system (the system which has $(0, 0)$ as equilibrium point). Then consider the intersection point x_1^0 of one of these lines with the line $\{v = h\}$. A similar point x_2^0 can be found for the other linear topology. Now, consider the only solution φ_1^0 of system 1 (the system which has $(0, 0)$ as equilibrium point) passing through x_1^0 , and the only solution φ_2^0 of system 2 (the system which has $(V_{in}, V_{in}/R)$ as equilibrium point) passing through x_2^0 .

Then, configuration (0) is preserved. By moving x_1^0 on the vertical line $\{v = h\}$ and x_2^0 on the vertical line in opposite directions by a small amount ϵ , and taking the only two solutions passing through these two points, configuration (1) is obtained.

Continuously increasing $\epsilon > 0$, and by the theorem of continuity of the solutions of systems of differential equations, it is found a $\delta > \epsilon > 0$ so that configuration (2) is obtained, where the two solutions meet at the point x^* .

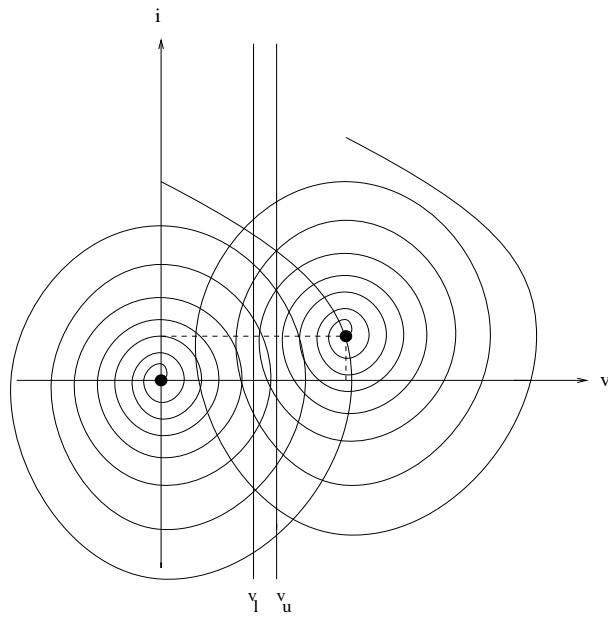


Figure 4.4: Joined phase-space corresponding to the two-topologies system.

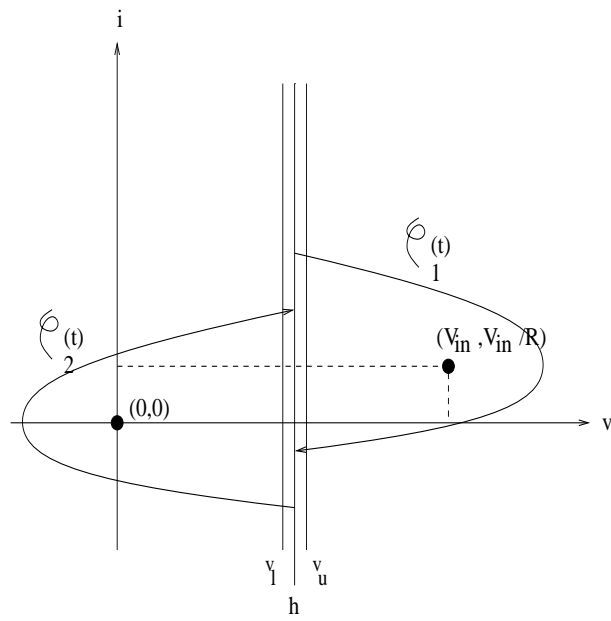


Figure 4.5: Configuration of two orbits in the phase space.

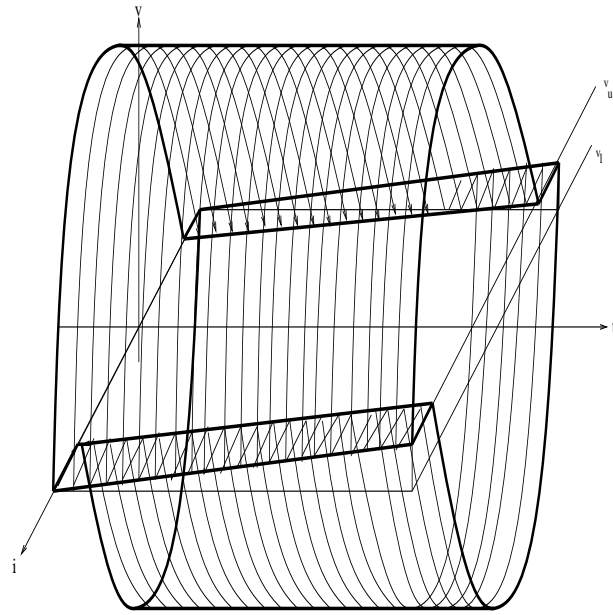


Figure 4.6: A trapping region for one cycle of operation.

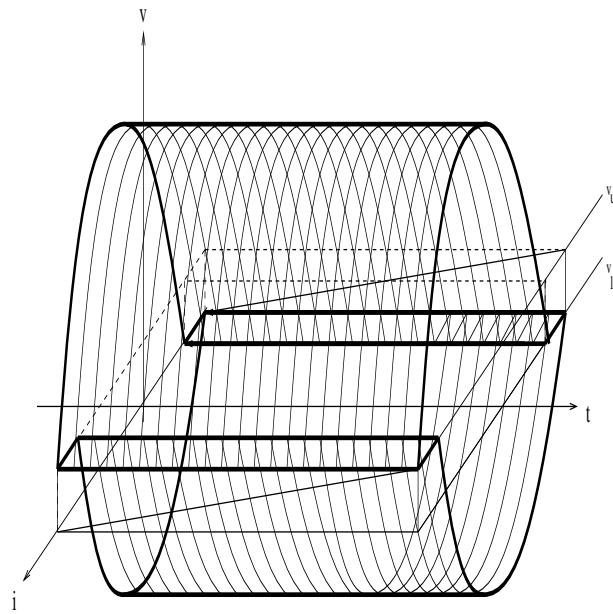


Figure 4.7: A trapping region for the system.

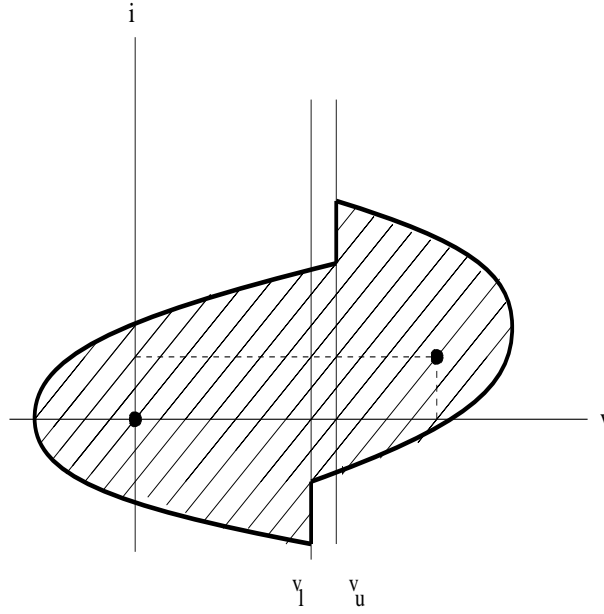


Figure 4.8: Projection of the three-dimensional trapping region in the phase-space.

Finally, increasing δ a little more, the final configuration is obtained. We may then conclude that there exist φ_1, φ_2 solutions of the respective systems with the desired configuration. If a strict trapping region is required, i.e. with the vector field pointing inwards strictly, a modified trapping region can be constructed following Fig. 4.10, where two auxiliary solutions φ_{ext} and φ_{int} are taken such that the distance between φ_{ext} and φ_{int} is small.

Once a trapping region is found, we conclude that

$$\bigcap_{t>0} \phi(t, U) = \mathcal{A}$$

is an attracting set; or, in the discrete version, the attracting set is

$$\bigcap_{n>0} P^n(U) = A$$

The next step is to show that A contains a chaotic invariant set Γ . This was numerically observed in Fig. 4.3, where a fine structure was detected. The fact that A contains a chaotic invariant set Γ can be directly proved showing that inside U there is a homoclinic orbit which has an invariant Cantor set associated with it on which the dynamics are topologically conjugate to a full shift on N symbols. So, A would contain a mechanism that gives rise to sensitive dependence on initial conditions. It is difficult to prove that A contains a homoclinic orbit. However, the existence of a region in the phase space in which

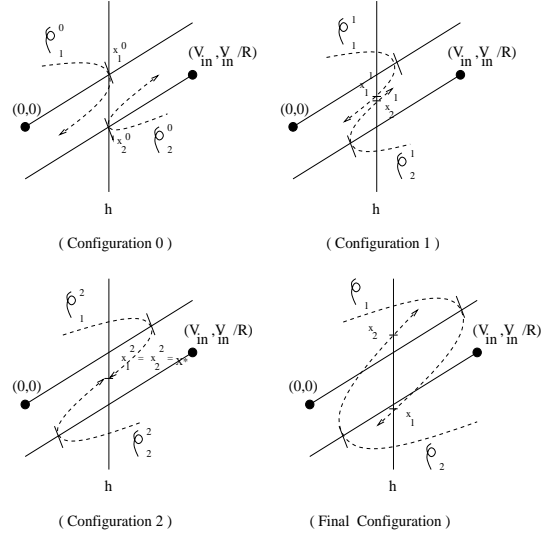


Figure 4.9: Initial to final configurations for the two desired pieces of orbits.

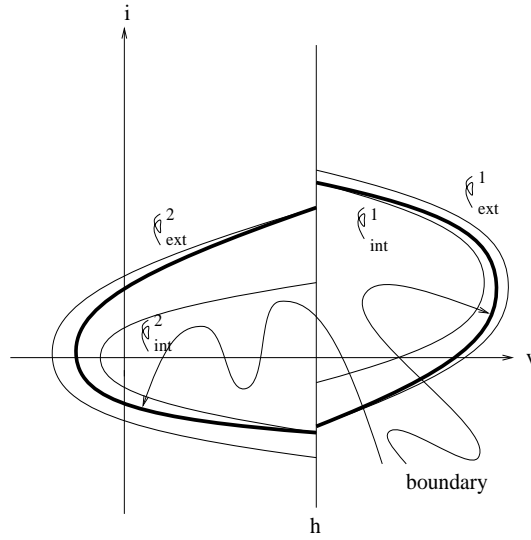


Figure 4.10: Modified boundaries of the projection of the trapping region to obtain a strict one.

the dynamics are topologically conjugate to a full shift on 2 symbols will be proved directly in Section 4.5 in a geometrical way. Proving this includes both geometrical reasoning and careful numerical computing.

4.3 A First Numerical View of the Attractor

If we observe the behaviour of the sequence $\{P(x_n)\}_{n \in \mathbb{N}}$ in detail when the strange attractor has been reached, we may point out several characteristics of the orbits in the plane (v_{co}, i) . First of all, the orbit visits five zones on a regular basis. The last one corresponds to multiple crossings in the ramp per cycle, while for the other four two crossings at most appear. We have (see also Fig. 4.11)

- zone 1: 1 crossing.
- zone 2: 1 or 2 crossings.
- zone 3: 0 or 1 crossing.
- zone 4: 1 crossing.
- zone 5: multiple crossings (0 to ∞).

Fig. 4.12 shows 40 iterations of the Poincaré map, starting with initial conditions near the strange attractor. The accumulation of points in the five zones is apparent. Fig. 4.13 plots the same trajectory in the phase space (v, i) and Fig. 4.14 displays the 40 cycles in the temporal representation of v_{co} . These 40 cycles are plotted in more detail in Fig. 4.15, where a certain degree of periodicity (every 5 cycles) can be observed, together with the five zones previously described.

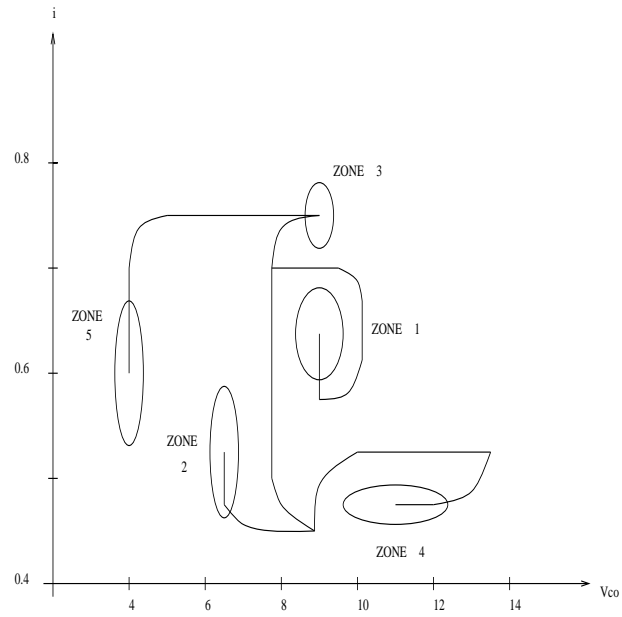
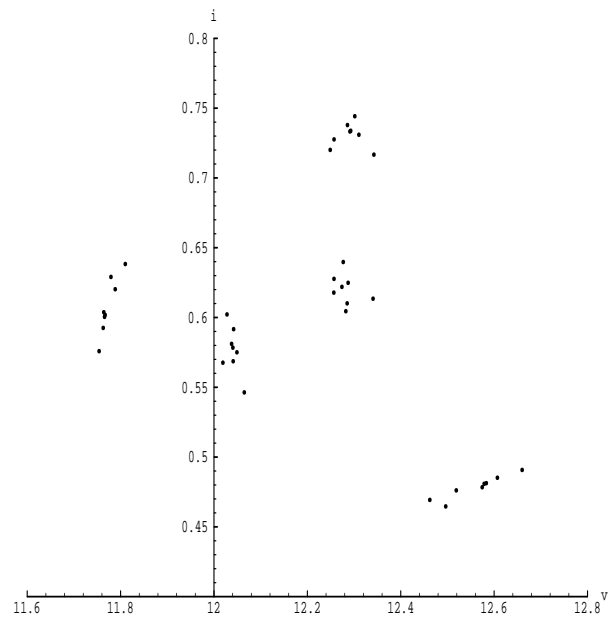
Multiple crossings per cycle with the ramp pose serious difficulties to the detailed study of the dynamics of the system. What is done in the following is to try to delimitate the zone of multiple crossings depending on the initial conditions. In general, one observes that the number of crossings increases with V_{in} .

Taking $V_{in} = 35V$, inside the proposed chaotic zone where the strange attractor appears, Fig. 4.16 shows, for each (v_0, i_0) , the number of crossings in the ramp in the first cycle when the system evolves from the initial conditions (v_0, i_0) . The black zone corresponds to zero crossings, the gray zone to one crossing, the light gray zone to two crossings, and finally, the white zone to three or more crossings. Thus, the zone that corresponds to multiple crossings is bounded in the phase space. Fig. 4.17 shows the white zone and its neighbourhood in more detail, where the concatenation of the regions of multiple crossings is seen. The central point is

$$v_l = V_{ref} + \frac{V_L}{a} \approx 11.75238095$$

$$i_l = \frac{v_l}{R} + \frac{C(V_U - V_L)}{aT} \approx 0.595746753$$

which corresponds to the initial conditions necessary to get theoretically ∞ crossings of the ramp (see Fig. 4.18). Notice that this central point is independent of the input voltage V_{in} .

Figure 4.11: Scheme of the attractor for $V_{in} = 35V$.Figure 4.12: 40 iterations of the Poincaré map ($V_{in} = 35V$).

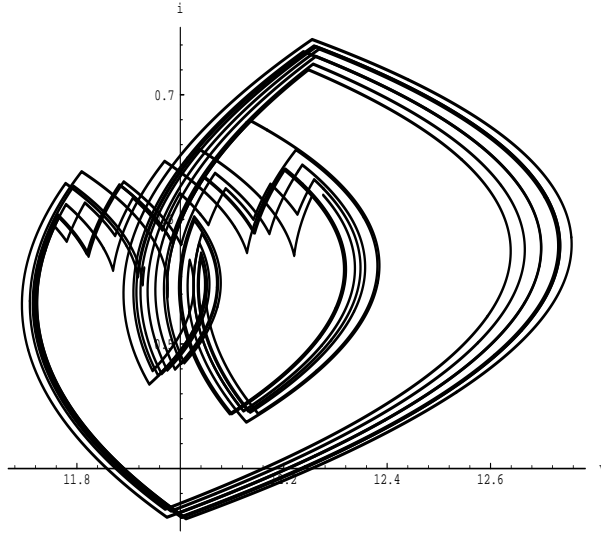


Figure 4.13: The orbit in figure 4.12 in the phase plane (v, i) .

Looking at Fig. 4.16 and Fig. 4.17, a partition of the phase space (v, i) into regions R_0, R_1, R_2, \dots , can be defined,

Definition:

It is defined for all $n \geq 0$, $R_n = \{ \text{initial conditions } x_0 = (v_0, i_0) \in \mathbb{R}^2 \text{ which give } n \text{ crossings in the ramp in the first cycle} \}$. For convenience, we also define

$$R_n^- = R_n \cap \{x_0 \in \mathbb{R}^2 : v_0 < v_l\} \quad \text{and} \quad R_n^+ = R_n \cap \{x_0 \in \mathbb{R}^2 : v_0 > v_l\} \quad (4.5)$$

such that

$$\mathbb{R}^2 = \left(\bigcup_{n \geq 0} R_n^- \right) \cup \left(\bigcup_{n \geq 0} R_n^+ \right) \cup \gamma \quad (4.6)$$

γ being the boundary of these regions.

With these definitions, the points in R_n are the interior points in the phase space at which the trajectory starting on them crosses the ramp voltage exactly n times in the first cycle. From Figs. 4.16 and 4.17, it can be deduced that the boundary of these regions is $\gamma = \gamma_1 \cup \gamma_2$, γ_1 and γ_2 being respectively a straight line and a piecewise smooth double spiral curve which focuses at the point x_l . Then, $\gamma_1 \cup \gamma_2$ divides the phase space \mathbb{R}^2 into a countable set of regions which can be naturally indexed by the number of crossings in the ramp. All the regions have two bounded and connected components, except for R_0 and R_1 which are unbounded. Moreover, R_0 has boundary only with R_1 , and, for $j \geq 1$, R_j has boundary only with R_{j-1} and R_{j+1} .

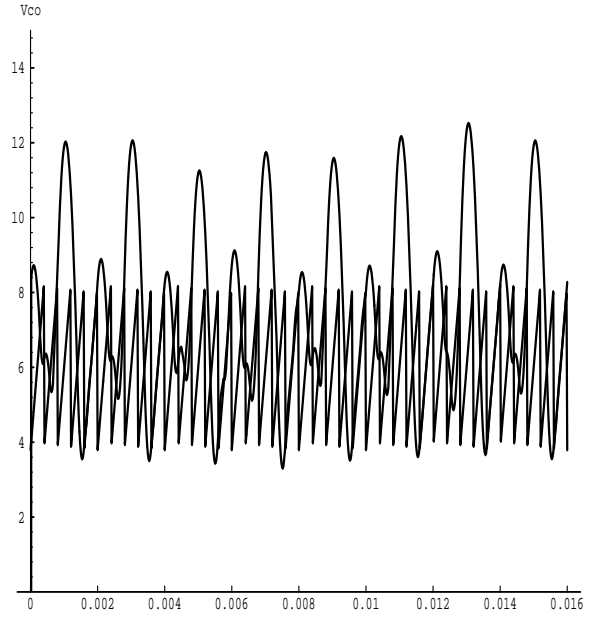


Figure 4.14: The orbit in figure 4.12 in the temporal representation of the control voltage v_{co} and the ramp.

Definitions:

A piecewise smooth curve $\gamma \in \mathbb{R}^2$ will be called a spiral focused at $x \in \mathbb{R}^2$ if and only if $x \notin \gamma$ is the only point such that every line through x cuts γ in a bi-infinite number of different points.

A set γ will be called a double spiral focused at $x \in \mathbb{R}^2$ if and only if $\gamma = \gamma_1 \cup \gamma_2$ such that $\gamma_1 \cap \gamma_2 = \emptyset$ and γ_1, γ_2 are both spirals focused at x .

We have computed the images of the regions R_j when we apply the Poincaré map to them; that is, the Poincaré map restricted to R_j

$$\begin{aligned} P : R_j &\longrightarrow \mathbb{R}^2 \\ (v_0, i_0) &\longrightarrow (v(T), i(T)) \end{aligned}$$

Figure 4.19 shows part of the images of R_0 and R_1 (they are not bounded) and the whole images of R_2 and $\cup_{j \geq 3} R_j$. The images correspond to the dotted zones. The regions corresponding to zero crossings, one crossing and two or more crossings have also been displayed schematically.

The first plot of Fig. 4.19 tells us that the image of R_0 is divided into the zones of zero crossings, R_0 , and one crossing, R_1 . That is, the cycle following a cycle with zero crossings can have either zero or one crossing. The second plot indicates that the cycle following a cycle with one crossing can have any number of crossings, since the image of R_1 has no empty intersection with the zone of multiple crossings, and it includes the central point x_l . The third

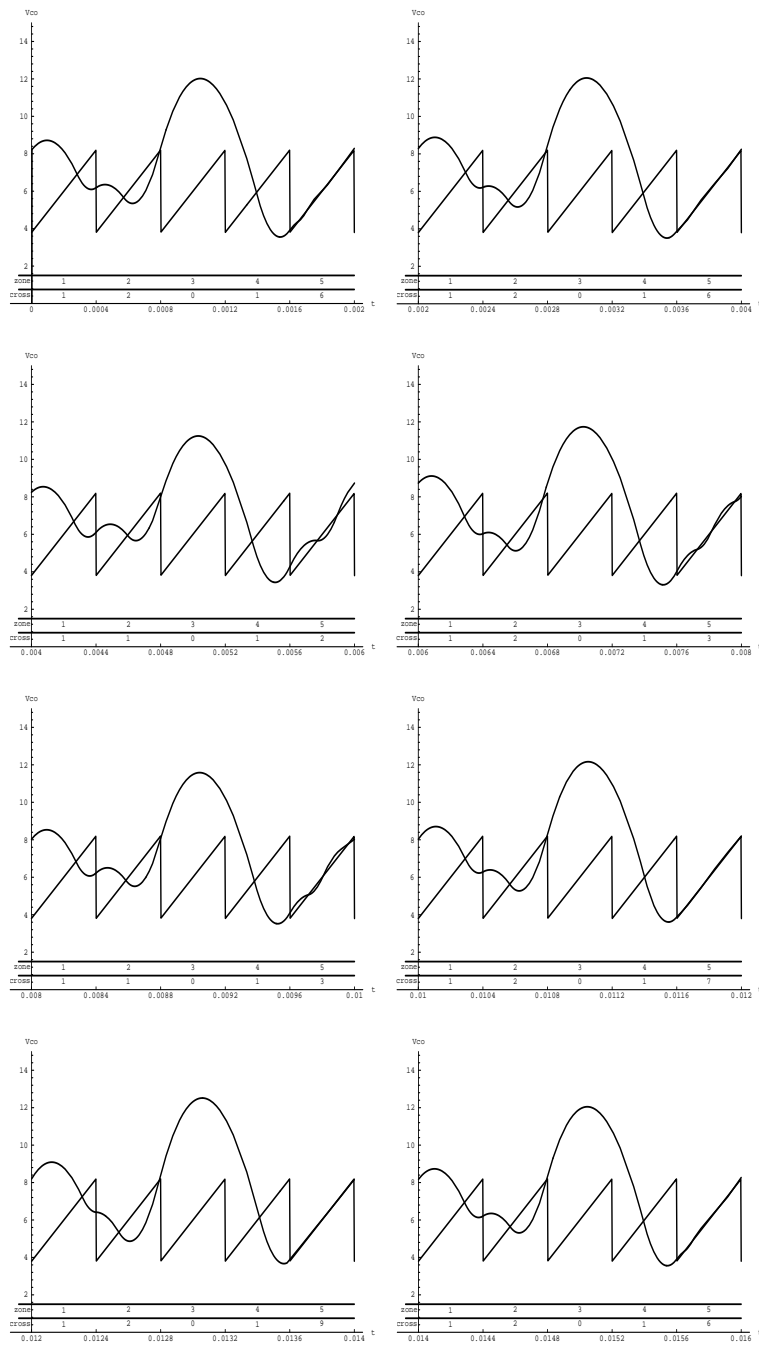


Figure 4.15: The 40 cycles of the orbit in figure 4.12 displayed in groups of 5.

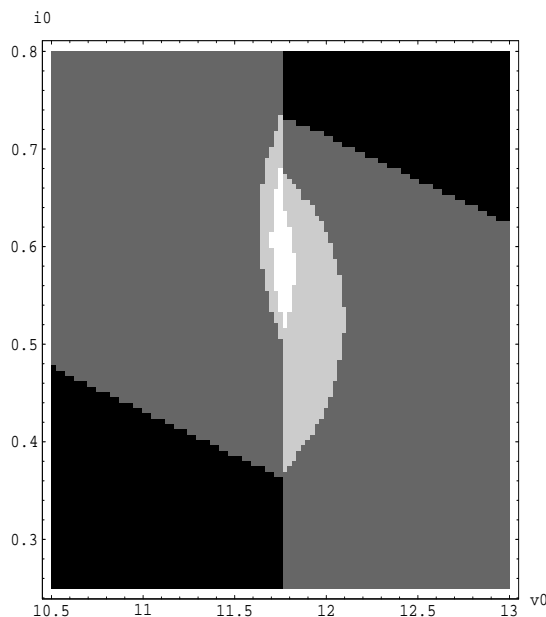


Figure 4.16: Number of crossings in the ramp ($V_{in} = 35V$). Black stands for no crossings, gray for one crossing, light gray for two crossings and white for more than two crossings.

plot shows that after a cycle with two crossings, only a cycle with one or zero crossings may follow, and finally, one crossing is expected after a cycle with three or more crossings, as shown by the fourth plot. This is in agreement with the movement between the zones of the attractor that was previously mentioned. If we distinguish between the "+" and "-" zones of R_n , then Fig 4.21 schematically represents the possible trajectories. Dashed lines correspond to very improbable routes that briefly leave the zone of the attractor, and heavy lines to the most visited trajectories when the attractor is reached. Simulations show that the typical excursions are $R_0^+ R_1^+ R_{>2}^+ R_1^+ R_1^+$ and $R_0^+ R_1^+ R_{>2}^+ R_1^+ R_2^+$ ($R_{>2} = \cup_{n>2} R_n$), and both of them contain multiple pulsing [Olivar and Fossas, 1995]. Finally, it is important to point out that a detailed study of the images by the Poincaré map of R_4 , R_5 and R_6 , which are all within the region in the phase space $[11.70, 11.86]V \times [0.52, 0.68]A$, shows a very pronounced winding (see Fig. 4.20). This motivates the search for a Smale horseshoe embedded in the Poincaré map, whose existence would confirm the chaotic behaviour that we are looking for, in the range of values of V_{in} near $35V$.

4.4 A Partition of the Phase Space

The numerics shown in the last section suggest that

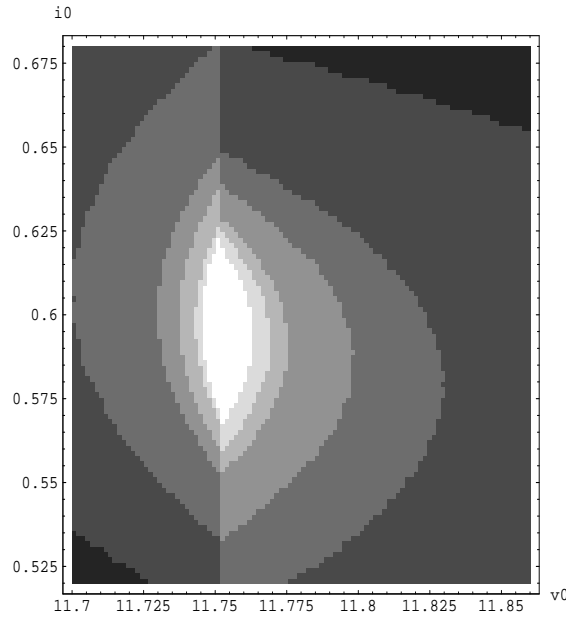


Figure 4.17: Number of crossings in the ramp. Detail of the central zone ($V_{in} = 35V$). Lighter gray corresponds to increasing number of crossings.

i) The dynamics evolve with a certain type of $5T$ -periodicity (therefore, there may be a $5T$ -periodic orbit nearby, inside the trapping region which, in a sense, governs the dynamics).

ii) The number of crossings in the ramp for one cycle plays an important role in the dynamics.

Thus we attempt to find numerically a $5T$ -periodic orbit near $V_{in} = 35V$ with an approximate shape of Fig. 4.15, and also to define precisely and investigate the partition in the phase space.

4.4.1 Existence of a $5T$ -Periodic Orbit

The first of the two points can be achieved with a scheme close to that of the $1T$ -periodic and $2T$ -periodic orbits of Chapter 3, and with the help of an equation solver like MAPLE. The two schemes close to the numerical simulations of the last section are those in Fig. 4.22, which include infinite crossings in the ramp in one of the cycles; thus, the corresponding trajectories in the phase space pass through x_l and x_u .

The equations for case 1 are the following:

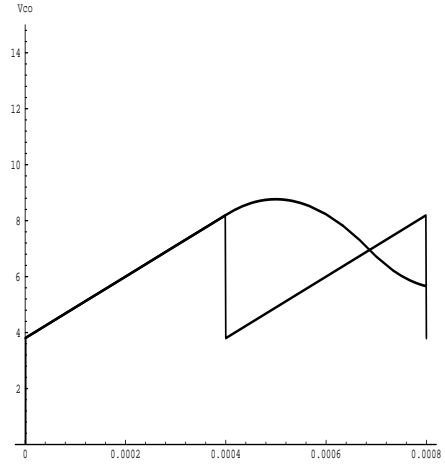


Figure 4.18: The control voltage when we take the central point $x_l = (v_l, i_l)$ as initial conditions, giving ∞ crossings in the ramp in the first cycle.

$$\begin{aligned}
 X(\alpha_1) &= N(\alpha_1)x_u \\
 X(1) &= V_{in}[N(0) - N(1 - \alpha_1)]b + N(1 - \alpha_1)X(\alpha_1) \\
 X(\alpha_2) &= N(\alpha_2)X(1) \\
 X(2) &= V_{in}[N(0) - N(1 - \alpha_2)]b + N(1 - \alpha_2)X(\alpha_2) \\
 X(3) &= N(1)X(2) \\
 X(\alpha_3) &= N(\alpha_3)X(3) \\
 x_l &= V_{in}[N(0) - N(1 - \alpha_3)]b + N(1 - \alpha_3)X(\alpha_3)
 \end{aligned} \tag{4.7}$$

with the additional conditions

$$\begin{aligned}
 a(v(t_1) - V_{ref}) &= V_L + (V_U - V_L)\alpha_1 \\
 a(v(t_2) - V_{ref}) &= V_L + (V_U - V_L)\alpha_2 \\
 a(v(t_3) - V_{ref}) &= V_L + (V_U - V_L)\alpha_3
 \end{aligned} \tag{4.8}$$

Equations (4.7) yield the expression

$$V_{in}[N(0) - N(1 - \alpha_3) + N(2) - N(3 - \alpha_2) + N(3) - N(4 - \alpha_1)]b = x_l - N(4)x_u$$

to be satisfied, together with conditions (4.8). MAPLE could not find any solution for this case. For case 2, the equations are

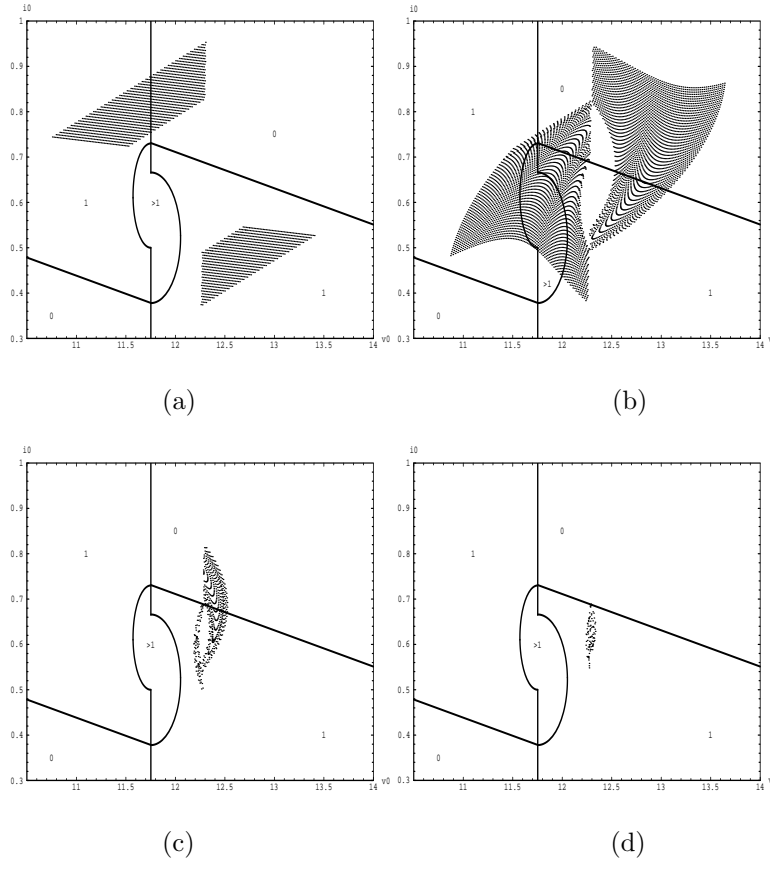


Figure 4.19: Images of the regions when the Poincaré map is applied to them ($V_{in} = 35V$). (a) Partial image of R_0 ; (b) Partial image of R_1 ; (c) $P(R_2)$; (d) $P(\cup_{n>2} R_n)$.

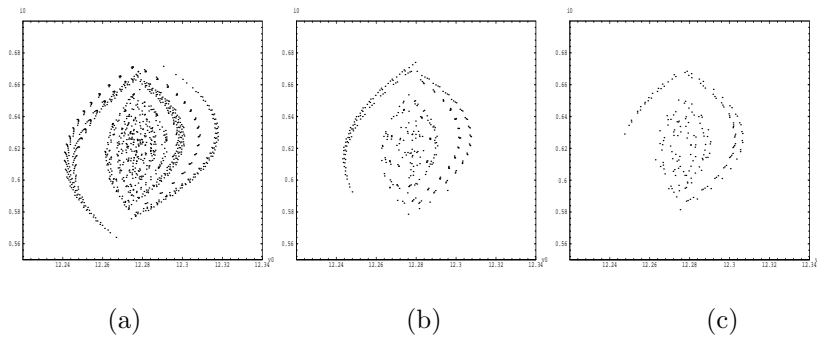


Figure 4.20: Images of the regions R_4 , R_5 and R_6 by the Poincaré map ($V_{in} = 35V$). (a) $P(R_4)$; (b) $P(R_5)$; (c) $P(R_6)$.

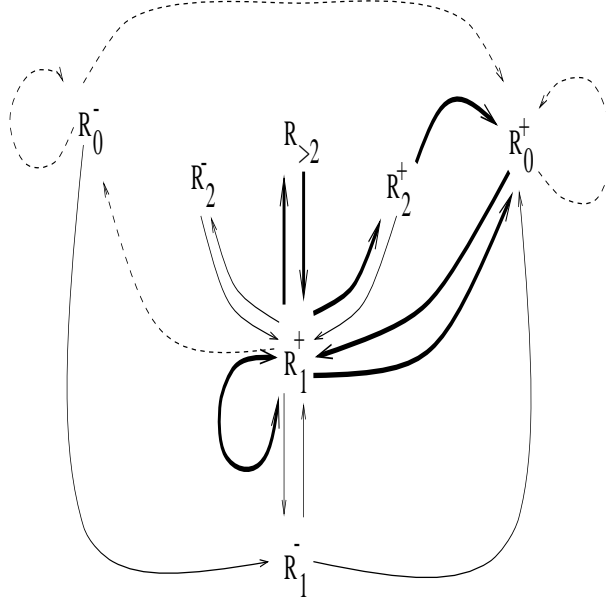


Figure 4.21: Scheme of the possible routes for $V_{in} = 35V$. Dashed lines correspond to very improbable routes and heavy lines to most visited trajectories.

$$\begin{aligned}
X(\alpha_1) &= N(\alpha_1)x_u \\
X(1) &= V_{in}[N(0) - N(1 - \alpha_1)]b + N(1 - \alpha_1)X(\alpha_1) \\
X(\alpha_2) &= N(\alpha_2)X(1) \\
X(\alpha_3) &= V_{in}[N(0) - N(\alpha_3 - \alpha_2)]b + N(\alpha_3 - \alpha_2)X(\alpha_2) \\
X(2) &= N(1 - \alpha_3)X(\alpha_3) \\
X(3) &= N(1)X(2) \\
X(\alpha_4) &= N(\alpha_4)X(3) \\
x_l &= V_{in}[N(0) - N(1 - \alpha_4)]b + N(1 - \alpha_4)X(\alpha_4)
\end{aligned} \tag{4.9}$$

with the additional conditions

$$\begin{aligned}
a(v(t_1) - V_{ref}) &= V_L + (V_U - V_L)\alpha_1 \\
a(v(t_2) - V_{ref}) &= V_L + (V_U - V_L)\alpha_2 \\
a(v(t_3) - V_{ref}) &= V_L + (V_U - V_L)\alpha_3 \\
a(v(t_4) - V_{ref}) &= V_L + (V_U - V_L)\alpha_4
\end{aligned} \tag{4.10}$$

Equations (4.9) yield the expression

$$V_{in}[N(0) - N(1 - \alpha_4) + N(3 - \alpha_3) - N(3 - \alpha_2) + N(3) - N(4 - \alpha_1)]b = x_l - N(4)x_u$$

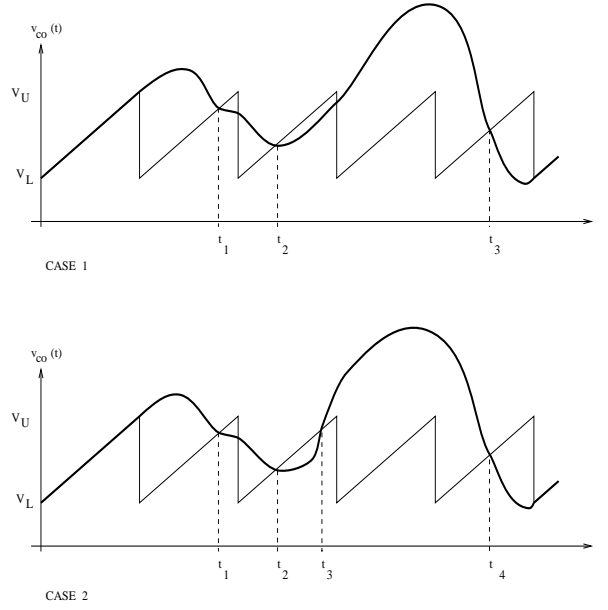


Figure 4.22: The two schemes for a $5T$ -periodic orbit close to that numerically observed in Fig. 4.15.

to be satisfied, together with conditions (4.10).

In this case, MAPLE solves the system with the following solution:

$$V_{in} = 34.33998523V$$

$$\alpha_1 = 0.7059566600 \quad \alpha_2 = 0.4092714402 \quad \alpha_3 = 0.9860506834 \quad \alpha_4 = 0.4809075344$$

The existence of this orbit suggests the existence of a $5T$ -periodic orbit in a certain range of the bifurcation parameter V_{in} , with a high number of crossings in one of its five cycles. Although it is an unstable $5T$ -periodic orbit and an equilibrium point cannot exist nearby, it is observed that the dynamics in a neighbourhood of the orbit is quite similar to the dynamics near an homoclinic orbit in a homoclinic tangle; and so a horseshoe mechanism can be present in that range of values of the bifurcation parameter.

The second item which was pointed out for study at the beginning of this section was the number of crossings in the ramp. This is studied in detail in the rest of this chapter.

4.4.2 Mechanism for the Creation of the Regions

Since the cause of non-smoothness in the system is the switching instants, it must be clear that the number of switchings in the ramp surface during a cycle introduces the lack of smoothness in the Poincaré map P . This can be expressed in the following proposition,

Proposition:

Let $x \in \mathbb{R}^2$ and define $\Gamma_x = \{(t, \phi_t^1(x)) : t \in [0, T]\}$. ($\phi_t = (\phi_t^1, \phi_t^2)$) Let also $\Gamma_r = \{(t, v_r(t)) : t \in [0, T]\}$. Assume that $\text{Card}(\Gamma_{x_0} \cap \Gamma_r) = m$. (so, the trajectory starting at x_0 , hits the ramp m times in the first cycle)

Then

P is smooth (differentiable) at $x_0 \Leftrightarrow \text{Card}(\Gamma_x \cap \Gamma_r) = m$ for all $x \in N(x_0)$ where $N(x_0)$ is some neighbourhood of x_0 .

Proof:

\Leftarrow) Assume that $\text{Card}(\Gamma_x \cap \Gamma_r) = m$ for all $x \in N(x_0)$, where $N(x_0)$ is a neighbourhood of x_0 .

Let $\{y_n\}_{n \in \mathbb{N}}$ be a sequence of points in \mathbb{R}^2 such that $\lim_{n \rightarrow \infty} y_n = x_0$ and $y_n \in N(x_0)$ for all n . Let $x_i = \alpha_i(x_0)$, $i = 1, \dots, m$ be the switching states in the first cycle when initial conditions are taken at x_0 and let $\alpha_i(y_n)$, $i = 1, \dots, m_n$ be the switching states in the first cycle when initial conditions are taken at y_n .

As $y_n \in N(x_0)$ we have $m_n = m$, and by the continuity of P , also

$$\lim_{n \rightarrow \infty} \alpha_i(y_n) = \alpha_i(x_0) \text{ for } i = 1, \dots, m.$$

Now, DP can be easily evaluated at the points $\{y_n\}_{n \in \mathbb{N}}$, since P is a composition of $m + 1$ \mathcal{C}^∞ mappings, and its expression $DP(y_n)$ finally depends only on y_n and the switching states $\alpha_i(y_n)$, $i = 1, \dots, m_n$.

Then, $\lim_{n \rightarrow \infty} DP(\alpha_i(y_n)) = DP(\alpha_i(x_0))$ for all $i = 1, \dots, m$, and thus, $\lim_{n \rightarrow \infty} DP(y_n) = DP(x_0)$ for all $i = 1, \dots, m$. This implies that P is smooth at x_0 .

\Rightarrow) Assume now that for all $N(x_0)$ neighbourhood of x_0 , there exists $y \in N(x_0)$ such that $\text{Card}(\Gamma_{y_n} \cap \Gamma_r) \neq m$.

Then, two sequences $\{y_n\}_{n \in \mathbb{N}}$ and $\{N_n(x_0)\}_{n \in \mathbb{N}}$ can be found such that $y_n \in N_n(x_0)$ and $\text{Card}(\Gamma_{y_n} \cap \Gamma_r) \neq m$ with $\lim_{n \rightarrow \infty} y_n = x_0$.

As $\lim_{n \rightarrow \infty} y_n = x_0$, there will exist two subsets $\{i_1, \dots, i_r\} \subseteq \{1, 2, \dots, m\}$ and $\{j_1, \dots, j_r\} \subseteq \{1, 2, \dots, m\}$ such that

$$\lim_{n \rightarrow \infty} \alpha_{i_1}(y_n) = \alpha_{j_1}(x_0), \dots, \lim_{n \rightarrow \infty} \alpha_{i_r}(y_n) = \alpha_{j_r}(x_0),$$

but since $\text{Card}(\Gamma_{y_n} \cap \Gamma_r) \neq m$ for all y_n , then, $m \neq m_n$ and taking into account the contributions of $\alpha_k(y_n)$ to $DP(y_n)$ when $k \in \{i_1, \dots, i_r\}^c$ then

$$DP(y_n) = DP(\alpha_1(y_n), \dots, \alpha_{m_n}(y_n))$$

will be different from

$$DP(x_0) = DP(\alpha_1(x_0), \dots, \alpha_m(x_0))$$

since each contribution of $\alpha_i(y_n)$ to $DP(y_n)$ is given by

$$V_{in} N'(1 - \alpha_i(y_n)) b \frac{d\alpha_i(y_n)}{dy_n} \neq 0$$

Thus, we have found a sequence $\{y_n\}_{n \in \mathbb{N}}$ such that $\lim_{n \rightarrow \infty} y_n = x_0$ but $\lim_{n \rightarrow \infty} DP(y_n) \neq DP(x_0)$ and then, P is non-smooth at x_0 .

So, the points in the state space which are not differentiable for P are those where a change in the number of crossings in the ramp is detected, i.e. those in the boundary of the regions R_n .

Analytical Expressions for the Boundaries of the Regions

In the last subsection, it was shown numerically that the regions R_n are bounded by piecewise smooth curves γ_1 and γ_2 . Now, analytical expressions for some of these boundaries will be given. The expressions for the boundaries dividing the zones of zero and one crossing are relatively simple, but a considerable algebraic effort must be made to give the expressions of the boundaries dividing the zones of one and two crossings. Analytical expressions for the rest of the boundaries cannot be given because they depend on the roots of more than one transcendental equation. As was mentioned before, the boundaries of the regions R_n are of two different types: *vertical* boundaries, corresponding to the line γ_1 and *horizontal* boundaries, corresponding to the double spiral γ_2 . Thus, there are essentially two types of mechanisms for changing the number of crossings in the ramp from R_j to R_{j+1} , associated to each type of boundary which is crossed. There is a special case when a boundary is crossed through a point p_l^j . In this case the number of crossings in the ramp is changed by two.

Crossing a boundary

Let us fix a point $x_0 = (v_0, i_0)$ such that $x_0 \in (\bar{R}_1 \cap \gamma_2) - \gamma_1$ and assume that the tangent to the boundary at the point x_0 is not vertical. Then, near to i_0 , i_1 and i_2 can be found such that $i_1 < i_0 < i_2$ and $(v_0, i_1) \in R_1 - (\gamma_1 \cup \gamma_2)$ and $(v_0, i_2) \in R_2 - (\gamma_1 \cup \gamma_2)$. So, a boundary between R_1 and R_2 is crossed when the current is increased from i_1 to i_2 . The crossing is produced at $i = i_0$, i.e. when i_0 is such that $P(x_0) = (v_u, \cdot)$. A *horizontal* boundary has been crossed (see Fig. 4.23), concretely, when $x_0 \in P^{-1}(r_u)$, where

$$r_u = \{x = (v, i) \in \mathbb{R}^2 : v = v_u\} \quad (4.11)$$

A similar argument can be employed to justify that all the crossings of *horizontal* boundaries take place when the final voltage in a cycle is v_u . So, we can state that $P(\gamma_2) = r_u$.

Let us fix now a point $x_0 = (v_l, i_0)$ such that $x_0 \in (\bar{R}_0 \cap \gamma_1) - \gamma_2$. Then, near to v_l , v_1 and v_2 can be found such that $v_1 < v_l < v_2$ and $(v_1, i_0) \in R_0 - (\gamma_1 \cup \gamma_2)$ and $(v_2, i_0) \in R_1 - (\gamma_1 \cup \gamma_2)$. So, a boundary between R_0 and R_1 is crossed when the voltage is increased from v_1 to v_2 through v_l . The crossing is produced at $v = v_l$ (see Fig. 4.24), concretely, when $x_0 \in \gamma_1$,

A similar argument can be employed to justify that all the crossings of *vertical* boundaries take place when the initial voltage in a cycle is v_l .

Double crossings of boundaries can occur when this takes place through a point $p \in \gamma_1 \cap \gamma_2$. This means a change by two in the number of crossings. A point $p \in \gamma_1 \cap \gamma_2$ means that $p = (v_l, \cdot)$ such that $P(p) = (v_u, \cdot)$ (see Fig. 4.25).

Consequently, the points in the state space where a change in the number of crossings in the ramp is detected are those in the following sets:

$$\gamma_1 = \{x \in \mathbb{R}^2 : v = v_l\} \quad \gamma_2 = P^{-1}\{x \in \mathbb{R}^2 : v = v_u\}$$

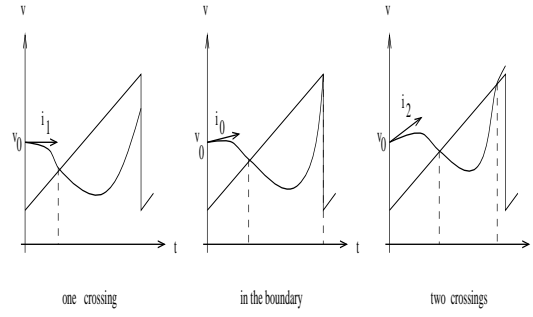
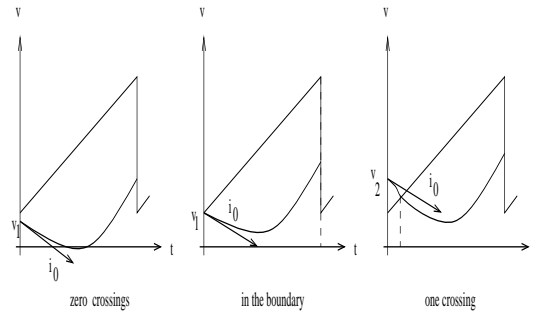
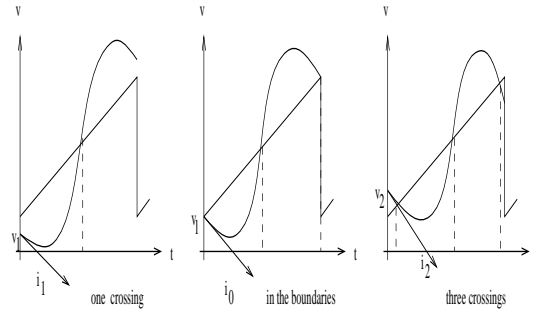
Figure 4.23: Crossing a *horizontal* boundary.Figure 4.24: Crossing a *vertical* boundary.

Figure 4.25: Crossing a double boundary.

and the following consequence can be stated

Consequence:

Let $\gamma_1 = \{x \in \mathbb{R}^2 : v = v_l\}$, and $\gamma_2 = P^{-1}\{x \in \mathbb{R}^2 : v = v_u\}$
 (P is a Poincaré map of a flow; then it is invertible and P^{-1} can be considered)

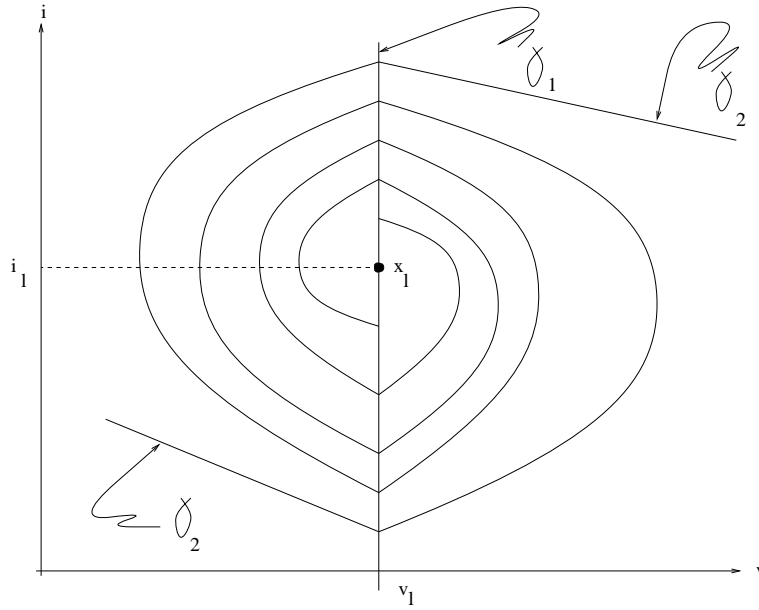


Figure 4.26: The phase space \mathbb{R}^2 is partitioned into infinitely many regions. The boundary of these regions is the union of two sets γ_1 and γ_2 . γ_1 is a vertical line and γ_2 is a piecewise smooth double spiral which focusses at x_l .

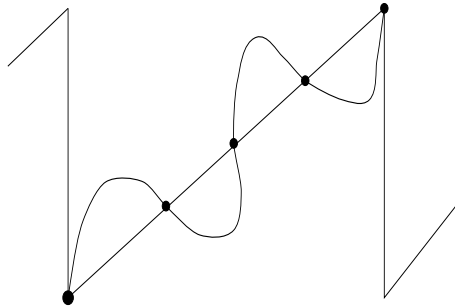


Figure 4.27: Trajectory with initial condition at a point $x = (v_l, i_l)$ such that $P(x) = (v_u, i_2)$. Then x must belong to $\gamma_1 \cap \gamma_2$.

Then

P is smooth in $\mathbb{R}^2 - \{\gamma_1 \cup \gamma_2\}$

Proof:

$\gamma_1 \cup \gamma_2$ is the set for the change in the number of crossings, and the last proposition can be applied.

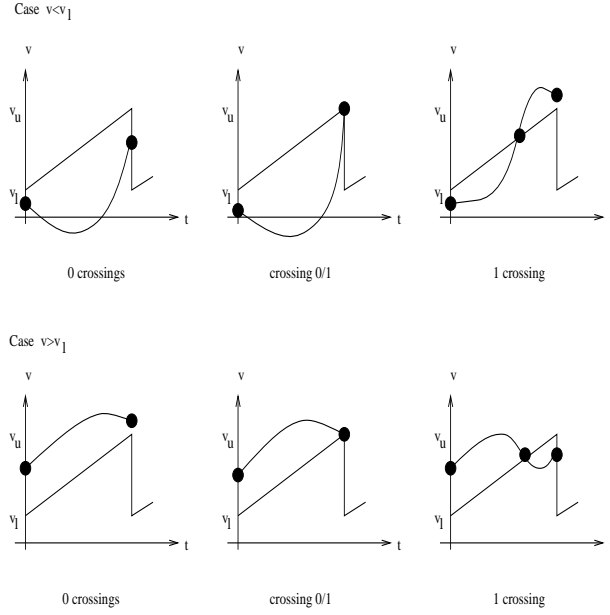


Figure 4.28: Scheme for the boundary between the 0 and 1 zones.

Observation:

The intersection set $\gamma_1 \cap \gamma_2 = \{p_l^r\}_{r=-\infty, \dots, +\infty}$ consists in a bi-infinite sequence of points in the line γ_1 , which can be ordered by the current component, with $p_l^0 = (v_l, i_l) = x_l$.

Borders of the regions with zero and one crossings

As has been proved, one of the boundaries, γ_1 has an explicit expression

$$\gamma_1 = \{x = (v, i) \in \mathbb{R}^2 : v = v_l\}$$

which is a vertical line. Consequently, the expressions to be computed are those for γ_2 . This part of the boundary corresponding to the 0/1 zones can be divided into two cases (see Fig. 4.28): one, which corresponds to $x_0 = (v_0, i_0)$ with $v_0 < v_l$ and the other with $v_0 > v_l$. In the phase space, Fig. 4.29 shows where this boundary is crossed.

Thus, we simply have to find (v_0, i_0) such that $v(v_0, i_0, t = T) = v_u$ (with $v_0 < v_l$ for one of the cases and $v_0 > v_l$ for the other). In both cases, only one of the topologies is active and there are no crossings in the ramp. This is the cause of a simple expression for this part of the spiral boundary. The equations for them are thus

$$x_T = N(1)x_0 + V_{in}[I - N(1)]b \quad x_T = N(1)x_0$$

respectively for case (a) and (b), where $x_T = (v_u, i_T)$ with i_T free.

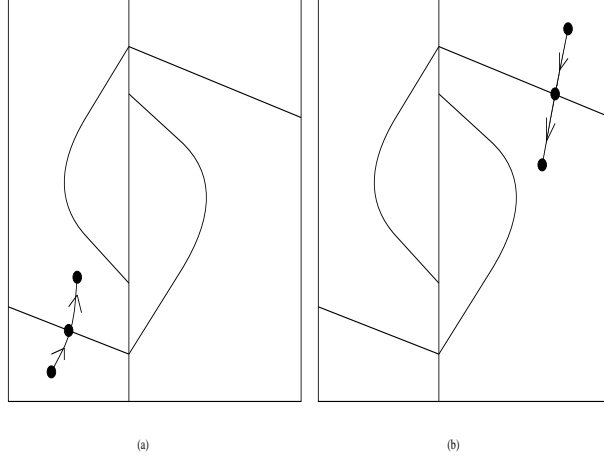


Figure 4.29: Crossing the 0 and 1 zones. (a) $v < v_l$;
(b) $v > v_l$.

From case (a), it is obtained

$$v_u = V_{in} + e^{-kT} \left\{ \left(\cos(wT) - \frac{k}{w} \sin(wT) \right) (v_0 - V_{in}) + \left(i_0 - V_{in}/R \right) \frac{1}{Cw} \sin(wT) \right\}$$

From this latter expression, $i_0 = i_0(v_0)$ for $v_0 < v_l$ can be obtained

$$i_0 = \frac{V_{in}}{R} + \frac{Cw}{\sin(wT)} \left[(v_u - V_{in}) e^{kT} - (v_0 - V_{in}) \left(\cos(wT) - \frac{k}{w} \sin(wT) \right) \right] \quad (v_0 < v_l)$$

which corresponds to a half-line.

From case (b),

$$v_u = e^{-kT} \left\{ v_0 \left(\cos(wT) - \frac{k}{w} \sin(wT) \right) + i_0 \frac{1}{Cw} \sin(wT) \right\}$$

and then

$$i_0 = \frac{Cw}{\sin(wT)} \left[v_u e^{kT} - v_0 \left(\cos(wT) - \frac{k}{w} \sin(wT) \right) \right] \quad (v_0 > v_l)$$

which corresponds to another half-line.

Observation:

The half-line in case (a) depends on V_{in} , while in case (b) it does not. Therefore, this latter boundary stands for all the values of the parameter V_{in} .

Borders of the regions with one and two crossings

In this case, since one transcendental equation is involved in the computations, an explicit expression for the boundary is not possible, although a parametric

expression can be obtained

$$\{(v_0(\alpha), i_0(\alpha)) : \alpha \in I = [0, \alpha_{max}]\}$$

where the parameter α is the duty cycle, and I stands for a certain interval whose limits must be found numerically. In Fig. 4.30 the relation between the phase space and the representation in time are shown.

Passing through situation (a) to (e) is produced when the duty cycle α increases from $\alpha = 0$ to $\alpha = \alpha_{max}$. The limiting value α_{max} can be obtained with the intersection of the line γ_1 and the curve for the $1/2^+$ boundary, which is only valid for $v_0 > v_l$. This intersection is solved numerically, since a transcendental equation is involved.

Figure 4.31 shows both cases.

Case (a)

The equations for this case are

$$x_T = N(1 - \alpha)x_1 + V_{in}[I - N(1 - \alpha)]b$$

where $x_T = (v_u, i_T)$ with i_T free is the value of the state at the end of the cycle, and $x_1 = (v_1, i_1)$ is the phase point when the ramp is crossed for $t = \alpha T$. Now, using the expressions obtained in the 0/1 regions and the condition for crossing the ramp

$$v_1 = v_l + \alpha(v_u - v_l)$$

the expression for $i_1 = i_1(v_1)$ is obtained

$$i_1(v_1) = \frac{V_{in}}{R} + \frac{Cw}{\sin(wT(1 - \alpha))}[(v_u - V_{in})e^{kT(1 - \alpha)} - (v_l + (v_u - v_l)\alpha - V_{in}) \cdot (\cos(wT(1 - \alpha)) - \frac{k}{w}\sin(wT(1 - \alpha)))] \quad (v_0 < v_l)$$

and so the expression for $(v_1(\alpha), i_1(\alpha))$ is obtained. The next step is to find (v_0, i_0) such that the values for (v, i) corresponding to $t = \alpha T$ are the computed (v_1, i_1) . Using again the expression which was computed for the 0/1 regions,

$$i_0(v_0) = \frac{Cw}{\sin(wT\alpha)}[(v_l + \alpha(v_u - v_l))e^{kT\alpha} - v_0(\cos(wT\alpha) - \frac{k}{w}\sin(wT\alpha))]$$

The final step is to impose that $i_1 = i(v_0, i_0(v_0), t = \alpha T)$; to do this, we use $x_1 = N(\alpha)x_0$. This results in

$$e^{-kT\alpha} \left\{ -\frac{v_0}{Lw} \sin(wT\alpha) + i_0 \left(\cos(wT\alpha) - \frac{k}{w} \sin(wT\alpha) \right) \right\} = \frac{V_{in}}{R} + \frac{Cw}{\sin(wT(1 - \alpha))} [(v_u - V_{in})e^{kT(1 - \alpha)} - (v_l + (v_u - v_l)\alpha - V_{in})(\cos(wT(1 - \alpha)) - \frac{k}{w}\sin(wT(1 - \alpha)))]$$

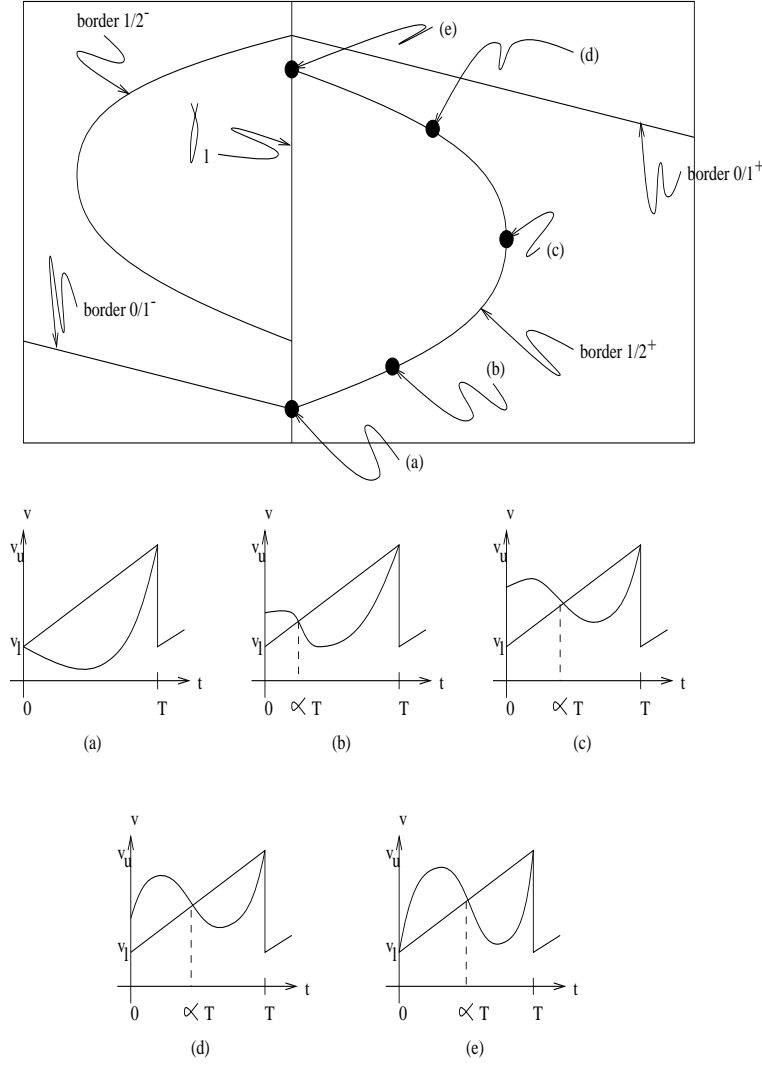


Figure 4.30: Crossing the 1 and 2 zones. (a) double boundary 0/1/2, $\alpha = 0$; (b) increasing the initial condition for the voltage; (c) maximum value for the initial condition for the voltage; (d) decreasing the initial condition for the voltage; (e) double boundary 1/2/3, $\alpha = \alpha_{max}$.

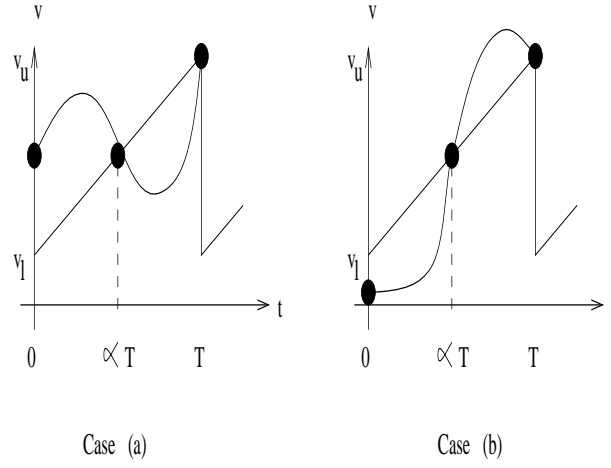


Figure 4.31: Schemes for the 1/2 boundaries.

In this equality, one can substitute i_0 for $i_0(v_0)$ and obtain $v_0 = v_0(\alpha)$, which after collecting terms, gives the desired parametric expressions for $v_0 = v_0(\alpha)$ and $i_0 = i_0(\alpha)$

$$\begin{aligned}
 v_0(\alpha) = & (\cos(wT\alpha) + \frac{k}{w}\sin(wT\alpha))(v_l + \alpha(v_u - v_l))e^{kT\alpha} + \\
 & (\cos(wT(1-\alpha)) - \frac{k}{w}\sin(wT(1-\alpha)))(v_l - V_{in} + \alpha(v_u - v_l))\frac{\sin(wT\alpha)}{\sin(wT(1-\alpha))}e^{kT\alpha} - \\
 & (v_u - V_{in})e^{kT}\frac{\sin(wT\alpha)}{\sin(wT(1-\alpha))} - \frac{V_{in}}{RCw}e^{kT\alpha}\sin(wT\alpha) \\
 i_0(\alpha) = & \frac{1}{Lw}\sin(wT\alpha)(v_l + \alpha(v_u - v_l))e^{kT\alpha} + \frac{V_{in}}{R}(\cos(wT\alpha) - \frac{k}{w}\sin(wT\alpha)) \\
 & e^{kT\alpha} + Cw(v_u - V_{in})e^{kT}\frac{\cos(wT\alpha) - \frac{k}{w}\sin(wT\alpha)}{\sin(wT(1-\alpha))} - Cw(v_l - V_{in} + \alpha(v_u - v_l))e^{kT\alpha} \\
 & \frac{(\cos(wT\alpha) - \frac{k}{w}\sin(wT\alpha))(\cos(wT(1-\alpha)) - \frac{k}{w}\sin(wT(1-\alpha)))}{\sin(wT(1-\alpha))}
 \end{aligned}$$

Case (b)

In this case, similar considerations yield the following expressions

$$\begin{aligned}
 v_0(\alpha) = & (\cos(wT\alpha) + \frac{k}{w}\sin(wT\alpha))(v_l - V_{in} + \alpha(v_u - v_l))e^{kT\alpha} + \\
 & (\cos(wT(1-\alpha)) - \frac{k}{w}\sin(wT(1-\alpha)))(v_l + \alpha(v_u - v_l))\frac{\sin(wT\alpha)}{\sin(wT(1-\alpha))}e^{kT\alpha} -
 \end{aligned}$$

$$\begin{aligned}
& v_u e^{kT} \frac{\sin(wT\alpha)}{\sin(wT(1-\alpha))} + V_{in} \left(1 + \frac{1}{RCw} e^{kT\alpha} \sin(wT\alpha)\right) \\
i_0(\alpha) = & \frac{1}{Lw} \sin(wT\alpha) (v_l - V_{in} + \alpha(v_u - v_l)) e^{kT\alpha} + \frac{V_{in}}{R} (1 - e^{kT\alpha} (\cos(wT\alpha) - \\
& \frac{k}{w} \sin(wT\alpha))) + Cw v_u e^{kT} \frac{\cos(wT\alpha) - \frac{k}{w} \sin(wT\alpha)}{\sin(wT(1-\alpha))} - Cw (v_l + \alpha(v_u - v_l)) \\
& e^{kT\alpha} \frac{(\cos(wT\alpha) - \frac{k}{w} \sin(wT\alpha)) (\cos(wT(1-\alpha)) - \frac{k}{w} \sin(wT(1-\alpha)))}{\sin(wT(1-\alpha))}
\end{aligned}$$

For an input voltage $V_{in} = 35V$, MAPLE gives the following values for α_{max} : for case (a), $\alpha_{max} = 0.63621676$ and for case (b), $\alpha_{max} = 0.39277083$.

In the general case, the boundaries between the regions of $n/n+1$ crossings cannot be computed analytically because more than one transcendental equation is involved, and this means that no closed form expression exists for the boundaries without including the roots of transcendental equations, i.e. in explicit or parametric form. In summary, for every chosen value for V_{in} , analytical exact expressions have been found for the boundaries dividing the zero crossings region, the one crossing region and the multiple crossings (two or more) regions. This is important since the multiple crossings region has much to do with the chaotic behaviour which is observed for some values of the bifurcation parameter V_{in} .

4.5 Images of the Regions by the Poincaré Map

4.5.1 Images of the Regions of Zero and One Crossing

Based on the numerical results obtained in the last section, some images of the regions R_n are analytically deduced to obtain a scheme for a horseshoe mechanism embedded in the Poincaré map, giving rise to an invariant set with sensitive dependence on initial conditions included in the trapping region. First of all, an easy proposition is proved which reflects the general nonlinear character of the Poincaré map in a significant region of the phase space.

Proposition:

P is affine on R_0^- , linear on R_0^+ and nonlinear on all the other regions.

Proof:

On R_0^- , we have the scheme in Fig.4.32a. Then,

$$P(x_0) = V_{in}[I - N(1)]b + N(1)x_0$$

which is affine with x_0 .

On R_0^+ , we have the scheme in Fig.4.32b. Then,

$$P(x_0) = N(1)x_0$$

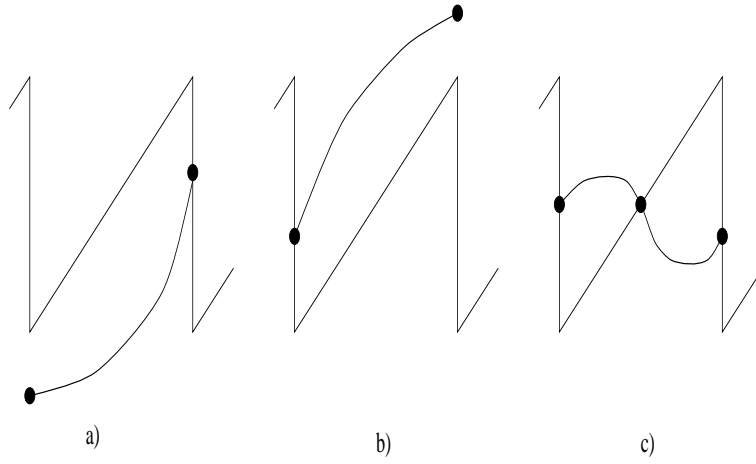


Figure 4.32: Initial condition for a) belongs to R_0^- , initial condition for b) belongs to R_0^+ and initial condition for c) belongs to R_1^+ .

which is linear with x_0 .

On other regions R_n , with $n > 0$, we have n crossings in the ramp. These crossings introduce n instants $\alpha_1(x_0), \alpha_2(x_0), \dots, \alpha_n(x_0)$ which depend on x_0 in the expression for $P(x_0)$. This makes P nonlinear in R_n for $n > 0$. As an example, for $x_0 \in R_1^+$ (see Fig. 4.32c), we have for the switching time α_s

$$x(\alpha_s) = N(\alpha_s)x_0$$

and

$$P(x_0) = V_{in}[I - N(1 - \alpha_s)]b + N(1 - \alpha_s)x(\alpha_s) = V_{in}[I - N(1 - \alpha_s)]b + N(1)x_0,$$

which nonlinearly depends on $\alpha_s = \alpha_s(x_0)$.

As mentioned before, the curves γ_1 and γ_2 play an important role in the Poincaré map P . The following notation will be used to distinguish between the spirals and the lines

$$\begin{aligned} r_l &\equiv \gamma_1 = \{x = (v, i) \in \mathbb{R}^2 : v = v_l\} \\ r_l^+ &= \{x = (v, i) \in \mathbb{R}^2 : v = v_l, i > i_l\} \\ r_l^- &= \{x = (v, i) \in \mathbb{R}^2 : v = v_l, i < i_l\} \end{aligned} \quad (4.12)$$

such that $r_l = r_l^+ \cup r_l^- \cup x_l$

$$\begin{aligned} r_u &\equiv P(\gamma_2) = \{x = (v, i) \in \mathbb{R}^2 : v = v_u\} \\ r_u^+ &= \{x = (v, i) \in \mathbb{R}^2 : v = v_u, i > i_u\} \\ r_u^- &= \{x = (v, i) \in \mathbb{R}^2 : v = v_u, i < i_u\} \end{aligned} \quad (4.13)$$

such that $r_u = r_u^+ \cup r_u^- \cup x_u$

$$\begin{aligned} s_l &\equiv \gamma_2 = P^{-1}(\{x = (v, i) \in \mathbb{R}^2 : v = v_u\}) \\ s_l^+ &= s_l \cap \{x = (v, i) \in \mathbb{R}^2 : v > v_l\} \\ s_l^- &= s_l \cap \{x = (v, i) \in \mathbb{R}^2 : v < v_l\} \end{aligned} \quad (4.14)$$

such that $s_l = s_l^+ \cup s_l^- \cup x_l$

By a continuity argument, $P(r_l^-)$ and $P(r_l^+)$ are spirals focused at x_u . Thus, we can define

$$\begin{aligned} s_u &= P(r_l) \\ s_u^+ &= s_u \cap \{x = (v, i) \in \mathbb{R}^2 : v > v_u\} \\ s_u^- &= s_u \cap \{x = (v, i) \in \mathbb{R}^2 : v < v_u\} \end{aligned} \quad (4.15)$$

such that $s_u = s_u^+ \cup s_u^- \cup x_u$.

With these definitions, the next step is to compute the images of some regions R_n by the Poincaré map P . Some of the first intersections $r_l \cap s_l$ which delimits the regions are numbered, and their images computed. In particular, the images of the points in the phase space labeled 1,2,3,4,5 and 6 according to Fig. 4.33 are computed. As they all belong to s_l , their image must be in r_u . Point labeled 1 corresponds to (v_1, i_1) with $v_1 = v_l$ and $i_1 < i_l$, in the boundary of the regions of 0/1/2 crossings. This means that the trajectory with initial conditions at (v_1, i_1) , in the first cycle, only crosses the ramp voltage at the end of the ramp for $t = T$, and consequently, as $i_1 < i_l$, then the current at the end of the ramp i_1' will verify $i_1' > i_u$. So P maps the point labeled 1 at some point in r_u^+ . With a similar argument, a point labeled α in s_l^- , which belongs to the boundary of the regions of 0/1 crossings, will be mapped to a point $P(\alpha)$ in r_u with a current larger than i_1' . Then, as P is one to one and continuous, the piece of the boundary between the points labeled α and 1 will be mapped to the piece of line between $P(\alpha)$ and $P(1)$, as shown in Fig. 4.33. Similar arguments stand for the points labeled 6 and w and the corresponding images $P(6)$ and $P(w)$, as well as for the rest of the points, which are mapped as in Fig. 4.33 and Fig. 4.34.

Now take a point labeled X in r_l , with a very small current component. Then, as X is a point with voltage v_l , in the boundary between regions of 0/1 crossings, but with a current lower than i_1 , the trajectory with initial conditions at X will end at the end of the ramp with a voltage lower than v_u and a current lower than i_1' (the final voltage and current will be much lower than v_u and i_1' as the initial current is taken lower and lower). So $P(X)$ will be applied at some point in the phase space with very low voltage and current. Then the region delimited by α -1-X (which is part of R_0^-) is mapped by P to the region delimited by $P(\alpha)$ - $P(1)$ - $P(X)$. As x_l is not included in R_0^- , then $P(R_0^-)$ does not include x_u , and so $P(R_0^-)$ is the zone indicated in Fig. 4.35. In a similar way, taking a point Y in the phase space on r_l^+ with a large current, its image $P(Y)$ can be sketched, and so $P(R_0^+)$. Now, the region R_1^- is delimited by the points labeled α -1-5-6-Y. So its image by P will be delimited by $P(\alpha)$ - $P(1)$ - $P(5)$ - $P(6)$ - $P(Y)$. The piece from $P(1)$ to $P(5)$ is for the moment unknown, but it must be a certain curve between these points. As $P(R_1^-)$ cannot contain x_u and the curve

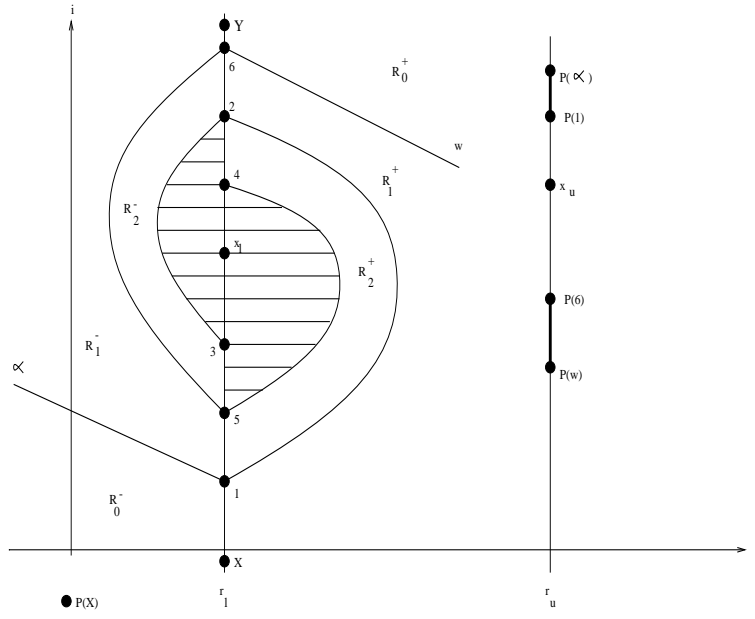


Figure 4.33: Points labeled 1,2,3,4,5,6, α , w in the phase space and images of the pieces of boundaries $\alpha-1$ and $6-w$.

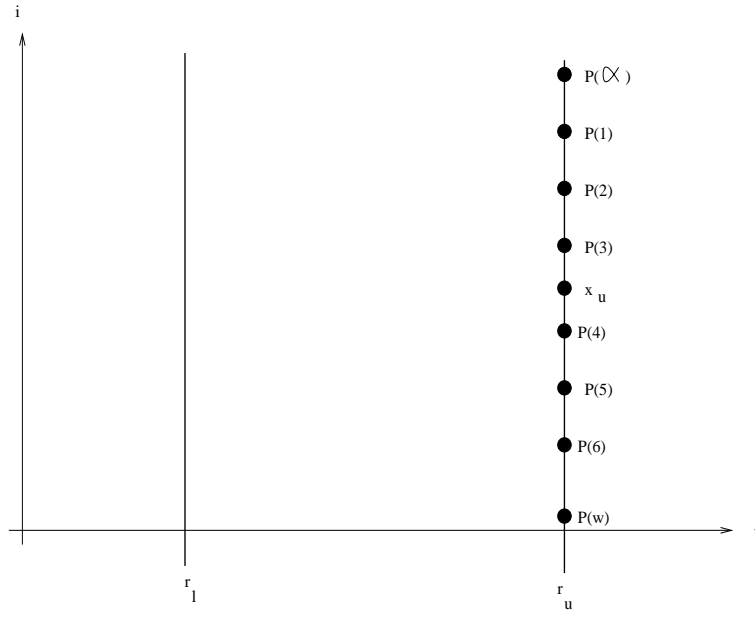


Figure 4.34: Images of the points labeled 1,2,3,4,5,6, α , w , X in the phase space.

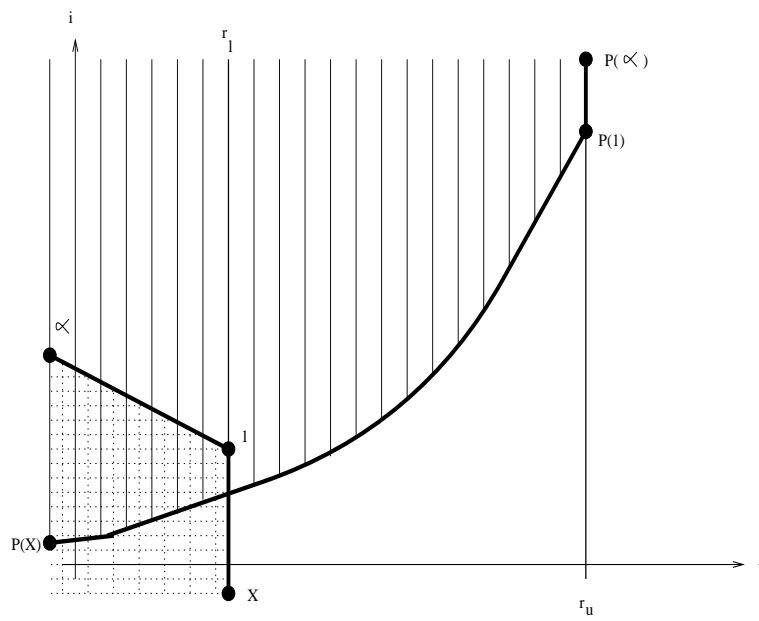
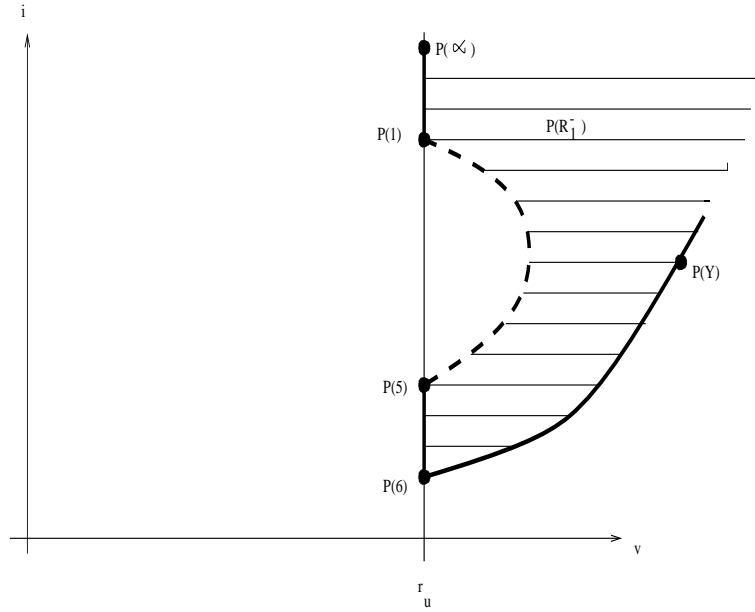


Figure 4.35: Region R_0^- and its image by the Poincaré map. Dotted region: R_0^- ; region with lines: $P(R_0^-)$.

Figure 4.36: Image of the region R_1^- .

cannot intersect r_u (otherwise there would be another piece of spiral in R_1^-), the region $P(R_1^-)$ must be like that in Fig. 4.36. With similar arguments, it can be deduced that the qualitative picture for the regions of zero and one crossing, and their respective images is that in Fig. 4.37.

Note:

$P(r_u)$ is not spiraling (at least, between r_l and r_u)

Proof:

Observe first that the line r_u is entirely contained inside the region $R_0^+ \cup R_1^+$. Then $P(r_u) \subseteq P(R_0^+) \cup P(R_1^+)$, and thus the images of the points of r_u can only have zero or one crossing in the ramp. Taking initial conditions on the line r_u means fixing $v = v_u$ and varying the current i from $-\infty$ to ∞ . Then there exist i_1, i_2, i_3, i_4 , such that

$$P(v_u, i_1) = (v_u, i_3) \quad \text{and} \quad P(v_u, i_2) = (v_l, i_4) \quad \text{with} \quad i_1 > i_2, \quad i_4 > i_3$$

(see Fig. 4.38)

The values for these currents can be easily obtained because the number of crossings in the ramp of their respective trajectories is zero or one. For example, if $V_{in} = 34.33998523V$, the equations are put into the MAPLE solver and the results are

$$i_1 = 0.69059201A \quad i_2 = 0.40050334A \quad i_3 = 0.44153429A \quad i_4 = 0.67723511A.$$

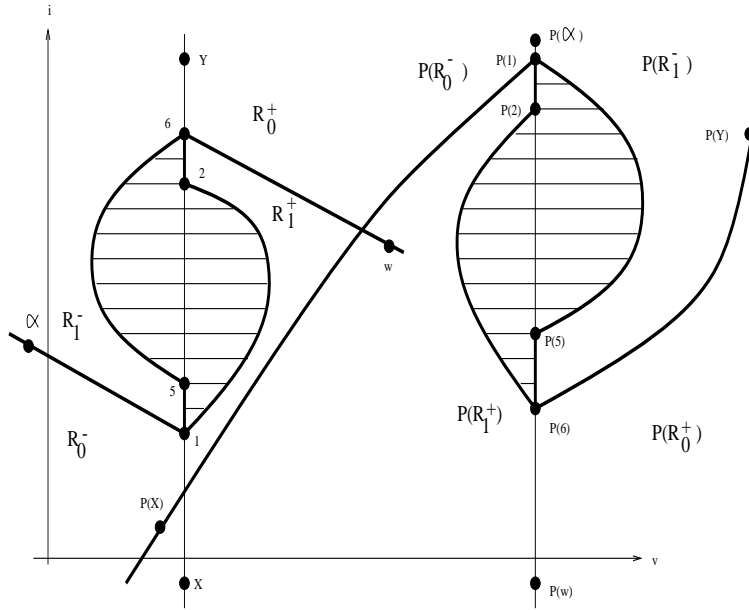


Figure 4.37: Qualitative picture of regions R_0^- , R_1^- , R_0^+ , R_1^+ , $P(R_0^-)$, $P(R_1^-)$, $P(R_0^+)$ and $P(R_1^+)$. The zones with lines correspond to $\bigcup_{i \geq 2} R_i$ and $P(\bigcup_{i \geq 2} R_i)$.

4.5.2 A Horseshoe Mechanism

In the previous subsection it was proved that $P(r_l) = s_u$ and $P(s_l) = r_u$, so that the Poincaré map P transforms a certain line into a *double* spiral focused at one point in the phase space, and also transforms a certain *double* spiral focused at a certain point into a line. This is symptomatic of a folding action in the phase space, as was also numerically observed in Section 4.3 of this chapter. This can result in a horseshoe mechanism embedded in the Poincaré map.

This folding mechanism can be analytically deduced with the continuity arguments that were employed in the last subsection. Specifically, if a rectangular region R containing the point x_l is chosen in the phase space like that in Fig. 4.39, following the same arguments that were applied before (basically $P(r_l) = s_u$ and $P(s_l) = r_u$), it can be deduced that the image $P(R)$ is folded many times around the point x_u . The number of foldings around x_u depends very clearly on the number of pieces of regions that R contains, which is directly related to the thickness of R .

P contains an expanding-stretching-folding action, clearly seen in Fig. 4.40, which is drawn analytically, following the same arguments as before. From this figure, it can be deduced that the image of a region M totally included in only one region R_n^\pm will be deformed, but it will not spiral around x_u . However, when P is applied to a region M which has no empty intersection with at least

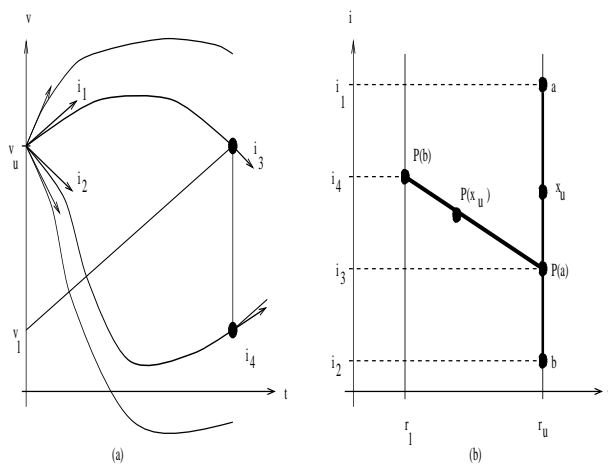


Figure 4.38: (a) Scheme of the trajectories with initial conditions on r_u ; (b) A piece of $P(r_u)$.

four consecutive regions, then at least one turn around x_u exists.

It has been proved that near the region of multiple crossings, i.e. near x_l , P has embedded a stretching-folding mechanism, which maps a region R near x_l to a region $P(R)$ near x_u . Moreover, for a certain value V_{in}^0 , a $5T$ -periodic orbit with $P^4(x_u) = x_l$ has been found. So for this value, a rectangular region R near x_l like that in Fig. 4.39 is first transformed by P in a spiral-like region $P(R)$ near x_u which includes the point x_u . Then the successive mappings $P^2(R), P^3(R), P^4(R)$ do not change qualitatively the shape of the region, because as was pointed out in a previous section, no more than two crossings in the ramp are met in each cycle. So, $P^4(R)$ has the same spiral-like shape as $P(R)$. Finally, when P is applied once more on $P^4(R)$, as $P^4(x_u) = x_l$, this region turns back near x_l . Summarizing, a rectangular region near x_l is mapped by P^5 to a spiral-like region centered also at x_l . Then a horseshoe mechanism must be found near x_l for the map P^5 when the parameter V_{in} is in a certain range including V_{in}^0 .

4.5.3 A Numerically Found Horseshoe

Although rectangular regions can be found near x_l which are mapped by P^5 into spiral-like regions centered at x_l , this is not enough to conclude the existence of an invariant set with horseshoe dynamics. The regions R and $P^5(R)$ must intersect in a certain way for the existence of an invariant set to be proved. In order to see this, two consecutive regions R_k^-, R_{k+1}^- , $k > 1$ are first chosen. Then by the same continuity arguments that were applied throughout this chapter, the image $P(R_k^- \cup R_{k+1}^-)$ turns one time around x_u in the way shown in Fig. 4.41 (this is also valid for R_k^+ and R_{k+1}^+).

Then, after 5 iterations of P , and for some values of k which will be nu-

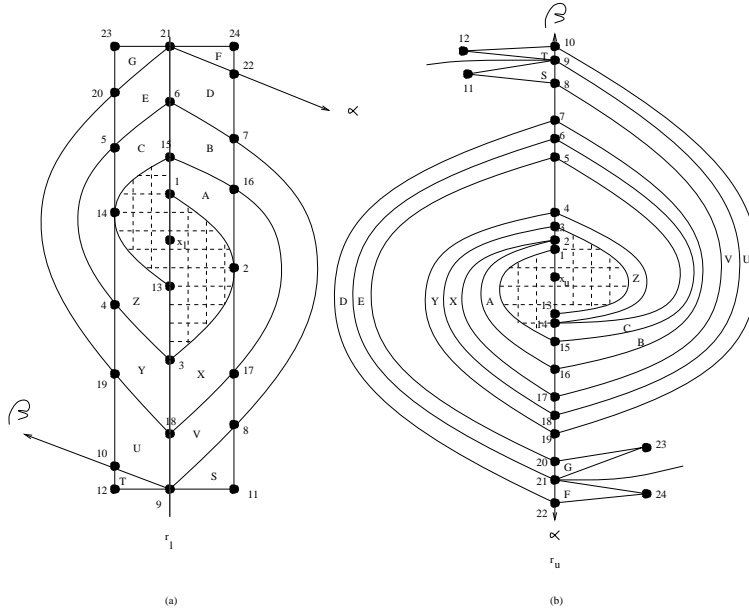


Figure 4.39: (a) Scheme of the rectangular region R with edges labeled 11-12-23-24; (b) $P(R)$. The dotted region is mapped to the dotted region, while the rectangular region is mapped to the spiraling region.

merically computed, the intersection shown in Fig. 4.42 is obtained, and the existence of an invariant set with horseshoe dynamics is concluded. It is worth noting that due to the very high stretching in the phase space when P^5 is applied, the intersections of the numerically computed regions are hard to see, and thus only some schemes have been presented in the figures.

In order to numerically obtain the regions R_k^\pm and their images, the following steps are carried out:

1) Compute the points on r_l which divide the regions. This has been done with precision parametrising the line r_l , computing $P(r_l)$ and saving the number of crossings in the ramp. These points are denoted (v_l, l_k) when the current component of $P(v_l, l_k)$ is smaller than i_u , and they are denoted (v_l, l_k^*) when the current component is larger than i_u . This is equivalent to the ordering imposed by the successive intersections of the line r_l with the double spiral s_l , when the latter is monotonically followed (see Fig. 4.43). x_l is also denoted $(v_l, l_\infty) = (v_l, l_\infty^*)$.

2) Compute the points on r_u which divide the regions. They are obtained simply as $(v_u, u_k) = P(v_l, l_k)$ and $(v_u, u_k^*) = P(v_l, l_k^*)$. Once these points are obtained, the boundaries of the regions R_n can be easily obtained computing P^{-1} applied to the piece of r_u which is limited by the points with currents u_k, u_{k+1} or u_k^*, u_{k+1}^* . It is worth noting that P^{-1} is also available in closed form, except for the times where the ramp is crossed, as happens with P .

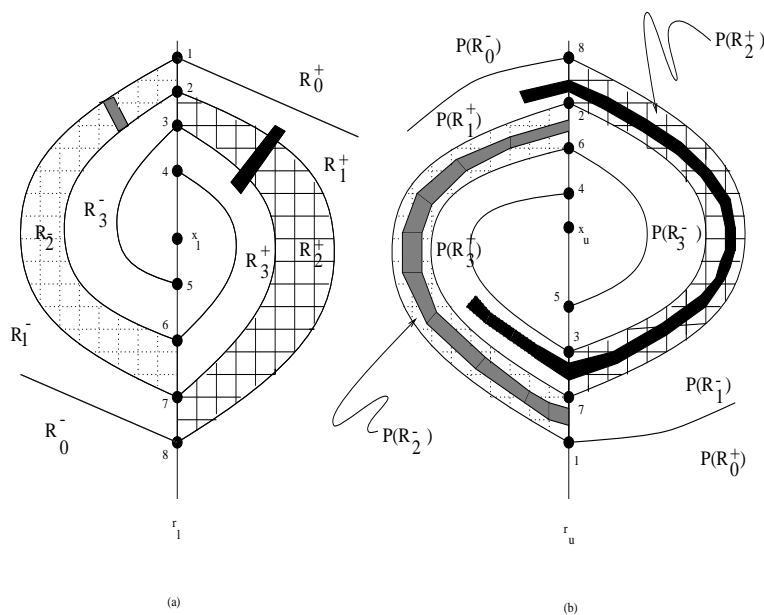


Figure 4.40: Some regions in the phase space and their respective images. The expanding-stretching in opposite directions and the folding mechanism is clearly seen. (a) Initial regions; (b) Respective images.

The values for l_k, l_k^*, u_k and u_k^* for $V_{in} = 34.33998523V$ (value for which there exists a $5T$ -periodic orbit passing through x_l) were computed with MATHEMATICA for $k = 0$ to $k = 14$ and are shown in Table 4.1.

Graphically inspecting the regions and their images, it turns out that $R_{13}^+ \cup R_{14}^+$ intersects $P^5(R_{13}^+ \cup R_{14}^+)$ in the way qualitatively shown in Fig. 4.42. To find this intersection, P^5 is applied to the piece of r_l with currents in the intervals $I_1 = [0.607092, 0.608797]A$ and $I_2 = [0.581308, 0.583372]A$, which are the *vertical* boundaries of $R_{13}^+ \cup R_{14}^+$. The *horizontal* boundaries of $R_{13}^+ \cup R_{14}^+$ are computed as the inverse image of the pieces of r_u with currents in the intervals $I_3 = [0.6068, 0.6081]A$ and $I_4 = [0.6086, 0.6095]A$. Finally, to find the last two boundaries of $P^5(R_{13}^+ \cup R_{14}^+)$, P^4 is applied to the points in r_u , $\{(v_u, i) : i \in I_3 \cup I_4\}$. Then, the intersections obtained are as in Fig. 4.44.

4.6 Summary

In this chapter, the Poincaré map P induced by the flow has been studied and a horseshoe mechanism has been found in the phase space near the point x_l . This means that an invariant set with sensitive dependence to initial conditions exists in a certain range of the bifurcation parameter. In this case, P is an invertible two-dimensional map, which is continuous but only piecewise smooth

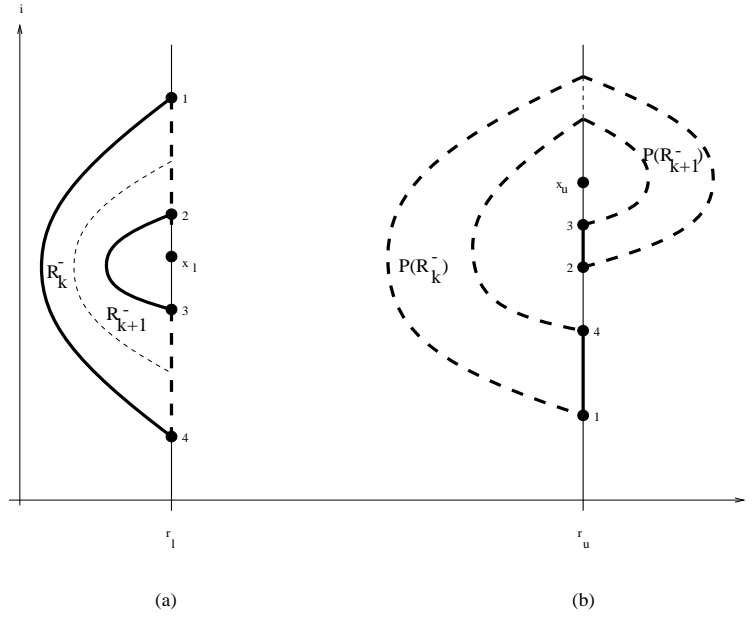


Figure 4.41: Image of a region in the phase space.
 (a) $R_k^- \cup R_{k+1}^-$; (b) $P(R_k^- \cup R_{k+1}^-)$. Heavy lines are mapped to heavy lines, and dashed lines to dashed lines.

Table 4.1: Values of the currents dividing the regions and their images.

k	l_k	l_k^*	u_k	u_k^*
0	0.737173	0.367108	0.4937	0.8190
1	0.508041	0.681535	0.5421	0.6954
2	0.649282	0.533084	0.5721	0.6747
3	0.552242	0.638785	0.5812	0.6576
4	0.628766	0.559454	0.5904	0.6516
5	0.566844	0.624449	0.5941	0.6450
6	0.619638	0.570191	0.5984	0.6421
7	0.574059	0.617322	0.6004	0.6386
8	0.614445	0.575999	0.6031	0.6369
9	0.578429	0.613007	0.6043	0.6348
10	0.611148	0.579699	0.6059	0.6337
11	0.581308	0.610130	0.6068	0.6323
12	0.608797	0.582195	0.6081	0.6315
13	0.583372	0.608067	0.6086	0.6305
14	0.607092	0.584028	0.6095	0.6299

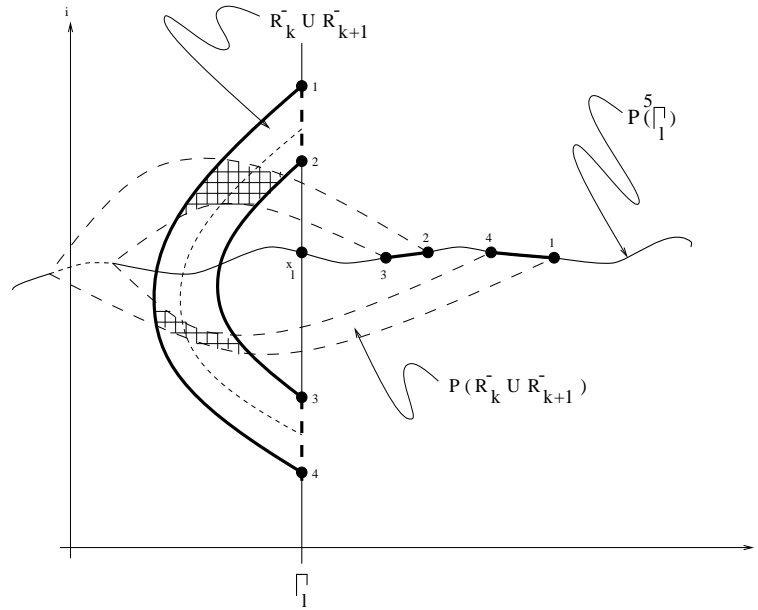


Figure 4.42: Image by P^5 of a region in the phase space. Heavy lines are mapped to heavy lines, and dashed lines to dashed lines.

and nonlinear, with a *singular* point x_l (it is the focus of a double spiral curve, which is a curve of non-smooth points dividing regions of smooth points for P).

Once the Poincaré stroboscopic map has been precisely defined, the dynamics of the system can be simplified to the dynamics of this stroboscopic global Poincaré map. It can be said beforehand that this class of maps have not been studied deeply in the scientific community. The literature mainly concerns diffeomorphisms. Related works, including border-collision bifurcations arising in non-smooth systems with a low number of regions of smoothness, can be found in [Nusse and Yorke, 1992; Nusse, Ott and Yorke, 1994]. There, a border-collision bifurcation, i.e. when a periodic point crosses the curve of non-smoothness, is introduced, and examples are shown where period- p to period- q , p -piece attractor to q -piece attractor and chaotic saddle to chaotic saddle bifurcations are found. Also, the Jacobian matrix is shown to change discontinuously at border-crossing fixed points. The case of piecewise-linearity and the case of square-root singularity in the derivative with an infinite cascade of reverse period-adding bifurcations are also studied.

Published works dealing with non-smooth maps are mainly reduced to special cases such as one-dimensional piecewise smooth maps, two-dimensional piecewise linear maps and two-dimensional non-invertible maps [Mira, 1980; Mira, 1987; Mira and Narayaminsamy, 1993; Mira, Fournier-Prunaret, Gardini, Kawakami and Cathala, 1993; Mira and Rauzy, 1995; Barugola, Cathala and Mira, 1995; Maistrenko, Maistrenko and Chua, 1993; Maistrenko, Maistrenko

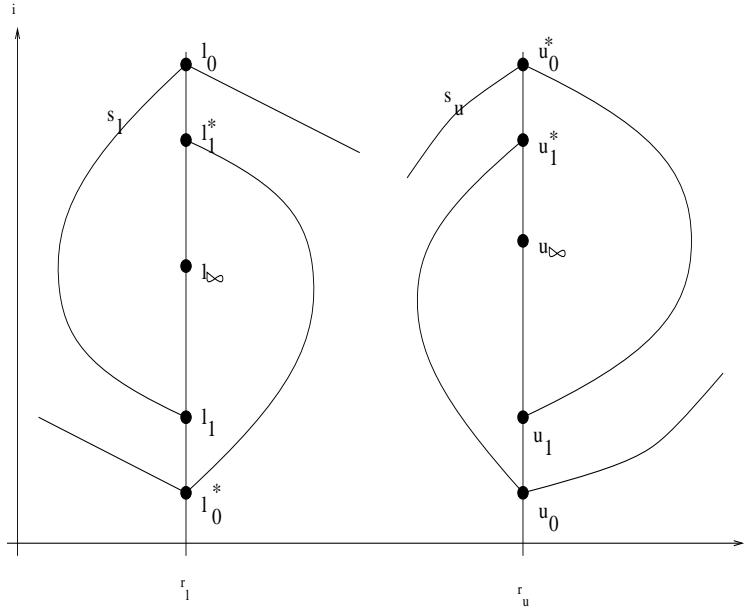


Figure 4.43: Points $(v_l, l_k), (v_l, l_k^*), (v_u, u_k)$ and (v_u, u_k^*) .

and Sushko, 1994; Maistrenko, Maistrenko, Vikul and Chua, 1995].

The considered Poincaré map with a double spiral curve of non-smoothness and an accumulation point is not classified in any of the above classes, so different types of behavior and bifurcations can be expected. We anticipate that, in the map which is studied, non-standard types of bifurcations and border-collision bifurcations will be obtained when P is considered as a one-parameter family of maps, taking V_{in} as the bifurcation parameter. Some of the bifurcations that will be shown in the next chapter are

i) *Singularity bifurcation:*

A stable fixed point turns into a stable fixed point, plus two 3T-subharmonic unstable orbits and a non-attracting invariant set.

ii) *Instant chaos bifurcation:*

Sudden existence of an attracting chaotic invariant set which is initially reduced to a stable orbit.

iii) *Saddle-saddle bifurcation:*

Sudden existence of two 3T-subharmonic unstable orbits.

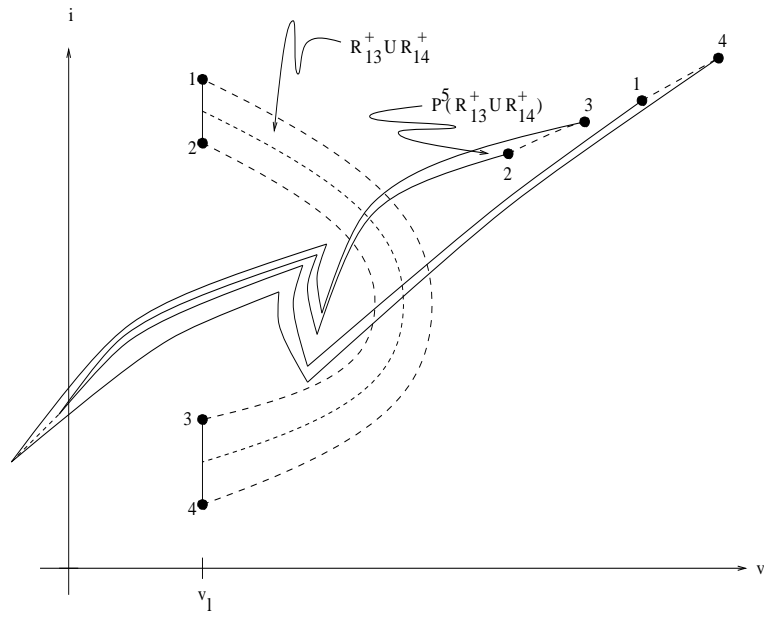


Figure 4.44: $R_{13}^+ \cup R_{14}^+$ and $P(R_{13}^+ \cup R_{14}^+)$, showing an intersection which leads to an invariant set with horseshoe dynamics.

Chapter 5

Secondary Bifurcations and Chaotic Attractors

Abstract

In the first section of the previous chapter, period-doubling route to chaos in the DC/DC buck converter was shown to occur. Also, in the work of Deane and Hamill, it was checked experimentally. A chaotic attractor is then found at the end of the sequence, suddenly followed by an increase of its size. In this chapter, new secondary bifurcations and high periodic phenomena coexisting with the main sequence are detected and analysed over the same range of parameters. Local and global analyses are made by means of different computational tools to obtain impact and stroboscopic maps, unstable orbits, bifurcation diagrams, invariant manifolds of direct and inverse saddles and basins of attraction. These tools are put together to reveal the dynamical richness of this non-smooth system. The topological mechanisms which entail onset and disappearance of various attractors, and the main and secondary evolutions to chaos are identified. Special attention is devoted to the analysis of non-smooth bifurcations and sudden bifurcational events characterizing the global dynamics, associated with the topological behaviour of the invariant manifolds of several direct, inverse and grazing saddles.

5.1 Introduction

Basic features of nonlinear dynamics in dc-dc converters have been reported in [Deane and Hamill, 1990a; Deane, 1992; Tse, 1994a; Zafrany and Ben-Yacov, 1995; Chakrabarty, Poddar and Banerjee, 1996; Fossas and Olivar, 1996; di Bernardo, Garofalo, Glielmo and Vasca, 1997]. In the previous chapter, a period-doubling route to chaos was discovered, followed by a sudden increase in

the size of the attractor. This was also checked experimentally in the pioneering work [Deane and Hamill, 1990a], showing an extraordinary agreement with numerical simulations. Some of these phenomena were justified analytically in [di Bernardo, Garofalo, Glielmo and Vasca, 1997], where a new kind of mapping for this closed loop converter, the impact map, was introduced. Recently, some other attractors coexisting with the main bifurcation branch have also been outlined [Banerjee, 1997; di Bernardo, Fossas, Olivar and Vasca, 1997].

In this chapter, secondary bifurcations of the main branch attractor are studied and some branches of unstable orbits are continued. Namely, secondary saddle-node bifurcations are investigated, at which branches of stable 6T-periodic and 12T-periodic orbits are created; their independent period-doubling bifurcations and sudden changes in the size of the resulting chaotic attractors are discussed. Moreover, three-piece chaotic attractors and a large five-zones chaotic attractor are studied, and their structure justified as organised by corresponding unstable orbits. Features of smooth systems such as period-doubling, merging bands of chaos, and interior crises are reported for the main attractor; boundary crises, periodic windows and metamorphoses of the basins of attraction are also shown for secondary evolutions. A continuation of 3T-periodic unstable branches reports an adding-orbit process, probably ending in a chaotic saddle. On the way, grazing (or border-collision) bifurcations are found [Nusse and Yorke, 1992; Nusse, Ott and Yorke, 1994].

The numerical computations are performed with a variety of available tools, and, when necessary, specific C code has been prepared. Specific code in C has been developed to carefully compute orbits, stroboscopic maps, invariant manifolds and basins of attraction. Although the data finally supports numerical methods, very much advantage is taken of the algorithms since the solutions are piecewise analytically known. Only the bifurcation diagrams which were drawn with INSITE to check some results use a standard numerical integrator which does not take advantage of the analytical solutions. In this case, numerical precision is improved to obtain high quality data.

A method is deduced to compute the characteristic multipliers of periodic orbits. Analytical expressions for the multipliers are obtained, where only a final easy numerical step is needed. This method can be applied to find period-doubling and saddle-node smooth bifurcations as well as the jump discontinuity in border-collision non-smooth bifurcations.

A new kind of discrete-time mapping, the impact map, is introduced. Then, the bifurcation diagram of the system is reported as the input voltage varies. The remaining sections present the analysis of the nonlinear phenomena appearing in the bifurcation diagram as the input voltage is increased, by means of the invariant manifolds and basins of attraction.

Definitions:

In what follows, we give some definitions, which are used in the rest of the chapter. Looking at the converter scheme, we say that the system is in the OFF (ON) phase when the capacitor voltage is larger (smaller) than the ramp signal.

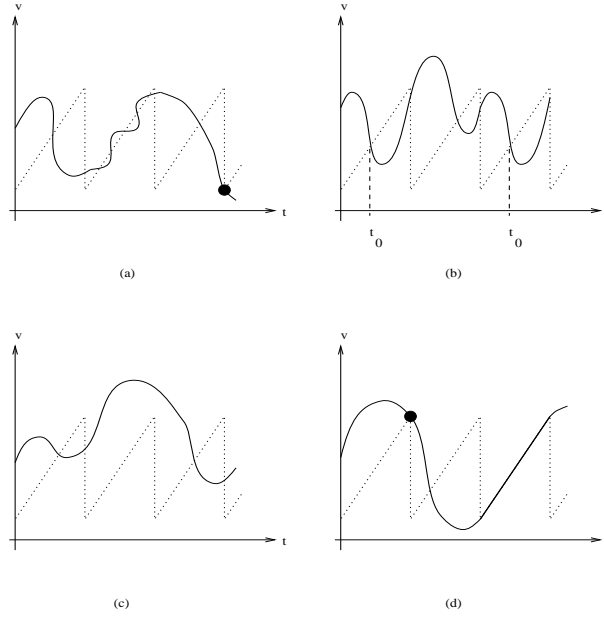


Figure 5.1: Possible behaviors: (a) multiple impacts and grazing, (b) $P(2,2)$ orbit, (c) skipping phenomenon, (d) grazing and sliding.

Consequently, a *switching* occurs whenever the following condition is satisfied:

$$v(t) = \gamma + \eta(t \bmod T). \quad (5.1)$$

Among the switchings, we will define *impact* as a switching taking place within a cycle of the ramp, and *T -switching* the one occurring at multiples nT of the ramp period T . During standard operating conditions, the system evolves along a $1T$ -periodic one-impact per cycle orbit, i.e. one impact and one T -switching occurring during each cycle of the ramp. In addition to this, we recall that the following situations found in previous chapters are possible (see Fig. 5.1):

- more than one impact occurs during the same cycle of the modulating ramp (*multiple impacts*);
- the system evolves along a generic nT -periodic orbit, characterized by m impacts per nT -period ($P(m,n)$ orbit);
- the voltage misses one or more T -switchings (*skipping* phenomenon);
- an infinite number of impacts occur within the same cycle of the ramp (*sliding*);
- the voltage touches the bottom or the top of the ramp at time instants multiples of T (*grazing*).

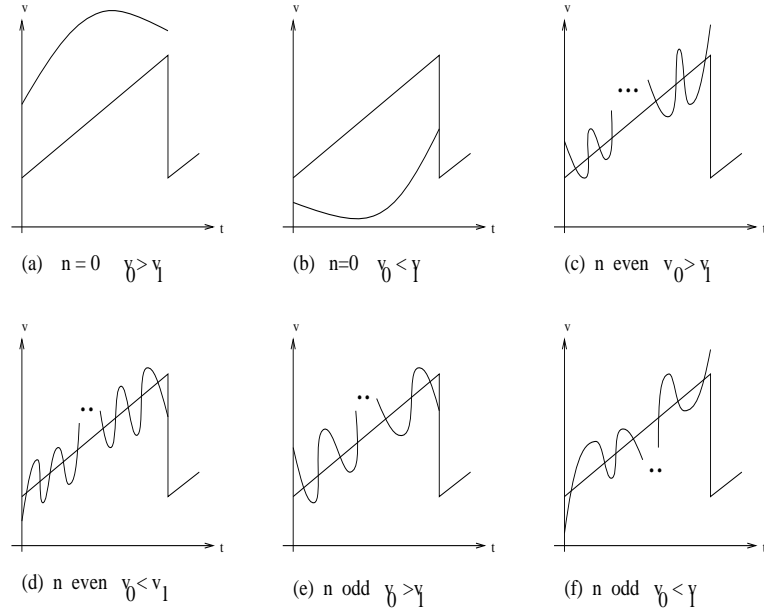


Figure 5.2: The six different possibilities for the stroboscopic map, depending on the parity (n even or n odd) of the number of crossings in the ramp and the initial voltage ($v_0 < v_l$ or $v_0 > v_l$).

Notice that, as reported in the previous chapter, a sliding occurs when the voltage derivative is equal to that of the ramp signal at a T -switching (*infinite local stretching* condition).

5.1.1 The Stroboscopic Map

The stroboscopic map P , closely studied in the previous chapter, was obtained by considering the current and voltage at every T -switching [Kassakian, Schlecht and Verghese, 1991]. To compare it with the impact map now, we recall its definition

$$(v_n, i_n) \mapsto (v_{n+1}, i_{n+1}). \quad (5.2)$$

where $v_n = v(nT)$ and $i_n = i(nT)$.

It is relevant to point out that the structure of the stroboscopic map changes according to the number of impacts between one switching and the next. Thus, the analytical form of the mapping can be derived once the system evolution between the two T -switchings has been specified. The expressions for the six possibilities, depending on the parity of the number of crossings in the ramp and the initial value for the voltage, are the following (see also Fig. 5.2):

$$n = 0, v_0 > v_l : \quad P(X_0) = N(1)X_0$$

$$n = 0, v_0 < v_l : \quad P(X_0) = N(1)X_0 + V_{in}[I - N(1)]b$$

$$n \text{ even}, v_0 > v_l : \quad P(X_0) = N(1)X_0 + V_{in}\left[\sum_{j=1}^n (-1)^j N(1 - \alpha_j)\right]b$$

$$n \text{ even}, v_0 < v_l : \quad P(X_0) = N(1)X_0 + V_{in}\left[I - \sum_{j=1}^n (-1)^j N(1 - \alpha_j) - N(1)\right]b$$

$$n \text{ odd}, v_0 > v_l : \quad P(X_0) = N(1)X_0 + V_{in}\left[I + \sum_{j=1}^n (-1)^j N(1 - \alpha_j)\right]b$$

$$n \text{ odd}, v_0 < v_l : \quad P(X_0) = N(1)X_0 + V_{in}\left[-\sum_{j=1}^n (-1)^j N(1 - \alpha_j) - N(1)\right]b$$

where $\{\alpha_j\}_{j=1,\dots,n}$ are the normalized switching instants.

Then, construction of the map requires the solution of the following conditions with respect to the normalized impact instants $\{\alpha_j\}_{j=1,\dots,n}$:

$$v(\alpha_j) = \gamma + \eta T \alpha_j \quad j = 1, \dots, n \quad (5.3)$$

Therefore, though possible, it is hard to derive a closed form for the stroboscopic map to obtain analytically the jacobian, and perform the investigation of the stability of the system orbits via its eigenvalues. An alternative mapping, the impact map, can be used [di Bernardo, Garofalo, Glielmo and Vasca, 1997].

5.1.2 The Impact Map

The impact map is defined as the mapping from a normalized impact instant $\alpha_m = (t_m \bmod T)/T$ and the corresponding current i_m to the next pair:

$$(\alpha_m, i_m) \mapsto (\alpha_{m+1}, i_{m+1}). \quad (5.4)$$

As for the stroboscopic map, the structure of the impact map changes according to the specific system evolution. In this case, however, only three different impact to impact elementary behaviours can be outlined, as represented in Fig. 5.3. Then, the analytical form of the impact map can be obtained for any orbit of the converter by appropriately combining the three elementary sub-mappings. Moreover, the availability of the analytical expression of the map allows one to compute the jacobian and then the stability of any orbit, as in the stroboscopic map.

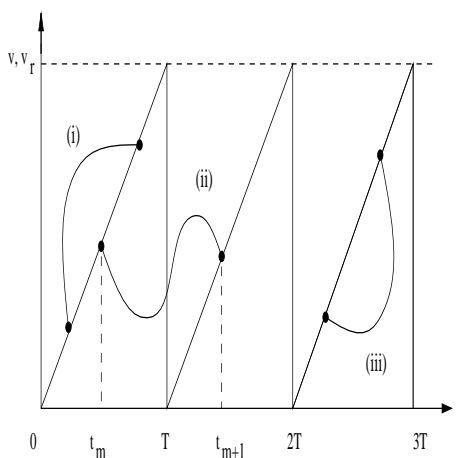


Figure 5.3: Different typical behaviors of the control voltage between two impacts: (a) OFF-OFF, (b) ON-OFF, (c) ON-ON.

5.2 The Buck Converter Bifurcation Diagram

As presented in previous chapters, the voltage controlled DC/DC buck converter exhibits several bifurcations and chaos when the input voltage is varied. Bifurcations apply usually to fixed or mT -periodic points x_0 (which is then a fixed point of the m th iteration of the map), but they also attain to more complex sets like chaotic attractors and saddles. The type of fixed point x_0 is determined through calculation of the eigenvalues of the jacobian $DP(x_0)$. It can be either stable (sink, S), or unstable (saddle) depending on whether both eigenvalues, or only one of them, stay inside the unit circle in the complex plane. By varying the bifurcation parameter V_{in} , directly (D-saddle cycle) or inversely (I-saddle cycle) unstable periodic solutions are established through saddle-node (SN) or period-doubling (PD) smooth bifurcations, respectively, when an eigenvalue of DP becomes larger than 1 or smaller than -1. Also, non-smooth bifurcations of grazing (or border-collision) type (GR) can be obtained which correspond to a jump in the eigenvalues. The notations S_j^m , D_j^m and I_j^m will be used to denote mT -periodic sinks, direct saddles and inverse saddles, respectively, the subscript $j = 1, 2, \dots, m$ referring to different image points of the periodic solution. Chaotic attractors made of a finite number m of disconnected pieces are obtained in several situations. They are denoted as C_j^m attractors, the subscript $j = 1, 2, \dots, m$ referring to the different pieces contained in subdomains of the whole basin.

Figure 5.4 represents the bifurcation diagram for the following converter parameters: $R = 22.00\Omega$, $L = 20.00mH$, $C = 47.00\mu F$, $\gamma = 11.75$, $\eta = 1309.52$, $T = 400.0\mu s$, as in the previous chapter.

The main $P(1, 1)$ branch bifurcates into a $P(2, 2)$ orbit at $V_{in} = 24.516V$ as experimentally and numerically observed in [Deane and Hamill, 1990a]. Suc-

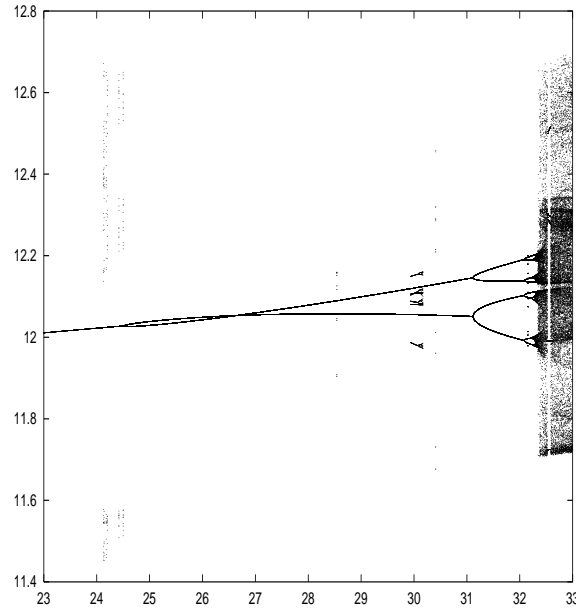


Figure 5.4: Buck bifurcation diagram in the range (23, 33)V. Several secondary bifurcations and attractors are outlined.

cessive period-doublings can be found at $V_{in} = 31.121V$, $V_{in} = 32.095V$, $V_{in} = 32.239V$, $V_{in} = 32.270V$, $V_{in} = 32.277V$ and $V_{in} = 32.278V$. Once chaos is established in the system, merging bands begin to occur at $V_{in} = 32.279V$ approximately. Then, while a four-bands chaos is present, there is a sudden enlargement of the attractor at $V_{in} = 32.336V$.

It is also worth noticing what happens at

$$V_{in} = V_{ref} + \frac{V_L}{a} = 11.75238095V.$$

which corresponds to the lower voltage of the ramp. As the bifurcation parameter passes through this value, a stable equilibrium point in the phase space turns into a stable 1T-periodic orbit. If the trajectories are inspected in the three-dimensional cylindrical space $\mathbb{R}^2 \times \mathbb{S}^1$, the 1T-periodic orbit exists even before the bifurcation value, but its projection in the phase space is seen as an equilibrium point because the trajectory in $\mathbb{R}^2 \times \mathbb{S}^1$ is simply a circumference contained in a horizontal surface below the ramp surface. At the bifurcation, the 1T-periodic orbit begins to torsion due to the impact with the ramp surface, and then its projection in the phase space is seen as a 1T-periodic orbit instead of an equilibrium point (see Fig. 5.5).

Apart from the initial period-doubling route to chaos, other secondary phenomena are also present in the bifurcation diagram. Three-piece chaos in the interval [24.16, 25.01], period-doubling route to chaos starting on 6T-periodic

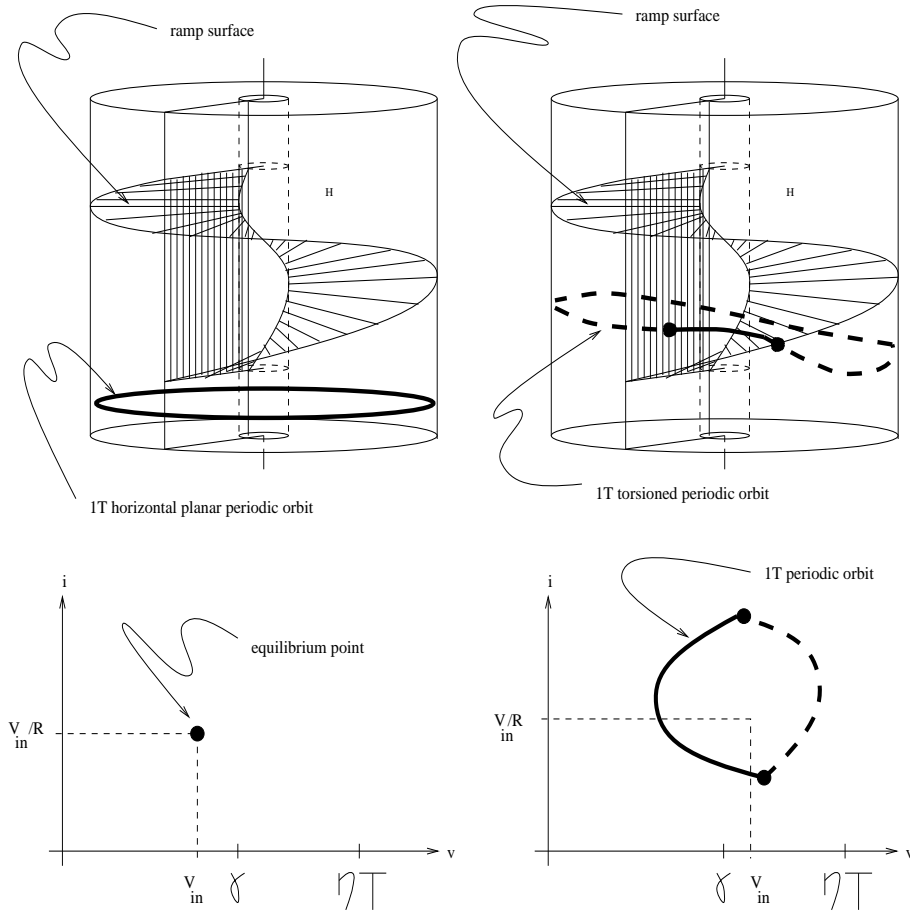


Figure 5.5: Non-standard bifurcation for $V_{in} = 11.752381V$.

and 12T-periodic orbits and a 5T-periodic window are clearly seen in Fig. 5.4. Moreover, other secondary phenomena not appearing in the bifurcation diagram were detected, such as a non-smooth route to chaos starting on a 3T-periodic orbit.

5.2.1 Analytically Computing the First Period-doubling

Flip and saddle-node bifurcations can be analytically predicted via the impact map [di Bernardo, Garofalo, Glielmo and Vasca, 1997] or using the stroboscopic map. For example, the first period-doubling bifurcation can be found as follows:

Let $x_0 = (v_0, i_0)$ be the initial conditions for a fixed point by the stroboscopic map P . The eigenvalues of $DP(x_0)$, or characteristic multipliers, λ_1, λ_2 must

be the roots of the equation

$$x^2 - tr(DP(x_0))x + det(DP(x_0)) = 0 \quad (5.5)$$

where tr and det stands for the trace and the determinant respectively. In a period-doubling bifurcation, one of the characteristic multipliers passes through -1 , and thus, $DP(x_0)$ must satisfy

$$1 + tr(DP(x_0)) + det(DP(x_0)) = 0. \quad (5.6)$$

The equations for an orbit with a switching at a normalised time α_1 in the first cycle are

$$\begin{aligned} x_1 &= N(\alpha_1)x_0 \\ x_T &= V_{in}[I - N(1 - \alpha_1)]b + N(1)x_0 \end{aligned} \quad (5.7)$$

with $x_1 = (v_1, i_1)$ is the point in the phase space which corresponds to the switching. To get a $P(1, 1)$ periodic orbit, $x_T = x_0$ must be imposed, and so the following expression for x_0 is obtained

$$x_0 = V_{in}[I - N(1)]^{-1}[I - N(1 - \alpha_1)]b \quad (5.8)$$

together with the switching condition

$$a(v_1 - V_{ref}) = V_L + \alpha_1(V_U - V_L). \quad (5.9)$$

Now, differentiation respect to x_0 of equation

$$P(x_0) = N(1)x_0 + V_{in}[I - N(1 - \alpha_1)]b \quad (5.10)$$

which gives the image of x_0 by the stroboscopic map yields

$$DP(x_0) = N(1) + V_{in}[N'(1 - \alpha_1)]b \frac{d\alpha_1}{dx_0}. \quad (5.11)$$

Also, differentiation of equation (5.7) respect to x_0 yields

$$\frac{dx_1}{dx_0} = N(\alpha_1) + N'(\alpha_1)x_0 \frac{d\alpha_1}{dx_0}. \quad (5.12)$$

Finally, differentiation of equation (5.9) yields

$$a \frac{dv_1}{dx_0} = (V_U - V_L) \frac{d\alpha_1}{dx_0} \Rightarrow \frac{d\alpha_1}{dx_0} = \frac{a}{V_U - V_L} \frac{dv_1}{dx_0}. \quad (5.13)$$

Thus,

$$\frac{dx_1}{dx_0} = N(\alpha_1) + N'(\alpha_1)x_0 \frac{a}{V_U - V_L} \frac{dv_1}{dx_0}. \quad (5.14)$$

and this equation gives

$$\frac{dv_1}{dv_0} \quad \text{and} \quad \frac{dv_1}{di_0}$$

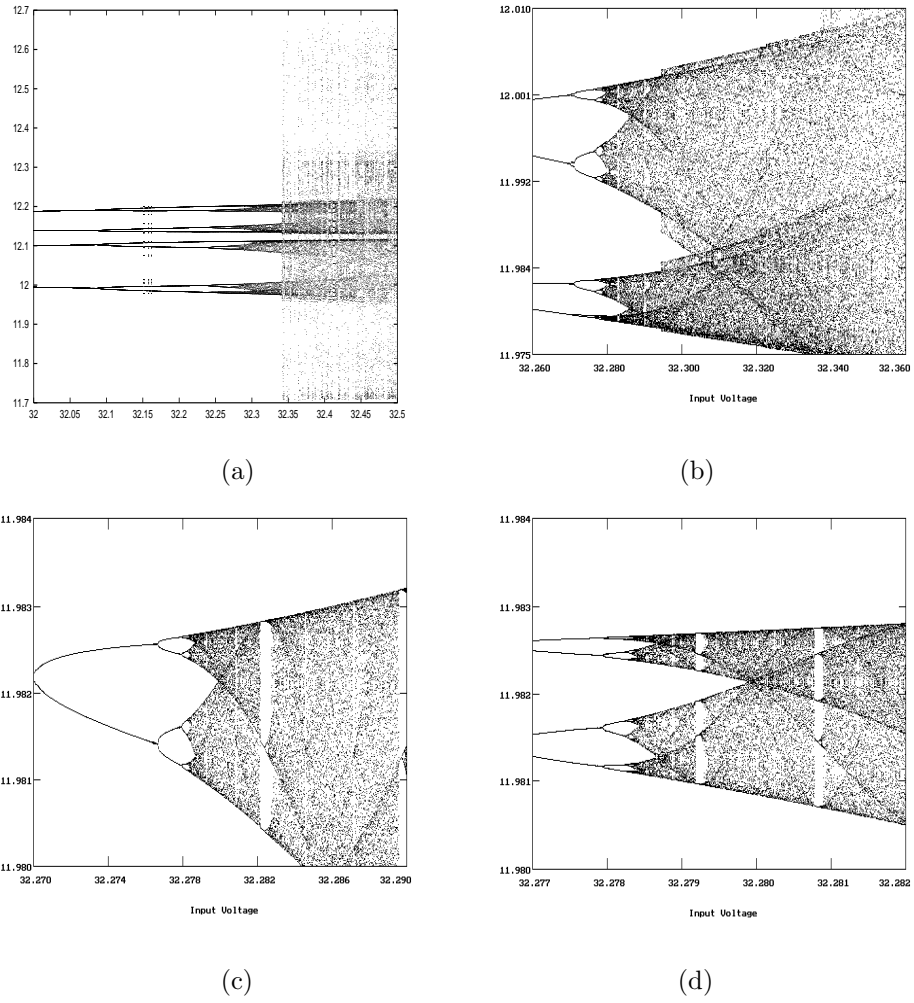


Figure 5.6: Successive enlargements of the main branch of the buck bifurcation diagram.

as functions of α_1, v_0, i_0 . Using also (5.13), this can be put into equation (5.11), and an expression for $DP(x_0)$ is obtained, which depends on $V_{in}, \alpha_1, v_0, i_0$. Then, imposing the condition for period-doubling (5.6), the condition for the switching (5.9) and the condition for periodicity (5.8), one obtains a system of four nonlinear equations in the unknowns V_{in}, α, v_0, i_0 , which can be solved with MAPLE. The result is

$$V_{in} = 24.516573V \quad \alpha_1 = 0.50950957 \quad v_0 = 12.027709V \quad i_0 = 0.60808429A$$

which is in perfect accordance with the numerical simulations in the previous chapter.

After this first period-doubling, a period-doubling cascade then follows, ending in a narrow four-piece chaotic attractor. Such evolution occurs via successive interior crises of merging type; in the sequel, they will be referred to as interior crises of first kind (IC1). At each of them, due to the collision with an inverse saddle I_j^n , the $2n$ pieces of a chaotic attractor merge two by two giving rise to a n -piece chaotic attractor. The mergings corresponding to successive halvings can be detected in Fig. 5.6. It is worth commenting briefly on the geometrical mechanism which produces this interior crisis (IC1) by examining the evolution of the invariant manifolds of the I_j^n saddle. The $2n$ -piece chaotic attractor contains all the inverse saddles of higher order $I_j^{2n}, I_j^{4n}, I_j^{8n}, \dots$, corresponding to periodic solutions becoming progressively unstable in the period-doubling cascade. It is also contained within the closure of the unstable manifold of the saddle I_j^n belonging to the period-doubling cascade. At the bifurcation parameter values for which the stable and unstable manifolds of I_j^n do not touch, the attractor is made of $2n$ disconnected pieces belonging to the subdomains separated by the n stable manifolds of I_j^n . Just after their first homoclinic tangency, a tangle develops, and an infinite number of progressively longer and thinner fingers accumulate onto the stable manifold of I_j^n in each subdomain from the companion one, giving rise to strong fractal basin boundary between couples of subdomains. Correspondingly, the $2n$ pieces of the attractor merge with a denser filling of the previously void portion of the unstable manifold of I_j^n as denser is the accumulation of the relevant fingers around I_j^n [Grebogi, Ott and Yorke, 1982; Grebogi, Ott and Yorke, 1983b; Lai, Grebogi and Yorke, 1992; Rega and Salvatori, 1996].

After the period-doubling cascade, near $V_{in} = 32.279V$, merging bands and periodic windows can be seen in the diagrams (Fig. 5.6(d)), these latter corresponding to saddle-node bifurcations followed by interior crises (IC2), when the merging attractor touches the saddle born at the saddle-node bifurcation. Between $V_{in} = 32.280V$ and $V_{in} = 32.281V$ a 5T-periodic window is also detected. Similar phenomena is apparent on a larger scale in (Fig. 5.6(c)), where a 3T-window due to a tangent bifurcation and interior crisis is also seen. Close inspection of the larger scale figure 5.6(b) shows that an interior crisis of second kind (IC2) occurs at approximately $V_{in} = 32.295V$, when a saddle touches the attractor and forces it to widen. Another more important interior crisis of second kind is responsible for the larger jump observed at the end, at $V_{in} = 32.336V$, when the chaotic attractor is organized in a five-zones basis. This is analysed in a later section of this chapter. In addition to this, Fig. 5.4 shows the existence of many other dynamical behaviors coexisting with those belonging to the main bifurcation diagram described above. Namely:

- a three-piece stable chaotic attractor is found for $V_{in} \in (24.160, 25.010)V$;
- a parallel branch of $P(6, 6)$ orbits is detected in a neighbourhood of $V_{in} = 30.000V$. This undergoes its own period-doubling cascade which leads to a six-piece stable chaotic attractor;
- a further branch of $P(12, 12)$ orbits is found in a neighbourhood of $V_{in} = 32.150V$, which gives rise to a twelve-piece chaotic attractor via a period-doubling cascade;

- a window of $P(7, 5)$ stable orbits is found around $V_{in} = 32.550V$.

Moreover, a non-smooth route to chaos is detected starting on a 3T-periodic orbit around $V_{in} = 13.380V$. The richness of this dynamical scenario motivates the search for possible links between the new dynamical evolutions outlined above, and some well known dynamics of the converter. For instance, the analysis of $P(7, 5)$ orbits can provide an explanation for the five-zones chaotic attractor exhibited by the system after the jump to *larger* chaos. It is important to point out that due to the competition between different dynamical evolutions the numerical computation of the bifurcation diagram, Fig. 5.4, has been carried out by considering a cluster of initial conditions for each value of the input voltage. Namely, the cluster was chosen as the main diagonal of the phase plane $v \in (11.75, 12.70)$, $i \in (0.43, 0.75)$. Assuming a time interval of $5000T$, for each pair of initial conditions the system evolution is simulated and the last 100 stroboscopic points are stored so that transient has settled down.

5.3 $P(\cdot, 3)$ Orbits and the Three-piece Chaotic Attractor

As was mentioned in the previous section, stable chaotic regime exists for $V_{in} \in (24.160, 25.010)V$, and also for $V_{in} \in (13.542, 13.880)V$. The existence of these three-piece chaotic attractors, (one of them is depicted in Fig. 5.7), suggests that they might originate from a branch of unstable $P(\cdot, 3)$ orbits. Although they are unstable, they can provide a deeper insight into the dynamics of a chaotic system, as outlined in [Ogorzalek and Chua, 1993].

5.3.1 Two Branches of 3T-Periodic Orbits

Due to the analytical closed form of the system solutions, which are combinations of exponential and trigonometric functions, it is possible to solve numerically the necessary conditions for their existence. These conditions can be obtained by constructing the stroboscopic map corresponding to the desired orbit and imposing the periodicity constraint as was done in Chapter 3 with 1T-periodic and 2T-periodic orbits. To show how this is done in the case of 3T-periodicity, let us consider the case of a $P(3, 3)$ orbit characterized by one impact per cycle. Assuming the continuity of the solutions, the state variables at the switching instants can be written as

$$\begin{aligned}
 x(\alpha_1) &= N(\alpha_1)x(0) \\
 x(1) &= V_{in}[I - N(1 - \alpha_1)]b + N(1 - \alpha_1)x(\alpha_1) \\
 x(\alpha_2) &= N(\alpha_2)x(1) \\
 x(2) &= V_{in}[I - N(1 - \alpha_2)]b + N(1 - \alpha_2)x(\alpha_2) \\
 x(\alpha_3) &= N(\alpha_3)x(2) \\
 x(3) &= V_{in}[I - N(1 - \alpha_3)]b + N(1 - \alpha_3)x(\alpha_3)
 \end{aligned} \tag{5.15}$$

where we recall that $\alpha_j = (t_j \bmod T)/T$ with $j = 1, 2, 3$. Each of the equations can now be substituted into the next and, noting that $N(\alpha + \beta) = N(\alpha)N(\beta)$

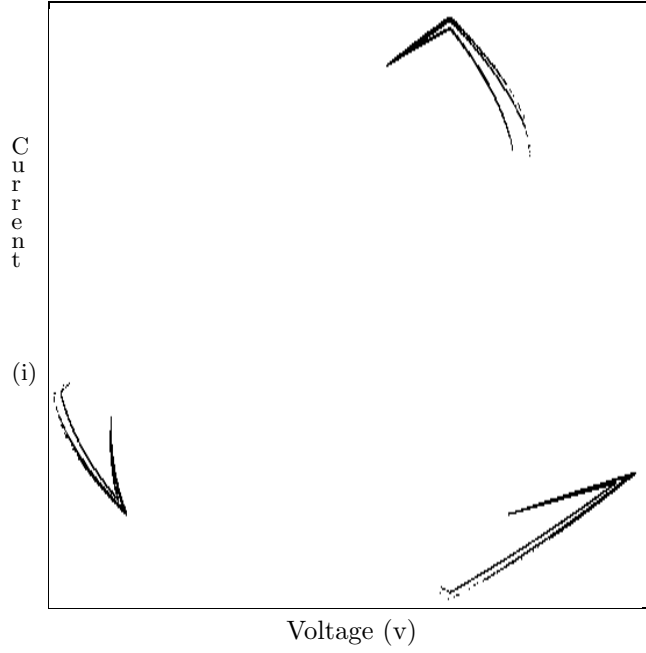


Figure 5.7: Three-piece chaotic attractor in the (v, i) phase space for $V_{in} = 24.160V$. v range is $(11.41, 12.70)$ and i range is $(0.42, 0.75)$.

and $N(0) = I$ [Fossas and Olivar, 1996], we get the following expression for $x(3)$:

$$x(3) = N(3)x(0) + \begin{bmatrix} N(1) - N(3) \\ N(2) - N(3) \\ N(3) - N(1) \end{bmatrix} b \quad (5.16)$$

where α_1, α_2 and α_3 are the unknown normalized impact instants. Now, by imposing the periodicity constraint $x(3) = x(0)$ from (5.16),

$$\bar{x} = V_{in}[I - N(3)]^{-1}[I - N(1 - \alpha_3) + N(1) - N(2 - \alpha_2) + N(2) - N(3 - \alpha_1)]b, \quad (5.17)$$

is obtained, where the existence of the inverse matrix of $I - N(3)$ was proved in [Fossas and Olivar, 1996].

Then, \bar{x} can be substituted into the three impact conditions

$$\begin{aligned} v(\alpha_1, \bar{x}) &= \gamma + \eta\alpha_1, \\ v(\alpha_2, \bar{x}) &= \gamma + \eta\alpha_2, \\ v(\alpha_3, \bar{x}) &= \gamma + \eta\alpha_3, \end{aligned} \quad (5.18)$$

giving a system of three nonlinear transcendental equations, which can be solved numerically with respect to α_j , $j = 1, 2, 3$.

Note that once a solution has been obtained, it must be checked to be sure it is of the specified type, since the conditions considered are only necessary.

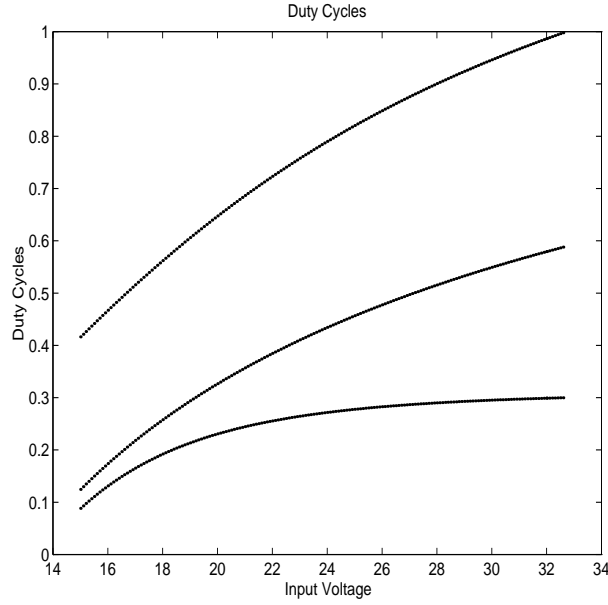


Figure 5.8: Duty cycles $\alpha_1, \alpha_2, \alpha_3$ for the main (3,3) branch of (111) m type.

The solutions α_j , $j = 1, 2, 3$ for different values of the input voltage V_{in} are represented in Fig. 5.8.

In a similar way, other topologies of $P(\cdot, 3)$ orbits can be analyzed. To distinguish among these topologies, one can label with $(m_1 m_2 m_3)c$ a $P(\cdot, 3)$ orbit which has m_1 impacts in the first cycle, m_2 in the second cycle, m_3 in the third, and

$$c = \begin{cases} l & \text{if } v(0) \in (-\infty, \gamma), \\ m & \text{if } v(0) \in (\gamma, \gamma + \eta T), \\ u & \text{if } v(0) \in (\gamma + \eta T, \infty). \end{cases}$$

For example, the $P(3, 3)$ orbit considered above can be classified as (111) m orbit, while we say that an orbit is of type (011) u if it is a $P(2, 3)$ orbit with no impact in the first cycle, one impact in the second, and one impact in the third cycle, with initial condition $v(0) > \gamma + \eta T$. It is worth noting that the same orbit can be labelled in different ways depending on which of the three cycles is taken as the first one.

In order to continue different $P(\cdot, 3)$ orbits, the same procedure outlined for the (111) m must be followed. The solutions of the resulting nonlinear system will be acceptable if $\alpha_j \in (0, 1)$, with j depending on the specific orbit, and \bar{x} leads to the specified type of trajectory. This allows us to identify ranges of V_{in} in which each kind of orbit exists. It must be remembered that this system is non-smooth due to the switching, and thus the usual continuation packages for periodic orbits, such as AUTO, are not suitable. A summary of

the computed orbits can be found in Fig. 5.9 and Fig. 5.10, where only one of the three stroboscopic points is plotted for each branch. It is worth pointing out that each type of $P(\cdot, 3)$ solution is no longer acceptable when the voltage touches the bottom or the top of the ramp at a multiple of the ramp period, nT , i.e. when a grazing phenomenon occurs.

We will now describe the most important features of the $P(\cdot, 3)$ orbits represented in Fig. 5.9. First, we observe a similar shape in the branches; we therefore call them parallel branches. The branch including the $P(3, 3)$ orbits of type $(111)m$ will be called the first 3T-branch and its parallel branch will be called the second 3T-branch (see Fig. 5.9).

Beyond $V_{in} = 21.289V$ a pre-existing $(110)m$ solution in the second 3T-branch turns into a $P(1, 3)$ orbit of type $(010)m$, which ends at $V_{in} = 25.010V$ with a reverse saddle-saddle grazing point [Grebogi, Ott and Yorke, 1983a], namely (Fig. 5.10(20)-(23)). We observe that once the $(010)m$ orbit has ceased to exist, it is possible to follow another parallel branch of $P(2, 3)$ orbits of type $(011)u$, by varying the input voltage backwards. This solution turns into a branch of orbits of type $(111)u$ at $V_{in} = 24.797V$, again through a grazing phenomenon. When this is no longer acceptable, by reversing the direction of the input voltage variation, a branch of $(112)m$ can be followed, and so on along a zig-zag structure of $(11m_3)$ -($11, m_3 + 1$) orbits which seems to accumulate on a (11∞) . Furthermore, something similar happens in the first 3T-branch.

Further computations, however, indicate that this expected sliding orbit of (11∞) type does not exist (Fig. 5.9(36)). An attempt was made to find it by imposing $v(0) = \gamma + \eta T$ and $\dot{v}(0) = \eta$, one impact per cycle in the following two cycles, and the local infinite stretching condition at the second T -switching, but MAPLE could not find a solution.

As the number of impacts grows to infinity, the 3T-periodic orbits approach the infinite stretching-grazing phase point at x_l , which corresponds to the initial conditions giving theoretically infinite impacts in the ramp. Thus, chaotic dynamics are expected in this narrow region of the phase space and parameter values. As will be shown later, a chaotic attractor is not observed in this region. Therefore the expected chaotic dynamics must be non-attracting. As a (11∞) type orbit does not exist, it is conjectured that the accumulation points for V_{in} which are saddle-saddle bifurcations probably accumulate in two different values $V_{in}^{(1)} < V_{in}^{(2)}$, respectively near the points labelled (35) and (1) in Fig. 5.9, and thus an infinite number of unstable orbits can be found in this range, providing a chaotic saddle for the system. Consequently, a new adding-unstable orbit process is described for the creation of a chaotic saddle. The chaotic saddle is later destroyed due to the reverse saddle-saddle bifurcations in the zig-zag series. The stability of all the computed orbits has been checked by three independent methods: the first one is direct time simulation of the system. This method of computation follows the algorithm described in [Deane and Hamill, 1990a], using the closed form expressions for the solutions and solving the transcendental equation for the impacts with a combined Newton and bisection method, with a relative precision of 10^{-16} . The second method consists in obtaining the analytical expression for the periodic orbits, and then using a numerical method like that in [Fossas and Olivar, 1996] to compute the characteristic multipliers.

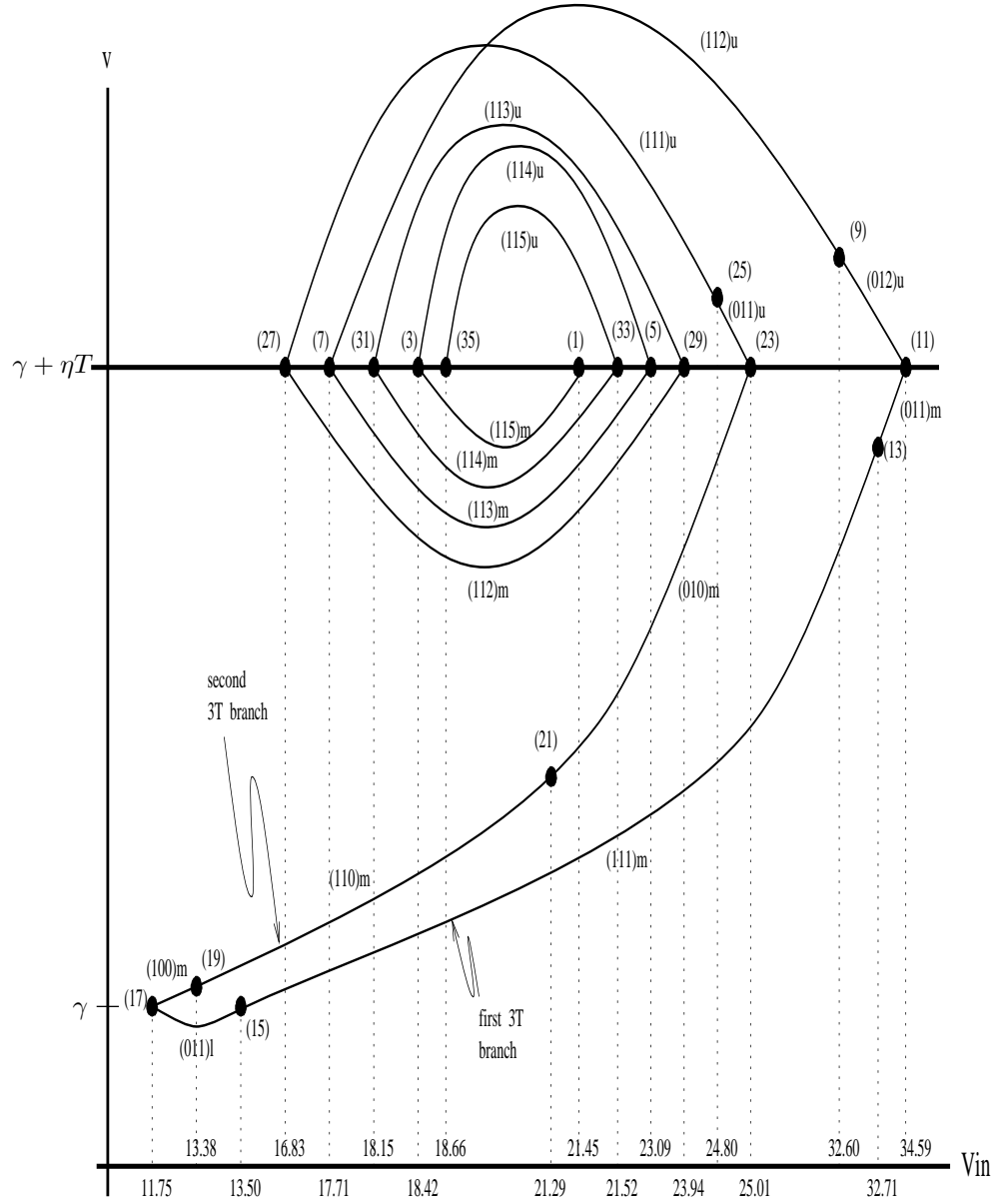


Figure 5.9: Scheme of the bifurcations of the types for the 3T-periodic unstable orbits. Dots stand for grazing bifurcations: the numbers are given according to Fig.5.10. Every point in the branch stands for one of the three stroboscopic points of the orbit.

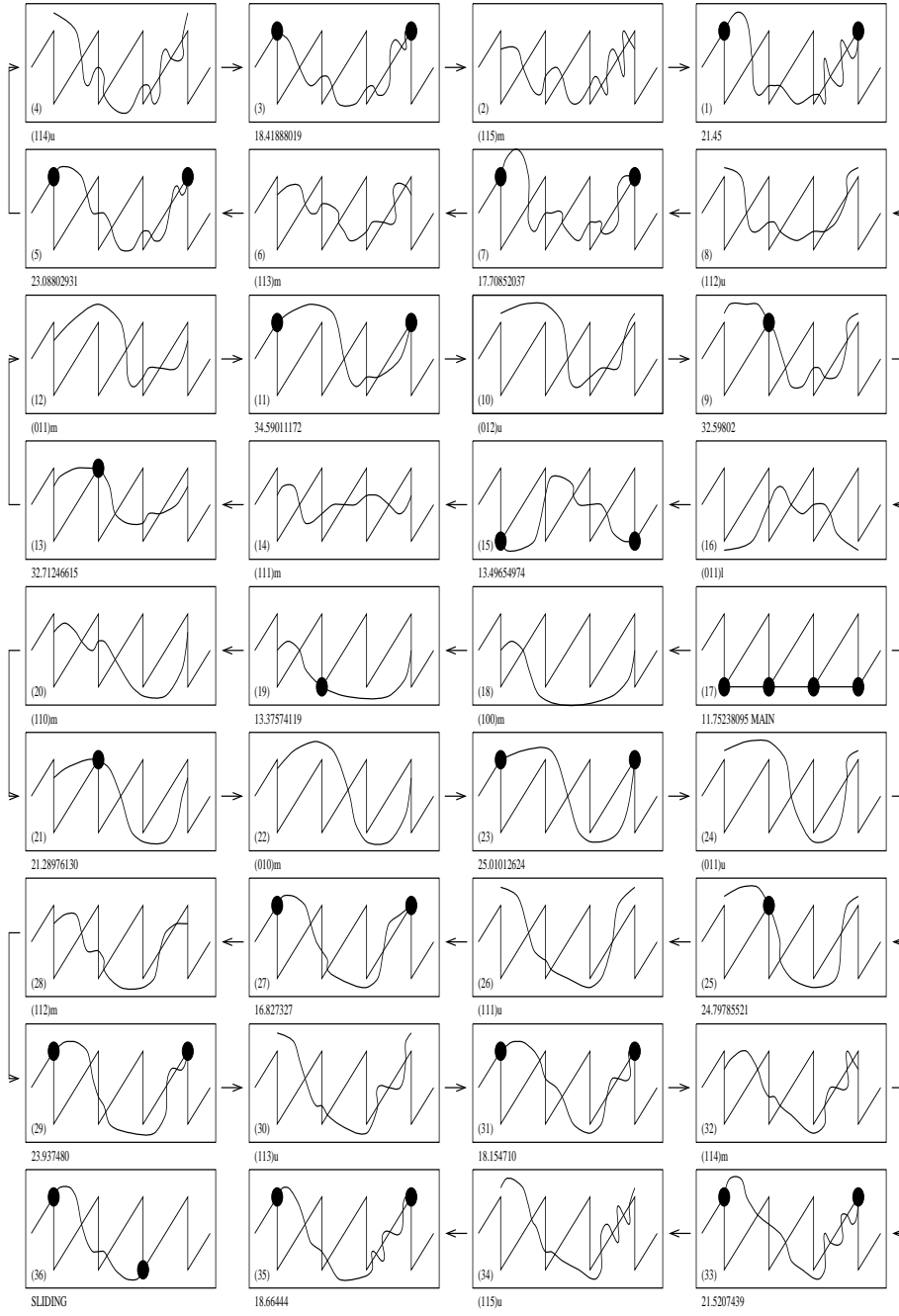


Figure 5.10: Patterns for the 3T-periodic unstable orbits. Dots stand for grazing points. Under each of the 36 patterns, the type of the orbit or the value of the input voltage is specified.

Finally, a third and more precise method is used to compute the characteristic multipliers as the eigenvalues of DP , which has been computed analytically (as in the method for obtaining the first period-doubling bifurcation). This last method is now explained in greater detail.

In general, the expression of the map for a kT -periodic orbit with r switchings (a $P(r, k)$ orbit), has the form

$$P^k(x_0) = N(k)x_0 + V_{in}\gamma(\alpha_1, \dots, \alpha_r)b. \quad (5.19)$$

The conditions for the switchings are

$$a(v_i - V_{ref}) = V_L + (V_U - V_L)\alpha_i \quad i = 1, \dots, r \quad (5.20)$$

and the expressions for the switching states x_i as functions of $x_0, \alpha_1, \dots, \alpha_r$, are

$$x_i = V_{in}\gamma_i(\alpha_1, \dots, \alpha_r)b + \delta_i(\alpha_1, \dots, \alpha_r)x_0 \quad i = 1, \dots, r \quad (5.21)$$

Differentiation of (5.19) with respect to x_0 yields

$$DP^k = N(k) + V_{in}\gamma'(\alpha_1, \dots, \alpha_r)b\frac{d\alpha}{dx_0} \quad (5.22)$$

and differentiation of (5.21) also with respect to x_0 yields for $i = 1, \dots, r$

$$\frac{dx_i}{dx_0} = V_{in}\gamma'_i(\alpha_1, \dots, \alpha_r)b\frac{d\alpha}{dx_0} + \delta'_i(\alpha_1, \dots, \alpha_r)x_0\frac{d\alpha}{dx_0} + \delta_i(\alpha_1, \dots, \alpha_r) \quad (5.23)$$

Finally, (5.20) can also be differentiated with respect to x_0 to obtain

$$a\left(\frac{dv_i}{dx_0}\right) = (V_U - V_L)\frac{d\alpha_i}{dx_0} \quad i = 1, \dots, r. \quad (5.24)$$

Then equation (5.24) can be substituted into (5.23) to yield

$$\frac{dx_i}{dx_0} = V_{in}\gamma'_i(\alpha_1, \dots, \alpha_r)b\frac{a}{V_U - V_L}\frac{dv}{dx_0} \quad (5.25)$$

$$+ \delta'_i(\alpha_1, \dots, \alpha_r)x_0\frac{a}{V_U - V_L}\frac{dv}{dx_0} + \delta_i(\alpha_1, \dots, \alpha_r) \quad i = 1, \dots, r. \quad (5.26)$$

which yields

$$\frac{dx_i}{dx_0} \quad i = 1, \dots, r$$

as a function of $x_0, \alpha_1, \dots, \alpha_r$, and so also

$$\frac{d\alpha_i}{dx_0} \quad i = 1, \dots, r$$

as a function of $x_0, \alpha_1, \dots, \alpha_r$. This can be substituted into (5.22) to obtain DP^k , and then we obtain the characteristic multipliers as the eigenvalues of this matrix. This method can be applied to compute period-doubling, saddle-node and border-collision bifurcations.

Almost all the $P(\cdot, 3)$ computed orbits turned out to be unstable, with the exception of the $(011)m$ at $V_{in} = 25.010V$, and some part of the branch of $(110)m$ near the bifurcation point labeled (19). It is worth noting that in all the grazing bifurcation points a discontinuous change in the characteristic multipliers occurs (although the product of them must be constant to $e^{-3T/(RC)}$) [Parker and Chua, 1989]. For example, at the bifurcation point (19), which corresponds to

$$V_{in} = 13.375741V,$$

the characteristic multipliers are

$$m_1 = -0.115834 \quad m_2 = -2.705132$$

while next to the right, at $V_{in} = 13.380V$, in the $(110)m$ branch, the multipliers are

$$m_1 = -0.319736 \quad m_2 = -0.979923$$

with a discontinuous change (without passing through -1^1). These characteristic multipliers correspond to an attracting 3T-periodic orbit. This 3T-periodic orbit can be followed forwards, experiencing a period-doubling at $V_{in} = 13.413V$, then instant chaos at $V_{in} = 13.542V$ [Nusse and Yorke, 1992; Ohnishi and Inaba, 1994] producing a six-piece chaotic attractor which monotonically enlarges until approximately $V_{in} = 13.715V$, when an interior crisis of first kind occurs, and thus the attractor merges from six to three pieces. Finally, at $V_{in} = 13.880V$ the attractor disappears due to a boundary crisis (see Fig. 5.11 and Fig. 5.12 [Pujol and Olivar, 1995]).

From $V_{in} = 13.375V$ backwards, continuing the $(100)m$ branch, one arrives at the limiting periodic orbit for $V_{in} = 11.752V$. For $V_{in} = 11.753V$, also in the $(100)m$ branch, the eigenvalues have smoothly varied from $V_{in} = 13.375V$, and yield

$$m_1 = -0.067733 \quad m_2 = -4.625855$$

while for $V_{in} = 11.753V$ in the parallel branch of $(011)l$ orbits, the characteristic multipliers are

$$m_1 = +0.067857 \quad m_2 = +4.617356$$

almost the same as in its parallel branch, but with the sign changed. From this point forwards the multipliers vary slowly, and for

$$V_{in} = 13.496550V,$$

in the grazing bifurcation point labelled (15), the multipliers are

$$m_1 = +0.071955 \quad m_2 = +4.354642.$$

Next to the right, for $V_{in} = 13.500V$, the characteristic multipliers are

$$m_1 = +0.085548 \quad m_2 = +3.662467.$$

¹Note that since the product of the characteristic multipliers $m_1 m_2$ must be constant to $e^{-3T/RC} < 1$, the only way they can pass through S^1 is by crossing at 1 or at -1.

and thus, another discontinuous change occurred at the point labelled (15). It is worth noting that apart from these non-smooth grazing bifurcations corresponding to a jump in the characteristic multipliers, and the saddle-saddle bifurcations mentioned before, some other non-smooth bifurcations are detected for $V_{in} = 11.752381V$, where the stable equilibrium point which existed before the bifurcation disappears and a 1T-periodic stable orbit plus two 3T-periodic unstable orbits appear. Furthermore, at the grazing bifurcation point labelled (23), the two unstable 3T-periodic orbits and a small three-piece chaotic attractor detected in the range $V_{in} \in (24.160, 25.010)V$ coalesce into a stable 3T-periodic orbit at (23), and then disappear. The size of this three-piece chaotic attractor decreases monotonically as the input voltage increases, and is left as a 3T-periodic orbit at (23) before disappearing. As the bifurcation parameter is decreased, the three-piece chaotic attractor increases its size until it disappears possibly due to a boundary crisis near $V_{in} = 24.160V$.

5.3.2 The Invariant Manifolds and Basins of Attraction

The study of the stability of periodic orbits gives a local description of the dynamics. Although the distribution of these periodic orbits in the phase space shows a global overview, it is far from complete. To get a deeper insight into the global dynamics, invariant manifolds and basins of attraction must be computed and analysed, and the geometrical shape when a bifurcation parameter is varied must also be investigated. Stable and unstable manifolds of the saddles play a fundamental role in basin organization, and when obtained systematically with a varying bifurcation parameter, they permit a thorough geometrical understanding of the numerically observed attractor and basin metamorphoses. Indeed, the main global bifurcations are associated with homoclinic and heteroclinic tangencies between the stable and unstable manifolds of a given direct (D^m) or inverse (I^m) saddle, and two different direct or inverse saddles, respectively. The closure of the stable manifold of a direct saddle and an inverse saddle coincides respectively with the border between two basins of attraction of different solutions and between the two distinct subdomains identifiable in the basin of a given solution under a mapping f^{2m} . When varying the bifurcation parameter, occurrence of manifold tangling is a sufficient condition for fractal basin boundary (and thus for unpredictability of response) and a necessary condition for the onset of a chaotic attractor in one basin. If it exists, this attractor is contained within the closure of $W_k^u(D_j^m)$, the k th branch of the unstable manifold of the direct saddle located on the relevant basin boundary, and within the closures of $W_k^u(I_j^m)$, with several m , which are the unstable manifolds of the inverse saddles from where it probably originated through period-doubling bifurcations. The sequence of homoclinic and heteroclinic tangencies, and intersections of saddle manifolds corresponding to coexisting unstable periodic solutions, govern the sequence of attractor-basin bifurcations and determine the possible occurrences of sudden change bifurcations and crises [Grebogi, Ott and Yorke, 1986; Grebogi, Ott and Yorke, 1987].

One of the points at which invariant manifolds are worth computing is $V_{in} = 11.752381V$. A stable equilibrium point which exists before this value turns

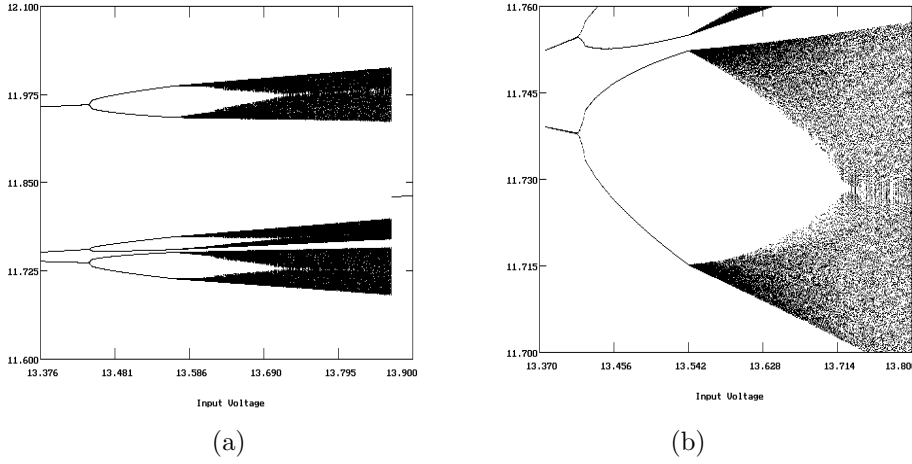


Figure 5.11: (a) Bifurcation of the 3T-attractor starting near $V_{in} = 13.376V$. After the non-smooth bifurcation creating the 3T-periodic orbit, a period-doubling bifurcation occurs. Next, instant chaos into a six-piece chaotic attractor is observed. An interior crisis of first kind producing merging bands turns the six-piece chaotic attractor into a three-piece chaotic attractor, and finally a boundary crisis destroys it. (b) Detail of the instant chaos bifurcation.

into a stable 1T-periodic orbit plus two saddle 3T-periodic orbits. Invariant manifolds can be computed for these two saddles. Figure 5.13(a,b) shows the stable and unstable manifolds for the saddles when $V_{in} = 11.800V$.

Apart from the many fingered shape of the manifolds, transversal homoclinic orbits also exist. Thus an invariant set with horseshoe dynamics can be found at an early value in this small region of the phase space. This concludes the investigation of the new type of non-smooth bifurcation at this point involving instant transversal homoclinic orbits: a stable equilibrium point before $V_{in} = 11.752381V$ turns into a stable 1T-periodic orbit and a chaotic saddle, which probably includes the two unstable 3T-periodic orbits after the bifurcation.

As the parameter is increased, this many-fingered tangle, which is small near $V_{in} = 11.800V$, widens and changes its shape for $V_{in} = 13.500V$ approximately, when a first grazing bifurcation takes place. At this point, trajectories are able to follow the ramp signal upwards since the fixed point of one of the two topologies $(V_{in}, V_{in}/R)$ is high enough up the upper voltage of the ramp, and so different behavior can be expected. Some snapshots of the invariant manifolds are taken for the 3T-periodic saddle of type $(111)m$ in the first 3T-branch. While the main stable 1T-periodic orbit exists, the interior unstable half-manifold spirals towards it, and each of the exterior half-manifold intersects transversely the stable manifold (see Fig. 5.13 and Fig. 5.14). On the other hand, something different occurs with the invariant manifolds of the second 3T-branch. None of

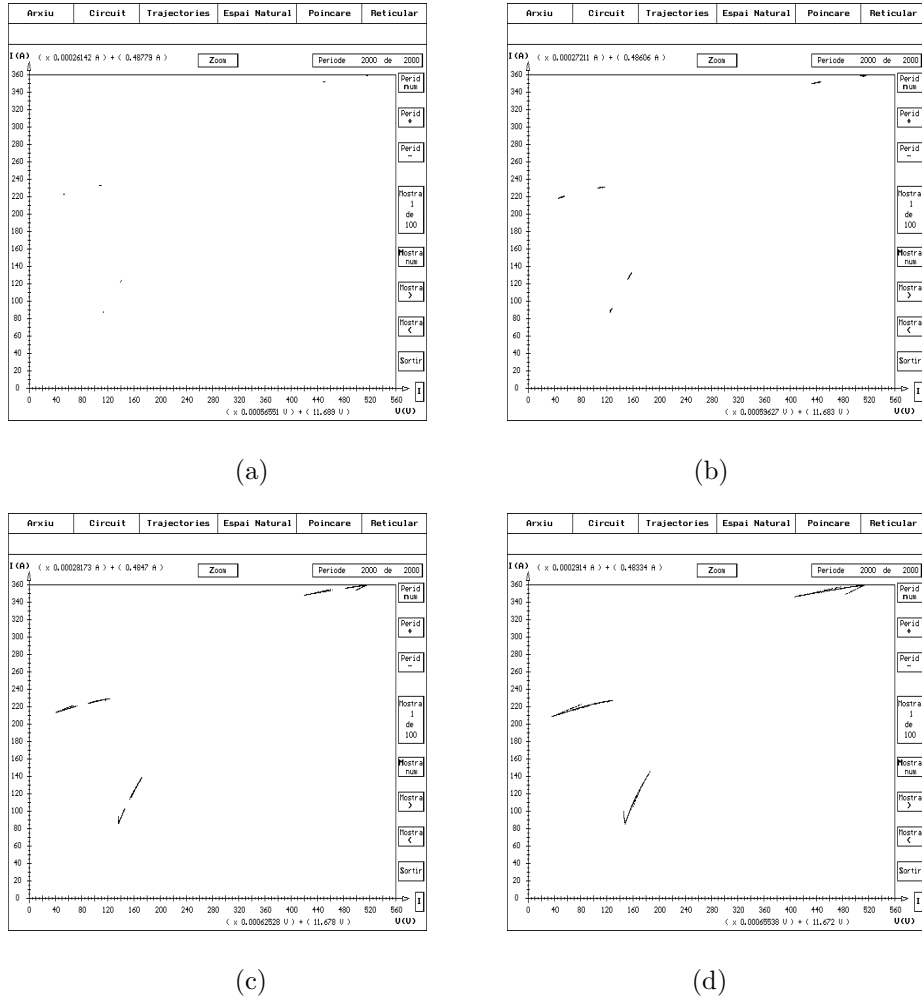


Figure 5.12: Evolution of the 3T-periodic orbit at $V_{in} = 13.376V$ in the phase-space (a) $V_{in} = 13.500V$ (6T-periodic attractor); (b) $V_{in} = 13.600V$ (six-piece chaotic attractor); (c) $V_{in} = 13.700V$ (six-piece chaotic attractor); (d) $V_{in} = 13.800V$ (three-piece chaotic attractor).

the unstable half-manifolds spiral to the main stable 1T-periodic orbit. They intersect the corresponding stable manifolds instead, providing a homoclinic tangle, and since this is non-attracting, they also provide a chaotic saddle for the system.

If V_{in} is increased before the first period-doubling of the main 1T-periodic attractor, the manifolds of the 3T-saddles also change their shape (see Fig. 5.13 and Fig. 5.14). While the interior unstable half-manifold is spiraling to the main

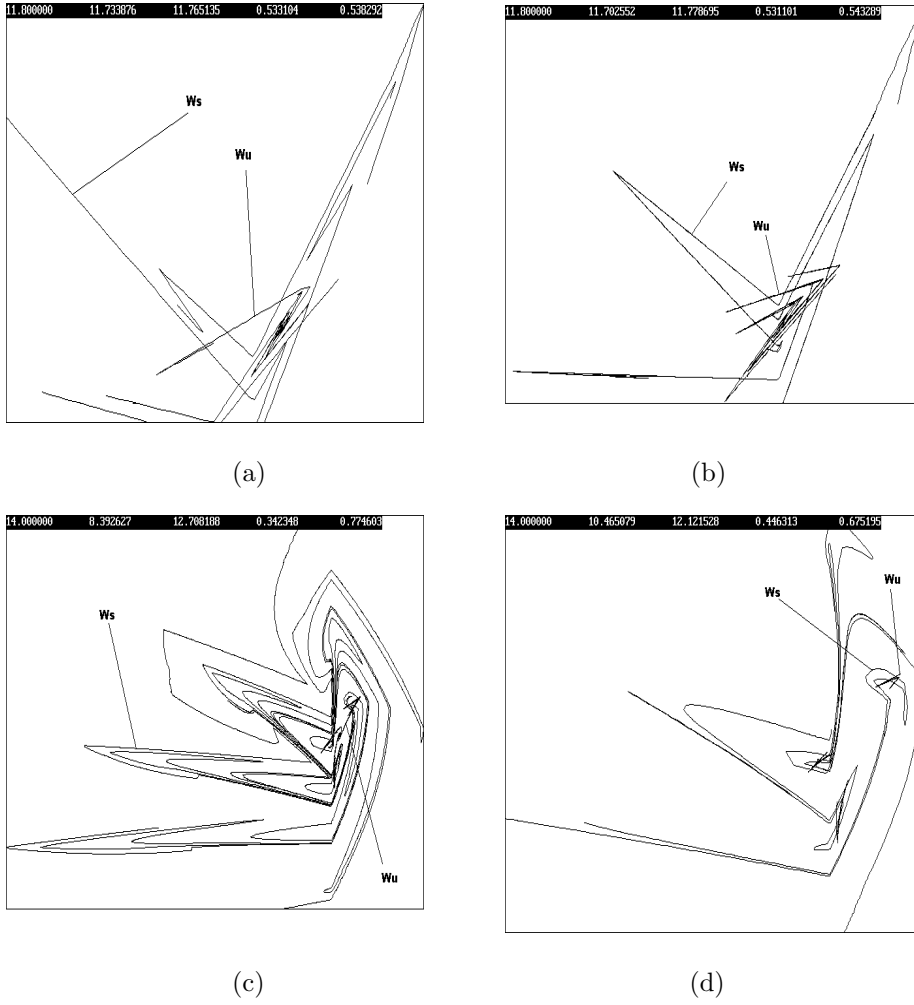


Figure 5.13: Invariant manifolds for the 3T-saddles in the 3T-branches. In the first 3T-branch, the interior part of the unstable manifold leads to the 1T-periodic attractor and the exterior part intersects the stable manifold; in the second 3T-branch, the interior and exterior parts of the unstable manifold intersect the stable manifold. (a) $V_{in} = 11.800V$, first 3T-branch; (b) $V_{in} = 11.800V$, second 3T-branch; (c) $V_{in} = 14.000V$, first 3T-branch; (d) $V_{in} = 14.000V$, second 3T-branch.

stable 1T-periodic orbit, the exterior unstable half-manifold also spirals and despirals around three zones in the phase space, which coincide with the three zones where the 3T saddle orbits accumulate. Thus, the manifolds approximate to the infinite-stretching point. As the manifolds pass near this zone of high

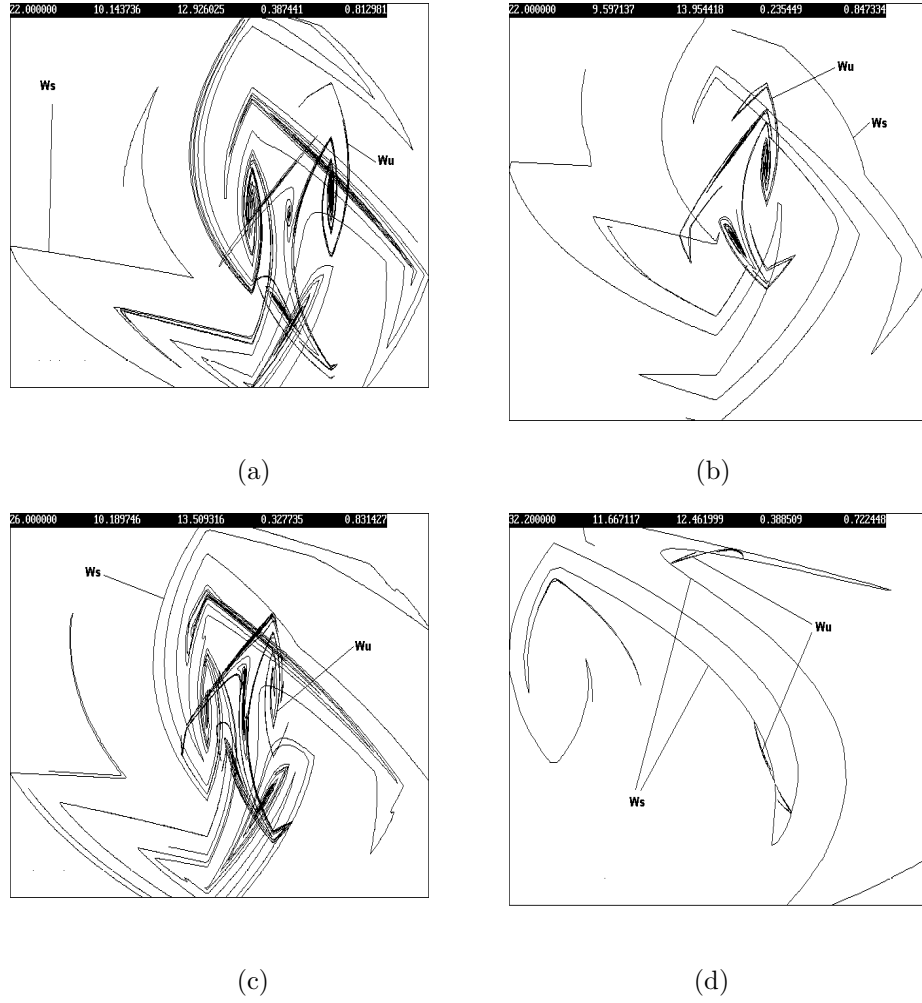


Figure 5.14: Invariant manifolds for the 3T-saddles of the 3T-branches and for the 2T-periodic inverse saddle created at the second period-doubling of the main branch attractor. (a) $V_{in} = 22.000V$, first 3T-branch; (b) $V_{in} = 22.000V$, second 3T-branch; (c) $V_{in} = 26.000V$, first 3T-branch; (d) $V_{in} = 32.200V$.

number of crossings, they are highly twisted and folded, and as the manifolds are invariant sets, this twist and fold propagates all along the manifolds. That is why their shape is like *dense spiraling islands*; they seem to open and widen their fingers, also spiraling to three zones in the phase space.

Around $V_{in} = 13.376V$, a three-piece chaotic attractor was found following a path of 3T-periodic stable orbits, which is later destroyed at a boundary crisis. Consequently, a coexisting attractor with the main 1T-periodic branch exists.

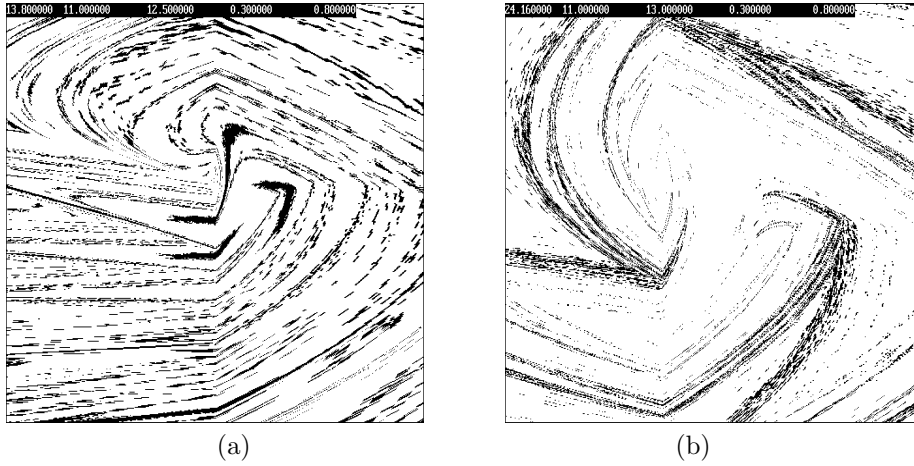


Figure 5.15: (a) Basins of attraction for $V_{in} = 13.800V$. Black corresponds to the 3T-attractor and white to the main 1T-attractor; (b) Basins of attraction for $V_{in} = 24.160V$. Black stands for the 1T-periodic basin, white for the three-piece chaotic attractor basin.

Furthermore, a three-piece chaotic attractor is also present near $V_{in} = 24.160V$, and until $V_{in} = 25.010V$. Their basins of attraction can be computed following a cell-to-cell mapping algorithm [Seydel, 1988; Hsu, 1992]. The stable manifold of the 3T-saddle corresponds to the basin boundary of the attractors, while the unstable manifold is the closure of the chaotic attractor. This can be seen in Fig. 5.15.

As the shapes of the manifolds change with increasing V_{in} , the future large chaotic attractor at V_{in} near $32.340V$ is also apparent. Thus it is conjectured that the five-zones chaotic attractor, which exists for large values of V_{in} , is in fact an evolution from the three-zones chaotic saddle from the intersection of the manifolds and the period-doubling evolution of the main branch attractor itself. For example, when the first period-doubling has taken place at $V_{in} = 26.000V$, the central part of the invariant manifold has widened and begins to connect the other three branches (see Fig. 5.14).

Invariant manifolds for the 1T-periodic inverse saddle can also be computed. It can be shown that additional transverse homoclinic orbits exist for $V_{in} = 30.000V$ after an homoclinic bifurcation. For $V_{in} = 29.000V$, the stable manifold is the boundary of the two subdomains of the stable 2T-periodic orbit. The corresponding unstable manifold leads to this orbit, but in a way that is reminiscent of the next 6T saddle-node bifurcation to appear. Homoclinic tangles also take place for the invariant manifolds of the 2T-periodic inverse saddle created at the second period-doubling of the main attractor. The unstable manifold begins to fold around $V_{in} = 32.000V$. This is more clearly seen

at $V_{in} = 32.200V$ (Fig. 5.14), and the homoclinic tangency occurs at a value between $32.200V$ and $32.400V$, probably at the same time as the small attractor becomes larger for V_{in} near $32.336V$. Thus this homoclinic tangle could be responsible for the sudden expansion of the attractor.

5.4 Bifurcations of the $P(6, 6)$ and $P(12, 12)$ Orbits

5.4.1 $P(6, 6)$ Orbits

In addition to the main attractor branch and the $P(\cdot, 3)$ orbits discussed in the previous section, there also exists a secondary attractor in a neighborhood of $V_{in} = 30.000V$, as shown in Fig. 5.4. This is a $P(6, 6)$ sink, together with its 6T-periodic direct saddle, which is generated after a saddle-node bifurcation at $V_{in} = 29.906V$. This is located by computing the characteristic multipliers of the $P(6, 6)$, one impact per cycle, stable orbit and its corresponding direct saddle, which is computed with the same method as the $P(\cdot, 3)$ unstable orbits. Taking initial conditions on the direct saddle, and letting the system evolve, one recovers the stable 6T-sink, and so the 6T-direct saddle belongs to the boundary of the basin of attraction of the 6T-sink all over the range of existence of the sink. As shown in Tab. 5.1, one of the multipliers clearly assumes unitary modulus at $V_{in} = 29.906V$. This is also confirmed by the solution of the necessary conditions of existence of the $P(6, 6)$.

Figure 5.16 shows that the $P(6, 6)$ bifurcates into chaos through a standard period-doubling cascade, which ends in a six-piece chaotic attractor coexisting with the main 2T-periodic stable orbit. The structure of the chaotic attractor is shown in Fig. 5.17. Table I shows very clearly the passing of one of the multipliers through -1 , which corresponds to the first period-doubling. Note that when the multipliers are not real numbers, they follow the circle of radius $r = 0.313$. The resulting period-doubled $P(12, 12)$ stable orbit also follows the same route with a circle of radius $r = (0.313)^2$.

Successive period-doublings can be found at $V_{in} = 30.076V$, $V_{in} = 30.125V$ and $V_{in} = 30.137V$. Chaos is found approximately at $V_{in} = 30.140V$. Then, merging bands from 48 to 24, 24 to 12, and 12 to 6 pieces are detected. At $V_{in} = 30.175V$, the six-piece chaotic attractor suddenly vanishes after a boundary crisis, when the chaotic attractor and the corresponding 6T-periodic direct saddle, generated in the saddle-node bifurcation, collide. This phenomenon has also been reported in other oscillators [Kleczka, Kreuzer and Wilmers, 1989; Rega and Salvatori, 1996].

To discuss the metamorphoses of the basins of attraction, several were computed which show the competition between the two attractors: the main $P(2, 2)$ stable orbit and the attractors generated by the $P(6, 6)$ period-doubling cascade. Fig. 5.18 shows a clear geometric structure for the basins of attraction. This was explained by computing the stable and unstable manifolds of the direct saddle originated at the saddle-node bifurcation. The closure of the stable manifold of this direct saddle turns out to be the boundary of the basins of the compet-

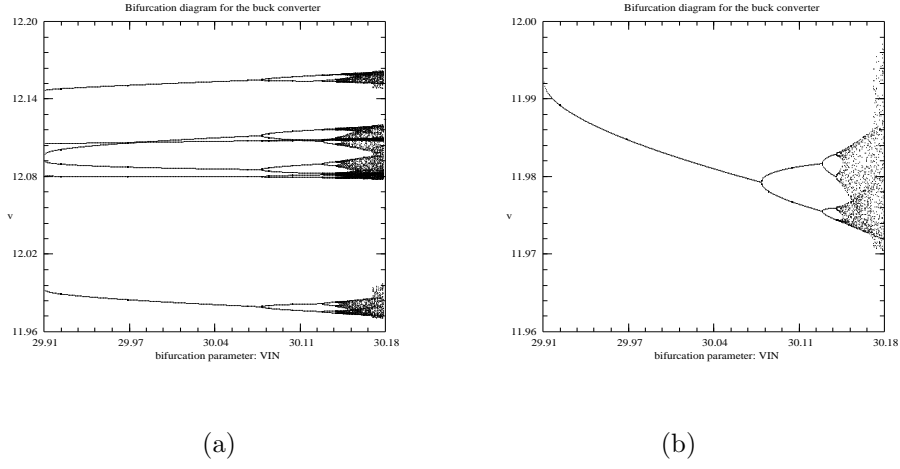


Figure 5.16: (a) Bifurcation diagram for the 6T attractor; (b) One of the 6 subbranches of the 6T attractor.

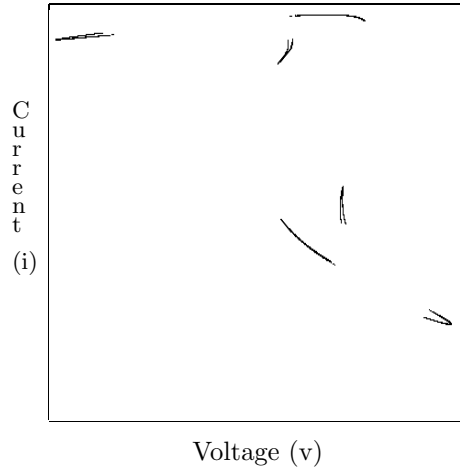


Figure 5.17: Six-piece chaotic attractor in the (v, i) phase space for $V_{in} = 30.170V$. v range is $(11.95, 12.17)$ and i range is $(0.497, 0.684)$.

ing attractors (see Fig. 5.18). Invariant manifolds are also computed near the saddle-node bifurcation value, namely, at $V_{in} = 29.000V$ and $V_{in} = 30.000V$ for the inverse saddle originated at the first period-doubling of the $P(1, 1)$ orbit at $V_{in} = 24.516V$. Figure 5.18 show these manifolds just before and just after the homoclinic tangency. After the homoclinic tangency, fractal basin boundaries are expected. When the saddle-node bifurcation occurs, very thin

Table 5.1: Characteristic multipliers for the 6T-periodic orbits.

V_{in}	multipliers m_1, m_2	$\max\{ m_1 , m_2 \}$
29.905725	0.099, 0.998	0.998
29.906	0.105, 0.933	0.933
29.907	0.115, 0.854	0.854
29.908	0.122, 0.802	0.802
29.909	0.130, 0.755	0.755
29.910	0.136, 0.720	0.720
29.920	0.296, 0.333	0.333
29.930	$0.233 \pm 0.209 j$	0.313
29.940	$0.162 \pm 0.268 j$	0.313
29.950	$0.098 \pm 0.297 j$	0.313
29.960	$0.038 \pm 0.311 j$	0.313
29.970	$-0.019 \pm 0.313 j$	0.314
29.980	$-0.074 \pm 0.305 j$	0.314
29.990	$-0.126 \pm 0.287 j$	0.313
30.000	$-0.177 \pm 0.258 j$	0.313
30.010	$-0.228 \pm 0.215 j$	0.313
30.020	$-0.277 \pm 0.146 j$	0.313
30.030	-0.418, -0.235	0.418
30.040	-0.578, -0.170	0.578
30.050	-0.704, -0.140	0.704
30.060	-0.818, -0.120	0.818
30.070	-0.924, -0.106	0.924
30.07633	-0.992, -0.099	0.992

basins are born for the 6T-periodic orbit, which lies almost within the boundary. Then the basin for the 6T grows as the bifurcation parameter is increased. At $V_{in} = 29.990V$, (Fig. 5.19) the 6T-periodic orbit lies well inside its basin, which has experienced a considerable expansion. Figure 5.19 also shows part of the basins. In this figure one may observe that these basins are mixed in a fractal way, but the boundary of the 6T seems to be smooth. Thus, regions of the basin boundary with different dimension are interwoven on arbitrarily fine scale, as happens for example with the double rotor system [Ott, 1993].

At $V_{in} = 30.175V$, it can be seen that the basin of the 2T enters into the 6T basin and this latter is eroded, and consequently decreases in extension. Figure 5.19 shows the strong mixing in the basins at an input voltage value in the range of existence of the six-piece chaotic attractor zone. Invariant manifolds are also computed for the 6T-direct saddle. At $V_{in} = 30.050V$, the exterior part of the unstable manifold begins to fold and grow. This manifold is folded more and more as the parameter increases until homoclinic tangency occur for V_{in} near $30.175V$, which coincides with the boundary crisis. This mechanism has also been reported in [Rega and Salvatori, 1996].

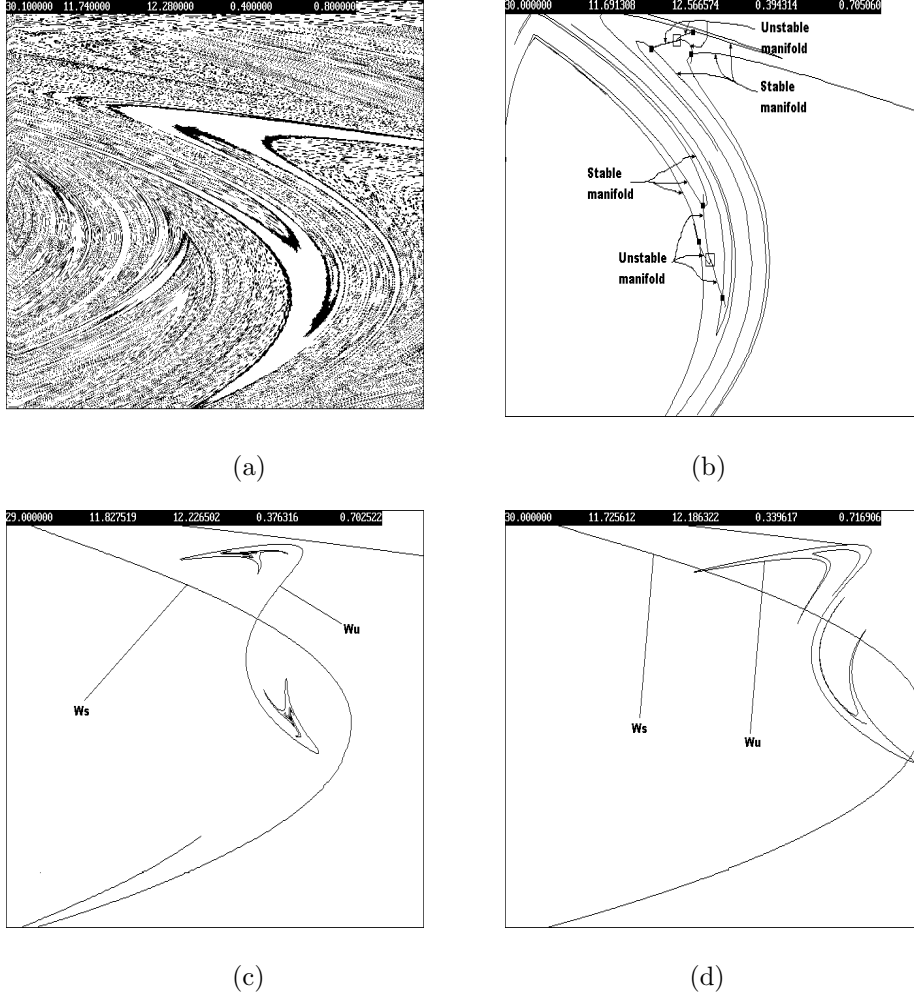


Figure 5.18: (a) Basins of attraction for $V_{in} = 30.100V$. Black corresponds to the 6T basin, white to the 2T basin. v range is (11.74,12.28); i range is (0.40,0.80); (b) Invariant manifolds for the 6T-direct saddle. The stable manifold coincides with the basin boundary for the 2T-solution. $V_{in} = 30.000V$. v range is (11.69,12.57); i range is (0.39,0.71); (c) Invariant manifolds for the main inverse saddle just before the homoclinic tangency. $V_{in} = 29.000V$. v range is (11.70,13.13); i range is (0.38,0.70); (d) Invariant manifolds for the main inverse saddle just after the homoclinic tangency. Fractal boundary basins are expected. $V_{in} = 30.000V$. v range is (11.67,13.08); i range is (0.34,0.72).

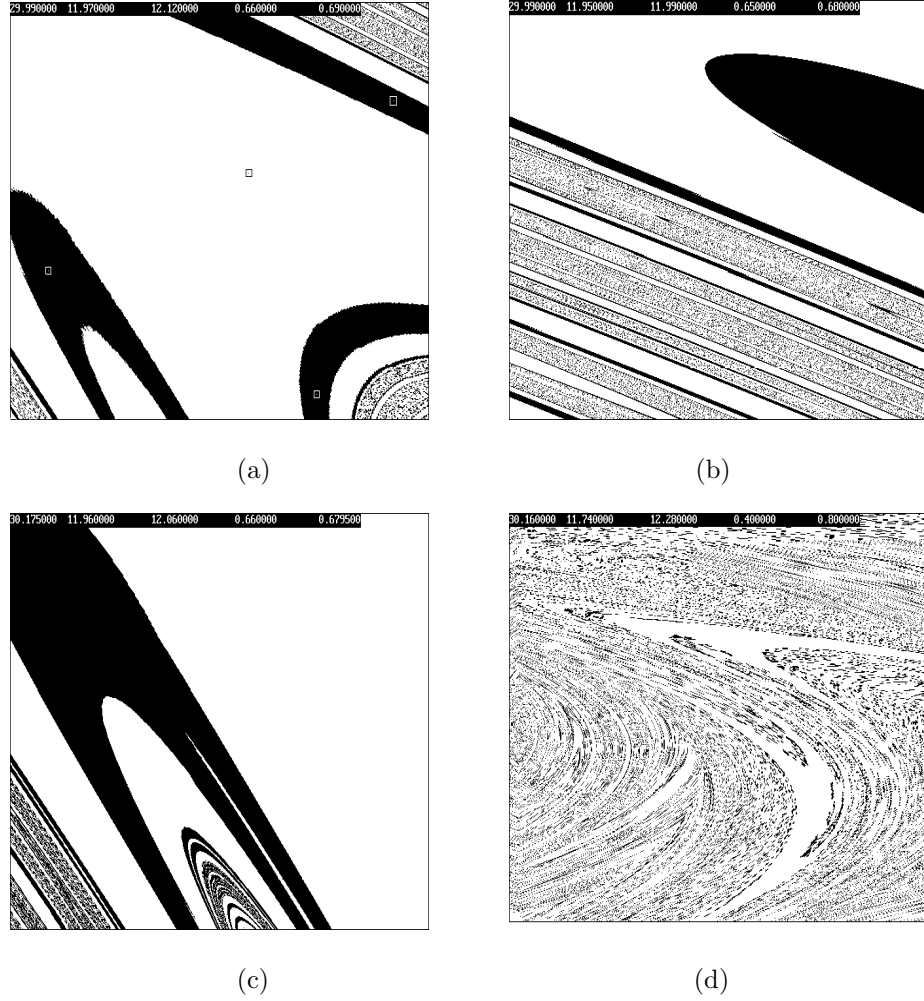


Figure 5.19: (a) Basins of attraction for $V_{in} = 29.990V$. The 6T attractor lies inside the basin. Black corresponds to the 6T basin, white to the 2T basin. Part of the attractors are marked with rectangles. v range is (11.97,12.12); i range is (0.66,0.69); (b) Detail of the basins for $V_{in} = 29.990V$. v range is (11.95,11.99); i range is (0.65,0.68); (c) Basins of attraction for $V_{in} = 30.175V$, near the boundary crises. The 2T basin enters into the 6T basin. Black corresponds to the 6T basin, white to the 2T basin. v range is (11.9600,12.0600); i range is (0.6600,0.6795); (d) Basins of attraction for $V_{in} = 30.160V$, in the 6T-chaotic zone. The 6T basin shows some type of erosion. Black corresponds to the 6T basin, white to the 2T basin. v range is (11.74,12.28); i range is (0.40,0.80).

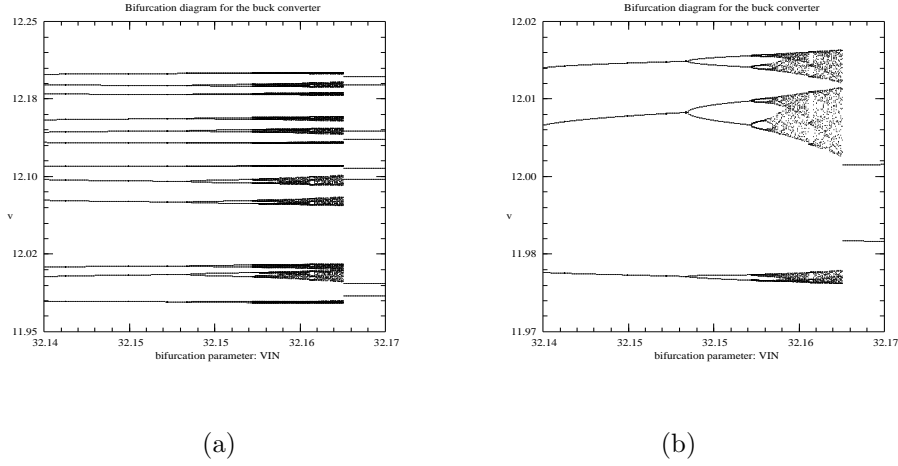


Figure 5.20: (a) Bifurcation diagram for the 12T; (b) Three subdomains of the 12T-attractor observing full chaos, crises and 3T windows in each of the three sub-branches.

5.4.2 $P(12, 12)$ Orbits

Coexisting with the $P(8, 8)$ stable orbit generated at the third period-doubling of the $P(1, 1)$, in the neighborhood of $V_{in} = 32.136V$, a $P(12, 12)$ stable orbit also appears. This is independent from the $P(12, 12)$ bifurcating from the $P(6, 6)$ and is born after a saddle-node bifurcation, occurring when the input voltage gets near $32.1365V$ (Fig 5.20). It is worth pointing out that this 12T-periodic orbit is organized in a different way from the preceding 12T-periodic orbit generated at the period-doubling of the 6T. The 12T period-doubled orbit is organized in six pairs around the previous existing 6T-periodic sink, while the 12T orbit born at the saddle-node bifurcation is arranged in four trios around the main 8T-periodic stable orbit (see Fig. 5.21).

This orbit was continued with the help of INSITE and it experiences a period-doubling cascade, which leads to a twelve-piece chaotic attractor coexisting with the stable 8T-periodic orbit. Successive period-doublings are found at $V_{in} = 32.151V$, $V_{in} = 32.157V$ and $V_{in} = 32.158V$. Afterwards, chaos is present. Successive merging bands from 48 to 24 and 24 to 12 pieces can be observed, leading to a twelve-piece chaotic attractor. Partial crisis in each of the twelve bands can also be distinguished for $V_{in} = 32.163V$. Again, the chaotic attractor disappears through a boundary crisis near this value, where the direct saddle originated in the saddle-node bifurcation collides with the attractor. In each of the twelve subbranches, full chaos, crisis and 3T-periodic and 5T-periodic windows (and thus, 36T-periodic and 60T-periodic windows in the full domain) exist (see Fig. 5.20). For $V_{in} = 32.150V$, the basins of attraction are mixed in a fractal way, as can be clearly observed in Fig. 5.22. Finally, the

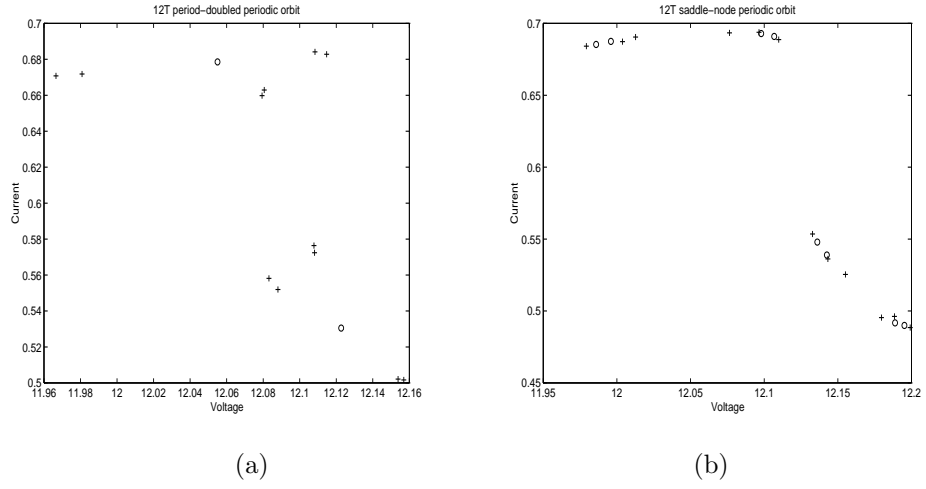


Figure 5.21: (a) Organization of the period-doubled 12T-periodic orbits. Crosses stand for the 12T, and circles for the coexisting 2T-stable periodic orbit; (b) Organization of the 12T-periodic orbits born at the saddle-node bifurcation. Crosses stand for the 12T, and circles for the coexisting 8T-stable periodic orbit.

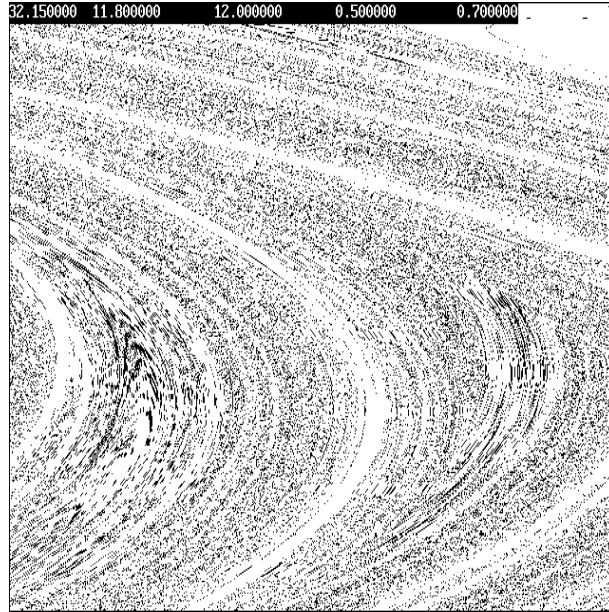


Figure 5.22: Basins of attraction for $V_{in} = 32.150V$. White stands for the 8T-periodic basin, while black stands for the 12T basin.

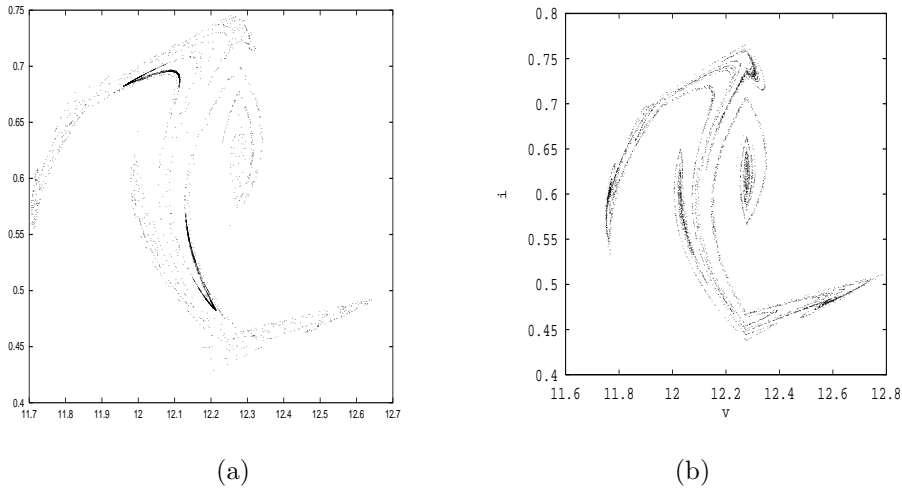


Figure 5.23: (a) Phase plane portrait just after the enlargement has occurred. The small scale chaotic attractor can be still clearly observed; (b) Large scale five-zones chaotic attractor.

characteristic multipliers of the $P(12, 12)$ periodic sink are computed, clearly showing the period-doubling and a walk along the circle of radius $r = 0.07$.

5.5 $P(\cdot, 5)$ Orbits and the Jump to Larger Chaos

As pointed out above and shown in Fig. 5.4, the main branch of the bifurcation diagram of the buck converter undergoes a period-doubling cascade which is suddenly interrupted when bands of chaos are merging around $V_{in} = 32.336V$. At this value of the input voltage, the amplitude of the voltage oscillations is abruptly enlarged. This phenomenon, which was observed experimentally for the buck in [Deane and Hamill, 1990a], has been detected in other systems [Ott, 1993]. A detailed simulation of the bifurcation diagram, shown in Fig. 5.6, indicates that when the jump occurs, the system is already evolving along a small scale chaotic attractor originated from the period-doubling cascade of the main branch (see Fig. 5.23). Then, as the voltage is increased, the system starts to evolve along the five-zones attractor depicted in Fig. 5.23.

An analytical investigation of this phenomenon is particularly difficult since the system is already chaotic when the sudden enlargement occurs. Nevertheless, it will be analysed in the following using the analytical and simulation tools presented before.

The fact that the large scale chaos is organised around five zones suggests a connection between the attractor itself and some $P(\cdot, 5)$ periodic solutions, as in the case of the three-piece chaos analysed before.

$P(7, 5)$ orbits are indeed detected as a window of periodicity embedded in the

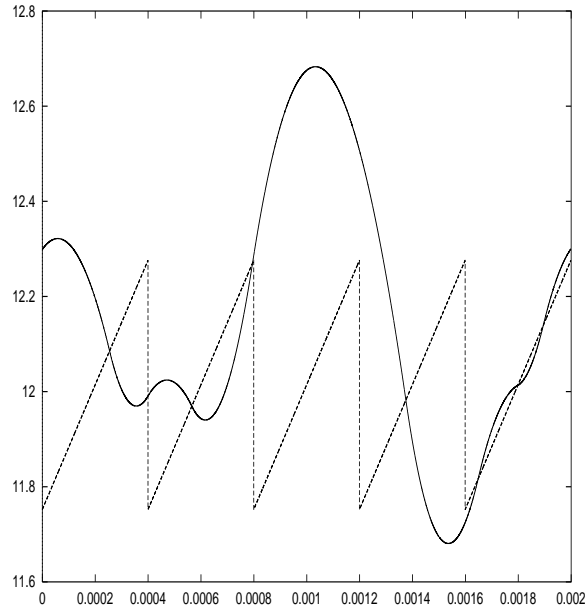


Figure 5.24: 5T-periodic organising orbit.

large scale chaotic attractor around $V_{in} = 32.550V$, as shown in Fig. 5.4. These orbits were continued backwards by imposing the necessary conditions for their existence. In so doing, an entire branch of unstable $P(7, 5)$ and $P(6, 5)$ orbits was detected in the intervals $(32.53, 32.59)$ and $(34.76, 34.78)$ approximately. These orbits are characterized by one impact in the first cycle, one or two impacts in the second cycle, a skipping in the third, one impact in the fourth, and three impacts in the last cycle (Fig. 5.24). It is important to point out that each stroboscopic point corresponds to the barycentre of each zone of the attractor, confirming the hypothesis that chaotic evolutions of the buck are organised around this type of $P(\cdot, 5)$ orbits when V_{in} grows beyond $32.336V$ (see Fig. 5.23). This is also confirmed by the changing in the average number of impacts per cycle as the input voltage is varied, which is reported in Fig. 5.25.

Up to the range of input voltages where the attractor enlargement takes place, all system dynamics are characterized by one impact per cycle. Then, when the jump occurs, the average number of impacts per cycle suddenly becomes different from one and starts to grow. This is predictable since the $P(6, 5)$ and $P(7, 5)$ solutions are characterized by multiple impacts in the last cycle. Moreover, the stroboscopic point preceding the multiple impacting cycle is near to the condition of infinite local stretching presented in [Fossas and Olivar, 1996; di Bernardo, Garofalo, Glielmo and Vasca, 1997]. Hence, the number of impacts in the last cycle is highly influenced by the initial condition at this point (theoretically infinite when the infinite local stretching condition is perfectly satisfied).

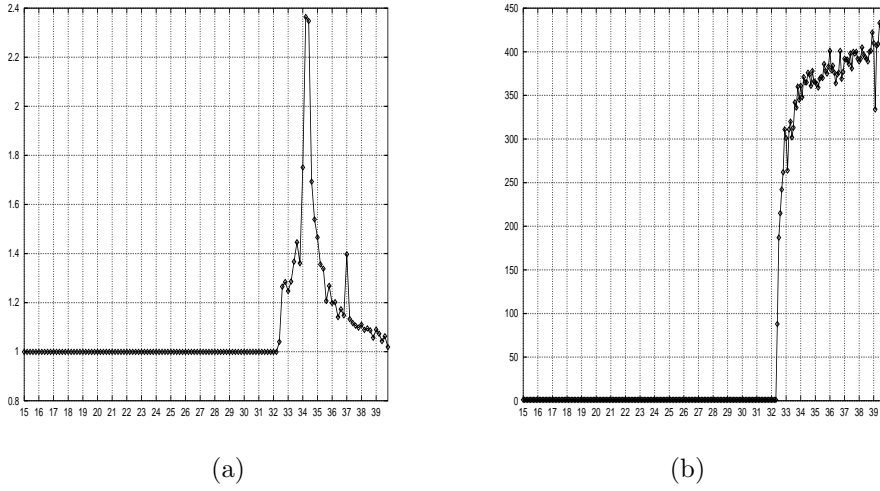


Figure 5.25: (a) Average number of impacts per period as V_{in} is increased; (b) Total number of skippings over 2000 periods for different V_{in} values.

Therefore, as V_{in} increases, the system states at the fourth stroboscopic point match the infinite stretching condition better and better, and more and more impacts occur in the last cycle of the $P(\cdot, 5)$. This yields a corresponding peak in the diagram reported in Fig. 5.25. In fact, a 5T-unstable periodic orbit fulfilling the infinite stretching condition was found for

$$V_{in} = 34.33998523V,$$

giving infinite impacts in the last cycle.

Finally, the jump from the small scale chaotic evolution, characterized by one impact per cycle, to the five-zones attractor is expected to take place when the first skipping occurs. This is confirmed by Fig. 5.25, where the number of skippings over 2000 cycles is plotted against the input voltage. We notice that the number of skippings becomes different from zero exactly when the large scale chaos appears, quickly settling down around 400 when the input voltage is increased. It is relevant to point out that the $P(7, 5)$ orbit, described above, is characterized by one skipping every five cycles [Olivar and Fossas, 1995], i.e. 400 skippings over 2000 periods. This confirms again that the large scale attractor is organised around this type of unstable periodic solution.

5.6 Tables of Local and Global Bifurcations

In this section, a summary of the bifurcations found in this chapter is presented in table-form. Some notation is introduced to distinguish the different signatures.

Table 5.2: Bifurcations in the main attractor: ITB stands for instant torsion bifurcation, PD for period-doubling bifurcation, IC1 for interior crisis of first kind, IC2 for interior crisis of second kind, BC for boundary crisis, S^j for a j T-periodic sink, I^j for a j T-periodic inverse saddle and C^j for a j -piece chaotic attractor.

V_{in}	Bifurcation	Signature
11.75238095	ITB	Stable Equilibrium $\rightarrow S^1$
24.516	PD	$S^1 \rightarrow I^1 + S^2$
31.121	PD	$S^2 \rightarrow I^2 + S^4$
32.095	PD	$S^4 \rightarrow I^4 + S^8$
32.239	PD	$S^8 \rightarrow I^8 + S^{16}$
32.270	PD	$S^{16} \rightarrow I^{16} + S^{32}$
32.277	PD	$S^{32} \rightarrow I^{32} + S^{64}$
32.2779	PD	$S^{64} \rightarrow I^{64} + S^{128}$
32.2782	PD	$S^{128} \rightarrow I^{128} + S^{256}$
32.2784	IC1	$C^{128} \rightarrow C^{64}$
32.2787	IC1	$C^{64} \rightarrow C^{32}$
32.2798	IC1	$C^{32} \rightarrow C^{16}$
32.286	IC1	$C^{16} \rightarrow C^8$
32.294	IC2	$C^8 \rightarrow C^8$
32.304	IC1	$C^8 \rightarrow C^4$
32.336	IC2	$C^4 \rightarrow C^1$
32.529	BC	$C^1 \rightarrow S^5$
32.587	IC2	$S^5 \rightarrow C^1$
34.76	BC	$C^1 \rightarrow S^5$
34.78	IC2	$S^5 \rightarrow C^1$

Table 5.3: Bifurcations in the secondary 3T-branches: ITB stands for instant torsion bifurcation, SGR for stability change grazing bifurcation, PD for period-doubling bifurcation, ICB for instant chaos bifurcation, IC1 for interior crisis of first kind, BC for boundary crisis, GR for standard grazing bifurcation, SS for saddle-saddle grazing bifurcation, R- for a reverse bifurcation, CS for a chaotic saddle, GU^j for a grazing j T-periodic saddle, GS^j for a grazing j T-periodic sink, S^j for a j T-periodic sink, I^j for a j T-periodic inverse saddle and C^j for a j -piece chaotic attractor.

V_{in}	Bifurcation	Signature	Localization
11.75238095	ITB	Stable Equilibrium $\rightarrow 2GU^3 + 2CS$	both 3T-branches
13.37574119	SGR	$GU^3 \rightarrow GS^3$	2 nd 3T-branch
13.413	PD	$GS^3 \rightarrow I^3 + S^6$	2 nd 3T-branch
13.49654974	GR	$GU^3 \rightarrow GU^3$	1 st 3T-branch
13.542	ICB	$S^6 \rightarrow C^6$	2 nd 3T-branch
13.715	IC1	$C^6 \rightarrow C^3$	2 nd 3T-branch
13.880	BC	$C^3 \rightarrow \emptyset$	2 nd 3T-branch
16.827327	SS	$\emptyset \rightarrow 2GU^3$	2 nd 3T-branch
17.70852037	SS	$\emptyset \rightarrow 2GU^3$	1 st 3T-branch
18.154710	SS	$\emptyset \rightarrow 2GU^3$	2 nd 3T-branch
18.4188819	SS	$\emptyset \rightarrow 2GU^3$	1 st 3T-branch
18.66444	SS	$\emptyset \rightarrow 2GU^3$	2 nd 3T-branch
(18.66,21.45)	SS and	unstable orbit	1 st and 2 nd
	R-SS	adding process	3T-branches
21.28976130	SGR	$GU^3 \rightarrow GU^3$	2 nd 3T-branch
21.45	R-SS	$2GU^3 \rightarrow \emptyset$	1 st 3T-branch
21.5207439	R-SS	$2GU^3 \rightarrow \emptyset$	2 nd 3T-branch
23.08802931	R-SS	$2GU^3 \rightarrow \emptyset$	1 st 3T-branch
23.937480	R-SS	$2GU^3 \rightarrow \emptyset$	2 nd 3T-branch
24.160	R-BC	$C^3 \rightarrow \emptyset$	2 nd 3T-branch
24.79785521	GR	$GU^3 \rightarrow GU^3$	2 nd 3T-branch
25.01012624	R-ICB	$C^3 \rightarrow \emptyset$	2 nd 3T-branch
32.59802	GR	$GU^3 \rightarrow GU^3$	1 st 3T-branch
32.71246615	GR	$GU^3 \rightarrow GU^3$	1 st 3T-branch
34.59011172	R-SS	$2GU^3 \rightarrow \emptyset$	1 st 3T-branch

Table 5.4: Bifurcations in the 6T-secondary attractor: SN stands for saddle-node bifurcation, PD for period-doubling bifurcation, IC1 for interior crisis of first kind, BC for boundary crisis, S^j for a j T-periodic sink, I^j for a j T-periodic inverse saddle, D^j for a j T-periodic direct saddle and C^j for a j -piece chaotic attractor.

V_{in}	Bifurcation	Signature
29.905725	SN	$\emptyset \rightarrow S^6 + D^6$
30.07633	PD	$S^6 \rightarrow I^6 + S^{12}$
30.125	PD	$S^{12} \rightarrow I^{12} + S^{24}$
32.1365	PD	$S^{24} \rightarrow I^{24} + S^{48}$
30.1389	PD	$S^{48} \rightarrow I^{48} + S^{96}$
30.1395	PD	$S^{96} \rightarrow I^{96} + S^{192}$
30.14175	IC1	$C^{24} \rightarrow C^{12}$
30.1485	IC1	$C^{12} \rightarrow C^6$
30.175	BC	$C^6 \rightarrow \emptyset$

Table 5.5: Bifurcations in the 12T-secondary attractor: SN stands for saddle-node bifurcation, PD for period-doubling bifurcation, IC1 for interior crisis of first kind, BC for boundary crisis, S^j for a j T-periodic sink, I^j for a j T-periodic inverse saddle, D^j for a j T-periodic direct saddle and C^j for a j -piece chaotic attractor.

V_{in}	Bifurcation	Signature
32.13630	SN	$\emptyset \rightarrow S^{12} + D^{12}$
32.15119	PD	$S^{12} \rightarrow I^{12} + S^{24}$
32.15710	PD	$S^{24} \rightarrow I^{24} + S^{48}$
32.15845	PD	$S^{48} \rightarrow I^{48} + S^{96}$
32.15885	PD	$S^{96} \rightarrow I^{96} + S^{192}$
32.15925	IC1	$C^{48} \rightarrow C^{24}$
32.16040	IC1	$C^{24} \rightarrow C^{12}$
32.16588	BC	$C^{12} \rightarrow \emptyset$

Chapter 6

Control of Chaos in the Buck Converter

Abstract

In this chapter, three different methods are deduced for controlling chaos in the PWM controlled buck converter, involving suppression of the chaotic regime by stabilizing an unstable periodic orbit. In the first section, the OGY method is applied to stabilize the unstable 1T-periodic branch of the main attractor. Stabilization in the presence of noise is studied, and the mean time of stabilization is also checked. With the second method, some schemes of control via time-delay are tried with this converter. In the case of the buck, the domain of control can be efficiently computed since analytical computations can be carried over. Finally, the idea of the third method consists essentially in bypassing the switching logic imposed by the PWM, and like the previous methods is also valid for stabilizing kT -periodic orbits with $K > 1$. To guess the robustness of the control, some simulations are performed with sinusoidal perturbations.

6.1 Introduction

Control of chaos, meaning suppression of the chaotic regime in a system by means of a small, time-dependent perturbation, has been a subject of interest in recent years [Shinbrot, Grebogi, Ott and Yorke, 1993]. In [Ott, Grebogi and Yorke, 1990], it was pointed out that the many unstable periodic orbits (UPOs) embedded in a strange attractor could be used to produce regular behaviour. This is to the advantage of engineers trying to control nonlinear systems in which chaotic fluctuations are present but undesirable.

Two main groups of methods of control of chaos, such that the feedback perturbation vanishes on the target orbit, have been considered in the literature:

The first method was proposed by Ott, Grebogi and Yorke [Ott, Grebogi and Yorke, 1990], where small perturbations to an accessible parameter are introduced. The method exploits the fact that during its wandering over the strange attractor, the system will eventually come near the target UPO on a given Poincaré section. When this happens, and only then, a small perturbation is applied to the parameter so as to make the orbit land on the stable manifold of the target orbit the next time it crosses the Poincaré section. One drawback is that the method is not suitable for complex systems, since a nontrivial computer analysis must be performed at each crossing of the Poincaré section. Moreover, small noise can drive the orbit away from the target orbit, and the control method must then wait for a while until the system comes near to the target orbit again.

The method proposed by Pyragas [Pyragas, 1992], called time-delayed autosynchronization (TDAS), involves a control signal formed with the difference between the current state of the system and the state of the system delayed by one period of the UPO. One variant, ETDAS [Socolar, Sukow and Gauthier, 1994], uses a particular linear combination of signals from the system delayed by integer multiples of the UPO's period. Still another variant [de Sousa, Lichtenberg and Lieberman, 1996] uses a nonlinear function of the difference between the present state and the delayed state. TDAS and its variants have the advantage that the only information needed about the target orbit is its period, and that no computer processing must be done to generate the control signal. The method has even been applied to systems described by partial differential equations [Bleich and Socolar, 1996b]. In general, the feedback gain which successfully stabilizes the orbit lies in a finite, and often narrow, orbit-dependent range. In the space of the feedback gain and the bifurcation parameter(s) of the system, the region where the TDAS can be applied with success is called the domain of control. In [Bleich and Socolar, 1996a] a method was proposed to compute the domain of control of a given system without having to explicitly integrate the resulting time-delay equations, which is a nontrivial matter due to the choice of initial conditions [Hale and Verduyn Lunel, 1993]. Essentially, the method reduces to the computation of the index around the origin of a curve in the complex plane.

Finally, a proposed third method of stabilization consists essentially in bypassing the switching logic and working in open loop, using the switching times of the target unstable periodic orbit. Although the method is quite simple and easily implemented, it is also quite general, and can be considered as an alternative to the OGY methods [Hunt, 1991; Ogorzalek, 1993; Romeiras, Grebogi, Ott and Dayawansa, 1992], which can be used when the system is in chaotic regime. Although the proposed method works in open loop, it stabilizes to an orbit of the closed-loop ramp-controlled system, and thus, as in the case of the OGY methods, it is specially interesting if the target orbit has some useful dynamical properties that should be preserved. In fact, since in chaotic regime there are many (possibly infinite) unstable periodic orbits embedded in the attractor, some of these may maximize some measure of the performance of the system in a way not possible for stable orbits.

6.2 Control of Chaos: The OGY Method

The OGY method [Ott, Grebogi and Yorke, 1990], which will be described and used in this section to stabilize unstable periodic orbits embedded in the chaotic attractor, has been thoroughly studied in the scientific community. For example, in a recent article [Aston and Bird, 1995] an enhanced OGY method is proposed, and velocity of the convergence is studied. Moreover, the robustness of the control against small perturbations in the parameters is also deduced. It has been applied with success to a great variety of systems in almost all areas and it is continuously revised in the literature. From 1990, other alternative methods have been deduced with the same aim, i.e. to stabilize unstable periodic orbits. The OGY method can be applied when the equations of the dynamics of the system are known as in the case of the converter, and from a sampled sequence of values of the chaotic signal when the equations are not known. Some type of OGY method has already been applied to a version of a buck converter [Poddar, Chakrabarty and Banerjee, 1995; Chakrabarty and Banerjee, 1995] stabilizing 1T-periodic and 2T-periodic unstable orbits, taking advantage of the piecewise-linear character of the system.

6.2.1 The Control Algorithm

The main idea of Ott, Grebogi and Yorke was to consider that there can be a great number of unstable periodic orbits embedded in the chaotic attractor. Thus, varying an available parameter $p \in [p^* - \Delta p_{max}, p^* + \Delta p_{max}]$ slightly in the system, the orbit can be stabilized, Δp_{max} being the maximum perturbation allowed in the available parameter, and p^* the value of the parameter for which the unstable periodic orbit is localized.

Let the system be described by

$$X_{n+1} = P(X_n, p_n)$$

where X is the state of the system, p_n is the available parameter and P is a map which describes the dynamics, which in our case will be some iteration of the Poincaré map. Let $x^* = P(x^*, p^*)$ be the unstable orbit to be stabilized. A first order approximation of P near (x^*, p^*) is

$$X_{n+1} \approx x^* + L(X_n - x^*) + w(p_n - p^*)$$

or equivalently

$$\Delta X_{n+1} \approx L \Delta X_n + w \Delta p_n$$

where $\Delta X_n = X_n - x^*$, $\Delta p_n = p_n - p^*$, $L = D_X P(x^*, p^*)$ and $w = D_p P(x^*, p^*)$. We also assume that x^* is a saddle periodic orbit with a one-dimensional stable manifold and a one-dimensional unstable manifold with stable direction e_s and unstable direction e_u (with respective stable eigenvalue λ_s and unstable eigenvalue λ_u). Thus L can be expressed

$$L = \lambda_u e_u f_u + \lambda_s e_s f_s$$

being f_s and f_u the contravariant vectors of e_s, e_u (and thus $f_s e_s = f_u e_u = 1$ and $f_u e_s = f_s e_u = 0$).

The idea of the method is to let the system act until the orbit is near the unstable orbit. At that moment the value for p is modified from p^* to $p^* + \Delta p$. With this small perturbation, the localization of the unstable orbit and its stable manifold is also varied in order to force the orbit to stay in the stable manifold of x^* in the next iteration. Thus, $p_n = p^* + \Delta p_n$ must be chosen to satisfy (in a first order approximation)

$$f_u \Delta X_{n+1} = 0$$

and then,

$$\Delta p_n = -\lambda_u \frac{f_u \Delta X_n}{f_u w} \quad \text{if } f_u w \neq 0$$

This perturbation is applied only if it does not exceed Δp_{max} . If this is not the case, $\Delta p_n = 0$ and $p = p^*$ is maintained. Theoretically, once the value x_{n+1} is on the stable manifold of x^* , the perturbation can be reset to zero. In practice, since the value for Δp_n was computed to first order approximation, the following iterations will not be exactly on the stable manifold and the orbit will be unstabilized. Thus, the perturbation must be applied at each iteration.

6.2.2 Simulations

The first step to implement the algorithm numerically is to compute the unstable orbits desired for stabilization. They were computed as in Chapter 3, by writing down the necessary equations for 1T-periodicity with one single switching in each cycle, and following the main branch attractor beyond the first period-doubling bifurcation at $V_{in} = 24.516V$. The derivatives of P with respect to the state and the parameter (which will be V_{in} in all the cases) are computed with a second order approximation. The maximum allowed perturbation is set to $2V$.

One hundred initial conditions were taken for each value of the parameter, and the mean time for stabilization was computed. Results are shown in Table 7.1 [Roncero and Olivar, 1996].

In general, the time for stabilization is lower for lower input voltage. However, for some initial conditions with low input voltage the system stabilizes in the stable 2T-periodic orbit of the system, and in this case the OGY method does not work properly.

Stabilization was also studied when a random noise of certain amplitude is injected at the end of every cycle. Several simulations are shown in Fig. 6.1. First, a stabilization is tried without noise, and later a noise with amplitude $\sigma = 10mV$ is injected to the state at every end of the cycle, and the system is considered under control if the signal is maintained inside a band of 2σ amplitude. The mean time of control when some noise of certain amplitude is applied is shown in Table 7.2. There, initial conditions are given in the unstable periodic orbit, and noise is applied in successive iterations. The percentage of the iterations inside the control band is computed. The results show that the percentage of control is higher with lower noise, and stabilizes approximately to 45% when the level of noise is raised.

Table 6.1: Mean number of cycles (M.N.C.) of stabilization and mean time (M.T.) of stabilization for different values of the input voltage.

V_{in} (in V)	M.N.C.	M.T. (in ms)	V_{in} (in V)	M.N.C.	M.T. (in ms)
26.00	28	11.20	39.00	161	64.40
27.00	32	12.80	40.00	225	90.00
28.00	32	12.80	41.00	172	68.80
29.00	25	10.00	42.00	252	100.80
30.00	39	15.60	43.00	236	94.40
31.00	31	12.40	44.25	201	80.40
31.75	89	35.60	45.00	230	92.00
33.50	155	62.00	46.00	238	95.20
34.00	146	58.40	47.50	185	74.00
35.00	114	45.60	47.50	185	74.00
36.25	194	77.60	48.75	233	93.20
37.25	116	46.40	50.00	212	84.40
38.50	224	89.60			

Table 6.2: Mean percentage of the orbit under control (M.P.C.), depending on the noise amplitude σ . $V_{in} = 35V$. Initial conditions are taken in the unstable 1T-periodic orbit.

σ (in V)	M.P.C.	σ (in V)	M.P.C.	σ (in V)	M.P.C.
0.005	97	0.013	39	0.017	42
0.010	82	0.014	43	0.018	46
0.011	59	0.015	43	0.019	43
0.012	57	0.016	39	0.020	44

6.3 Time-delay Autosynchronization

This technique involves continuous feedback of signals delayed by the orbit's period. One variant, ETDAS, uses information from further back in the past. In both cases, the feedback signal vanishes on the target periodic orbit and hence the stabilized periodic orbit belongs to the original dynamical system. Furthermore, this control method only requires the knowledge of the period of the unstable orbit.

In general, the amount of feedback gain needed to achieve stabilization varies with the bifurcation parameter of the system, resulting in a domain of control which can be computed without having to deal with the explicit integration of time-delay equations.

The main result is that the function g from the unit circle to the complex plane whose index determines the success of ETDAS can be analytically com-

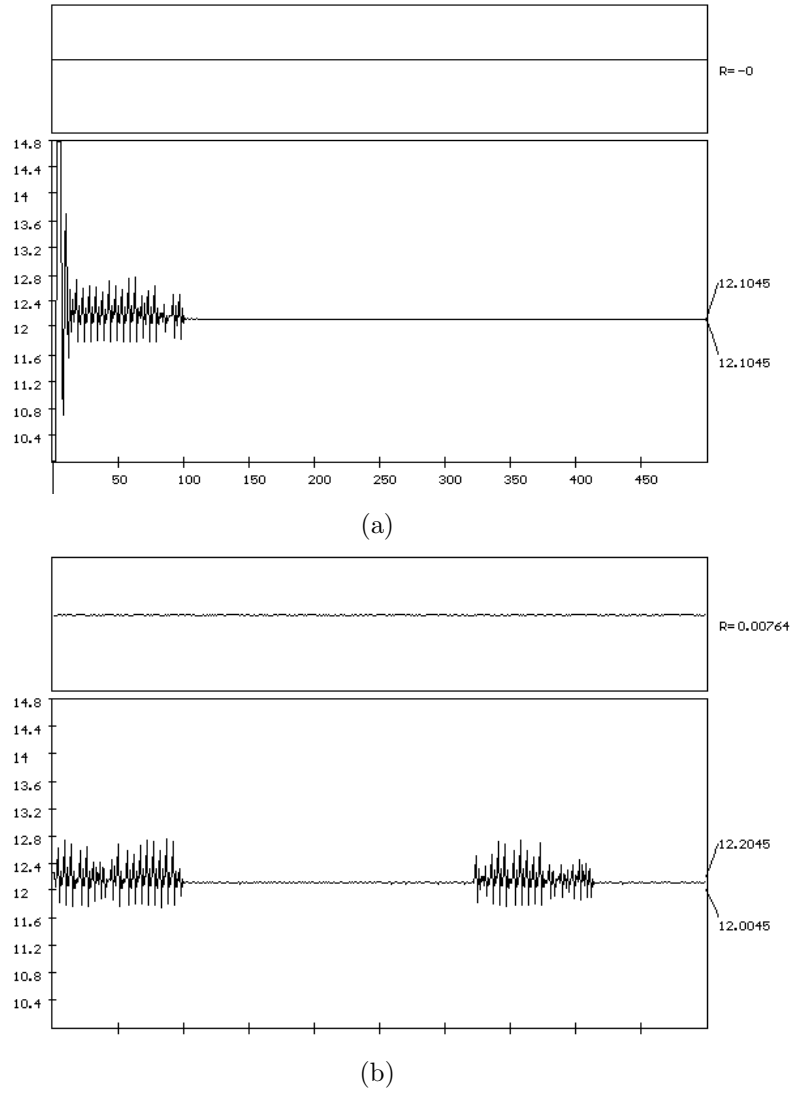


Figure 6.1: (a) Stabilized orbit for $V_{in} = 35V$. Initial conditions are taken at $(0, 0)$; no noise ($R = 0$) is added at the end of each cycle. (b) Stabilized orbit for $V_{in} = 35V$. Initial conditions are taken at the unstable 1T-periodic orbit. Random noise R of amplitude $\sigma = 10mV$ is added at every end of cycle, which is represented at the top of (b).

puted for the buck converter. The index can then be numerically evaluated and the domain of control can easily be constructed.

6.3.1 ETDAS for Variable Structure Systems

The PWM controlled buck converter, as well as other PWM controlled DC-DC converters, can be considered as particular cases of dynamical systems with equations of the form

$$\dot{x}(t) = A(t, [x])x(t) + b(t, [x]), \quad (6.1)$$

where $x, b \in \mathbb{R}^n$, $A \in \mathcal{M}(\mathbb{R}^n)$. We use the notations $A(t, [x])$ and $b(t, [x])$ to indicate that both A and b are local functionals of x . For the PWM controlled converters, A and b are piecewise constant, typically changing their values when a linear function of x crosses a given periodic function of t .

Consider now a 1T-periodic orbit $x^*(t)$ of this system and a nearby orbit $x(t)$. We wish to study the evolution of $y(t) = x(t) - x^*(t)$. We are principally concerned with unstable orbits $x^*(t)$, and our goal will be to modify the right-hand side of (6.1) so as to render $x^*(t)$ stable; that is, $\lim_{t \rightarrow +\infty} y(t) = 0$ for $x(t)$ initially close enough to $x^*(t)$. We do this by means of extended time-delay autosynchronization. Consider the following equation:

$$\dot{x}(t) = A(t, [x])x(t) + b(t, [x]) + \eta M(t, [x])(x(t) - (1-r) \sum_{k=1}^{+\infty} r^{k-1} x(t-k\tau)), \quad (6.2)$$

where $M \in \mathcal{M}(\mathbb{R}^n)$ is a matrix indicating how the delayed signal is fed back to the system, and η is the strength of the feedback gain.

We will study the evolution of $y(t)$ to first order in y under (6.2). One has

$$\begin{aligned} \dot{y}(t) &\approx A(t, [x])x(t) - A(t, [x^*])x^*(t) + b(t, [x]) - b(t, [x^*]) \\ &+ \eta M(t, [x^*])(y(t) - (1-r) \sum_{k=1}^{+\infty} r^{k-1} y(t-k\tau)) \end{aligned}$$

where the τ -periodicity of x^* has been used, terms of higher order in y have been discarded. Expanding the functionals around x^* gives

$$\begin{aligned} \dot{y}(t) &\approx A(t, [x^*])y(t) \\ &+ \left[\int_{-\infty}^{\infty} \sum_k \frac{\delta A(t, [x])}{\delta x_k(t')} \bigg|_{x=x^*} y_k(t') dt' \right] x^*(t) + \int_{-\infty}^{\infty} \sum_k \frac{\delta b(t, [x])}{\delta x_k(t')} \bigg|_{x=x^*} y_k(t') dt' \\ &+ \eta M(t, [x^*])(y(t) - (1-r) \sum_{k=1}^{+\infty} r^{k-1} y(t-k\tau)) \end{aligned} \quad (6.3)$$

Since the functionals are local, the functional derivatives will yield delta functions, and ignoring the higher order terms we get a variable coefficient, linear time-delayed differential equation for y which, with suitable definitions, can be written in the form

$$\dot{y}(t) = A_0(t)y(t) + \sum_{k=1}^{+\infty} A_k(t)y(t-k\tau), \quad (6.4)$$

where the time dependence of the coefficients is known since $x^*(t)$ is known. Notice also that these coefficients are periodic functions of time, since their explicit dependence of time is periodic and x^* is also periodic. From (6.3) and (6.4) one can easily read

$$A_k(t) = -(1-r)\eta M(t, [x^*])r^{k-1}, \quad k = 1, 2, \dots \quad (6.5)$$

We are not interested in the general solution of the time-delayed equation (6.4), but rather we would like to know if its zero solution is asymptotically stable. To this end, we look for solutions of the form

$$y(t) = p_\lambda(t)e^{\lambda t/\tau},$$

with $\lambda \in \mathbb{C}$ and $p_\lambda(t + \tau) = p_\lambda(t)$. This yields for p_λ an ordinary differential equation

$$\dot{p}_\lambda(t) = (A_0(t) - \frac{\lambda}{\tau}\mathbb{I})p_\lambda(t) + \sum_{k=1}^{+\infty} e^{-k\lambda} A_k(t)p_\lambda(t),$$

whose solution for a given initial condition can be expressed in terms of an evolution operator $U_\lambda(t)$ defined by

$$p_\lambda(t) = e^{-\lambda t/\tau} U_\lambda(t) p_\lambda(0)$$

and satisfying the equation

$$\dot{U}_\lambda(t) = \left(A_0(t) + \sum_{k=1}^{+\infty} e^{-k\lambda} A_k(t) \right) U_\lambda(t) \quad (6.6)$$

with initial condition $U_\lambda(0) = \mathbb{I}$. The general solution to (6.6) can be formally expressed as

$$U_\lambda(t) = \mathcal{T} \exp \left(\int_0^t (A_0(t') + \sum_{k=1}^{+\infty} e^{-k\lambda} A_k(t')) dt' \right), \quad (6.7)$$

where \mathcal{T} stands for time ordered product (this formal solution is also known as Peano-Baker series in the mathematical literature [Rugh, 1996]; it boils down to the standard exponential matrix if the coefficients of the differential equation are constant). In any case, $U_\lambda(t)$ retains the fundamental properties

$$U_\lambda(t_1 + t_2) = U_\lambda(t_1)U_\lambda(t_2), \quad U_\lambda(-t) = U_\lambda^{-1}(t). \quad (6.8)$$

Using (6.8) the condition $p_\lambda(t + \tau) = p_\lambda(t)$ is easily seen to be equivalent to

$$(e^{-\lambda} U_\lambda(\tau) - \mathbb{I}) p_\lambda(0) = 0$$

which implies

$$\det(e^{-\lambda} U_\lambda(\tau) - \mathbb{I}) = 0 \quad (6.9)$$

This equation determines the values of λ such that $p_\lambda(t)$ is a solution of our equation. As we want $y(t) = e^{\lambda t/\tau} p_\lambda(t)$ go asymptotically to zero, we must demand that $\Re \lambda < 0$ for all the solutions of (6.9). Defining the Floquet multiplier $\mu = e^\lambda$ and $U(\tau; \mu^{-1}) = U_\lambda(\tau)$, equation (6.9) becomes

$$g(\mu^{-1}) \equiv \det(\mu^{-1}U(\tau; \mu^{-1}) - \mathbb{I}) = 0 \quad (6.10)$$

with

$$U(\tau; \mu^{-1}) = \mathcal{T} \exp \left(\int_0^\tau (A_0(t) + \sum_{k=1}^{+\infty} \mu^{-k} A_k(t)) dt \right). \quad (6.11)$$

Summing up, stability of x^* is equivalent to the requirement that all the zeros of $g(\mu^{-1})$ lie outside the unit circle ($\|\mu^{-1}\| > 1 \Leftrightarrow \Re \lambda < 0$). Using (6.5), the series in (6.11) can be summed to yield

$$U(\tau; \mu^{-1}) = \mathcal{T} \exp \left(\int_0^\tau (A_0(t) - (1-r)\eta M(t, [x^*]) \frac{\mu^{-1}}{1-r\mu^{-1}}) dt \right). \quad (6.12)$$

For $r < 1$, $U(\tau; \mu^{-1})$, as a function of μ^{-1} , and hence $g(\mu^{-1})$, has no poles inside the unit circle. Now, the number of zeros of $g(\mu^{-1})$ inside the unit circle equals the index with respect to the origin of the curve traced by $g(\mu^{-1})$ when μ^{-1} runs over the unit circle. Therefore, the solution will be stable if and only if this index is zero. This way of computing the number of zeros inside the unit circle is numerically preferred to the obvious option of actually computing the zeros, which in fact are infinite (due to the time-delay character of the original equation).

The equations derived so far are completely general. In practice, however, analytical computation of $U(\tau; \mu^{-1})$ using (6.12) is not possible except for very special cases, so one must fall back on the defining differential equation (6.6) and numerically integrate it between 0 and τ . For the buck converter, the functional derivatives appearing in (6.3) are specially simple (in fact, A is constant), and the differential equation (6.6) can be analytically integrated. This is done for several choices of M in the next subsection.

6.3.2 Time-delayed Feedback for the Buck Converter

Figure 6.2 shows the basic scheme of the PWM controlled buck converter, together with the two different schemes we have studied to implement ETDAS. The control u can be written in terms of the step function

$$u(t) = 1 - \theta(v(t) - v_r(t))$$

The control signal $\Delta v(t)$ is given by

$$\Delta v(t) = \eta \left(v(t) - (1-r) \sum_{k=1}^{+\infty} r^{k-1} v(t - k\tau) \right),$$

where η is a dimensionless feedback gain and $r \in [0, 1)$ determines the relative weight of the increasingly delayed contributions. The case $r = 0$ corresponds to

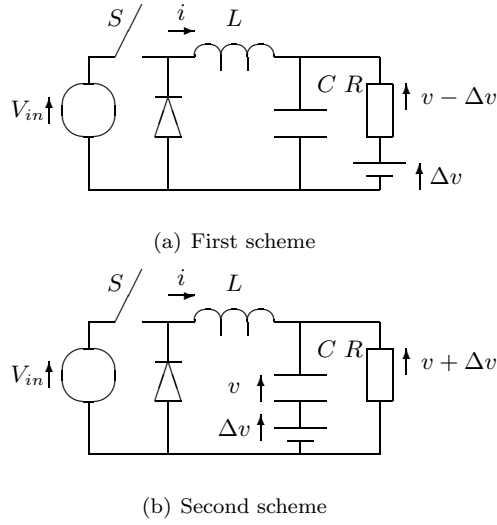


Figure 6.2: The two feedback schemes for time-delay autosynchronization of the buck converter.

TDAS. $\tau > 0$ is the period of the target UPO which, in our case, is always a multiple of the ramp period T . Notice that $\Delta v(t) \equiv 0$ if $v(t)$ is periodic with period τ .

We are primarily concerned with the stabilization of UPOs which cross the ramp exactly once every cycle, and such that at the beginning of every cycle one has $v(t) > v_r(t)$. More general situations can easily be treated as well, as will become clear in this section.

For the buck converter, one has

$$A(t, [x]) = \begin{pmatrix} -\frac{1}{RC} & \frac{1}{C} \\ -\frac{1}{L} & 0 \end{pmatrix} \equiv A \quad \text{and} \quad b(t, [x]) = \begin{pmatrix} 0 \\ \frac{V_{in}}{L} \end{pmatrix} (1 - \theta(v(t) - v_r(t)))$$

so that all the functional derivatives of $A(t, [x])$ are zero, and the only nonzero functional derivative of $b(t, [x])$ is

$$\frac{\delta b_2(t, [x])}{\delta v(\tau)} = -\frac{V_{in}}{L} \delta(v(t) - v_r(t)) \delta(t - \tau).$$

Then, equation (6.3) becomes, with $\tau = T$,

$$\begin{aligned} \dot{y}(t) = & Ay(t) - \frac{V_{in}}{L} \begin{pmatrix} 0 & 0 \\ 1 & 0 \end{pmatrix} y(t) \delta(v^*(t) - v_r(t)) \\ & + \eta M(t, [x^*]) \left(y(t) - (1 - r) \sum_{k=1}^{+\infty} r^{k-1} y(t - kT) \right) \end{aligned} \quad (6.13)$$

It is easy to see that the two feedback schemes described previously correspond to the following choices for the matrix M :

1.

$$M(t, [x]) = \begin{pmatrix} \frac{1}{RC} & 0 \\ 0 & 0 \end{pmatrix} \equiv M_1$$

2.

$$M(t, [x]) = \begin{pmatrix} -\frac{1}{RC} & 0 \\ -\frac{1}{L} & 0 \end{pmatrix} \equiv M_2$$

Integration of the resulting differential equation is very similar for the two cases. We will present the explicit computation of $g(\mu^{-1})$.

In the first feedback scheme one has

$$\begin{aligned} A_0(t) &= A + \eta M_1 - \frac{V_{in}}{L} \begin{pmatrix} 0 & 0 \\ 1 & 0 \end{pmatrix} \delta(v^*(t) - v_r(t)) \\ A_k(t) &= -\eta(1-r)r^{k-1}M_1, \quad k = 1, 2, \dots \end{aligned}$$

and the differential equation for $U(t)$ is, adding up the geometrical series,

$$\dot{U}(t) = \begin{pmatrix} -\frac{1}{RC}(1-\eta+\eta\mu^{-1}\frac{1-r}{1-r\mu^{-1}}) & \frac{1}{C} \\ -\frac{1}{L} - \frac{V_{in}}{L}\delta(v^*(t) - v_r(t)) & 0 \end{pmatrix} U(t) \quad (6.14)$$

If we write

$$U(t) = \begin{pmatrix} u_1(t) & u_2(t) \\ u_3(t) & u_4(t) \end{pmatrix}$$

we get two uncoupled systems of dimension two

$$\begin{aligned} \dot{u}_1(t) &= -a_1 u_1(t) + \frac{1}{C} u_3(t) \\ \dot{u}_2(t) &= -a_1 u_2(t) + \frac{1}{C} u_4(t) \\ \dot{u}_3(t) &= -\frac{1}{L} u_1(t) - \frac{V_{in}}{L} \delta(v^*(t) - v_r(t)) u_1(t) \\ \dot{u}_4(t) &= -\frac{1}{L} u_2(t) - \frac{V_{in}}{L} \delta(v^*(t) - v_r(t)) u_2(t) \end{aligned}$$

where

$$a_1 = \frac{1}{RC} \left(1 - \eta + \eta\mu^{-1} \frac{1-r}{1-r\mu^{-1}} \right),$$

with the initial conditions $u_1(0) = 1, u_2(0) = 0, u_3(0) = 0, u_4(0) = 1$. Therefore, we only need to solve twice the single system

$$\begin{aligned} \dot{x}(t) &= -a_1 x(t) + \frac{1}{C} y(t) \\ \dot{y}(t) &= -\frac{1}{L} x(t) - \frac{V_{in}}{L} \delta(v^*(t) - v_r(t)) x(t) \end{aligned} \quad (6.15)$$

for $t \in [0, T]$ with the two sets of initial conditions $(1, 0)$ and $(0, 1)$. If we assume that for each cycle of the auxiliary signal $v_r(t)$ there is one and only one $t = t_c \in (0, T)$ such that the system switches topology, then the delta function appearing in the above equation is

$$\delta(v^*(t) - v_r(t)) = \beta \delta(t - t_c), \quad (6.16)$$

where

$$\beta = \frac{1}{|\dot{v}^*(t_c) - \dot{v}_r(t_c)|} \quad (6.17)$$

is the inverse of the absolute value of the slope with which $v^*(t)$ crosses the ramp. This is well defined because $v(t)$ is everywhere differentiable, in contrast to $i(t)$, which is not differentiable at $t = t_c$. We get thus the time-varying linear system

$$\dot{x}(t) = -a_1x(t) + \frac{1}{C}y(t) \quad (6.18)$$

$$\dot{y}(t) = -\frac{1}{L}x(t) - \frac{\beta V_{in}}{L}\delta(t - t_c)x(t) \quad (6.19)$$

Although this is a variable coefficient system, it can be solved by Laplace transform since the delta function makes computing the transform of the last term of (6.19) trivial. We skip the details and write down the general solution for $t \in [0, T]$:

$$\begin{aligned} x(t) &= \left(-x(0)\frac{a_1 - \gamma_1}{2\gamma_1} + y(0)\frac{1}{\gamma_1 C} \right) e^{-\frac{1}{2}(a_1 - \gamma_1)t} \\ &\quad + \left(x(0)\frac{a_1 + \gamma_1}{2\gamma_1} - y(0)\frac{1}{\gamma_1 C} \right) e^{-\frac{1}{2}(a_1 + \gamma_1)t} \\ &\quad - \frac{V_{in}\beta}{LC\gamma_1}x(t_c)\theta(t - t_c) \left(e^{-\frac{1}{2}(a_1 - \gamma_1)(t - t_c)} - e^{-\frac{1}{2}(a_1 + \gamma_1)(t - t_c)} \right) \\ y(t) &= \left(-x(0)\frac{1}{L\gamma_1} + y(0)\frac{a_1 + \gamma_1}{2\gamma_1} \right) e^{-\frac{1}{2}(a_1 - \gamma_1)t} \\ &\quad + \left(x(0)\frac{1}{L\gamma_1} - y(0)\frac{a_1 - \gamma_1}{2\gamma_1} \right) e^{-\frac{1}{2}(a_1 + \gamma_1)t} \\ &\quad - \frac{V_{in}\beta}{2L\gamma_1}x(t_c)\theta(t - t_c) \left((a_1 + \gamma_1)e^{-\frac{1}{2}(a_1 - \gamma_1)(t - t_c)} - (a_1 - \gamma_1)e^{-\frac{1}{2}(a_1 + \gamma_1)(t - t_c)} \right) \end{aligned}$$

where

$$\gamma_1 = \sqrt{a_1^2 - \frac{4}{LC}}$$

and $x(t_c)$ is defined evaluating the expression for $x(t)$ at $t = t_c$. Notice that $x(t)$ is continuous at $t = t_c$, while $y(t)$ has a jump of value $-\beta V_{in}/Lx(t_c)$, as follows from (6.19).

Now putting $x(0) = 1$, $y(0) = 0$ we obtain, at $t = T$, $u_1(T)$ and $u_3(T)$, while $x(0) = 0$ and $y(0) = 1$ yield us $u_2(T)$ and $u_4(T)$. Then we can compute

$$\begin{aligned} g(\mu^{-1}) &= \det \begin{vmatrix} \mu^{-1}u_1(T) - 1 & \mu^{-1}u_2(T) \\ \mu^{-1}u_3(T) & \mu^{-1}u_4(T) - 1 \end{vmatrix} \\ &= \mu^{-2} (u_1(T)u_4(T) - u_2(T)u_3(T)) - \mu^{-1} (u_1(T) + u_4(T)) + 1 \end{aligned} \quad (6.20)$$

which, after a little algebra, yields

$$g_1(\mu^{-1}) = \mu^{-2}e^{-a_1T} - 2\mu^{-1}e^{-\frac{1}{2}a_1T} \left(\cosh\left(\frac{1}{2}\gamma_1T\right) - \frac{V_{in}\beta}{\gamma_1LC} \sinh\left(\frac{1}{2}\gamma_1T\right) \right) + 1 \quad (6.21)$$

Notice that, although γ_1 introduces a line cut where its argument vanishes, if we analytically extend the above expression by its series expansion, only even powers of γ_1 appear, and thus $g_1(\mu^{-1})$ has only pole-type singularities (outside the unit circle for $r < 1$).

In case 2, the equation obeyed by $U(t)$ is

$$\dot{U}(t) = \begin{pmatrix} -\frac{1}{RC}(1 + \eta - \eta\mu^{-1}\frac{1-r}{1-r\mu^{-1}}) & \frac{1}{C} \\ -\frac{1}{L}(1 + \eta - \eta\mu^{-1}\frac{1-r}{1-r\mu^{-1}}) - \frac{V_{in}}{L}\delta(v^*(t) - v_r(t)) & 0 \end{pmatrix} U(t)$$

Comparing with case 1, the differences amount to changing the sign of η and then replacing $1/L$ by $1/L(1 + \eta - \eta\mu^{-1}\frac{1-r}{1-r\mu^{-1}})$ without changing the combination V_{in}/L . Thus, the index function in this case is

$$g_2(\mu^{-1}) = \mu^{-2}e^{-a_2T} - 2\mu^{-1}e^{-\frac{1}{2}a_2T} \left(\cosh\left(\frac{1}{2}\gamma_2T\right) - \frac{V_{in}\beta}{\gamma_2LC} \sinh\left(\frac{1}{2}\gamma_2T\right) \right) + 1 \quad (6.22)$$

with

$$a_2 = \frac{1}{RC} \left(1 + \eta - \eta\mu^{-1}\frac{1-r}{1-r\mu^{-1}} \right)$$

and

$$\gamma_2 = \sqrt{a_2^2 - \frac{4}{LC} \left(1 + \eta - \eta\mu^{-1}\frac{1-r}{1-r\mu^{-1}} \right)}.$$

6.3.3 Numerical Analysis of $g(\mu^{-1})$

The index functions $g(\mu^{-1})$ of the previous subsection have been evaluated. Figure 6.3 shows the domains of control for the two feedback schemes with $r = 0.0$, $r = 0.6$ and $r = 0.9$. The black regions are those yielding index 0, when the time-delayed feedback successfully stabilizes the 1T-periodic orbit. Several features must be highlighted:

1. There are no big differences between the two schemes, apart from the sign of the feedback. The domain of control of the first scheme is slightly broader.
2. Use of extended time-delay feedback does not improve the domain of control for the two schemes. The index 1 zone expands with r at the expense of both the index 0 and index 2 zones, so in fact the stable region diminishes.

6.3.4 Stabilization of Higher Order Orbits

In this subsection we will show how to generalize the analytical results to situations more general than 1T-periodic UPOs with a single crossing per cycle. It will only be shown with the first feedback scheme.

Consider for instance a nT -periodic orbit with a single crossing per cycle at times $t_1 \in (0, T)$, $t_2 \in (0, 2T)$, ..., $t_n \in ((n-1)T, nT)$ and forced switchings

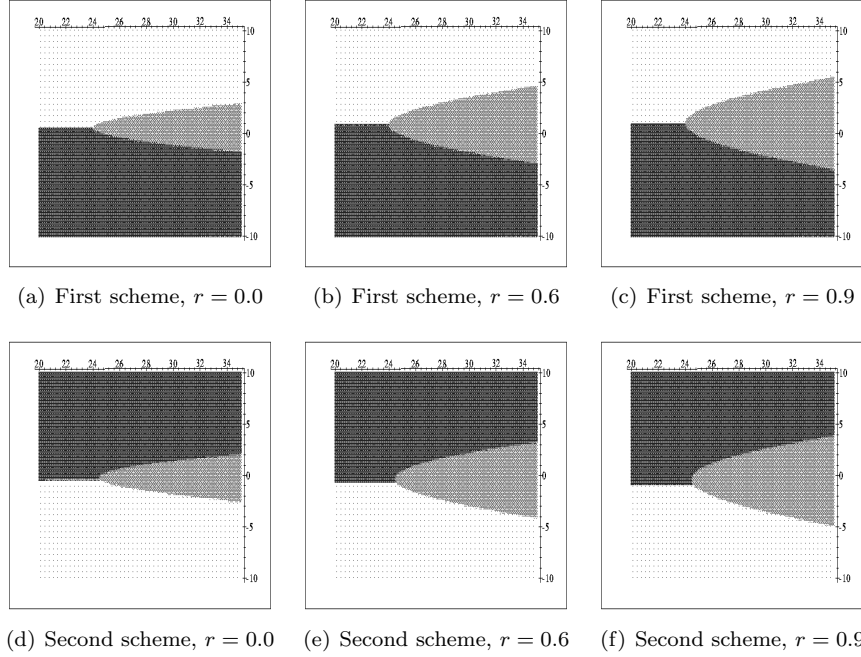


Figure 6.3: Domains of control for the two feedback schemes and several values of r . Vertical axis: η from -10 to 10 . Horizontal axis: V_{in} from 20 V to 35 V. Black = 0 (stable), Grey = 1 (unstable), White = 2 (unstable).

at the end of cycles $T, 2T, \dots, (n-1)T$. Now we have to integrate $U(t)$ over $[0, nT]$ and the system changes its topology at $T, 2T, \dots, (n-1)T$ in addition to t_1, t_2, \dots, t_n . However, both $x^*(t)$ and $x^*(t) + y(t)$ change the topology of the system at exactly $T, 2T, \dots, (n-1)T$, so we may ignore these changes since they do not take the orbits apart. Mathematically, this is reflected by the fact that only $\delta b(t, [x])/\delta v(t')$ enters the computations, and that this functional derivative is zero for all the variations of $b(t, [x])$ which do not depend on v , such as those occurring at the end of cycle.

In the first feedback scheme, we may now proceed to equations (6.15), which we will have to integrate between 0 and nT for the two sets of initial conditions $(1, 0)$ and $(0, 1)$. For each cycle of the auxiliary ramp $v_r(t)$, we have a zero of the delta function and hence

$$\delta(v^*(t) - v_r(t)) = \sum_{k=1}^n \beta_k \delta(t - t_k),$$

where

$$\beta_k = \frac{1}{|\dot{v}^*(t_k) - \dot{v}_r(t_k)|}.$$

Integration is now easily performed by means of a Laplace transform, and we obtain the result

$$\begin{aligned}
x(t) &= \left(-x(0) \frac{a_1 - \gamma_1}{2\gamma_1} + y(0) \frac{1}{\gamma_1 C} \right) e^{-\frac{1}{2}(a_1 - \gamma_1)t} \\
&\quad + \left(x(0) \frac{a_1 + \gamma_1}{2\gamma_1} - y(0) \frac{1}{\gamma_1 C} \right) e^{-\frac{1}{2}(a_1 + \gamma_1)t} \\
&\quad - \frac{V_{in}}{LC\gamma_1} \sum_{k=1}^n \left(\beta_k x(t_k) \theta(t - t_k) \left(e^{-\frac{1}{2}(a_1 - \gamma_1)(t - t_k)} - e^{-\frac{1}{2}(a_1 + \gamma_1)(t - t_k)} \right) \right) \\
y(t) &= \left(-x(0) \frac{1}{\gamma_1 L} + y(0) \frac{a_1 + \gamma_1}{2\gamma_1} \right) e^{-\frac{1}{2}(a_1 - \gamma_1)t} \\
&\quad + \left(x(0) \frac{1}{\gamma_1 L} - y(0) \frac{a_1 - \gamma_1}{2\gamma_1} \right) e^{-\frac{1}{2}(a_1 + \gamma_1)t} \\
&\quad - \frac{V_{in}}{2L\gamma_1} \sum_{k=1}^n (\beta_k x(t_k) \theta(t - t_k) \\
&\quad \left((a_1 + \gamma_1) e^{-\frac{1}{2}(a_1 - \gamma_1)(t - t_k)} - (a_1 - \gamma_1) e^{-\frac{1}{2}(a_1 + \gamma_1)(t - t_k)} \right))
\end{aligned}$$

with the $x(t_k)$ computed recursively from the expression for $x(t)$.

We will present explicit expressions for $g(\mu^{-1})$ only for the case $n = 2$. One gets

$$\begin{aligned}
g(\mu^{-1}) &= \mu^{-2} e^{-2a_1 T} - 2\mu^{-1} e^{-a_1 T} \left(\cosh(\gamma_1 T) - \frac{V_{in}}{\gamma_1 LC} (\beta_1 + \beta_2) \sinh(\gamma_1 T) \right. \\
&\quad \left. + \frac{V_{in}^2 \beta_1 \beta_2}{\gamma_1^2 L^2 C^2} (\cosh(\gamma_1 T) - \cosh(\gamma_1(t_1 - t_2 + T))) \right) + 1. \quad (6.23)
\end{aligned}$$

Domains of control for this case with $r = 0.0$, $r = 0.6$ and $r = 0.9$ are presented in Figure 6.4, and the same remarks made for the 1T-periodic orbits also apply here. Other situations, such as 1T-periodic orbits with several crossings per period, can be treated along the same lines.

6.3.5 ETDAS Simulations

In this subsection we report the results of several simulations of the time-delay controlled system.

Figure 6.5 shows a typical numerical simulation of the time-delay feedback control method. A chaotic orbit of the system ($\eta = 0$) is also shown for reference. The feedback starts to act after the first cycle and stabilizes the orbit in less than 10 cycles, *i.e.*, 4 ms for the system considered.

Figure 6.6 shows a simulation of an ETDAS with $r = 0.6$, $\eta = -5.0$ and $V_{in} = 33V$ using the first scheme. The series in (6.2) has been truncated to the first 80 terms. The figure shows the first 100 cycles, and the feedback starts to act after $t = 80T$. Notice that the collapse of the chaotic regime to the stabilized 1T-periodic orbit is nearly instantaneous.

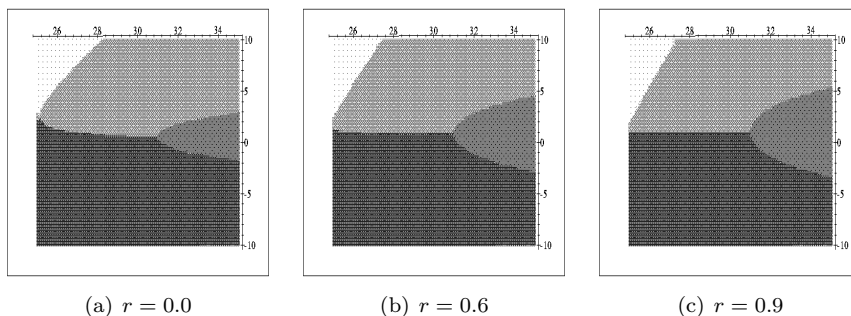


Figure 6.4: Domains of control for the first feedback scheme and 2T-periodic orbits and several values of r . Vertical axis: η from -10 to 10 . Horizontal axis: V_{in} from 25 V to 35 V. Black = 0 (stable), Dark gray = 1 (unstable), Light gray = 2 (unstable), White = 3 (unstable).

In order to check the boundary between the zones of the domain of control, we have numerically integrated the time-delay feedback equations for several values of the bifurcation parameter V_{in} and the feedback gain η on both sides of the analytically computed boundary, although occasionally numerical integration errors may produce a wrong result if η is too close to the boundary.

One of those checks is presented in Figure 6.7(a), which corresponds to input voltage $V_{in} = 30V$ with the first feedback scheme and $r = 0$. The solid line corresponds to $\eta = -1.3$ and the dashed one to $\eta = -1.2$. The expression (6.21) for $g_1(\mu^{-1})$ predicts index 0 for the former and index 1 for the later. The time span in the figure corresponds to four cycles of the auxiliary ramp and the vertical axis represents the capacitor voltage. We see indeed that $\eta = -1.3$ stabilizes the system to the 1T-periodic orbit, while $\eta = -1.2$ does not. In fact, $\eta = -1.2$ produces a 2T-periodic orbit which, however, is not the stable 2T-periodic orbit of the uncontrolled system which exists for this value of V_{in} and is also represented in the figure: there is some kind of competition between the stable 2T-periodic orbit and the time-delay feedback (which is not zero on this 2T-periodic orbit), which finally neither stabilizes to the unstable 1T-periodic orbit nor falls on the system's stable 2T-periodic orbit.

Another check, this time for 2T-periodic orbits, is illustrated by Figure 6.7(b), corresponding to $V_{in} = 32.5V$ and $r = 0.0$. Eight cycles of the auxiliary ramp, between $t = 0.06s$ and $t = 0.0632s$, are represented. Equation (6.23) predicts index 0 for $\eta = -1.1$ and index 1 for $\eta = -1.0$. A chaotic orbit of the system is also represented, and the same remarks for Figure 6.7 also apply. Notice that for this value of V_{in} there is also a 1T-periodic UPO, which, however, is not stabilized by the above values of η . Nevertheless, for $\eta \lesssim -1.6$, the system could choose to stabilize on either the 1T-periodic or 2T-periodic UPOs, since both are zero on the feedback control in this case. At present we do not have a way to predict which orbit would the system choose in a given case, or

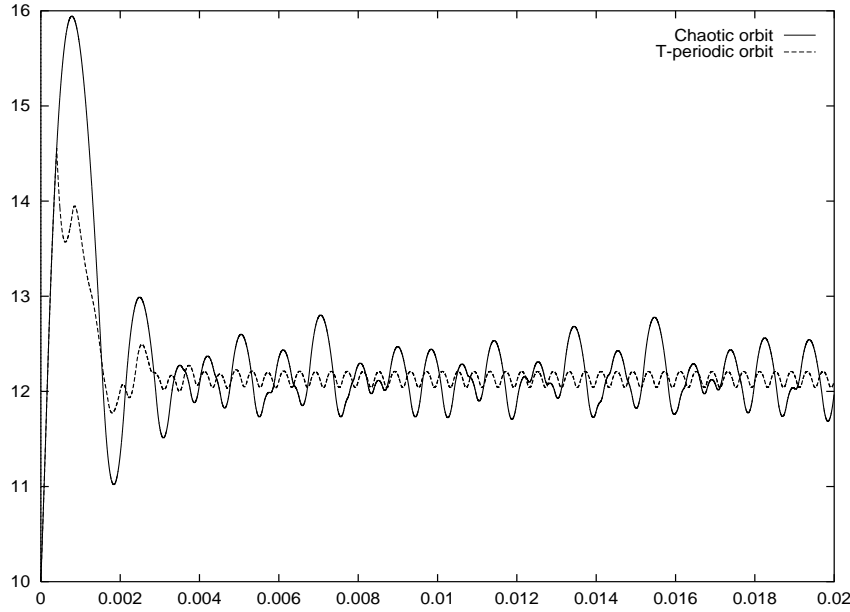


Figure 6.5: Load voltage chaotic waveform for $V_{in} = 35V$ (solid line) and time-delay feedback controlled orbit in the second scheme with $r = 0$ and $\eta = 4.0$ (dashed line). 50 cycles of the auxiliary ramp are shown.

whether there are well defined basins of attraction.

6.3.6 Another TDAS Scheme of Control

In the previous section, the time-delayed signal was fed directly into the converter in several ways. Although the gain feedback necessary to stabilize the unstable orbits was relatively small, it nevertheless implied that, in the initial phase of the stabilization, a certain amount of power was injected into the system. A TDAS scheme is now introduced in which the time-delayed signal is fed into the function which is compared to the ramp to effect the change of topologies.

In the TDAS scheme that we propose, instead of just $v(t)$ we use, as a function to compare with the ramp,

$$v(t) - \eta (M_1 (v(t) - v(t - \tau)) + M_2 (i(t) - i(t - \tau))),$$

where η is a (dimensionless) feedback gain, and M_1 (also dimensionless) and M_2 (measured in ohms) are adjustable parameters describing how v and i enter the feedback signal. Since a TDAS scheme is considered, we have now

$$\dot{y}(t) = A_0(t)y(t) + A_1(t)y(t - \tau) \quad (6.24)$$

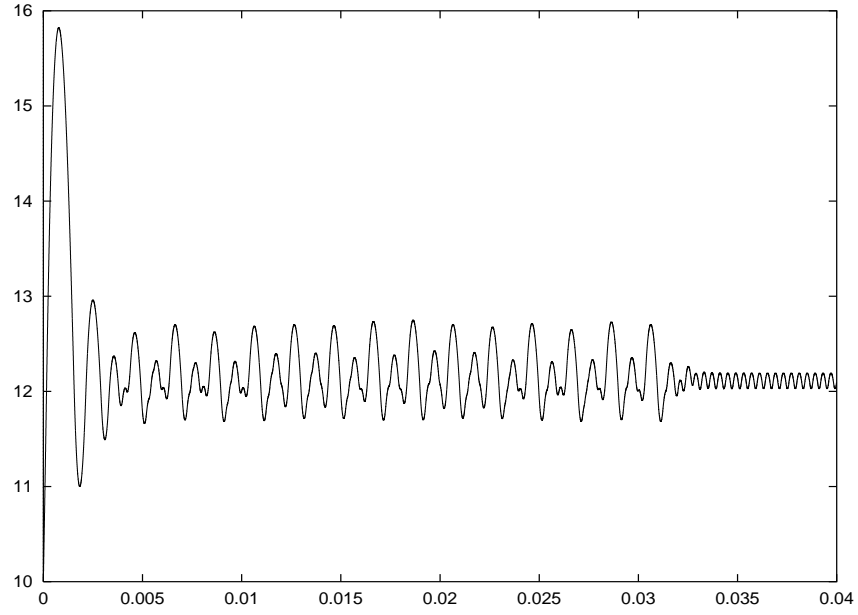


Figure 6.6: ETDAS simulations for the buck converter.

and

$$\dot{U}(t) = (A_0(t) + \mu^{-1}A_1(t))U(t) \quad (6.25)$$

Thus, in this case,

$$\begin{aligned} \dot{x}(t) = & Ax(t) + \begin{pmatrix} 0 \\ V_{in}/L \end{pmatrix} \cdot \\ & \cdot (1 - \theta(v(t) - v_r(t) - \eta M_1(v(t) - v(t - \tau)) - \eta M_2(i(t) - i(t - \tau)))) \end{aligned} \quad (6.26)$$

One can then easily evaluate the functional derivatives to obtain

$$\begin{aligned} A_0(t) &= A - \frac{V_{in}}{L} \delta(v^*(t) - v_r(t)) \begin{pmatrix} 0 & 0 \\ 1 - \eta M_1 & -\eta M_2 \end{pmatrix} \\ A_1(t) &= -\frac{V_{in}}{L} \delta(v^*(t) - v_r(t)) \begin{pmatrix} 0 & 0 \\ \eta M_1 & \eta M_2 \end{pmatrix} \end{aligned}$$

This yields for U the equation

$$\dot{U} = \begin{pmatrix} -\frac{1}{RC} & \frac{1}{C} \\ a_3(t) & a_4(t) \end{pmatrix} U$$

where

$$a_3(t) = -\frac{1}{L} - \frac{V_{in}}{L} (1 - \eta M_1(1 - \mu^{-1})) \delta(v^*(t) - v_r(t))$$

and

$$a_4(t) = \frac{V_{in}}{L} \eta M_2 (1 - \mu^{-1}) \delta(v^*(t) - v_r(t))$$

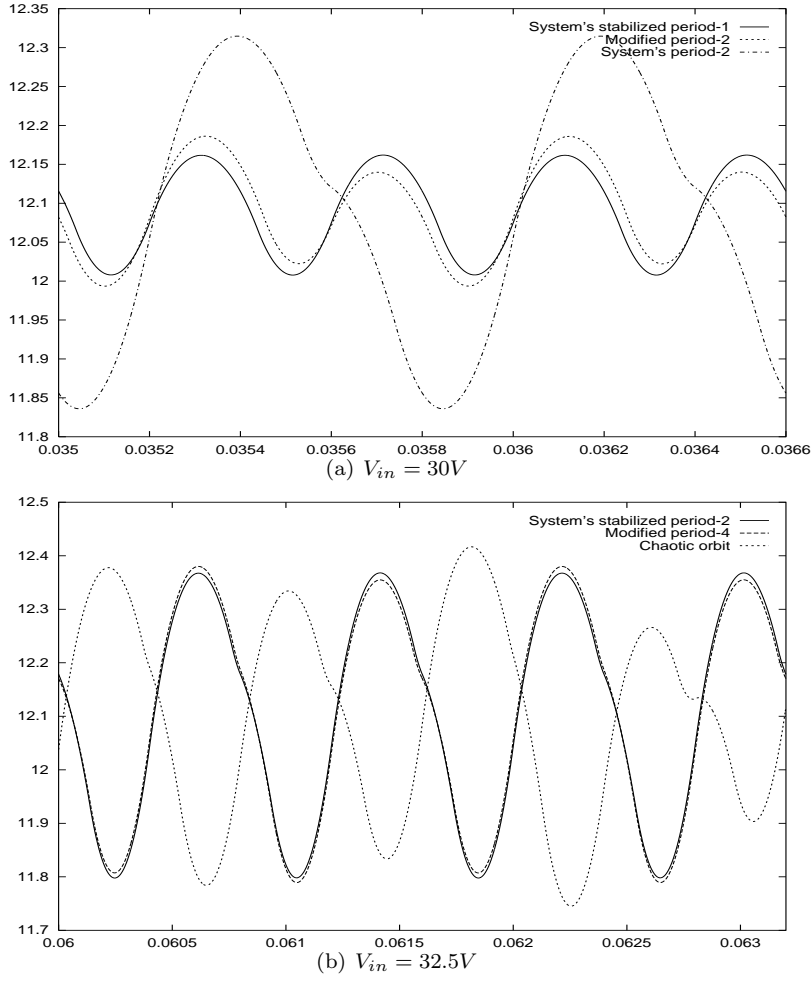


Figure 6.7: Simulation checks of the analytically computed limits of the control domains.

We see that, in terms of the matrix elements of U , we get two uncoupled copies of the two-dimensional system

$$\begin{aligned}
 \dot{x} &= -\frac{1}{RC}x + \frac{1}{C}y \\
 \dot{y} &= \left\{ -\frac{1}{L} - \frac{V_{in}}{L}(1 - \eta M_1(1 - \mu^{-1}))\delta(v^*(t) - v_r(t)) \right\} x \\
 &\quad + \frac{V_{in}}{L}\eta M_2(1 - \mu^{-1})\delta(v^*(t) - v_r(t))y
 \end{aligned} \tag{6.27}$$

which we have to solve twice for $t \in [0, T]$ with the two sets of initial conditions $(1, 0)$ and $(0, 1)$. If we assume that for each cycle of the ramp $v_r(t)$ there is one

and only one $t_c \in (0, T)$ such that $v(t_c) = v_r(t_c)$, as is the case for the unstable periodic orbits that concerns us, then Equations (6.16) and (6.17) apply (we are assuming also that $v^*(t)$ does not have a grazing contact with $v_r(t)$). We thus obtain the time-varying linear system

$$\begin{aligned}\dot{x} &= -\frac{1}{RC}x + \frac{1}{C}y \\ \dot{y} &= -\frac{1}{L}x + p\delta(t - t_c)x + q\delta(t - t_c)y\end{aligned}\quad (6.28)$$

where $p = -\frac{\beta V_{in}}{L}(1 - \eta M_1(1 - \mu^{-1}))$ and $q = \frac{\beta V_{in}}{L}\eta M_2(1 - \mu^{-1})$.

This system can be analytically integrated between $t = 0$ and $t = T$. Notice that y is not continuous at $t = t_c$ because its derivative contains delta functions at t_c . Indeed, one can show that

$$y_c^+ = y_c^- + \frac{p}{q}(e^q - 1)x_c^- + (e^q - 1)y_c^-$$

with $x_c^+ = x_c^-$. By using this, one can compute

$$g(\mu^{-1}) = \begin{vmatrix} \mu^{-1}u_1(T) - 1 & \mu^{-1}u_2(T) \\ \mu^{-1}u_3(T) & \mu^{-1}u_4(T) - 1 \end{vmatrix} =$$

$$\mu^{-2}(u_1(T)u_4(T) - u_2(T)u_3(T)) - \mu^{-1}(u_1(T) + u_4(T)) + 1 \quad (6.29)$$

which after a little algebra yields, with $k = \frac{1}{2RC}$, $\omega = +\sqrt{\frac{1}{LC} - k^2}$,

$$g(\mu^{-1}) = \mu^{-2}e^{-2kT+q} - \mu^{-1}\frac{e^{-kT}}{\omega^2 LC}(K_1 \cos \omega T + K_2 \sin \omega T) + 1 \quad (6.30)$$

where $K_1 = (1 - k^2 LC)(1 + e^q)$ and $K_2 = (\frac{p}{q}L\omega + L\omega Ck)(e^q - 1)$. Notice that information about the particular 1T-periodic orbit we are trying to stabilize only enters through β .

Numerical Analysis and Simulations

The index can be now numerically computed by varying μ^{-1} over the unit circle. Figure 6.8 shows the results with $\eta = 1$, $M_1 \in (-1, 1)$ and $M_2 \in (-10, 2)\Omega$ for $V_{in} = 23V$, $V_{in} = 28V$ and $V_{in} = 34V$.

$V_{in} = 23V$ corresponds to a regime where the 1T-periodic orbit is already stable, and hence $M_1 = M_2 = 0$ belongs to the domain of control. For $V_{in} = 28V$ the 1T-periodic orbit is unstable, and the natural stable motion of the system is a 2T-periodic orbit. Finally, $V_{in} = 34V$ yields a fully chaotic regime. We see that, in all cases, we can stabilize the 1T-periodic orbit using $M_1 \sim 0$ and $M_2 \lesssim 0$. Figure 6.9 corresponds to the domain of control for several values of M_1 and M_2 and η varying between -1 and 1 . Notice that the domain of control varies dramatically with the weights which v and i are given in the time-delay feedback signal.

Some simulations have been performed for the time-delay controlled system. Figure 6.10 shows simulations with $\eta = 0.5$, $M_1 = 0.1$ and $M_2 = -4.0\Omega$ for

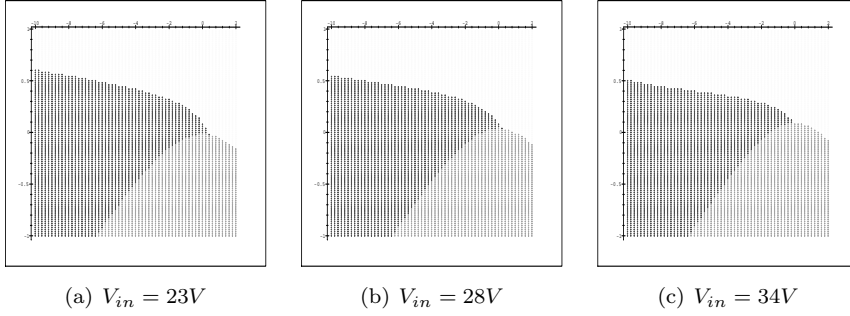


Figure 6.8: Vertical axis: $M_1 \in (-1, 1)$ Horizontal axis: $M_2 \in (-10, 2)\Omega$. Black = 0 (stable), Grey = 1 (unstable), White = 2 (unstable).

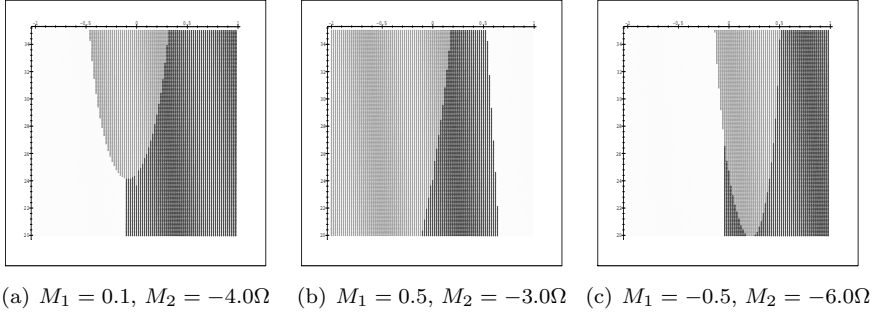


Figure 6.9: Horizontal axis: $\eta \in (-1, 1)$ Vertical axis: V_{in} from 20V to 35V. Black = 0 (stable), Grey = 1 (unstable), White = 2 (unstable).

both $V_{in} = 28V$ and $V_{in} = 34V$. In both cases, the control starts to act after 80 cycles of the ramp, so in the initial part the system exhibits the natural 2T-periodic and chaotic waveforms, respectively. One may observe that the control needs a transient of only a few cycles to stabilize the 1T-periodic orbit.

6.4 Stabilization by Control of the Switching Time

In this section, a new method to control chaos is introduced. Basically, it consists in the following: first, to find out the times where the orbit to be stabilized changes the topology, and second, to impose an open loop switching scheme based on the previous computed switching times, bypassing the PWM control. In what follows, a general situation is considered, and after the analytical results

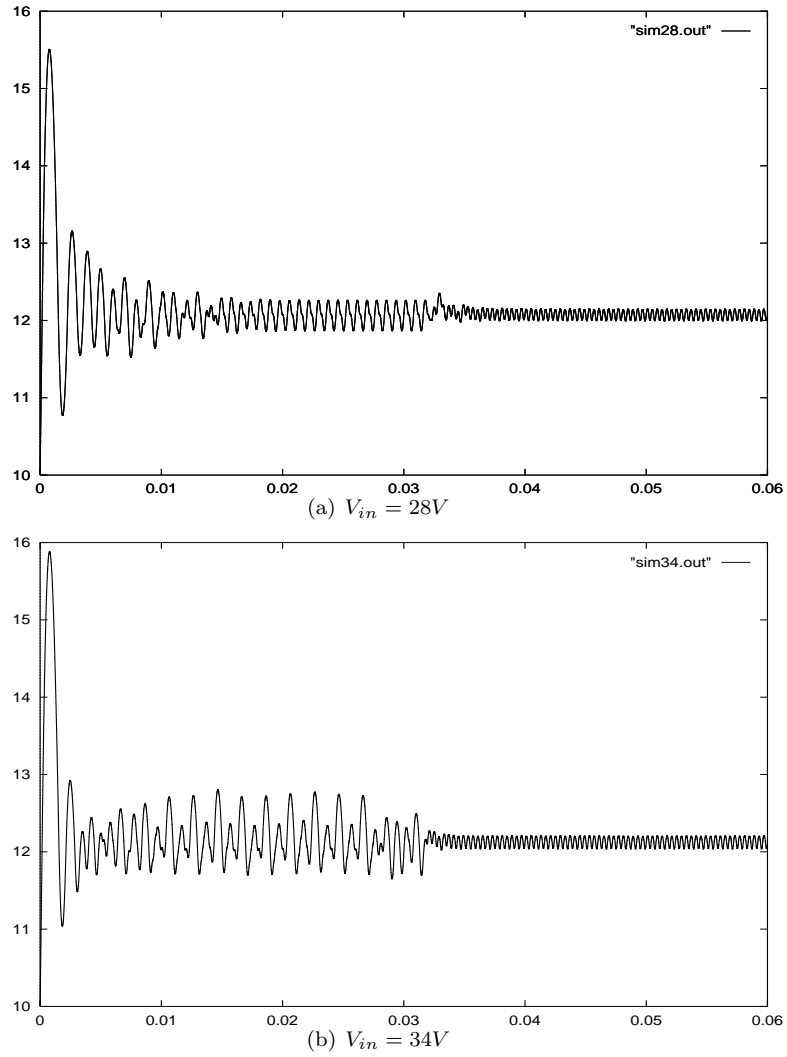


Figure 6.10: Time-delay feedback simulations.

are specified for the buck converter.

6.4.1 Two-topologies Systems

Consider a general dynamical system with two topologies

$$\dot{x} = \begin{cases} f(x) & \text{if } h(x(t), t) > 0 \\ g(x) & \text{if } h(x(t), t) < 0 \end{cases} \quad (6.31)$$

where $x \in \mathbb{R}^n$, $h(x(t), t+T) = h(x(t), T)$ and $T > 0$ is the period of an auxiliary signal used to switch between the two topologies. The vector fields in (6.31) are

supposed to depend on a certain parameter that we have not written explicitly, but which can act as a bifurcation parameter. We will call $h(x(t), t) = 0$ the switching condition and a time t_0 such that $h(x(t_0), t_0) = 0$ will be referred to as a switching time. It is assumed that the system is always in the first topology when a cycle of the auxiliary signal starts, although this is not essential.

Consider now a given periodic orbit $x^*(t)$ of (6.31), and assume it is unstable. For simplicity, we suppose it has period T and has a single switching time t_0^* in a cycle (measured from the start of the cycle):

$$\dot{x}^* = \begin{cases} f(x^*) & \text{if } t < t_0^* \\ g(x^*) & \text{if } t > t_0^* \end{cases}$$

so the system changes the topology both at the start of a cycle and at t_0^* . The method of stabilization that we propose applies equally well to more complicated periodic orbits, as will be apparent in what follows.

Let now $x(t)$ be another orbit close to $x^*(t)$ at a given time and with switching time t_0 in the present cycle (it will vary from cycle to cycle). We want to study the evolution of the difference $y(t) = x(t) - x^*(t)$:

$$\dot{y}(t) = \dot{x}(t) - \dot{x}^*(t) = \begin{cases} f(x(t)) - f(x^*(t)) & \text{if } 0 < t < t_0, t_0^* < T \\ f(x(t)) - g(x^*(t)) + \frac{\partial f}{\partial x} \Big|_{x=x^*(t)} y(t) & \text{if } 0 < t_0^* < t < t_0 < T \\ g(x(t)) - f(x^*(t)) & \text{if } 0 < t_0 < t < t_0^* < T \\ g(x(t)) - g(x^*(t)) & \text{if } 0 < t_0, t_0^* < t < T \end{cases} \quad (6.32)$$

where we have two possibilities for the intermediate evolution depending on whether $t_0^* < t_0$ or $t_0 < t_0^*$. In a linear approximation we have

$$\dot{y}(t) = \begin{cases} \frac{\partial f}{\partial x} \Big|_{x=x^*(t)} y(t) & \text{if } 0 < t < t_0, t_0^* < T \\ f(x^*(t)) - g(x^*(t)) + \frac{\partial f}{\partial x} \Big|_{x=x^*(t)} y(t) & \text{if } 0 < t_0^* < t < t_0 < T \\ g(x^*(t)) - f(x^*(t)) + \frac{\partial g}{\partial x} \Big|_{x=x^*(t)} y(t) & \text{if } 0 < t_0 < t < t_0^* < T \\ \frac{\partial g}{\partial x} \Big|_{x=x^*(t)} y(t) & \text{if } 0 < t_0, t_0^* < t < T \end{cases} \quad (6.33)$$

Assume now that, for any given time in the corresponding topology, both matrices

$$\frac{\partial f}{\partial x} \Big|_{x=x^*(t)} \quad \text{and} \quad \frac{\partial g}{\partial x} \Big|_{x=x^*(t)}$$

have eigenvalues with negative real part. It is then obvious that the origin of the instability of $x^*(t)$, and eventually of the chaotic regime, is the term $\pm(f(x^*(t)) - g(x^*(t)))$ present in the intermediate time when the reference orbit evolves with a different dynamics to that of the actual signal. In this case, an obvious control scheme follows: force the orbit $x(t)$ to switch topologies at $t = t_0^*$, bypassing the switching condition. This ensures the stability of the trivial solution $y(t) = 0$ of (6.33) and thus $\lim_{t \rightarrow +\infty} \|x(t) - x^*(t)\| = 0$. The method applies to higher period, multiple switching times per cycle orbits as well, and all that is needed is the collection of switching times of the reference unstable periodic orbit.

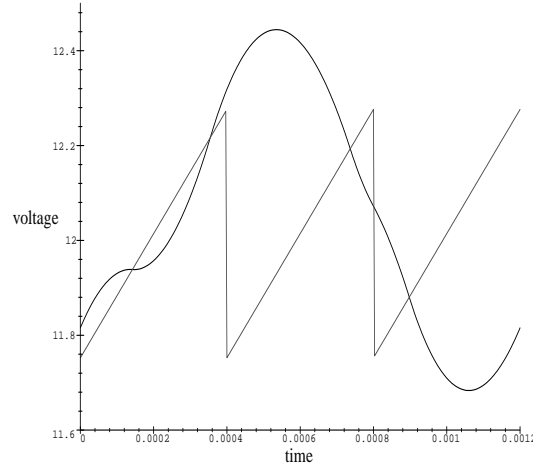


Figure 6.11: An unstable $3T$ -periodic orbit with $2+1+1$ switching times for the buck converter. The periodic ramp is also plotted.

A particular case of (6.31) is provided by the so-called bilinear systems, which encompass the basic DC-DC power converters:

$$\begin{aligned} f(x) &= Ax + a \\ g(x) &= Bx + b \\ h(x, t) &= \langle h, x \rangle - v_r(t), \end{aligned}$$

where $h = (h_1, \dots, h_n)$, $v_r(t + T) = v_r(t)$ and \langle, \rangle is the standard interior product in \mathbb{R}^n . Equations (6.33) are now exact and become

$$\dot{y}(t) = \begin{cases} Ay(t) & \text{if } 0 < t < t_0, t_0^* < T \\ (A - B)x^*(t) + a - b + Ay(t) & \text{if } 0 < t_0^* < t < t_0 < T \\ (B - A)x^*(t) + b - a + By(t) & \text{if } 0 < t_0 < t < t_0^* < T \\ By(t) & \text{if } 0 < t_0, t_0^* < t < T \end{cases} \quad (6.34)$$

The proposed method of stabilization will thus be effective if the eigenvalues of the constant matrices A and B have negative real parts (in fact, some zero real parts may be present and the stabilization might still work). Notice also that, since (6.34) is exact, the convergence to the target orbit will be global. Furthermore, even if t_0^* does not correspond to an orbit of the original, closed loop system, the trajectory will stabilize to a certain orbit.

6.4.2 Simulations for the Buck Converter

In this case,

$$v_r(t) = V_{ref} + \frac{V_L}{a} + \frac{V_U - V_L}{aT}t, \quad h = \begin{pmatrix} 1 \\ 0 \end{pmatrix}$$

and notice also that the eigenvalues of A are $-k \pm i\omega$, and so the stabilization procedure will work.

For the simulations, we have considered the same values of the parameters as in the previous chapters, that is, $R = 22\Omega$, $C = 47\mu\text{F}$, $L = 20\text{mH}$, $a = 8.4$, $T = 400\mu\text{s}$, $V_L = 3.8\text{V}$, $V_U = 8.2\text{V}$, $V_{ref} = 11.3\text{V}$ and V_{in} varying in the range $[15, 40]\text{V}$.

A 1T-periodic orbit is considered with $V_{in} = 35\text{V}$, which corresponds to a chaotic regime of the system, and thus it is an unstable orbit which can be checked also using the formulae for the stability given in Chapter 5. The numerical computations, performed with MAPLE, give a switching time $t_0^* = 261.32\mu\text{s}$, and thus the control function in open loop

$$u(t) = \begin{cases} 0 & \text{if } t < t_0^* \\ 1 & \text{if } t > t_0^* \end{cases}$$

extended T -periodically, is completely defined. Figure 6.12 corresponds to a ramp-controlled chaotic waveform. With the same initial conditions, Figure 6.13, which corresponds to numerical simulations performed with DSTOOL of the above open loop control function, shows the fast convergence to the target orbit, which has a smaller ripple.

We have also computed a $2 + 1 + 1$ periodic orbit for $V_{in} = 25\text{V}$ (see Figure 6.11 and Figure 6.14), which is unstable. Numerical solution of the equations for the switching times yields $t_{01}^* = 142.199\mu\text{s}$, $t_{02}^* = 354.874\mu\text{s}$, $t_{03}^* = 336.583\mu\text{s}$ and $t_{04}^* = 97.733\mu\text{s}$, and hence the open loop control function

$$u(t) = \begin{cases} 0 & \text{if } t < t_{01}^* \text{ or } t_{02}^* < t < T + t_{03}^* \text{ or } 2T < t < 2T + t_{04}^* \\ 1 & \text{if } t_{01}^* < t < t_{02}^* \text{ or } T + t_{03}^* < t < 2T \text{ or } t > 2T + t_{04}^* \end{cases}$$

extended periodically with period $3T$. Numerical simulation also shows the convergence of the state variables towards the computed unstable orbit.

This method was also successfully applied to other dc-dc converters such as the Čuk converter [Batlle, Fossas and Olivar, 1996]. When sinusoidal perturbations of a certain amplitude are added to the input voltage, the original unstable orbit is not stabilized, but a new orbit with the similar characteristics is (see Fig. 6.15).

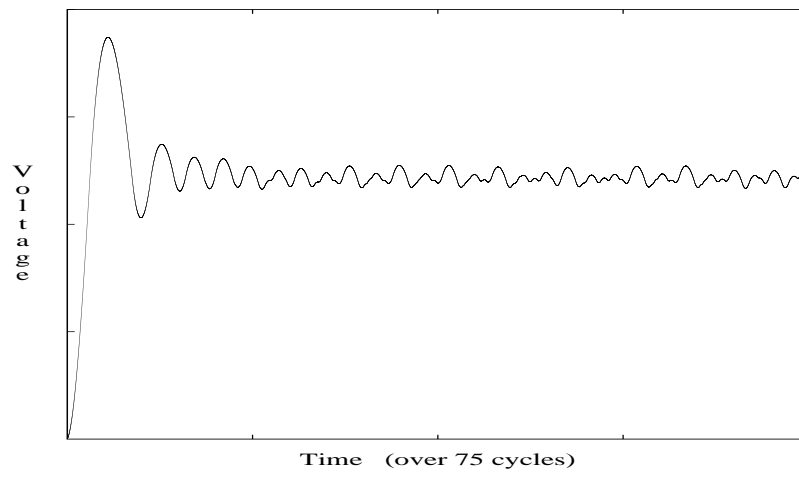


Figure 6.12: Ramp-controlled chaotic waveform for the buck converter ($V_{in} = 35V$). Voltage range is 0V to 20V.

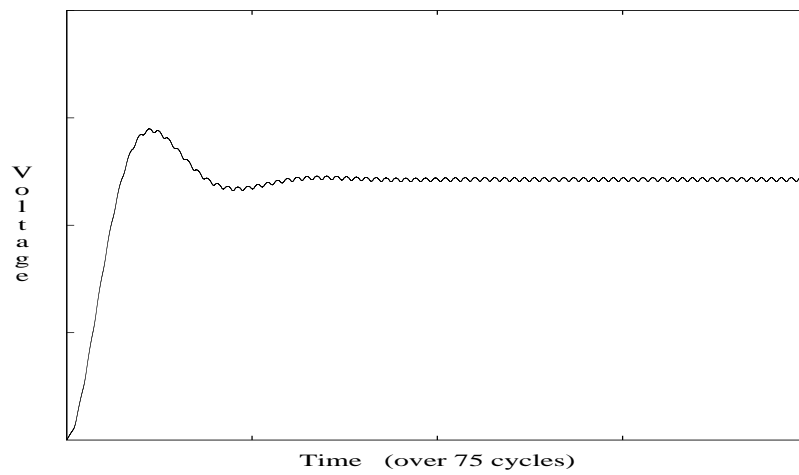


Figure 6.13: Open loop controlled orbit for the buck converter ($V_{in} = 35V$). Voltage range is 0V to 20V.

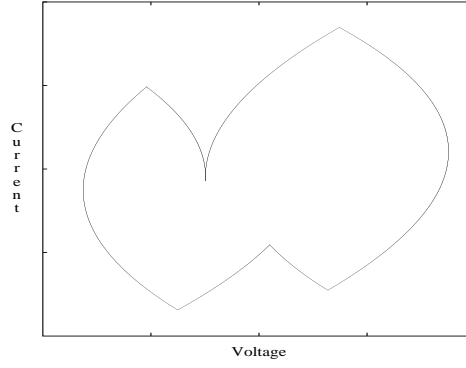


Figure 6.14: Unstable 3T-periodic orbit with 2+1+1 switching times, in the state space. Voltage range is 11.6V to 12.5V; current range is 0.4A to 0.7A. Non-differentiable points correspond to the changes in the topology of the circuit.

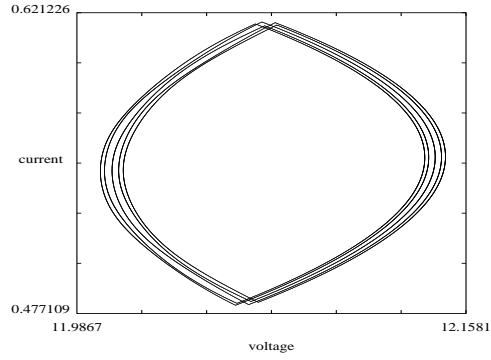


Figure 6.15: Stable 5T-periodic orbit obtained when trying to stabilize an unstable 1T-periodic orbit of the original system for $V_{in} = 27V$; a sinusoidal perturbation of amplitude 1V and frequency $100w$ is continuously added to the input voltage.

Chapter 7

Initial Explorations for Further Research

Abstract

In this chapter, initial computations are made with a variety of systems related to the buck converter which was described in the previous chapters, with the purpose of describing some future work that might be done beyond this thesis. Initially, a reduction of the number of parameters is obtained via linear transformations in the variables. The new ones are adimensional, and thus they can be useful for comparing the behaviour of the buck converter with other dynamical systems which are described by piecewise-linear vector fields. Some bidimensional bifurcation diagrams are outlined. Furthermore, a smooth version of the buck is given and some bifurcational events are traced with AUTO. Approximated mappings for the buck converter are deduced; they are useful for achieving faster simulations, although some differences from the original system are observed. Finally, it is shown how a general classification of two-topologies piecewise-linear systems in three-dimensional phase space with a planar switching surface can be carried over, the buck converter under PWM being a small step towards this classification.

7.1 Introduction

One of the basic approaches by which the detection and description of chaos in this thesis can be extended is by considering bifurcation parameters other than the input voltage [Chakrabarty, Poddar and Banerjee, 1996]. In this way one may see that when a system of differential equations is put into some type of normal form, then beyond the simplification of the equations, it may be compared with other dynamical systems which can be physically far apart from it,

but which retain the same structure. For example, this can be applied for example to Chua's oscillator [Shilnikov, 1993], DC motors [Hemati, 1994], electronic systems [Deane, 1992; Chakravarthy and Nayar, 1995], cable oscillators [Rega and Salvatori, 1996], and so on. In the case of the buck converter with PWM control, the system is described by two differential equations which include two state variables and nine parameters related to the circuit components. With some linear transformations in the state variables and time, this system can be brought to two differential equations with adimensional time, adimensional state variables and only four adimensional parameters. It is then ready for comparison with other similar systems.

With a first change in the temporal variable, $s = t/T$, the original system

$$\begin{aligned}\frac{dv}{dt} &= \frac{-1}{RC}v + \frac{1}{C}i \\ \frac{di}{dt} &= \frac{-1}{L}v + \frac{V_{in}}{L}u\end{aligned}$$

with

$$u = \begin{cases} 0 & \text{if } a(v - V_{ref}) > V_L + (V_U - V_L)Frac(t/T) \\ 1 & \text{if } a(v - V_{ref}) < V_L + (V_U - V_L)Frac(t/T) \end{cases} \quad (7.1)$$

is transformed into

$$\begin{aligned}\frac{dv}{ds} &= \frac{-T}{RC}v + \frac{T}{C}i \\ \frac{di}{ds} &= \frac{-T}{L}v + \frac{TV_{in}}{L}u\end{aligned}$$

with

$$u = \begin{cases} 0 & \text{if } a(v - V_{ref}) > V_L + (V_U - V_L)Frac(s) \\ 1 & \text{if } a(v - V_{ref}) < V_L + (V_U - V_L)Frac(s) \end{cases} \quad (7.2)$$

Now, an adimensional new variable x is introduced, defined as

$$x = \frac{v_{co} - V_L}{V_U - V_L} \iff v = V_{ref} + \frac{V_L}{a} + x \frac{V_U - V_L}{a}$$

Then,

$$\frac{dv}{ds} = \frac{V_U - V_L}{a} \frac{dx}{ds}$$

and one gets the following system

$$\begin{aligned}\frac{dx}{ds} &= \frac{-T}{RC}x + \frac{aT}{C(V_U - V_L)}i - \frac{T(V_L + aV_{ref})}{RC(V_U - V_L)} \\ \frac{di}{ds} &= \frac{-T(V_U - V_L)}{aL}v - \frac{T(V_L + aV_{ref})}{aL} + \frac{TV_{in}}{L}u\end{aligned}$$

with

$$u = \begin{cases} 0 & \text{if } x > Frac(s) \\ 1 & \text{if } x < Frac(s) \end{cases} \quad (7.3)$$

and thus the expression for the ramp is totally simplified. Finally, a third change can be done in the i variable to simplify the system and leave all the state variables adimensional. A linear change for suitable μ and ν ,

$$i = \mu y + \nu$$

transforms the equations into one of the following three possibilities:

Possibility a)

$$\begin{aligned}\frac{dx}{ds} &= -x + y \\ \frac{dy}{ds} &= K(u - x)\end{aligned}$$

with

$$u = \begin{cases} 0 & \text{if } x > \alpha + \beta \text{Frac}(s/T') \\ 1 & \text{if } x < \alpha + \beta \text{Frac}(s/T') \end{cases} \quad (7.4)$$

Possibility b)

$$\begin{aligned}\frac{dx}{ds} &= -k_1(x - y) \\ \frac{dy}{ds} &= -k_2(x + \alpha - \beta u)\end{aligned}$$

with

$$u = \begin{cases} 0 & \text{if } x > \text{Frac}(s) \\ 1 & \text{if } x < \text{Frac}(s) \end{cases} \quad (7.5)$$

Possibility c)

$$\begin{aligned}\frac{dx}{ds} &= -k_2x + k_1y \\ \frac{dy}{ds} &= -k_2(x + \alpha - \beta u)\end{aligned}$$

with

$$u = \begin{cases} 0 & \text{if } x > \text{Frac}(s) \\ 1 & \text{if } x < \text{Frac}(s) \end{cases} \quad (7.6)$$

In the following, possibility b) is chosen, which allows an easy expression for the ramp (it linearly varies from 0 to 1 with periodicity 1), and the parameter in the first equation is common for the two adimensional variables. The relation of the new parameters and variables to the former ones are:

$$\begin{aligned}k_1 &= \frac{T}{RC} & k_2 &= \frac{TR}{L} & \alpha &= \frac{V_L + aV_{ref}}{V_U - V_L} & \beta &= \frac{aV_{in}}{V_U - V_L} \\ s &= t/T & x &= \frac{v_{co} - V_L}{V_U - V_L} & y &= \frac{aRi - (V_L + aV_{ref})}{V_U - V_L}\end{aligned}$$

The new parameters k_1, k_2, α, β are all positive and the original condition to obtain complex eigenvalues

$$\frac{1}{LC} - k^2 > 0$$

is equivalent to

$$k_1 < 4k_2$$

Notice that once the component parameters of the ramp are fixed (V_L, V_U, T), the first two adimensional parameters k_1, k_2 are related to time constants of the *RCL*-circuit, while the other two parameters α, β are related to the control loop: α is related to V_{ref} while β is related to the input voltage V_{in} . Thus, varying V_{in} in the original system is equivalent to varying β in the new system of equations.

7.2 Bidimensional Bifurcation Diagrams

In this subsection, two bidimensional bifurcation diagrams are presented. They are computed with C code, taking advantage of the piecewise-linear form of the analytical solutions. Parameters k_1 and k_2 are fixed according to those in [Deane and Hamill, 1990], which have been employed throughout this thesis. These values give

$$k_1 = 0.386847195 \quad k_2 = 0.44 \quad (7.7)$$

The other two parameters, α and β , are varied in a region containing those of interest in [Deane and Hamill, 1990]. Specifically,

$$\alpha \in [0, 80] \quad \beta \in [0, 100]$$

which corresponds to

$$V_{ref} \in [-0.452380952, 41.45238095]V \quad V_{in} \in [0, 52.38095238]V$$

in the original system.

For each pair of values (α, β) in the ranges above, the same initial condition (x_0, y_0) has been chosen. Then, the system is simulated for 2000 cycles and the final state is classified into periodic or chaotic [Perelló and Olivar, 1995]. Notice that, as happened in Chapter 5, multiple attractors (and therefore, multiple basins of attraction) can be met at the same pair (α, β) of bifurcation parameters. The picture can only show one of these coexisting attractors, its periodicity being coded by some colour.

As shown in Fig. 7.1, there is 1T-periodic behaviour in a wide zone of the bifurcation space, which is delimited by a line of tangent approximately equal to 1, which in the original parameters space $V_{in} - V_{ref}$ would be $\{V_{ref} = V_{in}\}$. Moreover, for low α and β there also exists a region of 1T-periodicity delimited by a certain parabolic-like curve. Parabolic curves also delimit zones of 2T-periodicity and 4T-periodicity. A period-doubling route to chaos is then clearly seen when the parameter β varies from left to right. Some islands of periodicity exist inside the chaotic zone.

A region with complicated dynamics is also distinguished, and is recomputed in Fig. 7.2. In this diagram, the phenomenon of multiple basins of attraction could be the responsible for the sudden changes in the periodicity of the attractor. We observe periodic attractors of period 1T, 2T, 3T, 4T, 5T, 6T, 8T and 16T, intermingled in this region of the parameter space, which could provide an interesting subject for future work.

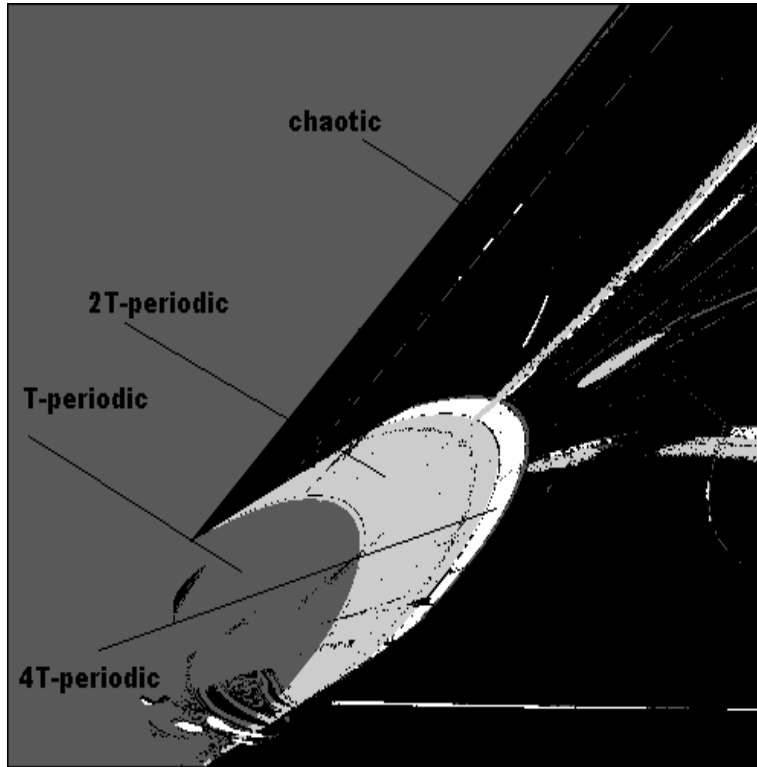


Figure 7.1: Bidimensional bifurcation diagram for the buck converter. Vertical axis: parameter α ; Range: (0,80). Horizontal axis: parameter β ; Range: (0,100). Parameters k_1 and k_2 are fixed to 0.386847195 and 0.44 respectively. Colour codes: black, chaotic; dark grey, 1T-periodic; light gray, 2T-periodic; white, 4T-periodic. Some islands of periodicity are shown inside the chaotic region. Also, a zone of complicated behavior is distinguished, which is recomputed and shown in the next figure.

7.3 A Smooth Version of the Buck Converter

Some standard packages, such as AUTO [Doedel and Wang, 1995], enable us to compute bifurcations of fixed points and periodic orbits, and continuation with regard to one or more parameters. One of the drawbacks to the modelling of the buck converter by a piecewise-linear vector field is the lack of smoothness at the switching instants. To compute periodic orbits and to do continuation, AUTO assumes that the vector field is everywhere smooth; this condition is clearly not verified in the modelisation of the buck. In spite of this, some smoothing techniques will be pointed out for converting the buck system into a smooth one, ready for AUTO to be applied. In addition, one of the requirements for computing with this package is to have an autonomous system. From the

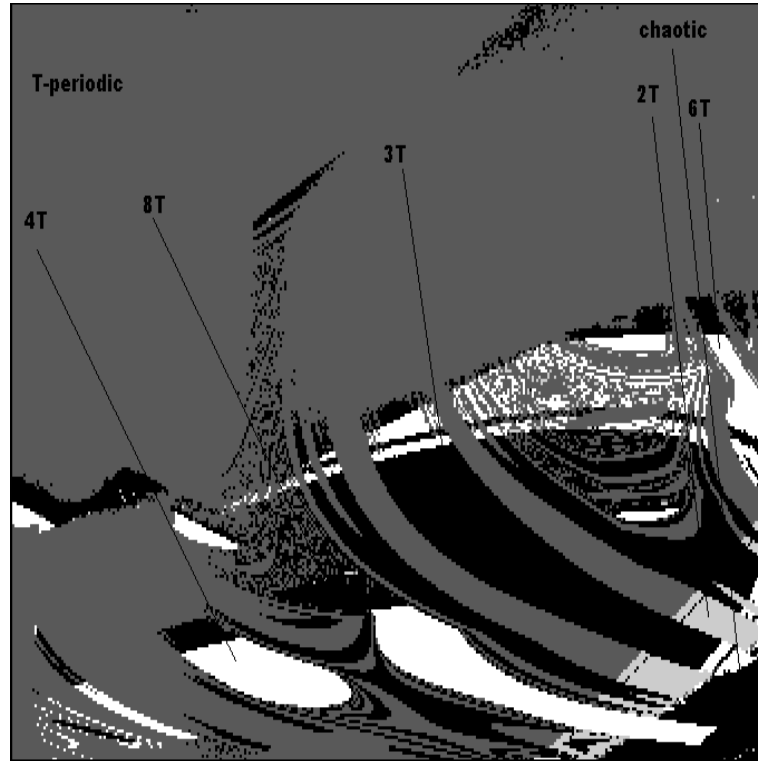


Figure 7.2: Bidimensional bifurcation diagram for the buck converter. Vertical axis: parameter α ; Range: (3,15). Horizontal axis: parameter β ; Range: (18,35). Parameters k_1 and k_2 are fixed to 0.386847195 and 0.44 respectively. Colour codes: black, chaotic and 3T-periodic; dark grey, 1T-periodic; light gray, 2T-periodic; white, 4T-periodic, 6T-periodic and 8T-periodic. Chaotic zones are found for low α to the right of the figure and also fractally intermingled in the 1T-periodic region. The rest of the black colour corresponds to 3T-periodic orbits, which are mixed with 6T-periodic behavior. 2T-periodic, 4T-periodic and 8T-periodic orbits are also found. Sudden changes probably occur because more than one attractor is present for the same bifurcation parameters.

theoretical point of view this is not a problem, because one more equation can be added to the system $\dot{t} = 1$ to make it autonomous. This procedure is not convenient for AUTO. Instead, an additional oscillator must be added to the equations in order to compute efficiently. How these steps are taken in the buck converter will be explained in more detail in the following.

7.3.1 An Autonomous System

The standard procedure for converting a non-autonomous system with a periodic forcing term of frequency ω into an autonomous system is to change the time variable and add an additional equation to the system, namely

$$z = \omega t / (2\pi) \quad \dot{z} = \omega / (2\pi).$$

This works in theory, but it is not the best way to do it with AUTO. Instead, it is better to add an oscillator which quickly converges to a stable solution

$$z = \sin(\omega t) \quad w = \cos(\omega t)$$

For example, for $\omega = 2\pi$, the usual way is to add the equations

$$\begin{aligned} \frac{dz}{dt} &= z + 2\pi w - z(z^2 + w^2) \\ \frac{dw}{dt} &= -2\pi z + w - w(z^2 + w^2) \end{aligned} \quad (7.8)$$

which has $(0, 0)$ as an unstable equilibrium point and the 2π circle as a stable limit set; that is,

$$z = \sin(2\pi t) \quad w = \cos(2\pi t)$$

is a stable solution of the system, provided the initial condition

$$z(0) = 0 \quad w(0) = 1$$

is given.

However, in the equations of the buck converter the forcing term is not only a trigonometric function, but a more complicated waveform $Frac(t)$. This problem is solved in the next section, since every periodic function (with some regularity conditions) can be developed in Fourier series, involving trigonometric functions.

7.3.2 A Smooth Version of the Ramp Voltage

One of the expressions in the system which must be smoothed is the ramp voltage. The equation for the ramp voltage is

$$ramp(t) = Frac(t)$$

and this function is discontinuous at the integer numbers \mathbb{Z} . One method for smoothing this function is via Fourier approximation. Then, instead of the ramp, its truncated Fourier can be considered

$$\frac{1}{2} - \sum_{k=1}^n \frac{1}{\pi k} \sin(2\pi k t) \quad (7.9)$$

Some values for n up to 256 have been investigated. As n increases, the ramp is better approximated, but the number of operations also rises dangerously, and

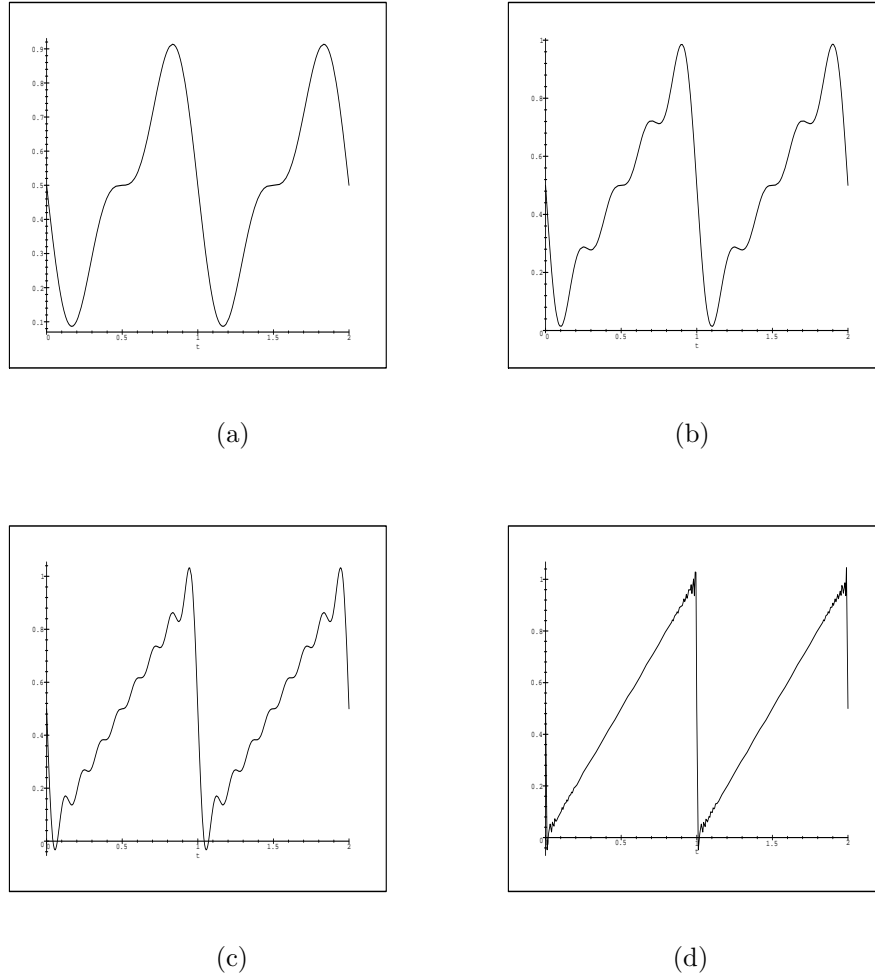


Figure 7.3: Fourier series approximating the ramp voltage $Frac(t)$. (a) $n = 2$; (b) $n = 4$; (c) $n = 8$; (d) $n = 64$.

this can be a source of error. To decide a particular value for n , a compromise was taken between the round error produced by the terms in the series and the shape of the approximated ramp, and $n = 8$ was chosen (see Fig. 7.3).

Notice that this smoothing will not allow us to find grazing bifurcations, since on the one hand the system will now be smooth and grazing bifurcations are only present in non-smooth systems; on the other hand, the approximated ramp has several oscillations near the edges of the ramp, and some different behavior other than the original ramp voltage must be expected in this zone.

To introduce this ramp into the system, and to be efficient in the computa-

tional work with AUTO, the functions

$$\sin(2\pi kt) \quad \cos(2\pi kt)$$

which appear in the series (7.9) must be expressed in terms of the solutions of the added oscillator,

$$z = \sin(2\pi t) \quad w = \cos(2\pi t).$$

Thus, the approximated ramp voltage with $n = 8$ can be expressed

$$\begin{aligned} v_8 = \frac{1}{2} - \frac{1}{\pi} [& z(1+w+w^2+w^3+w^4+w^5+w^6+w^7) - \frac{1}{3}z^3(1+3w+6w^2+10w^3+15w^4 \\ & +21w^5) + \frac{1}{5}z^5(1+5w+15w^2+35w^3) - \frac{1}{7}z^7(1+7w)] \end{aligned}$$

7.3.3 A Smooth Version of the Switching Action

The last thing to settle before introducing the equations into AUTO is the highly nonlinear switching action produced by the control u . This problem can be solved by the method proposed in [Klecza and Kreuzer, 1994]. This consists in approximating a discontinuity

$$d(x) = \begin{cases} h(x) & \text{if } s(x) > 0 \\ -h(x) & \text{if } s(x) < 0 \end{cases} \quad (7.10)$$

by the function $k(x)$ defined as

$$k(x) = h(x) \frac{2}{\pi} \lim_{c \rightarrow \infty} \arctan(cs(x))$$

where c is a smoothing constant which must be sufficiently high.

In the case of the buck converter,

$$s(x) = -(x - v_8)$$

must be considered, and thus the approximated discontinuity is given by

$$k(x) = \frac{2}{\pi} \arctan(-c(x - v_8))$$

In this case, $k(x)$ approximates -1 and 1. As the values which must be approximated are 0 and 1, $\frac{1}{2}(k(x) + 1)$ must be taken as an approximated control function \tilde{u}

$$\tilde{u} = \frac{1}{2} + \frac{1}{\pi} \arctan(-c(x - v_8))$$

Then, the system which is finally introduced into AUTO is

$$\begin{aligned} \frac{dx}{dt} &= -k_1(x - y) \\ \frac{dy}{dt} &= -k_2(x + \alpha - \beta[\frac{1}{2} + \frac{1}{\pi} \arctan(-c(x - v_8))]) \\ \frac{dz}{dt} &= z + 2\pi w - z(z^2 + w^2) \\ \frac{dw}{dt} &= -2\pi z + w - w(z^2 + w^2) \end{aligned}$$

where

$$v_8 = \frac{1}{2} - \frac{1}{\pi} [z(1+w+w^2+w^3+w^4+w^5+w^6+w^7) - \frac{1}{3}z^3(1+3w+6w^2+10w^3+15w^4+21w^5) + \frac{1}{5}z^5(1+5w+15w^2+35w^3) - \frac{1}{7}z^7(1+7w)] \quad (7.11)$$

7.3.4 Choosing a Value for c

Initially, to see how the approximated buck works with the AUTO software, bifurcations are traced taking β as the bifurcation parameter, which is equivalent to taking V_{in} in the original system. Thus, the results will be compared with those in the preceeding chapters. In so doing, the values for the adimensional parameters must be as in (7.7), with $\alpha = 22.43636363$. Then, the smoothing free parameter c must be chosen, although later c can act as the bifurcation parameter in order to check the dependence of the results against the approximating scheme.

To decide a value for c , $\beta = 66.81818181$ was fixed (which corresponds to $V_{in} = 35V$). This is a value where there exists a chaotic attractor with a well-known shape. Then, c was increased until a chaotic attractor like that in the original system was obtained. Numerical computing was performed with DSTOOL, a software package using a standard fourth-order Runge-Kutta integrator. The pictures obtained are those of Fig. 7.4, and the value $c = 50$ was chosen to do the main computations.

7.3.5 Simulations and Conclusions

To get a first view of what to expect from AUTO, the system was also introduced to INSITE, and some bifurcation diagrams for β were traced (see Fig. 7.5)

With regard to the original system, some similarities can be detected. A first bifurcation occurs when y is near 0; then, coexisting 1T-periodic and 3T-periodic attractors are shown in a certain range of the bifurcation parameter. The latter disappears through a boundary crises. Near $\beta = 44$ a period-doubling sequence follows, which ends in a sudden enlargement of the attractor. Some periodic windows are also distinguished. There are also important differences; the clearest is the existence of some additional period-doublings followed by reverse period-doublings in the range $\beta \in [25, 40]$. This can be produced by the smoothing effect in the ramp voltage and in the switching.

Some orbits can be now continued with AUTO [Angosto and Olivar, 1996]. The first corresponds to having $z = w = 0$ in the oscillator. As $z = w = 0$ all the time, the approximated ramp voltage is then identically equal to $1/2$ (see Eq. (7.11)), and this corresponds to a horizontal ramp voltage, which produces a very different behavior in the converter. Thus, the continuation of this orbit has no interest in this case. Apart from this orbit, a 1T-periodic orbit \mathcal{O}_1 and a 3T-periodic orbit \mathcal{O}_3 were found with DSTOOL, which correspond to those seen in Fig. 7.5. In what follows, only the continuation of the 1T-periodic orbit was tried, since it is the one which admits a comparison with the main attracting orbit in the original system throughout almost the whole range of the bifurcation

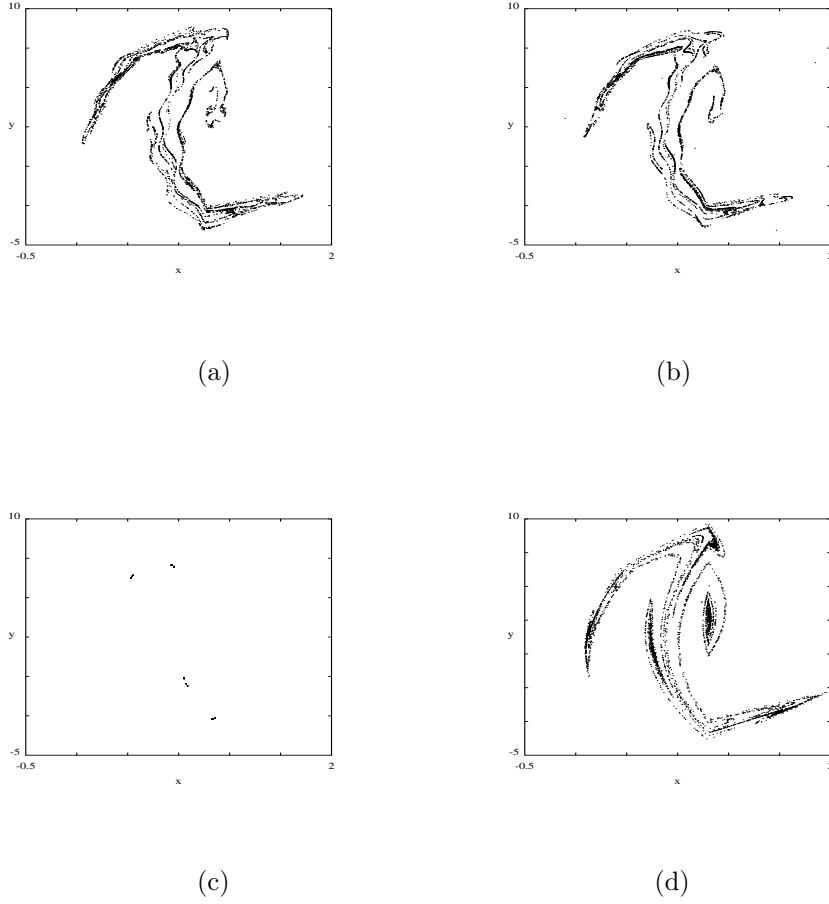


Figure 7.4: Attractors for different smoothing-constant c . (a) $c = 100$; (b) $c = 50$; (c) $c = 26$; (d) original system without smoothing. Notice in (a) and (b) the effect of smoothing, which produces a smoothed attractor. For $c = 26$, a different attractor is observed.

parameter. Once this orbit was introduced into AUTO, subsequently yielded regions of stability and regions of instability, separated by period-doubling bifurcations. From each of the period-doubling values, branches of $2T$ -periodic orbits were also continued. Finally, at the point labeled 15 in Fig. 7.6 c), some different type of bifurcation was detected, at the same time as a period-doubling occurs at the point labeled 9. Some similar results are obtained when $c = 100$ is chosen. In this case, a more complicated sequence of bifurcations is obtained

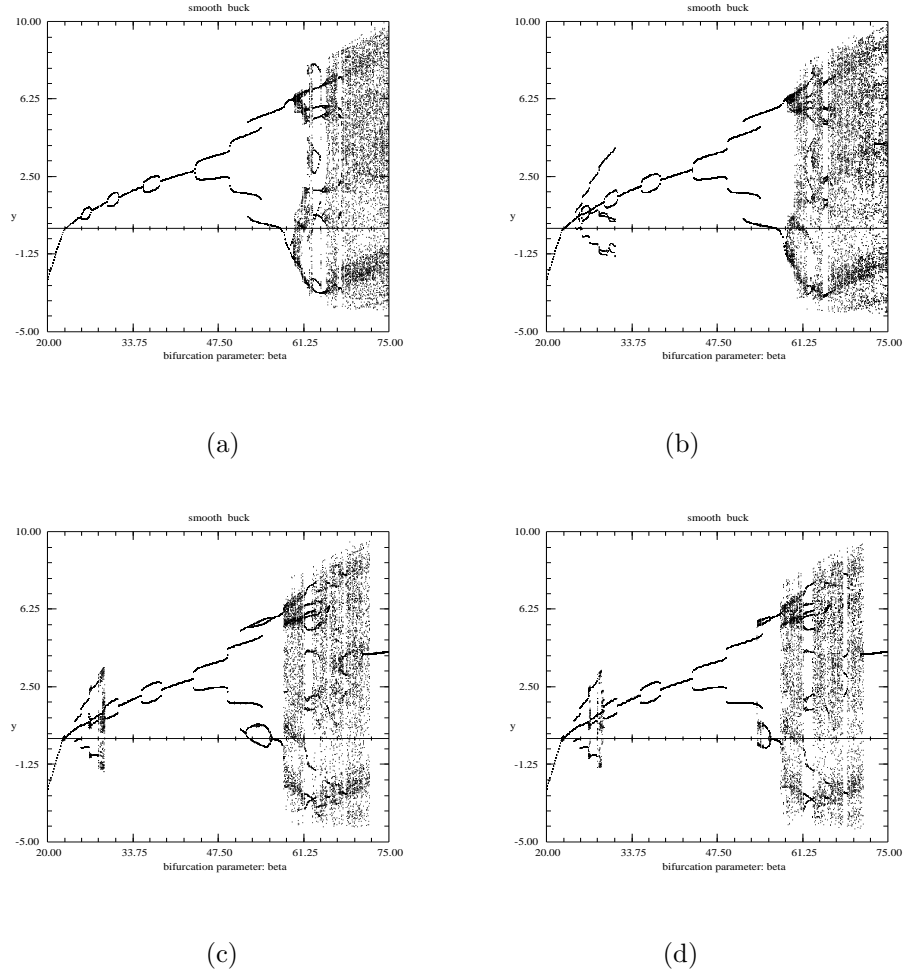


Figure 7.5: Bifurcation diagrams taking β as a bifurcation parameter. Different values for c are considered. (a) $c = 50$; (b) $c = 100$; (c) $c = 1000$; (d) $c = 500000$.

when following the 2T-periodic branch (Fig. 7.6 d). Figure 7.7 shows computed 1T-periodic orbits in the phase space, and the temporal waveforms of the x and y variables, which are associated to the voltage and current of the original system, respectively.

Figure 7.7 shows the two branches for different values of c . It can be observed that an important 2T-branch appears at approximately $\beta = 43.5$. This is equivalent to $V_{in} = 22.8V$ in the original system. Thus, this period-doubling bifurcation in the approximated system could be the equivalent period-doubling bifurcation of the main attractor branch in the original system, and corresponds to the main period-doubling bifurcation detected with INSITE (see Fig. 7.5).

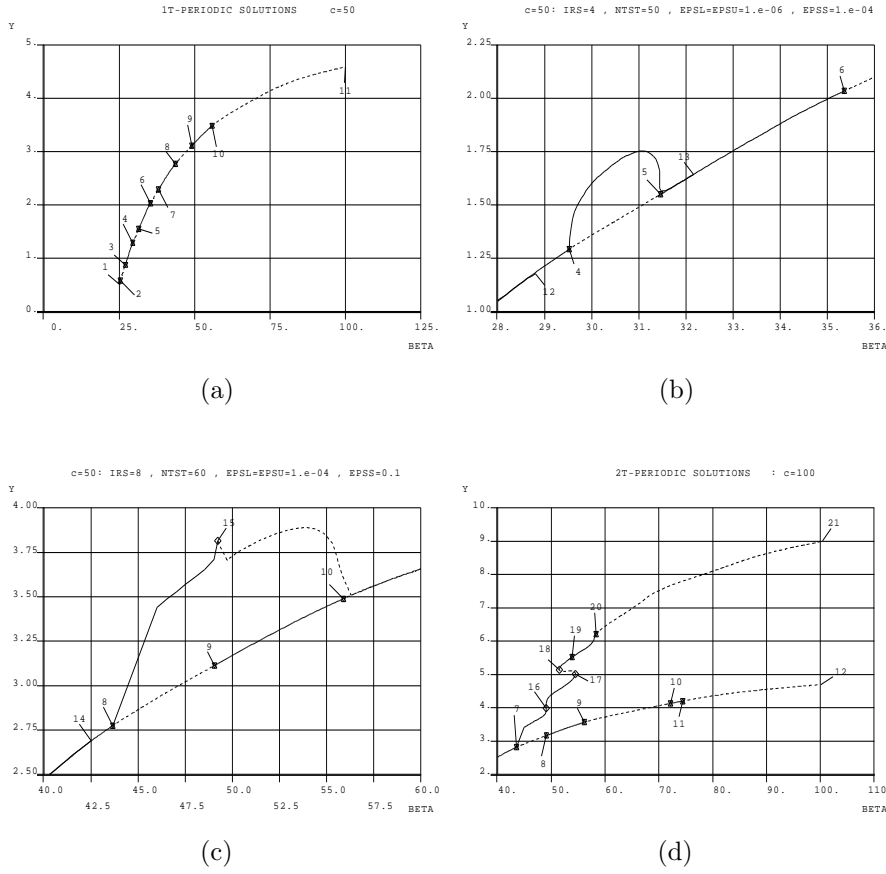


Figure 7.6: Branches of 1T-periodic and 2T-periodic orbits, computed with AUTO. Dashed trace corresponds to unstable orbits, continuous trace corresponds to stable orbits. Vertical axes correspond to the maximum value of the component in a cycle. (a) Branch of 1T-periodic orbits for $c = 50$. Some period-doubling bifurcations can be observed. (b) Detail of a period-doubling followed by a reverse period-doubling for $c = 50$. (c) A period-doubling bifurcation occurs at the point labeled 8. Then a new bifurcation in the 2T-periodic branch is found at the point labeled 15 ($c = 50$). (d) Some period-doubling bifurcations and possible folds in the 2T-periodic branch ($c = 100$).

Although research into this approximated system is only sketchy, it has been shown that the approximation step can retain some of the features of the original system. 1T-Periodic and 3T-periodic orbits which were computed with DSTOOL allow AUTO continuation. A deeper insight into this method includes continuation with regard to the smoothing parameter c , and continuation with

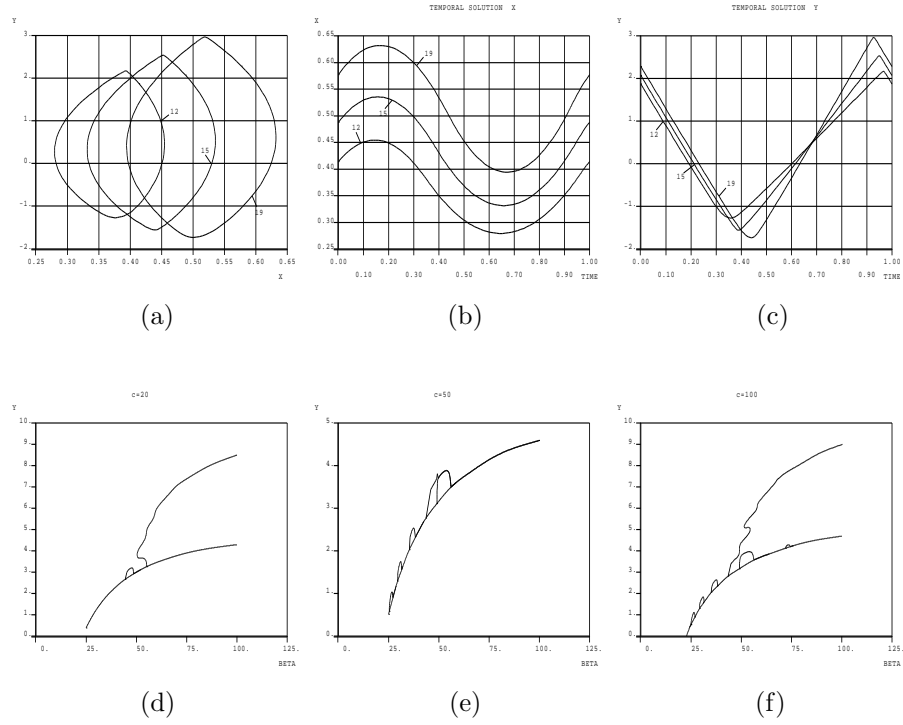


Figure 7.7: (a), (b) and (c): 1T-periodic orbits for $c = 50$. (d), (e) and (f): comparison of the branches for different values of the smoothing parameter c . Notice in (e) a different vertical scale. (a) Solutions in the phase space. Label 12 corresponds to $\beta = 36.81$; label 15 corresponds to $\beta = 40.75$; label 19 corresponds to $\beta = 46.74$. (b) First-component waveforms of the periodic orbits that appear in (a); this component is related to the voltage in the original system. (c) Second-component waveforms of the periodic orbits that appear in (a); this component is related to the current in the original system. Peaks are associated to changes in the topology of the original system. (d) $c = 20$; (e) $c = 50$; (f) $c = 100$. Apart from the small 2T-branches, probably corresponding to the smoothing effect, a large 2T-branch is observed near $\beta = 43.5$; it could be related to the first period-doubling of the main attractor observed in the original system.

regard to two different parameters. Furthermore, comparison with the original system must be done. All this is left for future work.

7.4 Approximated Mappings for the Buck

In this section, two approximated mappings for the buck converter are deduced. The first one fits the exponential and trigonometric functions by their second-order approximations, and thus the switching instant can be analytically computed, following a similar argument to that in [Tse, 1994a]. The second one concerns a qualitative approximation which yields some complex maps which have already been partially studied in the literature.

7.4.1 A Second-order Approximation

As we have seen, the exponential and trigonometric functions can be expanded in Taylor series to second order

$$\begin{aligned} e^{-kT\alpha} &\approx 1 - kT\alpha + \frac{(kT\alpha)^2}{2} \\ \sin(wT\alpha) &\approx wT\alpha \\ \cos(wT\alpha) &\approx 1 - \frac{(wT\alpha)^2}{2} \end{aligned} \quad (7.12)$$

Substituting Eq. (7.12) into the expressions of the analytical solution in the original system yields

$$\begin{aligned} v(\alpha) \approx & V_{in} + (1 - kT\alpha + \frac{k^2T^2\alpha^2}{2}) \{ (v_0 - V_{in})(1 - \frac{w^2T^2\alpha^2}{2}) + [(i_0 - \frac{V_{in}}{R})\frac{1}{Cw} \\ & - \frac{k}{w}(v_0 - V_{in})]wT\alpha \} \end{aligned}$$

Up to second order in α , this yields the following expression for $v(\alpha)$

$$\begin{aligned} v(\alpha) \approx & [\frac{(3k^2 - w^2)T^2}{2}(v_0 - V_{in}) - \frac{kT^2}{C}(i_0 - \frac{V_{in}}{R})]\alpha^2 + \\ & + [\frac{T}{C}(i_0 - \frac{V_{in}}{R}) - 2kT(v_0 - V_{in})]\alpha + v_0 \end{aligned} \quad (7.13)$$

and for $i(\alpha)$

$$i(\alpha) \approx [(v_0 - V_{in})\frac{kT^2}{L} - (i_0 - \frac{V_{in}}{R})\frac{T^2}{2LC}]\alpha^2 - \frac{T}{L}(v_0 - V_{in})\alpha + i_0 \quad (7.14)$$

If the condition for a switching is imposed

$$v(\alpha) = V_{ref} + \frac{V_L}{a} + \frac{V_U - V_L}{a}\alpha$$

then the following equation is obtained:

$$\begin{aligned} & [\frac{(3k^2 - w^2)T^2}{2}(v_0 - V_{in}) - \frac{kT^2}{C}(i_0 - \frac{V_{in}}{R})]\alpha^2 + [\frac{T}{C}(i_0 - \frac{V_{in}}{R}) - 2kT(v_0 - V_{in}) \\ & - \frac{V_U - V_L}{a}]\alpha + (v_0 - V_{ref} - \frac{V_L}{a}) = 0 \end{aligned} \quad (7.15)$$

which can be easily solved for α .

Then, computing trajectories cycle to cycle is as follows: from an initial condition (v_0, i_0) , the first switching time α is computed. If $\alpha > 1$, then $v(1)$ and $i(1)$ are computed and they are taken as the initial conditions for the next cycle. If $\alpha < 1$, then the state variables are computed at the switching instant, and the value for α is saved as α_1 . Next, switching α_2 is computed and it is checked if $\alpha_1 + \alpha_2 < 1$ or $\alpha_1 + \alpha_2 > 1$, and so on.

Notice that the equation to be solved from switching to switching is highly simplified, since it must be imposed that

$$\begin{aligned} & \left[\frac{(3k^2 - w^2)T^2}{2}(v_0 - V_{in}) - \frac{kT^2}{C}(i_0 - \frac{V_{in}}{R}) \right] \alpha^2 + \left[\frac{T}{C}(i_0 - \frac{V_{in}}{R}) - 2kT(v_0 - V_{in}) \right] \alpha \\ & + v_0 = v_0 + \frac{(V_U - V_L)}{a} \alpha \end{aligned} \quad (7.16)$$

Thus, v_0 can be simplified and this yields the solutions $\alpha = 0$ and

$$\alpha = \frac{2C(V_U - V_L) + 4akTC(v_0 - V_{in}) - 2aT(i_0 - \frac{V_{in}}{R})}{(3k^2 - w^2)aCT^2(v_0 - V_{in}) - 2akT^2(i_0 - \frac{V_{in}}{R})}$$

This map from cycle to cycle can be introduced into INSITE and the bifurcation diagrams checked when V_{in} is varied (see Fig. 7.8)

Although there is a good agreement in the first part of the diagram (before $V_{in} = 35V$), the approximation is bad for $V_{in} > 35V$. In the well-approximated zone, future work could be done on predicting bifurcation values, since a complete analytical expression for the map is available. Also, higher order approximations were not tried. They would probably extend the parameter range where the approximation is valid.

7.4.2 A Rotation Plus Translation Mapping

Consider once more Eq. (7.5), which corresponds to the adimensional version of the buck converter. The ramp equation in a cycle is given by

$$x_r(t) = t$$

and thus,

$$\frac{dx_r(t)}{dt} = 1$$

If it is imposed that $x_r(t)$ must obey the first equation in Eq. (7.5), then we have

$$y_r(t) = \frac{1}{k_1} + x_r(t) = \frac{1}{k_1} + t$$

Then, $(x_r(t), y_r(t))$, $t \in [0, 1]$ gives the curve in the phase space $x - y$ which a trajectory will follow when initial conditions are fixed at the beginning of the ramp, yielding infinite number of crossings, as happened with the original system. A transformation of the system of differential equations in order to

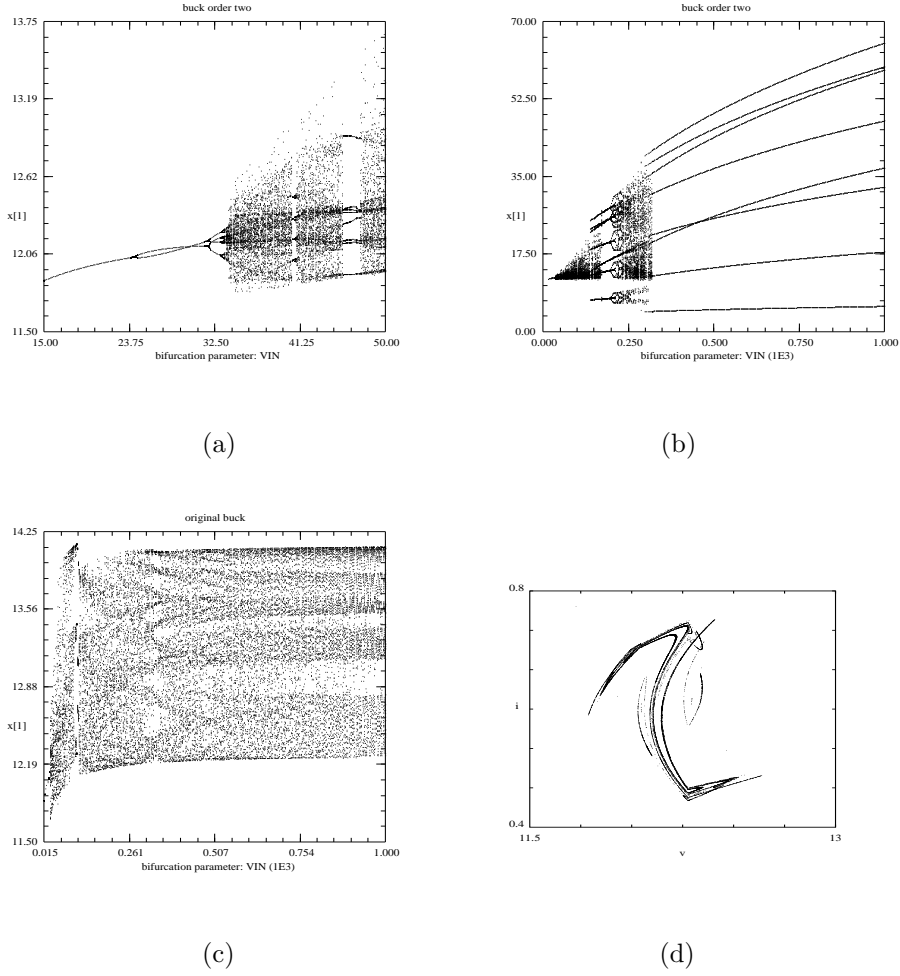


Figure 7.8: (a) and (b): Bifurcation diagrams for the second-order approximated map. (c) Bifurcation diagram for the original system. Notice that the range for the bifurcation parameter in (b) and (c) is $(0,1000)V$. While in the range $(15,35)V$ the approximation is good (see (a)), in the range $(35,1000)V$, the approximation is bad. (d) Shape of the approximated attractor for $V_{in} = 35V$.

convert this curve (a line) into a point is proposed; i.e., we consider the change of variables depending on time

$$\begin{aligned} z &= x - x_r(t) \\ w &= y - y_r(t) \end{aligned} \quad (7.17)$$

It must be taken into account that $x_r(t)$ and $y_r(t)$ are discontinuous at

the integers \mathbb{Z} . Then, at the end of each cycle, a translation of vector $(1, \frac{1}{k_1})$ (since $x_r(1) = 1$ and $y_r(1) = \frac{1}{k_1}$) must be applied to the state variables, which correspond to translating the ramp again to the point $(0, 0)$.

With these considerations, the following system is obtained:
for $t < 1$,

$$\begin{aligned}\frac{dx}{dt} &= -k_1(x - y) \\ \frac{dy}{dt} &= -k_2(x + \alpha' - \beta u + t)\end{aligned}$$

with

$$u = \begin{cases} 0 & \text{if } x > 0 \\ 1 & \text{if } x < 0 \end{cases} \quad (7.18)$$

and for $t = 1$ we apply the translation

$$\begin{aligned}x' &= x + 1 \\ y' &= y + \frac{1}{k_1}\end{aligned} \quad (7.19)$$

Figure 7.9 shows a typical trajectory in the state space, which is discontinuous in the two components.

In what follows, a qualitative approximation is made for this system. Simulations show that within each cycle, the origin acts as a stable spiraling focus. The trajectories are smooth except when crossing the line $\{x = 0\}$ (see Fig. 7.9). Moreover, the laps around the origin increase as the initial conditions are taken closer to it. Thus, a qualitative approximation within a cycle can be given by the following system with polar coordinates $x = r \cos \varphi$ $y = r \sin \varphi$,

$$\begin{aligned}\frac{dr}{dt} &= -Kr \\ \frac{d\varphi}{dt} &= \frac{w}{r}\end{aligned} \quad (7.20)$$

where $K > 0, w$ are parameters of the system and a translation of vector (a_1, a_2) must be applied at the end of the cycle.

System (7.20) retains the qualitative behaviour cited before, and can easily be solved yielding

$$\begin{aligned}r(t) &= r_0 e^{-Kt} \\ \varphi(t) &= \varphi_0 + \frac{w}{Kr_0} e^{Kt}\end{aligned} \quad (7.21)$$

These solutions are a particular case ($R = 1/2$) of a more general case with one more parameter

$$\begin{aligned}\frac{dr}{dt} &= -Kr \\ \frac{d\varphi}{dt} &= \frac{w}{r^{2R}}\end{aligned} \quad (7.22)$$

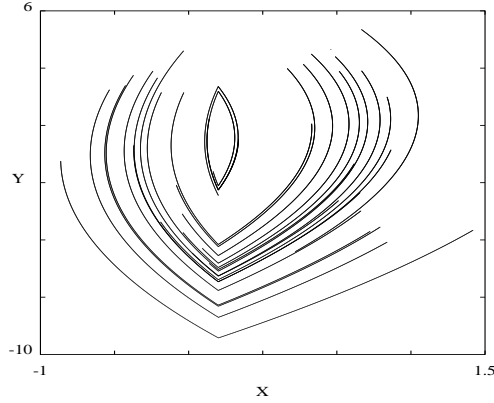


Figure 7.9: Trajectory in the state space $x - y$ corresponding to $V_{in} = 35V$ in the original system. The trajectory is discontinuous in both components. The ramp voltage has been reduced to the point $(0, 0)$.

which has solutions

$$\begin{aligned} r(t) &= r_0 e^{-Kt} \\ \varphi(t) &= \varphi_0 + \frac{w}{2RKr_0^{2R}} e^{2RKt} \end{aligned} \quad (7.23)$$

Now, if the solutions are considered in the cartesian plane, we obtain

$$\begin{aligned} x(t) &= r \cos(\varphi) = r_0 e^{-Kt} \cos\left(\varphi_0 + \frac{w}{2RKr_0^{2R}} e^{2RKt}\right) = \\ &= r_0 e^{-Kt} \left[\cos(\varphi_0) \cos\left(\frac{w e^{2RKt}}{2RKr_0^{2R}}\right) - \sin(\varphi_0) \sin\left(\frac{w e^{2RKt}}{2RKr_0^{2R}}\right) \right] \end{aligned}$$

and

$$\begin{aligned} y(t) &= r \sin(\varphi) = r_0 e^{-Kt} \sin\left(\varphi_0 + \frac{w}{2RKr_0^{2R}} e^{2RKt}\right) = \\ &= r_0 e^{-Kt} \left[\cos(\varphi_0) \sin\left(\frac{w e^{2RKt}}{2RKr_0^{2R}}\right) + \sin(\varphi_0) \cos\left(\frac{w e^{2RKt}}{2RKr_0^{2R}}\right) \right] \end{aligned}$$

and thus

$$x(t) = r_0 \cos(\varphi_0) e^{-Kt} \cos\left(\frac{w e^{2RKt}}{2RKr_0^{2R}}\right) - r_0 \sin(\varphi_0) e^{-Kt} \sin\left(\frac{w e^{2RKt}}{2RKr_0^{2R}}\right)$$

$$y(t) = r_0 \cos(\varphi_0) e^{-Kt} \sin\left(\frac{we^{2RKt}}{2RKr_0^2R}\right) + r_0 \sin(\varphi_0) e^{-Kt} \cos\left(\frac{we^{2RKt}}{2RKr_0^2R}\right)$$

Now, $x_0 = r_0 \cos(\varphi_0)$, $y_0 = r_0 \sin(\varphi_0)$ and also $r_0 = \sqrt{x_0^2 + y_0^2}$, and thus

$$x(t) = x_0 e^{-Kt} \cos\left(\frac{we^{2RKt}}{2RK(x_0^2 + y_0^2)R}\right) - y_0 e^{-Kt} \sin\left(\frac{we^{2RKt}}{2RK(x_0^2 + y_0^2)R}\right)$$

$$y(t) = x_0 e^{-Kt} \sin\left(\frac{we^{2RKt}}{2RK(x_0^2 + y_0^2)R}\right) + y_0 e^{-Kt} \cos\left(\frac{we^{2RKt}}{2RK(x_0^2 + y_0^2)R}\right)$$

If we take the state values at the end of a cycle, i.e., when $t = 1$, we obtain

$$x_1^* = x_0 e^{-K} \cos\left(\frac{we^{2RK}}{2RK(x_0^2 + y_0^2)R}\right) - y_0 e^{-K} \sin\left(\frac{we^{2RK}}{2RK(x_0^2 + y_0^2)R}\right)$$

$$y_1^* = x_0 e^{-K} \sin\left(\frac{we^{2RK}}{2RK(x_0^2 + y_0^2)R}\right) + y_0 e^{-K} \cos\left(\frac{we^{2RK}}{2RK(x_0^2 + y_0^2)R}\right)$$

and finally, applying a translation of vector (a_1, a_2) yields

$$x_1 = a_1 + e^{-K} \left[x_0 \cos\left(\frac{we^{2RK}}{2RK(x_0^2 + y_0^2)R}\right) - y_0 \sin\left(\frac{we^{2RK}}{2RK(x_0^2 + y_0^2)R}\right) \right]$$

$$y_1 = a_2 + e^{-K} \left[x_0 \sin\left(\frac{we^{2RK}}{2RK(x_0^2 + y_0^2)R}\right) + y_0 \cos\left(\frac{we^{2RK}}{2RK(x_0^2 + y_0^2)R}\right) \right]$$

with a_1 and a_2 being the translation parameters at the end of the cycle, K the contraction parameter towards the origin, and w, R rotation parameters around the origin. With complex variable $Z = x + iy$, the expression for this map can be considerably simplified. After some algebraic manipulation it yields

$$Z_1 = a + \lambda Z_0 e^{i\alpha|Z_0|^{-2R}} \quad (7.24)$$

with $a \in \mathbb{C} - \{0\}$, $\lambda = e^{-K} > 0$, $R > 0$ and $\alpha \in \mathbb{R}$.

Thus, in what follows, Eq. (7.24) will be considered as a complex iterative map

$$Z_{n+1} = a + \lambda Z_n e^{i\alpha|Z_n|^{-2R}} \quad (7.25)$$

modelling the dynamics of the converter. Further simplifications of Eq. (7.25) can be achieved, which provides a reduction in the number of parameters. Namely, considering $A \in \mathbb{C}$ such that $Aa = 1$ and with a change of variables $z = AZ$, we obtain

$$z_{n+1} = 1 + \lambda z_n e^{i\alpha|z_n|^{-2R}} \quad (7.26)$$

Taking into account the relation of the new parameters λ, α, R to the ones in the original system, it can be deduced that the region of interest can be

$$\alpha \in (0, 5) \quad \lambda \in (0, 1) \quad R \in (0, 1)$$

Analytical expressions for the inverse map and the jacobian of (7.26) are straightforward. This allows fast and precise computation with software packages like AUTO, DSTOOL and INSITE to obtain bifurcational behavior (see

Fig. 7.10). The hamiltonian case $\lambda = 1$ has already been studied in [Stolovitzky, Kaper and Sirovich, 1995] yielding a deep analysis of the homoclinic tangle of the system. The dissipative case $\lambda < 1$, which models the buck converter, can show very different dynamics, and it is left as future work to be done.

If $\frac{d\varphi}{dt} = \frac{w}{r}$ is replaced by $\frac{d\varphi}{dt} = \alpha - w \frac{r^2}{(1+r^2)^2}$ in the initial considerations of this section, imposing a limiting behaviour in the number of rounds around the origin, and the same analytical study is done with this system, then the following complex map is obtained

$$z_{n+1} = a + \lambda z_n e^{i(\alpha - \frac{p}{1+|z_n|^2})} \quad (7.27)$$

This map is known as the Ikeda map, and it has been extensively studied in the literature [Hammel, Jones and Moloney, 1985; Lai, Grebogi and Yorke, 1992]. Although for some parameter values it does not fit the dynamics of the converter quite well, it can model a buck with a restricted number of crossings in the ramp. A deeper analysis of this question is also left for the future.

7.5 Towards a General Classification

Finally, this section is concerned with how a general classification of a subset of two-topologies piecewise-linear vector fields on $\mathbb{R}^2 \times \mathbb{S}^1$ can be carried over. The family of systems

$$\dot{X} = AX + B + Cu \quad (7.28)$$

with $A \in \mathcal{M}_{2 \times 2}(\mathbb{R})$, $B \in \mathcal{M}_{2 \times 1}(\mathbb{R})$, $C \in \mathcal{M}_{2 \times 1}(\mathbb{R})$, and

$$u : \mathbb{R}^2 \times \mathbb{R} \rightarrow \{0, 1\}$$

models, among others, the buck converters with two topologies. Without further restrictions on the control u , this family can be very complicated to analyze with respect to bifurcations. Thus if it is imposed that u must be in the form

$$u = \begin{cases} 1 & \text{if } m_1 x_1 + m_2 x_2 < \alpha + \beta \tilde{t} \\ 0 & \text{if } m_1 x_1 + m_2 x_2 > \alpha + \beta \tilde{t} \end{cases} \quad (\tilde{t} = t \mod T) \quad (7.29)$$

then this family of systems will be easier to analyze.

Essentially, controls of this type include PWM with ramp control in voltage and current mode, and also the converters controlled by current mode, always considering the case of continuous conduction mode. The case of discontinuous conduction mode can be also treated in this way if more than two topologies are considered.

System (7.28) has a fixed point in each topology. When $u = 0$, the fixed point is $X_0 = -A^{-1}B$ while for $u = 1$, the fixed point is $X_1 = -A^{-1}(B + C)$. With a linear change $Y = X + A^{-1}B$ it can be assumed that one of the fixed points is the origin, and thus we can restrict the family to the systems

$$\dot{X} = AX + Bu \quad (7.30)$$

Next, one can consider the normal form for A which will be in the form of the following types

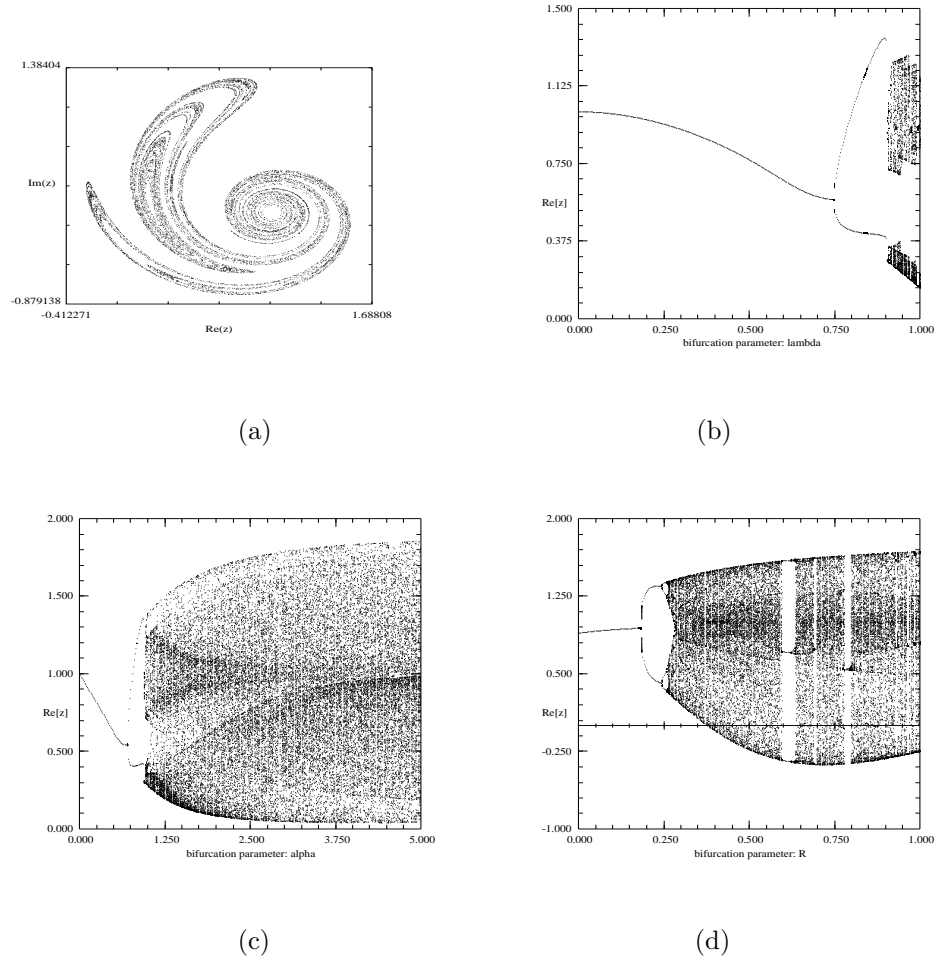


Figure 7.10: (a) Strange attractor for the approximated map of the buck converter. $\lambda = 0.85$, $R = 0.5$ and $\alpha = 3.0$. (b) Bifurcation diagram for $\text{Re}(z)$. $R = 0.5$ and $\alpha = 3$. (c) Bifurcation diagram for $\text{Re}(z)$. $R = 0.5$ and $\lambda = 0.85$. (d) Bifurcation diagram for $\text{Re}(z)$. $\lambda = 0.85$ and $\alpha = 3$.

$$\text{Type I: } \begin{pmatrix} \lambda_1 & 0 \\ 0 & \lambda_2 \end{pmatrix} \quad \text{Type II: } \begin{pmatrix} \lambda & 1 \\ 0 & \lambda \end{pmatrix} \quad \text{Type III: } \begin{pmatrix} k & w \\ -w & k \end{pmatrix}$$

It can be proved that, in each case, the vector B in (7.30) can be replaced without loss of generality by $(1, 1)^t$. Thus, the systems considered depend on five (Type II) or six (Type I and III) parameters. Notice that the parameters

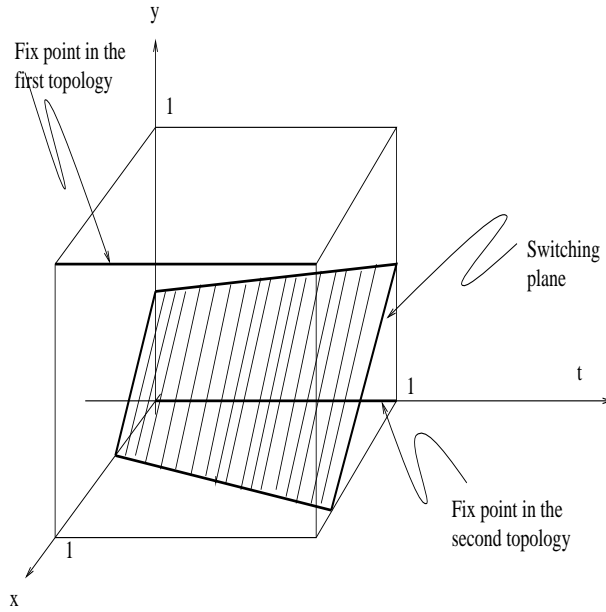


Figure 7.11: Scheme of the two-topologies system.

- m_1, m_2, α, β fix geometrically a certain plane in \mathbb{R}^3 .
- λ_1, λ_2 (or λ or k, w) fix the eigenvalues of the fixed points.

Notice that planes orthogonal to the time axis correspond to open-loop systems, since the switching instants only depend on a fixed time and not on the state variables; this case will not be considered. Moreover, planes parallel to the time axis imply a reduction in the order of the system (from three-dimensional to two-dimensional), and consequently this case is of no interest either. With this reduction, the equation of the plane $m_1x_1 + m_2x_2 = \alpha + \beta t$ can be changed to $m_1x + m_2y = m_1m_2 + \beta t$, and one more parameter is avoided (Fig. 7.11). From this point of view, the general situation (7.30) can be analysed into different cases and a general classification can be started.

In the case of the buck converter which has been studied throughout this thesis, the resulting normal form is

$$\begin{aligned} \frac{dx}{dt} &= kx - wy - (k + w)u \\ \frac{dy}{dt} &= -wy + kx - (k - w)u \end{aligned}$$

with

$$u = \begin{cases} 1 & \text{if } (-k + w)x + (k + w)y < \alpha(1 + \lambda \text{Frac}(t)) \\ 0 & \text{if } (-k + w)x + (k + w)y > \alpha(1 + \lambda \text{Frac}(t)) \end{cases} \quad (7.31)$$

which corresponds to a particular case of Type III.

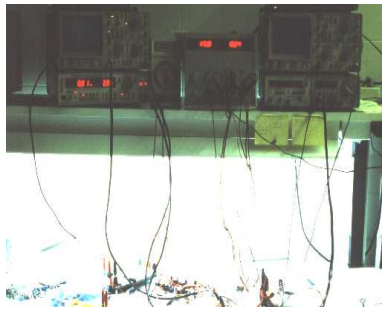
The relation of the new parameters with the older ones are

$$k = -\frac{T}{2RC} \quad w = \sqrt{\frac{T^2}{LC} - k^2}$$

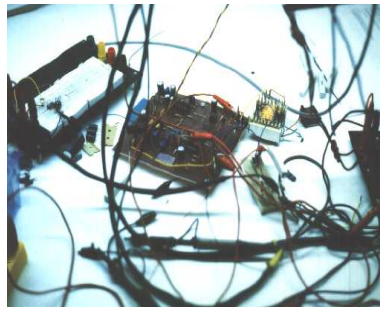
$$\alpha = \frac{2w}{a} \frac{V_L + aV_{ref}}{V_{in}} \quad \lambda = \frac{V_U - V_L}{V_L + aV_{ref}}$$

Some simulations have been done with INSITE, showing an important dependence on the parameters.

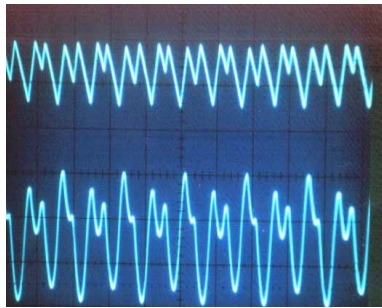
Control schemes other than voltage-controlled PWM have been proved to yield chaotic behaviour in the buck converter. Among others, a sliding-mode control has been shown to exhibit a standard period-doubling route to chaos [Guinjoan, private communication], and PWM with flip-flop also displays chaos when the input voltage V_{in} is varied [Iglesias and Fossas, 1992], or different parameters like V_{ref} or T are also changed [Toribio, private communication] (see Fig. 7.12). It goes without saying that the work in this thesis dealing with detection and explanation of the chaotic behaviour in the buck converter is only a small brick in the wall.



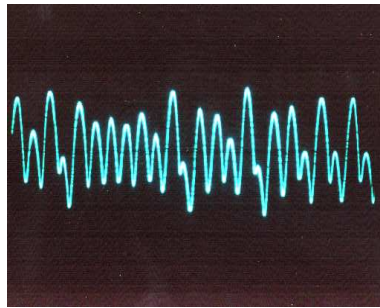
(a)



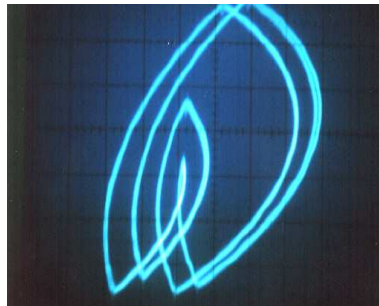
(b)



(c)



(d)



(e)

Figure 7.12: Experimental buck converter. (a) Measure instruments. (b) Buck prototype. (c) Experimental measures of the capacitor voltage and the inductor current. The input voltage corresponds to the periodicity range. (d) Experimental measure of the capacitor voltage. The input voltage corresponds to the chaotic range. (e) Experimental measures of the capacitor voltage and the inductor current in the phase space. The input voltage corresponds to the periodicity range.

Appendix A

Control of Switching Converters

Abstract

In this appendix, different methods for controlling DC-DC switching converters are reviewed. A very concise discussion of the development of these methods in dc-dc power converters is outlined.

Averaging

Research into many important branches of switching converter control has been based on averaged circuits. The earliest work on averaged circuit models for switching converters was that of [Wester and Middlebrook, 1972]. In this communication, the technique used to obtain an averaged circuit realization for a given switching converter was that of performing directly in the circuit. In particular, the authors suggested the construction of an averaged circuit model whose branch variables are one-cycle averages of the corresponding branch variables of the underlying switched circuit. This very physical approach results in an averaged circuit that closely resembles the underlying circuit.

The later synthesis method of [Middlebrook and Čuk, 1976; Čuk and Middlebrook, 1976], termed *hybrid modeling*, is based on the state-space averaged model. This technique results in circuit synthesis that do indeed implement the state-space averaged models for their underlying models. The development in [Čuk and Middlebrook, 1977] illustrated an analogous approach to synthesizing averaged circuits for switching converters operating in the discontinuous conduction mode. Averaged circuit models have also been developed for the analysis of switched capacitor filters. In particular, the paper [Tsividis, 1979] illustrates the replacement of a capacitor and switch pair by a simple resistor.

Averaging techniques [Middlebrook and Čuk, 1976] have become a useful tool for small-signal modeling of switching converters. The relationship between the averaged models and the original systems has been studied in [Lau and Middlebrook, 1986; Verghese and Mukherji, 1981]. The results of any approximation process, including averaging, might differ depending on the assumptions involved. This is particularly evident in power electronics, where numerous small-signal models have been proposed. In the work [Krein, Bentsman, Bass and Lesieutre, 1990] some fundamental questions are answered and applied to the open-loop PWM boost and buck converters and the feedback PWM buck converter. A generalization of averaging, known as the KBM (Krylov-Boguliov-Mitropolsky) method, considers a change of variables

$$x(t) = y(t) + \epsilon\phi_1(t, y) + \epsilon^2\phi_2(t, y) + \dots$$

where ϕ_i are zero-average functions of time, which transform the original system

$$\dot{x} = \epsilon F(t, x) \quad (\epsilon \ll 1, x(t_0) = x_0)$$

into the time-invariant system

$$\dot{y} = \epsilon G_1(y) + \epsilon^2 G_2(y) + \dots$$

In [Krein, Bentsman, Bass and Lesieutre, 1990], the authors state the validity of these averaging techniques when applied to small-signal and large-signal models, and ripple corrections are found and estimated from the behavior of the averaged model.

Also, state-space averaging has been applied to resonant switching converters and other alternative switching schemes [Witulski and Erickson, 1990; Maksimovic and Čuk, 1989]. The extended state-space averaging results indicate that the modeling techniques used so successfully in modeling PWM converters, such as the canonical equivalent circuit model [Middlebrook and Čuk, 1976], can also be applied to resonant switch and current-mode control converters [Witulski and Erickson, 1990; Maksimovic and Čuk, 1989]. In the work of Witulski, PWM analysis techniques are applied to the full and half-wave versions of the zero currents switch (ZCS), the zero voltage switch (ZVS) and the nonlinear resonant zero current switch (NRS) in a buck converter. In addition, Czarkovski and Kazimierczuk have presented a systematic method for including parasitic resistances and offset voltage sources of power switches in averaged dynamic large-signal and small-signal circuit models of PWM converters operating in continuous conduction mode. This method is based on the principle of energy conservation and leads to the same characteristics obtained from state-space averaging method.

Switching law control

A switching law control determines the discrete-valued input to the model at each instant, using partial or full state information. This method of control is

presently in use in various power electronic circuits. A simple application area is in the inductor current control loops of some dc-dc converters that use current mode programming [Deisch, 1978; Capel, Ferrante, O'Sullivan and Weinberg, 1978; Kailath, 1980]. The position of a switch is set by comparing the current level in the inductor with a commanded current level.

Sliding mode control

The theory of variable structure systems and the use of their associated sliding regimes for control design purposes has been extensively developed during the last 25 years [Emelyanov, 1967; Itkis, 1976; Utkin, 1977; Utkin, 1978; Utkin, 1981; Utkin, 1983;] with a growing number of applications in power systems control. A rigorous mathematical definition of the sliding motion was given by [Filippov, 1984]. In his doctoral thesis, Wood developed a sliding mode control algorithm for buck converters with second and fourth order output filters [Wood, 1973]. He demonstrated the global stability of these power circuits under his sliding mode control algorithm, and proposed the extension to converters with higher order output filter stages. A sliding mode controller for a buck converter was also proposed in the work [Venkataramanan, Sabonovic and Ćuk, 1985]. One interesting feature of the sliding curve proposed in this paper is that the switch (transistor, diode) current can be limited to a design value during transients if sliding operation is maintained. The authors are also concerned with the more complex problem of designing sliding surfaces for converters beyond the buck converter. In particular, a sliding mode control law is derived for a boost converter. The development of sliding mode control laws for switching power electronic circuits is also treated in the papers of Sira-Ramírez and Ilic [Sira-Ramírez, 1987, Sira-Ramírez and Ilic, 1988]. Sira-Ramírez applies sliding-mode control to buck, buck-boost and Ćuk-type converters [Sira-Ramírez, 1987]. Although the presentations in [Sira-Ramírez and Ilic, 1988] are made in a more general setting, all of the sliding surfaces considered in [Sira-Ramírez and Ilic, 1988] for dc-dc converters are of the form $x_j = K$ for some state variable x_j that is desired to be regulated at the level K . Sira-Ramírez proposes the use of slow manifolds as sliding surfaces for the variable structure feedback control [Sira-Ramírez and Ilic, 1988; Sira-Ramírez, 1989a]. The sliding mode control scheme of [Sira-Ramírez and Ilic, 1988] uses the slow manifold of the open-loop state-space averaged model as the sliding surface. This control method requires that the open-loop switching converter circuit has a dominant real eigenmode. With such a scheme, the dynamical behavior in the sliding mode is governed by the same dynamics that asymptotically governs the open-loop behavior. It has also been applied to the buck converter with input filter in [Domínguez, Fossas and Martínez, 1994; Fossas, Martínez and Ordinas, 1992].

Results on non-sliding switching law controls for converters with intrinsically nonlinear state-space models (i.e. buck-boost and boost converters) have been obtained using state-space methods [Burns and Wilson, 1977; Huffman, Burns, Wilson and Owens, 1977]. In particular, in [Burns and Wilson, 1977] the authors completed detailed studies of state-plane control laws for the basic converters. A serious problem lies in the necessity of accurate parameter

and state information. In that paper the relative insensitivity of the converter behavior under this control algorithm to variations in load conditions is demonstrated with simulations, and the same insensitivity was experimentally verified in [Huffman, Burns, Wilson and Owens, 1977]. However, if some circuit parameters are not known precisely, behavior that appears to be chaotic can result.

Recently, a current-programmed control technique was presented to control the average value of the Čuk converter output current [Poveda, Martínez, Perpinyà, Font and Manuel, 1993]. The method distinguishes between the slow variation components and the fast variation ones; applied to the Čuk converter, it results in a transfer function of the open voltage regulating loop that exhibits better single-pole approximation behavior than the classical current mode controls. Introducing some small modifications in the control circuit, the same paper [Poveda, Martínez, Perpinyà, Font and Manuel, 1993] presents a good fixed-frequencies realization of a high-efficiency time-variable gyrator for power applications, as was presented in [Singer, 1988]. More recently, double bridge converters have also been modeled by the gyrator theory to analyze their average dynamics [Ehsani, Husain and Bilgiç, 1993]. Discrete models have also been used in small-signal model switching dc-dc converters in simulations, partitioning the state vector into slow and fast variables and obtaining a nonlinear discrete recurrence.

Time-optimal control

The transient optimization problem of a bidirectional buck converter has also been studied by [Jammes, Bidan and Marpinard, 1991]. In this paper, a piecewise-linear output voltage control with a maximum inductor current modulator is proposed, ensuring both transient optimization and steady state control system, resulting in time-optimal control.

Large-signal state-space averaged models

Some pitfalls of control designs based on small signal models obtained by linearizing large signal averaged models are outlined in the paper [Erickson, Čuk and Middlebrook, 1982]. After discussing the development of large signal averaged models for switching converters, which have the form

$$x' = Ax + (Bx + b)u \quad (\text{A.1})$$

the effects of the quadratic nonlinearity introduced into the bilinear state-space model (A.1) by linear state feedback are considered. It is noted that the transient response to a strong perturbation can be substantially different from the transient expected from the small signal design. One noted feature of the feedback system with quadratic nonlinearity is the possible presence of multiple equilibria, which prohibit global stability. The effect of saturation due to the constraints on the duty ratio is also noted.

Control design for the large-signal state-space averaged model using the so-called quantitative feedback synthesis was explored in the paper [Horowitz, Sidi

and Erickson, 1984]. Their method characterizes a class of plant inputs (duty ratio waveforms) for each member of a set of possible plant models. The plant inputs are selected to produce a given desired output behavior (such as a start-up transient). The obtained input waveforms associated with the selected output waveforms are then used to determine approximate input-output transfer functions. Simulations results in [Horowitz, Sidi and Erickson, 1984] indicate the feasibility of this approach.

In order to avoid the discontinuous conduction mode and, at the same time, to allow the existence of light load levels, the bidirectional switch was introduced, which led to a bilinear description of the switching converters [Salut, Marpinard and Valentin, 1985; Valentin, 1984]. The transformation of the canonical buck, boost or buck-boost structures into bidirectional cells has extended the dynamic performances of the power converters. Large-signal control becomes mandatory in such converters.

Dissipative systems

One important approach to control of dynamical systems is via the theory of dissipative systems [Willems, 1972a; Willems, 1972b]. An n -input, n -output system modeled by

$$x' = f(x, u) \quad y = h(x, u)$$

is said to be dissipative with respect to the supply rate $w(u, y)$ if there is a non-negative definite internal storage function $V(x)$ such that

$$\frac{d}{dt}V - w(u, y) \leq 0.$$

The supply function that is of interest here is given by

$$w(u, y) = u^T y.$$

Some of the important features of dissipative systems are:

- i) a point in the state space where the storage function attains a local maximum defines a stable equilibrium and the storage function is a Lyapunov function for this equilibrium.
- ii) feedback interconnections of dissipative systems are dissipative [Willems, 1972a; Willems, 1972b].

The theory of dissipative systems was applied by Wood to obtain feedback control schemes for switching converters. The approach used in [Wood, 1973] was to view a closed-loop system (switching converter and controller) as the feedback interconnection of two dissipative systems. Wood began with an input-output model for a given switching converter from duty ratio to a selected averaged output variable. Such a model is not necessarily nor usually dissipative. The controller was selected to be linear, time-invariant, and such that its transfer function could be factored into two factors: one which combined with the

plant input-output model to form a dissipative operator (a passive system), and a second which combined with the saturation constraint to also result in a passive input-output model. The stability of the resulting closed-loop system was derived by using the Lyapunov function corresponding to the sum of the storage functions of the two interconnected dissipative systems. The set of passive, linear, time-invariant transfer functions which result in passive operators when cascaded with a monotone nonlinearity were termed O'Shea functions in [Wood, 1973] (they were characterized in the paper [O'Shea, 1966]). Wood worked mainly with buck converters for which input-output models are essentially linear. In the work of [Brockett and Wood, 1974], a control scheme is outlined. It is closely related to the dissipative system approach, and applied to the type of bilinear system that arises in switching power circuits.

Controllable linear equivalent systems

There has also been significant work done on the problem of characterizing systems that are controllable linear equivalents, i.e. those that can be brought to the phase canonical form

$$x'_1 = x_2, \quad x'_2 = x_3, \quad \dots, \quad x'_n = f(x_1, x_2, \dots, x_n, u) \quad (\text{A.2})$$

via some nonlinear change of coordinates [Brockett, 1978; Su, 1982; Hunt, Su and Meyer, 1983; Isidori, 1985]. In [Sira-Ramírez and Ilic, 1990] the problem of feedback linearization for various dc-dc converters is investigated. With a system in the form (A.2), one can consider choosing the feedback control $u(x_1, \dots, x_n)$ so that the system behaves as a prescribed linear time-invariant model.

An approach to the feedback control problem for power electronic circuits along the lines of this so-called feedback linearization was taken in [Salut, Marpinard and Valentin, 1985]. There, a simple feedback law is selected so that the capacitor voltage obeys a stable first order linear, time-invariant differential equation. It is then demonstrated that the other state variables exhibit stable behavior.

Pseudolinearization

It turns out that many state-space systems modeling switching converters cannot be brought to the form (A.2) by some state-space transformation. A similar approach termed pseudolinearization that may have wider application has been developed in [Reboulet and Champetier, 1984]. This approach involves determining nonlinear transformations of the state and control inputs so that the tangent model (small signal linearization) of the transformed system is in phase canonical form (A.2). This approach to control has been applied by [Sira-Ramírez, 1989b] for the feedback control of bilinear switched networks such as the boost and the buck-boost power converters. A physically meaningful local diffeomorphic state coordinate transformation, expressible in terms of stored energy and consumed power, is found, which turns the average perturbed model into a Brunovsky canonical form independent of the operating

point. The linearized model is then used for the specification of a stabilizing feedback loop whose control action regulates the duty ratio around its nominal operating value. A similar but conceptually different approach was taken in [Sanders, Verghese and Cameron, 1986] for the variable structure control of the boost converter using feedback linearization [Hunt, Su and Meyer, 1983].

The work reported in [Majó, Martínez, Fossas, Poveda, García de Vicuña, Guinjoan and Sánchez, 1990], exhibits control via pseudolinearization applied to a Čuk-type converter. This technique was also applied to the elementary boost converter in [Fossas, Martínez and Biel, 1991].

Appendix B

Basic Tools for Analyzing Chaos

Abstract

In this appendix, some basic mathematical tools are introduced, which will be of extreme interest when describing chaos in the basic cell converters. Some final remarks are also made regarding the particular systems under consideration.

Poincaré Maps

The idea of reducing the study of continuous time systems (flows) to the study of an associated discrete time system (map) is due to Poincaré (1899), who first utilized it in his studies of the three body problem in celestial mechanics. Nowadays, virtually any discrete time system which is associated to an ordinary differential equation is referred to as a Poincaré map. This technique offers several advantages in the study of ordinary differential equations, three of which are the following:

- 1) Dimensional reduction
- 2) Global dynamics
- 3) Conceptual clarity

In the following cases, the construction of a specific type of Poincaré map can in some sense be said to be canonical.

- 1) In the study of the orbit structure near a periodic orbit of an ordinary differential equation.

- 2) In the case where the phase space of an ordinary differential equation is periodic.
- 3) In the study of the orbit structure near a homoclinic or heteroclinic orbit.

The relationship between periodic ordinary differential equations and Poincaré maps is straightforward. Consider the following ordinary differential equation

$$\dot{x} = f(x, t), \quad x \in \mathbb{R}^n \quad (\text{B.1})$$

where $f : U \longrightarrow \mathbb{R}^n$

Suppose that the time dependance of f is periodic with fixed period $T = 2\pi/\omega > 0$ (i.e. $f(x, t) = f(x, t + T)$). We can rewrite (B.1) in the form of an autonomous equation in $n + 1$ dimensions by defining the function

$$\begin{aligned} \theta : \mathbb{R}^1 &\longrightarrow S^1 \\ t &\mapsto \theta(t) = \omega t \mod(2\pi) \end{aligned} \quad (\text{B.2})$$

Using (B.2), equation (B.1) becomes

$$\begin{aligned} \dot{x} &= f(x, \theta) \\ \dot{\theta} &= \omega \end{aligned} \quad (x, \theta) \in \mathbb{R}^n \times S^1 \quad (\text{B.3})$$

Denote by

$$\phi(t) = (x(t), \theta(t)) \equiv \omega t + \theta_0 \mod(2\pi)$$

the flow generated by (B.3).

We define a global cross-section $\Sigma^{\bar{\theta}_0}$ to the vector field (B.3) by

$$\Sigma^{\bar{\theta}_0} = \{(x, \theta) \in \mathbb{R}^n \times S^1 \text{ such that } \theta = \bar{\theta}_0 \in (0, 2\pi]\}$$

We define the Poincaré map of $\Sigma^{\bar{\theta}_0}$ into itself as follows:

$$\begin{aligned} P_{\bar{\theta}_0} : \Sigma^{\bar{\theta}_0} &\longrightarrow \Sigma^{\bar{\theta}_0} \\ (x(\frac{\bar{\theta}_0 - \theta_0}{\omega}), \bar{\theta}_0) &\mapsto (x(\frac{\bar{\theta}_0 - \theta_0 + 2\pi}{\omega}), \bar{\theta}_0 + 2\pi \equiv \bar{\theta}_0) \end{aligned}$$

or simply

$$x(\frac{\bar{\theta}_0 - \theta_0}{\omega}) \mapsto x(\frac{\bar{\theta}_0 - \theta_0 + 2\pi}{\omega})$$

Definition:

x^* is a fixed point of the map P if $x^* = P(x^*)$.

The set $\{x_1^*, \dots, x_m^*\}$ is a period- m closed orbit of P if

$$x_{k+1}^* = P(x_k^*) \quad \text{for } k = 1, \dots, m-1 \text{ and } x_1^* = P(x_m^*)$$

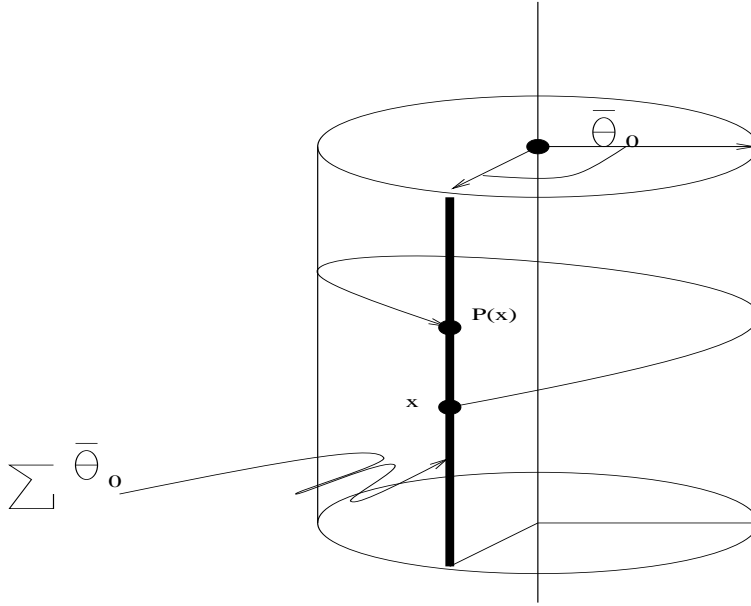


Figure B.1: Poincaré map $P : \Sigma^{\bar{\theta}_0} \rightarrow \Sigma^{\bar{\theta}_0}$.

Thus, the Poincaré map merely tracks initial conditions in x at a fixed phase after successive periods of the vector field. Fixed points of $P_{\bar{\theta}_0}$ correspond to $2\pi/\omega$ -periodic orbits of (B.1), which pierce $\Sigma^{\bar{\theta}_0}$ k times before closing.

Characteristic (Floquet) multipliers

The stability of a periodic solution is determined by its characteristic multipliers, also called Floquet multipliers. Characteristic multipliers are a generalization of the eigenvalues at an equilibrium point.

Consider a fixed point x^* of a map P . The local behavior of the map near x^* is determined by linearizing the map at x^* . In particular, the linear map

$$\delta x_{k+1} = DP(x^*)\delta x_k$$

governs the evolution of a perturbation δx_0 in a neighbourhood of the fixed point x^* .

Let p be the dimension of the Poincaré map P .

Let the eigenvalues of $DP(x^*)$ be $m_i \in \mathbb{C}$, with corresponding eigenvectors $\eta_i \in \mathbb{C}^p$ for $i = 1, \dots, p$. Assuming that the eigenvectors are distinct, the orbit of P with initial condition $x^* + \delta x_0$ is, to first order,

$$x_k = x^* + \delta x_k = x^* + DP(x^*)^k \delta x_0 = x^* + c_1 m_1^k \eta_1 + \dots + c_p m_p^k \eta_p$$

where $c_i \in \mathbb{C}$ are constants chosen to achieve the correct initial conditions.

The eigenvalues m_i are called the characteristic multipliers of the periodic solution. Like eigenvalues at an equilibrium point, the characteristic multipliers position in the complex plane determines the stability of the fixed point. If m_i is real, then η_i and c_i are also real, and it is clear that the characteristic multiplier is the amount of contraction (if $m_i < 0$) or expansion (if $m_i > 0$) near x^* in the direction of η_i for one iteration of the map.

In the case of complex eigenvalues, the magnitude of m_i gives the amount of expansion (if $|m_i| > 1$) or contraction (if $|m_i| < 1$) for one iteration of the map; the angle of the characteristic multiplier is the frequency of rotation.

Invariant manifolds

Roughly speaking, an invariant manifold is a surface contained in the phase space of a dynamical system whose property is that orbits starting on the surface remain on the surface throughout the course of their dynamical evolution.

Let $S \subseteq \mathbb{R}^n$ be a set.

Then,

a) Continuous time: S is said to be invariant under the vector field $\dot{x} = f(x)$ if for any $x_0 \in S$ we have $x(t, 0, x_0) \in S$ for all $t \in \mathbb{R}$.

b) Discrete time: S is said to be invariant under the map $x \mapsto g(x)$ if for any $x_0 \in S$, we have $g^n(x_0) \in S$ for all n .

An invariant set $S \subseteq \mathbb{R}^n$ is said to be a \mathcal{C}^r , ($r \geq 1$) invariant manifold if S has the structure of a \mathcal{C}^r differentiable manifold.

Additionally, the set of orbits which approach or recede from an invariant manifold \mathcal{M} asymptotically in time under certain conditions are also invariant manifolds which are called the stable and unstable manifolds, respectively, of \mathcal{M} .

Knowledge of the invariant manifolds of a dynamical system, as well as the intersection of their respective stable and unstable manifolds, is absolutely crucial in order to obtain a complete understanding of the global dynamics.

Suppose we have

$$\dot{x} = f(x) \quad x(0) = 0 \quad x \in \mathbb{R}^n, \quad (\text{B.4})$$

where $f : \mathbb{R}^n \rightarrow \mathbb{R}^n$. We make the following assumptions:

I) $f(0) = 0$

II) $Df(0)$ has $n - k$ eigenvalues having positive real parts and k eigenvalues having negative real parts.

Definition:

$x = 0$ is called a hyperbolic fixed point for $\dot{x} = f(x)$ if $f(0) = 0$ and $Df(0)$ has no eigenvalues with zero real part.

Linearizing the system, we can denote by

$$v_1, \dots, v_{n-k}$$

the generalized eigenvectors corresponding to the eigenvalues having positive real parts, and

$$v_{n-k+1}, \dots, v_n$$

the generalized eigenvectors corresponding to the eigenvalues having negative real parts. Then, the linear subspaces of \mathbb{R}^n defined as

$$E^u = \text{span}\{v_1, \dots, v_{n-k}\} \qquad E^s = \text{span}\{v_{n-k+1}, \dots, v_n\}$$

are invariant manifolds for the linear system which are known as the unstable and stable subspaces, respectively.

The stable manifold theorem for hyperbolic fixed points tell us that in a neighbourhood U of the fixed point $x = 0$, there exist a $(n - k)$ -dimensional surface $W_{loc}^u(0)$ tangent to E^u at $x = 0$ and a k -dimensional surface $W_{loc}^s(0)$ tangent to E^s at $x = 0$, with the properties that orbits of points on $W_{loc}^u(0)$ approach $x = 0$ asymptotically in negative time (i.e. as $t \rightarrow -\infty$) and orbits of points on $W_{loc}^s(0)$ approach $x = 0$ asymptotically in positive time (i.e. as $t \rightarrow \infty$). $W_{loc}^u(0)$ and $W_{loc}^s(0)$ are known as the local unstable and local stable manifolds, respectively, of $x = 0$.

Let us denote the flow generated by (B.4) as $\phi_t(x)$; then, we can define global stable and unstable manifolds of $x = 0$ by using points on the local manifolds as initial conditions.

$$W^u(0) = \bigcup_{t \geq 0} \phi_t(W_{loc}^u(0)) \qquad W^s(0) = \bigcup_{t \leq 0} \phi_t(W_{loc}^s(0))$$

$W^u(0)$ and $W^s(0)$ are called the unstable and stable manifolds, respectively, of $x = 0$.

All of this can be defined when a map $P : \mathbb{R}^n \rightarrow \mathbb{R}^n$ is considered. Intuitively, the stable manifold of a fixed point x_0 of P will be the set of all points x such that $P^k(x)$ approaches x_0 as $k \rightarrow \infty$, and the unstable manifold will be defined as the set of all points x such that $P^k(x)$ approaches x_0 as $k \rightarrow -\infty$.

Chaos and strange attractors

Assume that $\Lambda \subseteq \mathbb{R}^n$ is a compact set, invariant under the flow $\phi_t(x)$ of a vector field $\dot{x} = f(x)$. This flow is said to have sensitive dependence on initial conditions on Λ if there exists $\epsilon > 0$ such that for all $x \in \Lambda$ and any neighbourhood U of x , there exists $y \in U$ and $t > 0$ such that $|\phi_t(x) - \phi_t(y)| > \epsilon$. An analogous definition can be stated for a map.

Roughly speaking, this definition says that for any point $x \in \Lambda$ there is at least one point arbitrarily close to Λ that diverges from x . Some authors require the rate of divergence to be exponential. This is not very convenient, because there are examples where the strange attractors observed in numerical experiments of typical dynamical systems arising in applications will not, in general, be hyperbolic. Hence, one should expect parts of the attractor to exhibit nonexponential contraction or expansion rate.

Definition:

A closed connected set $D \subseteq \mathbb{R}^n$ is called a trapping region if $\phi_t(D) \subseteq D$ for all $t > 0$.

Definition:

A closed invariant set $\mathcal{A} \subseteq \mathbb{R}^n$ is called an attracting set if there is some neighbourhood U of \mathcal{A} such that

$$\forall x \in U, \forall t \geq 0, \phi_t(x) \in U \text{ and } \phi_t(x) \rightarrow \mathcal{A} \text{ as } t \rightarrow \infty$$

Definition:

A flow $\phi_t(x)$ is said to be topologically transitive on a closed invariant set Λ if, for any two open sets $U, V \subseteq \Lambda$, there exists $t \in \mathbb{R}$ such that $\phi_t(U) \cap V \neq \emptyset$.

A topologically transitive attracting set is called an attractor.

Definition:

Λ is said to be chaotic if

- 1.- $\phi_t(x)$ has sensitive dependence on initial conditions on Λ
- 2.- $\phi_t(x)$ is topologically transitive on Λ

Definition:

Suppose $\mathcal{A} \subseteq \mathbb{R}^n$ is an attractor. Then \mathcal{A} is called a strange attractor if it is chaotic.

Hence, if we want to prove that a dynamical system has a strange attractor we might proceed as follows:

Step 1: Find a trapping region \mathcal{M} in the phase space.

Step 2: Show that \mathcal{M} contains a chaotic invariant set Λ . In practice, this means showing that inside \mathcal{M} there is a homoclinic orbit (or heteroclinic cycle) [Guckenheimer and Holmes, 1983] which has associated with it an invariant Cantor set on which the dynamics are topologically conjugate to a full shift on N symbols.

Then

$$\mathcal{A} \equiv \bigcap_{t>0} \phi_t(\mathcal{M})$$

is an attracting set and $\Lambda \subseteq \mathcal{A}$, so that \mathcal{A} contains a mechanism that gives rise to sensitive dependence on initial conditions; in order to conclude that \mathcal{A} is a strange attractor we need only to demonstrate the following:

- a) The sensitive dependence on initial conditions on Λ extends to \mathcal{A}
- b) \mathcal{A} is topologically transitive

Showing that \mathcal{A} is topologically transitive is the most difficult step. This is because a single stable orbit in \mathcal{A} will destroy topological transitivity, and some known results state that periodic sinks are always associated with quadratic homoclinic tangencies. Moreover, as a result of Newhouse's work, at least for two-dimensional dissipative maps, these homoclinic tangencies are persistent in the sense that if we destroy a particular tangency, we will create another elsewhere in the homoclinic tangle. This is largely the reason why there is still no analytical proof of the existence of a strange attractor for the periodically forced, damped Duffing oscillator, despite an enormous amount of numerical evidence.

At present, there exist rigorous results concerning strange attractors in the areas of one-dimensional non-invertible unimodal maps, hyperbolic attractors of two-dimensional maps and Lorenz-like systems, where the topology avoids many of the problems associated with Newhouse sinks. Also, the Henon map has been proven to possess a strange attractor for certain values of the parameters.

Final remarks:

1) The dynamics of the full shift on N symbols best describes what is meant by the term chaos as applied to deterministic dynamical systems. The system is purely deterministic; however, the dynamics are such that our inability to precisely specify the initial conditions results in a behavior that appears random or unpredictable.

2) Unlike some authors, we have not included the requirement of density of periodic orbits in the definition of the chaotic invariant set. If the chaotic invariant set is hyperbolic, then, by the shadowing lemma [Guckenheimer and Holmes, 1983], it follows immediately that the periodic orbits are dense.

3) One of the fundamental hypothesis in the statements and theorems on bifurcations and chaotic dynamics is the \mathcal{C}^r -condition ($r \geq 1$) on the vector field f that defines the system. This is largely due to the capability of linearizing f at periodic or fixed points. When dealing with switching converters, f has inherent discontinuities that make all the results regarding smooth vector fields invalid. In spite of this, numerical evidence is found to suggest that very similar situations and results can be stated for discontinuous vector fields f that behave like a continuous one in a neighbourhood of a fixed or periodic isolated discontinuous point of f .

Appendix C

Bibliography

- Abarbanel H.D.I. and Linsay P.S. [1993].
“Secure communications and unstable periodic orbits of strange attractors.” *IEEE Transactions on Circuits and Systems-II*, VOL. 40, NO. 10. pp. 643-645. October 1993.
- Aguirre L.A. and Billings S.A. [1994].
“Validating Identified Nonlinear Models with Chaotic Dynamics”. *International Journal of Bifurcation and Chaos*, Vol. 4, No. 1, pp. 109-125, February 1994.
- Angosto J. and Olivar G. [1996].
“Calcul de bifurcations amb AUTO”. *Final Project*, EUPVG, July 1996.
- Anishchenko V.S., Safonova M.A. and Chua L.O. [1993].
“Confirmation of the Afraimovich-Shilnikov torus-breakdown theorem via a torus circuit.” *IEEE Transactions on Circuits and Systems-I*, VOL. 40, NO. 11. pp. 792-800. November 1993.
- Arrowsmith D.K. and Place C.M. [1990].
“An introduction to dynamical systems”. *Cambridge University Press*, Cambridge, 1990.
- Aston P.J. and Bird C.M. [1995].
“Analysis of the control of chaos-rate of convergence”. *International Journal of Bifurcation and Chaos*, VOL. 5, No. 4, 1995. pp. 1157-1165, 1995.
- Baillieul J., Brockett R.W. and Washburn R.B. [1980].
“Chaotic motion in nonlinear feedback systems”. *IEEE Transactions on Circuits and Systems*, VOL. 27, NO. 11. pp. 990-997. November 1980.
- Bai-Lin H. [1984].
“Chaos”. *World Scientific*, Singapore, 1984.

- Bai-Lin H. [1990].
 “Chaos II”. *World Scientific, Singapore, 1990.*
- Banerjee S. [1997].
 “Coexisting Attractors, Chaotic Saddles and Fractal Basins in a Power Electronic Circuit”. (submitted to the IEEE Transactions on Circuits and Systems, Part I).
- Barugola A., Cathala J.C. and Mira C. [1995].
 “Extension of the notion of chaotic area in second-order endomorphisms”. *International Journal of Bifurcation and Chaos*, Vol. 5, No. 3, pp. 751-777, 1995.
- Bass R.M., Heck B.S. and Khan R.A. [1994].
 “Average Modelling of Current-Controlled Converters: Instability Predictions”. *International Journal of Electronics*, Vol. 77, No. 5, pp. 613-628, November 1994.
- Battle C., Fossas E. and Olivar G. [1996a].
 “Stabilization of periodic orbits in Variable Structure Systems”. *Proceedings of NDES’96*, pp. 339-344, Seville, June, 1996.
- Battle C., Fossas E. and Olivar G. [1996b].
 “Time-delay stabilization of periodic orbits of the Buck converter”. *Preprint chao-dyn/9609009* available at xyz.lanl.gov, September, 1996.
- Battle C., Fossas E. and Olivar G. [1996c].
 “Stabilization of periodic orbits in Variable Structure Systems. Application to DC-DC Power Converters”. *International Journal of Bifurcation and Chaos*, Vol. 6, No. 12B, pp. 2635-2643, December, 1996.
- Bleich M.E. and Socolar J.E.S. [1996a].
 “Stability of periodic orbits controlled by time-delay feedback”. *Preprint chao-dyn/9510019*, available at xyz.lanl.gov, October, 1995.
- Bleich M.E. and Socolar J.E.S. [1996b].
 “Controlling spatiotemporal dynamics with time-delay feedback”. *Preprint chao-dyn/9601006*, available at xyz.lanl.gov, January, 1996.
- Bose B.K. [1992].
 “Modern Power Electronics: Evolution, Technology and Applications”. *IEEE Press*, New York 1992.
- Brockett R.W. [1978].
 “Feedback invariants for nonlinear systems”. *IFAC Congress, Helsinki, 1978.*
- Brockett R.W. and Wood J.R. [1974].
 “Electrical networks containing controlled switches”. *Addendum to IEEE Symposium on Circuit Theory*. April 1974.
- Burns W. and Wilson T. [1977].
 “Analytic derivation and evaluation of a state-trajectory control law for dc-dc converters”. *IEEE PESC Record*, pp. 70-85, 1977.

- Buskirk R.V. and Jeffries C. [1995].
 "Observation of chaotic dynamics of coupled nonlinear oscillators".
Physical Review A, VOL. 31, NO. 5. pp. 3332-3357. May 1995.
- Capel A., Ferrante G., O'Sullivan D. and Weinberg A. [1978].
 "Application of the injected current model for the dynamical analysis of switching regulators with the new concept of LC^3 modulator". *IEEE PESC Record*, pp. 135-147, 1978.
- Carbonell J.M. and Olivar G. [1994].
 "Estudi numèric del comportament caòtic d'un convertidor DC-DC".
Final Project, EUPVG, Setember 1994.
- Carroll T.L. and Pecora L.M. [1991].
 "Synchronizing chaotic circuits". *IEEE Transactions on Circuits and Systems*, VOL. 38, NO. 4. pp. 453-456. April 1991.
- Carroll T.L. and Pecora L.M. (editors) [1995].
 "Nonlinear Dynamics in Circuits". *World Scientific*, Singapore, 1995.
- Chakrabarty K. and Banerjee S. [1995].
 "Control of Chaos in Piecewise-linear Systems with Switching Nonlinearity". *Physics Letters A* 200, pp. 115-120, 1995.
- Chakrabarty K., Poddar G. and Banerjee S. [1996].
 "Bifurcation Behavior of the Buck Converter". *IEEE Transactions on Power Electronics*, Vol. 11, No. 3, pp. 439-447, May 1996.
- Chakravarthy S.K., Nayar C.V. [1995].
 "Parallel (Quasi-periodic) Ferroresonant Oscillations in Electrical Power Systems". *IEEE Transactions on Circuits and Systems, Part I*, Vol. 42, No. 9, pp. 530-534, September 1995.
- Chen G. [1994].
 "Control and synchronization of chaotic systems (bibliography)". *EE Dept.*, *University of Houston*, TX. May 1994.
- Chiang H.D. and Fekih-Ahmed L. [1993].
 "Persistence of saddle-node bifurcations for general nonlinear systems under unmodeled dynamics and applications". *Proceedings of the 1993 International Symposium of Circuits and Systems*, pp. 2656-2659, 1993.
- Chua L.O. (editor) [1987].
 "Special Issue on Chaotic Systems". *Proceedings of the IEEE*. August 1987.
- Chua L.O., Hasler M., Neirynck J. and Verburgh P. [1982].
 "Dynamics of a piecewise-linear resonant circuit". *IEEE Transactions on Circuits and Systems*, Vol. 29, No. 8, pp. 535-547, August 1982.
- Cuomo K.M., Oppenheim A.V. and Strogatz S.H. [1993].
 "Synchronization of Lorenz-based chaotic circuits with applications to communications". *IEEE Transactions on Circuits and Systems-II*, VOL. 40, NO. 10. pp. 626-633. October 1993.

- Čuk S. and Middlebrook R.D. [1976].
 “Modeling, analysis and design of switching converters”. *NASA Report CR-135174*.
- Čuk S. and Middlebrook R.D. [1977].
 “A general unified approach to modeling switching converters in discontinuous conduction mode” *IEEE PESC Record*, pp. 36-57, 1977.
- Dahlquist G. and Bjorck A. [1974]
 “Numerical Methods”. *Englewood-Cliffs, NJ. Prentice-Hall*, 1974.
- de Sousa Vieira M., Lichtenberg A.J. and Lieberman M.A. [1996]
 “Nonlinear feedback for control of chaos”. *Preprint cond-mat/9601127*, available at xyz.lanl.gov, January 1996.
- Deane J.H.B. [1992].
 “Chaos in a current-mode controlled boost dc-dc converter”. *IEEE Transactions on Circuits and Systems-I, VOL. 39, NO. 8*. pp. 680-683. August 1992.
- Deane J.H.B. and Hamill D.C. [1990a].
 “Analysis, simulation and experimental study of chaos in the buck converter”. *IEEE Power Electronics Specialists Conference*, Vol. II, PESC’90 Records, pp. 491-498, San Antonio TX, June 1990.
- Deane J.H.B. and Hamill D.C. [1990b].
 “Instability, subharmonics, and chaos in power electronic systems”. *IEEE Transactions on Power Electronics, VOL. 5, NO. 3*. pp. 260-268. July 1990.
- Deane J.H.B. and Hamill D.C. [1991].
 “Chaotic behaviour in current-mode controlled dc-dc convertor”. *Electronic Letters, VOL. 27, NO. 13*. pp. 1172-1173. June 1991.
- Dedieu H. and Ogorzalek M. [1994].
 “A simple and robust method for controlling chaotic systems”. *Proceedings of the 1994 International Symposium of Circuits and Systems*, pp. 85-88, 1994.
- Deisch C.W. [1978].
 “Simple switching control method changes power converter into a current source”. *IEEE PESC Record*, pp. 300-306, 1978.
- Devaney R.L. [1989].
 “An introduction to chaotic dynamical systems”. *Addison-Wesley, Redwood City*, 1989.
- di Bernardo M., Champneys A., Garofalo F., Glielmo L. and Vasca F. [1996].
 “Nonlinear phenomena in the DC-DC Buck Converter”. *Proceedings of NDES’96: Fourth International Workshop on Nonlinear Dynamics of Electronic Systems*, pp. 51-56, June 1996.

- di Bernardo M., Fossas E., Olivar G. and Vasca F. [1997].
 “Secondary Bifurcations and High Periodic Orbits in Voltage Controlled Buck Converter”. (to appear in December 1997 in the International Journal of Bifurcations and Chaos).
- di Bernardo M., Garofalo F., Glielmo L. and Vasca F. [1996].
 “Quasi-Periodic Behaviors in Dc-Dc Converters”. *PESC’96*, pp. 1376-1381, Milan, June 1996.
- di Bernardo M., Garofalo F., Glielmo L. and Vasca F. [1997].
 “Impacts, Bifurcations and Chaos in Dc-Dc Converters” (submitted to the Transactions on Circuits and Systems, Part I).
- Diener M. [1981].
 “On the perfect delay convention or the revolt of the slaved variables (from Chaos and order in nature)”. *Springer Series in Synergetics*, 1981.
- Doedel E.J. and Wang X.J. [1995].
 “AUTO94: Software for continuation and bifurcation problems in ordinary differential equations”. *Technical Report CRPC-95-2*, California Institute of Technology (Pasadena).
- Domínguez F., Fossas E. and Martínez L. [1994].
 “Stability analysis of a buck converter with input filter via sliding-mode approach”. *Proceedings of the 20th International Conference on Industrial Electronics Control and Instrumentation. (IECON’94), VOL. 3*, pp. 1438-1442, September 1994.
- Drazin P.G. [1992].
 “Nonlinear systems”. *Cambridge University Press, Cambridge*, 1992.
- Eckmann J.P. [1981].
 “Roads to turbulence in dissipative systems”. *Reviews of Modern Physics*, VOL. 53, NO. 4, Part I. pp. 643-654. October 1981.
- Eckmann J.P. and Ruelle D. [1985].
 “Ergodic theory of chaos and strange attractors”. *Reviews of Modern Physics*, VOL. 57, NO. 3, Part I. pp. 617-656. July 1985.
- Ehsani M., Husain I. and Bilgiç M.O. [1993].
 “Power converters as natural gyrators”. *IEEE Transactions on Circuits and Systems-I*, VOL. 40, NO. 12, pp. 946-948, December 1993.
- Emelyanov S.V. [1967].
 “Variable structure control”. *Nauka, Moscow*, 1967.
- Erickson R.W., Čuk S., and Middlebrook R.D. [1982].
 “Large-signal modeling and analysis of switching regulators”. *IEEE PESC Record.*, pp. 240-250, 1982.

- Fillipov A.F. [1984].
 “Differential equations with discontinuous right-hand side”. *Translations of the American Mathematical Society, series 2, VOL. 2*, pp. 199-231, 1984.
- Foale S. and Thompson J.M.T. [1991].
 “Geometrical concepts and computational techniques of nonlinear dynamics”. *Computer methods in applied mechanics and engineering*, Vol. 89, pp. 381-394, 1991.
- Font J.M., Rodríguez-Manero J.L. and Verghese G.C. [1995].
 “Chaos in dc-dc Converters under Current-Mode Control” (In Spanish). *Memoria Técnica del Seminario Anual de Automática y Electrónica Industrial*, Tarragona (Spain), September 1995.
- Fossas E., Martínez L. and Biel D. [1991].
 “Computer-aided large-signal analysis-and-control of boost converter-based switching regulators”. *Proceedings of the 34th Midwest Symposium on Circuits and Systems, 1991*.
- Fossas E., Martínez L. and Ordinas J. [1992].
 “Sliding mode control reduces audiosusceptibility and load perturbations in the Čuk converter”. *IEEE Transactions on Circuits and Systems-I, VOL. 39, NO. 10*, pp. 847-849, October 1992.
- Fossas E. and Olivar G. [1996].
 “Study of Chaos in the Buck Converter”. *IEEE Transactions on Circuits and Systems, Part I*, Vol. 43, No. 1, pp. 13-25, January 1996.
- Freire E., Franquelo L.G. and Aracil J. [1984].
 “Periodicity and chaos in an autonomous electronic system”. *IEEE Transactions on Circuits and Systems, VOL. 31, NO. 3*, pp. 237-247, March 1984.
- Gollub J.P., Brunner T.O. and Danly B.G. [1978].
 “Periodicity and chaos in coupled nonlinear oscillators”. *Science, VOL. 200*, 1978.
- Grebogi C., Mc Donald S.W., Ott E. and Yorke J. [1983].
 “Final state sensitivity: an obstruction to predictability”. *Physics Letters*, Vol. 99 A, No. 9, pp. 415-418, 1983.
- Grebogi C., Ott E. and Yorke J. [1982].
 “Chaotic attractors in crises”. *Physical Review Letters*, Vol. 48, No. 22, pp. 1507-1510, 1982.
- Grebogi C., Ott E. and Yorke J. [1983a].
 “Fractal basin boundaries, long-lived chaotic transients and unstable-unstable pair bifurcations”. *Physical Review Letters*, Vol. 50, No. 13, pp. 935-938, 1983.

- Grebogi C., Ott E. and Yorke J. [1983b].
 “Crises, sudden changes in chaotic attractors and transient chaos”.
Physica 7D, pp. 181-200, 1983.
- Grebogi C., Ott E. and Yorke J. [1986].
 “Metamorphoses of basin boundaries of nonlinear systems”. *Physical Review Letters*, Vol. 56, No. 10, pp. 1011-1014, 1986.
- Grebogi C., Ott E. and Yorke J. [1987].
 “Basin boundaries metamorphoses: changes in accessible boundary orbits”. *Physica 24 D*, pp. 243-262, 1987.
- Hale J.K. and Verduyn Lunel S.M. [1993].
 “Introduction to Functional Differential Equations”. *Springer-Verlag*.
- Hammel S.M., Jones C.R.K.T. and Moloney J.V. [1985].
 “Global dynamical behavior of the optical field in a ring cavity”. *J. Opt. Soc. Am. B*, VOL. 2, NO 4, pp. 552-564, April 1985.
- Hamill D.C. [1992].
 “Chaos in switched-mode dc-dc converters”. *Proceedings of the IEE Colloquium on Static Power Conversion*, pp. 5/1-5/4, IEE digest no. 1992/203, London, November 1992.
- Hamill D.C. [1993].
 “Learning About Chaotic Circuits with Spice”. *IEEE Transactions on Education*, Vol. 36, No. 1, pp. 28-35, February 1993.
- Hamill D.C. [1995].
 “Power Electronics: A Field Rich in Nonlinear Dynamics”. *Proceedings of the 3rd International Specialists Workshop on Nonlinear Dynamics of Electronic Systems NDES’95*, pp. 165-178, Dublin 1995.
- Hamill D.C., Deane J.H.B. and Jeffries D.J. [1992].
 “Modeling of chaotic dc-dc converters by iterated nonlinear mappings”. *IEEE Transactions on Power Electronics*, VOL 7, NO 1. pp. 25-36. January 1992.
- Hamill D.C. and Jeffries D.J. [1988].
 “Subharmonics and chaos in a controlled switched-mode power converter”. *IEEE Transactions on Circuits and Systems*, VOL. 35, NO. 8. pp. 1059-1061. August 1988.
- Hemati N. [1994].
 “Strange attractors in brushless DC Motors”. *IEEE Transactions on Circuits and Systems, Part I*, VOL. 41, NO. 1. pp. 40-45. January 1994.
- Hoppensteadt F.C. [1993].
 “Analysis and Simulation of Chaotic Systems”. *Applied Mathematical Sciences*, Vol. 94, Springer-Verlag, New York 1993.

- Horowitz I., Sidi M. and Erickson R. [1984].
 “Quantitative feedback synthesis for non-linear switched-mode uncertain regulators”. *International Journal of Electronics*, VOL. 57, NO. 4, pp. 461-476, 1984.
- Hsu, C. [1987].
 “Cell-to-Cell Mapping”. *Applied Mathematics Sciences*, 64, Springer-Verlag, New York, 1987.
- Hsu, C. [1992].
 “Global Analysis by cell mapping”. *International Journal of Bifurcation and Chaos*, Vol. 2, pp. 727-771, 1992.
- Huffman S., Burns W., Wilson T. and Owens H. [1977].
 “Fast-response free-running dc-dc converter employing a state-trajectory control law”. *IEEE PESC Record*, pp. 180-189, 1977.
- Hunt E.R. [1991].
 “Stabilizing High-Period Orbits in a Chaotic System: The Diode Resonator”. *Physical Review Letters*, VOL. 67, No. 15 pp. 1953-1955, October 1991.
- Hunt L.R. , Su R. and Meyer G. [1983].
 “Global transformations of nonlinear systems”. *IEEE Transactions On Automatic Control*, VOL. AC-28, pp. 24-31, January 1983.
- Iglesias A.M. and Fossas E. [1992].
 “Introducció al caos en sistemes no lineals i en l’electrònica de potència”. *Final Project*, EUPVG, January 1992.
- Isidori A. [1985].
 “Nonlinear control systems: An introduction”. *Springer Verlag Lecture Notes in Control and Information Sciences*, NO. 72, 1985.
- Itkis U. [1976].
 “Control systems of variable structure”. *Wiley, New York*, 1976.
- Jammes B., Bidan P. and Marpinard J.C. [1991].
 “Time optimal control of a buck converter used as pulsed supply”. *Proceedings of IMACS MCTS*, 1991.
- Jefferies D.J., Deane J.H.B. and Johnstone G.G. [1989].
 “An introduction to chaos”. *Electronics and Communication Engineering Journal*. pp. 115-123. May/June 1989.
- Kadanoff L.P. [1983].
 “Roads to chaos”. *Physics Today*. pp. 46-53. December 1983.
- Kailath T. [1980].
 “Linear systems”. *Prentice-Hall*, 1980.
- Kapitaniak T. and Wojewoda J. [1993].
 “Attractors of quasiperiodically forced systems”. *World Scientific, Singapore*, 1993.

- Kassakian J.G., Schlecht M.F. and Verghese G.C. [1991].
 “Principles of Power Electronics”. *Addison-Wesley*, 1991.
- Kennedy M.P. and Chua L.O. [1986].
 “Van der Pol and chaos”. *IEEE Transactions on Circuits and Systems*, VOL. 33, NO. 10. pp. 974-980. October 1986.
- Kevorkian P. [1993].
 “Snapshots of a dynamical evolution of attractors from Chua’s oscillator”. *IEEE Transactions on Circuits and Systems-I*, VOL. 40, NO. 10. pp. 762-780. October 1993.
- Kim J.H. and Stringer J. [1992].
 “Applied Chaos”. Wiley, New York, 1992.
- Kleczka M. and Kreuzer E. [1994].
 “On approximations of non-smooth functions in bifurcation analysis”, in *Nonlinearity and Chaos in Engineering Dynamics*, pp. 115-123, John Wiley and Sons, 1994.
- Kleczka M., Kreuzer E. and Wilmers C. [1989].
 “Crises in mechanical systems”, *IUTAM Symposium on Nonlinear Dynamics in Engineering Systems*, pp. 141-148, Springer-Verlag, 1989.
- Krein P.T. and Bass R.M. [1990].
 “Types of instability encountered in simple power electronic circuits: unboundedness, chattering, and chaos”. *Proceedings of the 1990 IEEE Applied Power Electronics Conference*. pp. 191-194. March 1990.
- Krein P.T., Bentsman J., Bass R.M. and Lesieutre B.L. [1990].
 “On the use of averaging for the analysis of power electronic systems”. *IEEE Transactions on Power Electronics*, VOL. 5, NO. 2, pp. 182-190, April 1990.
- Kuznetsov Yu.A. [1995].
 “Elements of Applied Bifurcation Theory”. *Applied Mathematical Sciences*, Vol. 112, Springer Verlag, New York 1995.
- Lai Y.C., Grebogi, C. and Yorke J.A. [1992].
 “Sudden changes in the size of chaotic attractors: how does it occur?”. in *Applied Chaos*, pp. 441-455, John Wiley and Sons, 1992.
- Lau B.Y. and Middlebrook R.D. [1986].
 “Small-Signal frequency response theory for piecewise-constant two-switched-network dc-to-dc converter systems”. *IEEE PESC Record*, pp. 186-200, 1986.
- Linsay P.S. [1981].
 “Period doubling and chaotic behavior in a driven anharmonic oscillator”. *Physics Review Letters*, VOL. 47, No. 19, pp. 1349-1352, November 1981.

- Lobry J. and Trecat J. [1995].
 “A Training Laboratory About Bifurcations and Chaos in Electrical Power Systems”. *International Journal of Electronic Engineering Education*, Vol. 32, No. 1, pp. 63-74, January 1995.
- Lonngren K.E. [1991].
 “Notes to accompany a student laboratory experiment on chaos”. *IEEE Transactions on Education*, Vol. 34, No. 1, pp. 123-128, February 1991.
- Maistrenko V.L., Maistrenko Yu. and Sushko I. [1994].
 “Noninvertible Two-dimensional Maps Arising in Radiophysics”. *International Journal of Bifurcation and Chaos*, Vol. 4, No. 2, pp. 383-400, 1994.
- Maistrenko Yu, Maistrenko V.L. and Chua L.O. [1993].
 “Cycles of chaotic intervals in a time-delayed Chua’s circuit”. *International Journal of Bifurcation and Chaos*, Vol. 3, No. 6, pp. 1557-1572, 1993.
- Maistrenko Yu, Maistrenko V.L., Vikul, S.I. and Chua L.O. [1995].
 “Bifurcation of attracting cycles from time-delayed Chua’s circuit”. *International Journal of Bifurcation and Chaos*, Vol. 5, No. 3, pp. 653-671, 1995.
- Majó J., Martínez L., Fossas E., Poveda A., García de Vicuña L., Guinjoan F. and Sánchez A.F. [1990].
 “Large-signal control of a bidirectional coupled-inductor Čuk converter via pseudolinearization”. *Proceedings of the 33rd Midwest Symposium on Circuits and Systems*, 1990.
- Maksimovic D. and Čuk S. [1989].
 “A general approach to synthesis and analysis of quasi-resonant converters”. *Proceedings of the 1989 IEEE PESC*, VOL. 2, pp. 713-727, 1989.
- Matsumoto T., Chua L.O. and Komuro M. [1985].
 “The double scroll”. *IEEE Transactions on Circuits and Systems*, VOL. 32, NO. 8. pp. 798-818. August 1985.
- Matsumoto T., Chua L.O. and Tokumasu K. [1986].
 “Double scroll via a two-transistor circuit”. *IEEE Transactions on Circuits and Systems*, VOL. 33, NO. 8. pp. 828-835. August 1986.
- Middlebrook R.D. and Čuk S. [1976].
 “A general unified approach to modeling switching power converter stages”. *IEEE PESC Record*, pp. 18-34, 1976.
- Mira C. [1980].
 “Complex dynamics in two-dimensional endomorphisms”. *Nonlinear Analysis, Theory, Methods and Applications*, 4, pp. 1167-1187, 1980.
- Mira C. [1987].
 “Chaotic dynamics. From the one-dimensional endomorphism to the two-dimensional diffeomorphism”. *World Scientific Singapore*, 1987.

- Mira C., Fournier-Prunaret D., Gardini L., Kawakami H. and Cathala J.C. [1994].
 “Basin Bifurcation of Two-dimensional Noninvertible Maps: Fractalization of Basins”. *International Journal of Bifurcation and Chaos*, Vol. 4, No. 2, pp. 343-381, 1994.
- Mira C. and Narayaminsamy T. [1993].
 “On behaviours of two-dimensional endomorphisms: Role of the critical curves”. *International Journal of Bifurcation and Chaos*, Vol. 3, No. 1, pp. 187-194, 1993.
- Mira C. and Rauzy C. [1995].
 “Fractal aggregation of basin islands in two-dimensional quadratic non-invertible maps”. *International Journal of Bifurcation and Chaos*, Vol. 5, No. 4, pp. 991-1019, 1995.
- Mohan N., Undeland T.M. and Robbins W.P. [1995].
 “Power Electronics: Converters, Applications and Design”, 2nd Edition, Wiley, New York 1995.
- Nusse H.E., Ott G. and Yorke J.A. [1994].
 “Border-collision Bifurcations: An explanation for observed bifurcation phenomena”, *Physical Review E*, Vol. 49, pp. 1073-1076, 1994.
- Nusse H.E. and Yorke J.A. [1992].
 “Border-collision Bifurcations including period 2 to period 3 for piecewise-smooth systems”, *Physica D*, Vol. 57, pp. 39-57 1992.
- Nusse H.E. and Yorke J.A. [1995].
 “Border-collision Bifurcations for Piecewise Smooth One-dimensional Maps”, *International Journal of Bifurcation and Chaos*, Vol. 5, No. 1, pp. 189-207, 1995.
- Ogorzalek M. [1993].
 “Taming Chaos: Part II - Control”. *IEEE Transactions on Circuits and Systems Part I*, pp. 700-706, 1993.
- Ogorzalek M. and Chua L.O. [1993].
 “Exploring chaos in Chua’s circuit via unstable periodic orbits”. *Proceedings of the ISCAS’93*, pp. 2608-2611, 1993.
- Ohnishi M. and Inaba I. [1994].
 “A singular bifurcation into instant chaos in a piecewise-linear circuit”. *IEEE Transactions on Circuits and Systems, Part I. VOL. 41, NO. 6*, pp. 433-442, June 1994.
- Olivar G. and Fossas, E. [1996].
 “Multiple Pulsing in the Buck Converter”. *ZAMM, Zeitschrift für Angewandte Mathematik und Mechanik*, Vol. 76, Supplement 5, pp. 367-368, December 1996.

- O'Shea R.P. [1966].
 "A combined frequency-time domain stability criterion for autonomous continuous systems". *IEEE Transactions on Automatic Control*, VOL. AC-11, NO. 3, pp. 477-484, July 1966.
- Ott E. [1993].
 "Chaos in dynamical systems". *Cambridge University Press, Cambridge, 1993*.
- Ott E., Grebogi C. and Yorke J.A. [1990].
 "Controlling Chaos". *Physics Review Letters*, Vol. 64, No. 11, pp. 1196-1199. March 1990.
- Parker T.S. and Chua L.O. [1989].
 "Practical Numerical Algorithms for Chaotic Systems". *Springer-Verlag, New York, 1989*.
- Pecora L.M. and Carroll T.L. [1990].
 "Synchronization in chaotic systems". *Physical Review Letters*, VOL. 64, NO. 8. pp. 821-824. February 1990.
- Pecora L.M. and Carroll T.L. [1991a].
 "Driving systems with chaotic signals". *Physical Review A*. pp. 2374-2383. August 1991.
- Pecora L.M. and Carroll T.L. [1991b].
 "Pseudoperiodic driving: eliminating multiple domains of attraction using chaos". *Physical Review Letters*, VOL. 67, NO. 8. pp. 945-948. August 1991.
- Perelló G. and Olivar G. [1995].
 "Estudi del comportament transitori del convertidor dc-dc buck". *Final Project, EUPVG*, September, 1995.
- Poddar G., Chakrabarty K. and Banerjee S. [1995].
 "Experimental Control of Chaotic Behavior of Buck Converter". *IEEE Transactions on Circuits and Systems, Part I*, Vol. 42, No. 8, pp. 502-504, August 1995.
- Poveda A., Martínez L., Perpinyà R., Font J. and Manuel A. [1993].
 "A novel current-mode technique for controlling the average value of converter switch current". *Proceedings of the 1993 International Symposium on Circuits and Systems*, pp. 2239-2342, 1993.
- Pujol P. and Olivar G. [1995].
 "Estudi gràfic del comportament caòtic d'un convertidor DC-DC". *Final Project, EUPVG*, October, 1995.
- Pyragas K. [1992].
 "Continuous control of chaos by self-controlling feedback". *Physics Letters A*, Vol. 170, pp. 421-428, 1992.

- Reboulet C. and Champetier C. [1984].
 “A new method for linearizing nonlinear systems: The pseudolinearization”. *International Journal of Control*, VOL. 40, NO. 4, pp. 631-638, 1984.
- Rega G. and Salvatori A. [1996].
 “Bifurcation structure at 1/3-subharmonic resonance in an asymmetric nonlinear elastic oscillator”. *International Journal of Bifurcation and Chaos*, VOL. 6, NO. 8, pp. 1529-1546, 1996.
- Romeiras F.J., Grebogi C., Ott E. and Dayawansa W.P. [1992].
 “Controlling chaotic dynamical systems”. *Physica D*, VOL. 58, pp.165-192, 1992
- Roncero O. and Olivar G. [1996].
 “Control de Órbitas periódicas”. *Final Project*, EUPVG, July 1996.
- Rössler O.E. [1977].
 “Chaos in abstract kinetics: two prototypes”. *Bulletin of Mathematical Biology*, VOL. 39, pp. 275-289, 1977.
- Rugh W.J.. [1996].
 “Linear System Theory (Second Edition)”. *Prentice Hall Information and System Sciences Series*.
- Saito T. and Mitsubori K. [1994].
 “Rigorous and realistic control of piecewise linear chaos”. *Proceedings of the 1994 International Symposium of Circuits and Systems*, pp. 81-84, 1994.
- Salan F.M.A. and Levi M.L. (editors) [1988].
 “Dynamical Systems Approaches to Nonlinear Problems in Systems and Circuits”. SIAM, Philadelphia 1988.
- Salut G., Marpinard J.C. and Valentin M. [1985].
 “Large signal feedback control for power switching converters”. *IEEE PESC Record*, pp. 741-750, 1985.
- Sanders S.R., Noworolski J.M., Liu X.Z. and Verghese G.C. [1991].
 “Generalized Averaging Method for Power Conversion Circuits”. *IEEE Transactions on Power Electronics*, Vol. 6, No. 2, pp. 251-259, April 1991.
- Sanders S.R., Verghese G.C. and Cameron D.F. [1986].
 “Nonlinear control laws for switching power converters”. *Proceedings of the 25th IEEE Conference on Decision and Control, Athens, Greece*. December 1986.
- Schuster H.G. [1988].
 “Deterministic chaos”. *VCH, Weinheim*, 1988.
- Seydel R. [1994].
 “Practical Bifurcation and Stability Analysis”. *Interdisciplinary Applied Mathematics*. Springer-Verlag, New York 1994.

- Sharkovsky A.N. and Chua L.O. [1993].
 “Chaos in 1-D discontinuous maps that appear in the analysis of electrical circuits”. *IEEE Transactions on Circuits and Systems-I*, VOL. 40, NO. 10. pp. 722-731. October 1993.
- Shilnikov L.P. [1993].
 “Chua’s circuit: rigorous results and future problems”. *IEEE Transactions on Circuits and Systems-I*, VOL. 40, NO. 10. pp. 784-786. October 1993.
- Shinbrot T., Grebogi C., Ott E. and Yorke J.A. [1993].
 “Using small perturbations to control chaos”. *Nature*, VOL. 363, pp. 411-417, June 1993.
- Singer S. [1988].
 “Loss-free gyrator realization”. *IEEE Transactions on Circuits and Systems*, VOL. 35, NO. 1, pp. 26-34, January 1988.
- Sira-Ramírez H.J. [1987].
 “Sliding motions in bilinear switched networks”. *IEEE Transactions on Circuits and Systems*, VOL. CAS-34, NO. 8, pp. 919-933, August 1987.
- Sira-Ramírez H.J. [1989a].
 “A geometric approach to pulse-width modulated control in nonlinear dynamical systems”. *IEEE Transactions on Automatic Control*, VOL. 34, NO. 2, pp. 184-187, February 1989.
- Sira-Ramírez H.J. [1989b].
 “Switched control of bilinear converters via pseudolinearization”. *IEEE Transactions on Circuits and Systems*, VOL. 36, NO. 6, pp. 858-865, June 1989.
- Sira-Ramírez H.J. and Ilic M. [1988].
 “A geometric approach to the feedback control of switch mode dc-to-dc power supplies”. *IEEE Transactions of Circuits and Systems*, VOL. 35, NO. 10, pp. 1291-1298, October 1988.
- Sira-Ramírez H.J. and Ilic M. [1990].
 “Exact linearization in switched mode dc to dc power converters”. *International Journal of Control*, VOL. 50, NO. 2, pp. 511-524, 1990.
- Sira-Ramírez H.J. and Ríos-Bolivar M. [1994].
 “Sliding Mode Control of Dc-Dc Power Converters Via Extended Linearization”. *IEEE Transactions on Circuits and Systems, Part I*, Vol. 41, No. 10, pp. 652-661, October 1994.
- Socolar J.E.S., Sukow D.W. and Gauthier D.J. [1994].
 “Stabilizing unstable periodic orbits in fast dynamical systems”. *Physical Review E*, VOL. 50, pp. 3245-3248, October 1994.
- Stolovitzky G., Kaper T.J. and Sirovich L. [1995].
 “A simple model of chaotic advection and scattering”. *Chaos*, Vol. 5, No. 4, pp. 671-686, 1995.

- Strogatz S.H. [1994].
 “Nonlinear dynamics and chaos”. *Addison-Wesley, Reading, 1994.*
- Su R. [1982].
 “On the linear equivalents of nonlinear systems”. *Systems and Control Letters, VOL. 2, NO. 1*, pp. 48-52, July 1982.
- Tang Y.S., Mees A.I. and Chua L.O. [1983].
 “Synchronization and chaos”. *IEEE Transactions on Circuits and Systems, VOL. 30, NO. 9*. pp. 620-626. September 1983.
- Tarter R.E. [1993].
 “Solid-State Power Conversion Handbook”. *Wiley-Interscience, New York 1993.*
- Thompson J.M.T. and Bishop S.R. [1994].
 “Nonlinearity and Chaos in Engineering Dynamics”. *Wiley, Chichester 1994.*
- Tokunaga R., Komuro M., Matsumoto T. and Chua L.O. [1989].
 “Lorenz attractor from an electrical circuit with uncoupled continuous piecewise-linear resistor”. *International Journal of Circuit Theory and Applications, VOL. 17*, pp. 71-85, 1989.
- Toribio A. and Toribio E. [1995].
 “Software para la caracterización no lineal del buck converter”. *Memoria Técnica del Seminario Anual de Automática y Electrónica Industrial, Tarragona (Spain), September 1995.*
- Tse C.K. [1994a].
 “Flip Bifurcation and Chaos in Three-State Boost Switching Regulators”. *IEEE Transactions on Circuits and Systems, Part I, Vol. 41, No. 1*, pp. 16-23, January 1994.
- Tse C.K. [1994b].
 “Chaos from a Buck Switching Regulator Operating in Discontinuous Mode”. *International Journal of Circuit Theory and Applications, Vol. 22, No. 4*, pp. 263-278, July/Agost 1994.
- Tse C.K. and Chan W.C.Y. [1995].
 “Instability and Chaos in a Current-Mode Controlled Cuk Converter”. *PESC'95*, pp. 608-613, Atlanta Georgia, 1995.
- Tsividis Y.P. [1979].
 “Analytical and experimental evaluation of a switched-capacitor filter and remarks on the resistor/switched capacitor correspondence”. *IEEE Transactions on Circuits and Systems, VOL. CAS-26, NO. 2*, pp. 140-144, February 1979.
- Tymerski R. [1991].
 “Volterra Series Modelling of Power Conversion Systems”. *IEEE Transactions on Power Electronics, Vol. 6, No. 4*, pp. 712-718, October 1991.

- Tymerski R. [1994].
 “Application of the Time-Varying Transfer Function for Exact Small-Signal Analysis”. *IEEE Transactions on Power Electronics*, Vol. 9, No. 2, pp. 196-205, March 1994.
- Utkin V.I. [1977].
 “Variable structure systems with sliding modes”. *IEEE Transactions on Automatic Control*, VOL. AC-22, pp. 212-222, 1977.
- Utkin V.I. [1978].
 “Sliding modes and their applications in variable structure systems”. *MIR, Moscow, 1978*.
- Utkin V.I. [1981].
 “Sliding modes in problems of optimization and control”. *Nauka, Moscow, 1981*.
- Utkin V.I. [1983].
 “Variable structure systems: Present and future”. *Automat. Remote Contr.*, VOL. 44, NO. 9, PT. 1, pp. 1105-1119, 1983.
- Valentin M. [1984].
 “Contribution a l’analyse des convertisseurs statiques et leur commande a fort signal”. *Ph. D. Thesis, Universite Paul Sabatier, Toulouse*. December 1984.
- Van der Pol B. and Van der Mark J. [1927].
 “Frequency demultiplication”. *Nature*, Vol. 120, No. 3019, pp. 363-364, September 1927.
- Veitch D. [1993].
 “The approach to constrained equations”. *Physics Letters A*, VOL. 183, NO. 4. pp. 319-326. December 1993.
- Venkataramanan R., Sabonovic A. and Ćuk S. [1985].
 “Sliding mode control of dc-to-dc converters”. *Proceedings of the 1985 International Conference on Industrial Electronics Control and Instrumentation. (IECON’85)*, pp. 251-258, 1985.
- Verghese G. and Mukherji U. [1981].
 “Extended averaging and control procedures”. *IEEE PESC Record*, pp. 329-336, 1981.
- Wester G.W. and Middlebrook R.D. [1972].
 “Low frequency characterization of switched dc-dc converters”. *IEEE PESC Record*, 1972.
- Wiggins S. [1988].
 “Global bifurcations and chaos”. *Springer-Verlag, New York, 1988*.
- Wiggins S. [1990].
 “Introduction to applied nonlinear dynamical systems and chaos”. *Springer-Verlag, New York, 1990*.

Willems J.C. [1972a].

“Dissipative dynamical systems. Part I: General theory”. *Arch. Rational Mech. Anal.*, VOL. 45, NO. 5, pp. 321-351, 1972.

Willems J.C. [1972b].

“Dissipative dynamical systems. Part II: Linear systems with quadratic supply rates”. *Arch. Rational Mech. Anal.*, VOL. 45, NO. 5, pp. 352-393, 1972.

Witulski A.F. and Erickson R.W. [1990].

“Extension of state space averaging to resonant switches and beyond”. *IEEE Transactions on Power Electronics*, VOL. 5, NO. 1 pp. 98-109, January 1990.

Wood J.R. [1973].

“Power conversion in electrical networks”. *Ph. D. Thesis, EECS Dept., MIT, 1973.*

Wood J.R. [1989].

“Chaos: a real phenomenon in power electronics”. *IEEE Applied Power Electronics Conference Record.* pp. 115-124, Baltimore MD, March 1989.

Wu C.W. and Chua L.O. [1994].

“Symbolic dynamics of piecewise-linear maps”. *IEEE Transactions on Circuits and Systems-II*, VOL. 41, NO. 6. pp. 420-423. June 1994.

Zafrany I. and Ben-Yaacov S. [1995].

“A Chaos Model of Subharmonic Oscillations in Current-Mode PWM Boost Converters”. *PESC'95*, pp. 1111-1117, Atlanta Georgia, 1995.